THÈSE POUR OBTENIR LE GRADE DE DOCTEUR DE L'UNIVERSITÉ DE MONTPELLIER

En Sciences de l'Eau

École doctorale GAIA

Unité de recherche Hydrosciences Montpellier (UMR 5151)

Apport des isotopes stables de l'antimoine pour le traçage des sources de pollution et des processus de transfert dans les milieux aquatiques

Présentée par Colin FERRARI

Le 6 Décembre 2022

Sous la direction de Corinne CASIOT,
Co-encadrée par Eléonore RESONGLES, Rémi FREYDIER et Merlin MEHEUT

Devant le jury composé de

Corinne CASIOT, Directrice de recherche au CNRS, Montpellier	Directrice
Yann SIVRY, Maître de conférences à l'Université Paris cité, Paris	Rapporteur
Anne-Catherine PIERSON-WICKMANN, Maître de conférences à l'Université de Rennes, Rennes	Rapportrice
Oleg POKROVSKY, Directeur de recherche au CNRS, Toulouse	Examinateur
Sophie AYRAULT, Cadre scientifique au CEA, Gif sur Yvette	Examinatrice
Françoise ELBAZ-POULICHET, Directrice de recherche au CNRS, Montpellier	Présidente du jury
Delphine BOSCH, Directrice de recherche au CNRS, Montpellier	Représentante UM
Eléonore RESONGLES, Chargée de recherche à l'IRD, Montpellier	Co-encadrante
Rémi FREYDIER, Ingénieur de recherche au CNRS, Montpellier	Co-encadrant, invité
Merlin MEHEUT, Maitre de conférences à l'Université Toulouse 3 Paul Sabatier, Toulouse	Co-encadrant, invité

UNIVERSITÉ DE MONTPELLIER

Remerciements

Après trois années passées au sein du laboratoire Hydrosciences, je tiens à remercier toutes les personnes qui, de près ou de loin ont été impliquées dans mon travail de thèse.

J'aimerais tout d'abord remercier ma directrice de thèse, Corinne Casiot et mes co-encadrants de thèse Eléonore Resongles, Rémi Freydier et Merlin Méheut. Je remercie sincèrement Corinne pour la confiance qu'elle m'a accordé dès notre premier entretien, pour son implication dans ce travail de thèse, sa disponibilité et sa bienveillance ainsi que ses conseils lors des phases de rédaction, qui ont fait ce qu'est devenu ce travail de thèse. Merci aussi à Eléonore, d'avoir été autant présente et enthousiaste de travailler avec moi, de toutes ces longues heures passées au multi-collecteur, en salle blanche ou sur le terrain dont je garderai d'excellents souvenirs. Merci pour cette rigueur que tu m'as enseignée, et de ta disponibilité. De même, j'aimerais remercier Rémi pour son implication au cours de cette thèse, et d'avoir supervisé tout le côté analytique et pour tout le temps passé à tenter d'optimiser les analyses au multi-collecteur et de sa bienveillance et sa passion lors de ses explications sur le fonctionnement des diverses machines. Et enfin, je tiens aussi à remercier Merlin pour son implication dans le volet calculs théoriques de cette thèse, et surtout de sa patience et du temps qu'il a pris pour m'expliquer (et me réexpliquer) les principes fondamentaux de la chimie quantique et de la théorie de la fonctionnelle de la densité, à moi qui étais totalement étranger à ces principes.

Vous avez été une équipe encadrante de thèse vraiment formidable, et c'est grâce à vous que j'ai pu autant m'épanouir au cours de ces trois années, et je ne vous remercierai jamais assez pour cela !

Je voudrais aussi remercier Patrick Seyler et Patrick Lachassagne, directeurs du laboratoire Hydrosciences Montpellier pour leur accueil et leur intérêt pour mon travail de thèse, ainsi que tout le personnel du laboratoire pour m'avoir aidé lors de ce travail de thèse : Sophie Delpoux pour son aide précieuse et son temps qui a été consacré aux analyses HG-ICP-MS et de spéciation, Léa Causse pour les analyses ICP-MS, Angélique Désœuvre et Marina Héry pour leur aide sur le volet microbiologie et pour leurs encouragements, Mylène Marie pour son aide et les bons moments au laboratoire ou en salle blanche, ainsi que tout le personnel administratif qui a notamment aidé pour les ordres de missions et la préparation de la mission de terrain en Bolivie. Et enfin, j'aimerais aussi remercier Roger Saraiva et aussi Kristine Gujda, pour sa bonne humeur, son sourire quotidien et son soutien de tous les jours. Je remercie aussi les membres du GET pour leur accueil lors de mon séjour en janvier 2020.

Merci aussi à toute l'équipe enseignante que j'ai côtoyée au cours de ces trois années de monitorat, Véronique(s), Marine, Séverin, Yohann, Christelle, Didier, François et Marina. Un grand merci aussi à l'équipe de terrain, Pierre et Rémi pour le temps passé ensemble avec les étudiants au bord du Lez. Et enfin, merci aussi à Jeyameera pour ces moments passés dans le cadre de la vulgarisation scientifique dans les divers lycées et collèges de la région.

J'aimerais maintenant remercier les membres de mon comité de thèse, Bruno Dhuime pour sa disponibilité, sa gentillesse et ses encouragements, Stéphane Guédron pour ses questions (pas toujours évidentes à répondre mais toujours pertinentes) et aussi Patrick Seyler. Merci aussi à tous les membres du jury de thèse : à Yann Sivry et Anne-Catherine Pierson-Wickmann d'avoir accepté d'être

rapporteur et de leur bienveillance lors de la soutenance, merci aussi à Oleg Pokrovsky, Sophie Ayrault, François Elbaz-Poulichet et Delphine Bosch pour leurs retours, leurs questions et pour avoir accepté de participer à mon jury de thèse.

J'aimerais aussi remercier Laurent Charlet, qui, lors de mon stage de master 2, m'a donné autant le goût pour la recherche et de son soutien.

Je tiens de même à remercier David, Naoual, Manon et Laura, les étudiants avec qui j'ai eu la chance de travailler au cours de ma thèse et des bons moments passés à travailler ou à discuter, mais surtout pour leur contribution à ce travail de thèse, et leur aide précieuse pour les expérimentations de sorption et microbiologiques. Merci aussi à Léa Pradeilles pour son aide lors des manips de sorption de l'antimoine, et de ces mesures de pH qui n'en finissaient plus.

Je voudrais maintenant prendre le temps de remercier mes collègues doctorants, post-doctorants et contractuels que j'ai eu beaucoup de plaisir à côtoyer. Merci à Vianney, Marie, Victor, Garance, Cyrine, Fatima, Junior, Chloé, Ben, Behshad, Coralie, Elia, Leila, Laïna, Nesrine, Clémence, Marjorie, Justine, Chrystelle, Aurélie, Raphaël, Yohann et Conny pour ces bons moments passés lors des repas, des pauses ou des sorties. Merci aussi et surtout à Camila, de m'avoir supporté dans son bureau pendant les trois années de la thèse, et tous ces moments que l'on a passé aux différents stades de nos thèses !

Enfin, j'aimerais remercier aussi mon entourage. Mes amis du lycée qui m'ont toujours soutenu tout au long de mes études : Minh, Antho, Nico, Thomas, Guigui, Susie, Adrian, Fiona ce fut toujours un plaisir et une bouffée d'air frais de vous retrouver en Ariège après ces longs mois passés à l'université. Ensuite, je voudrais remercier mes amis de mes premières années d'université, Nico, Bran, Mike, Anne et Hélène, et enfin, de mon master, merci à Chris, Kawtar, Julie et plus particulièrement à Carlos, qui a toujours pris le temps de m'écouter et de me conseiller lorsque je bloquais sur mes études.

Merci aussi à ma famille, à ma mère pour ses encouragements, son support et sa relecture du manuscrit. Et j'ai enfin une pensée spéciale pour mon père, pour son soutien et sa fierté inconditionnelle, mais qui n'aura jamais pu voir ce manuscrit achevé.

Et enfin, je voudrais aussi remercie Yang, pour son soutien de tous les jours, ces moments complices partagés et de m'avoir aidé à me sentir soutenu tout le long de ce doctorat.

Table des matières

Introduction générale.....11

Chapitre 1 : Synthèse bibliographique.....15

PARTIE A : L'antimoine, un polluant d'intérêt prioritaire 16

I. Généralités sur l'antimoine 16

1.a. Utilisation historique et moderne 16

1.b. Sources naturelles et anthropiques 17

1.c. Concentrations dans l'environnement 20

1.d. Exposition et toxicité pour l'humain 24

II. Comportement de l'antimoine en milieu aquatique 26

2.a. Spéciation en phase dissoute 26

2.b. Mécanismes de sorption 29

2.c. Interactions avec les micro-organismes 31

PARTIE B : Les isotopes stables des métaux comme traceurs de sources et de processus 33

I. Généralités sur les isotopes stables 33

1.a. Introduction..... 33

1.b. Nomenclature..... 34

1.c. Fractionnement cinétique vs fractionnement à l'équilibre..... 35

1.d. Principes généraux du fractionnement isotopique..... 36

1.e. Méthodes d'étude du fractionnement isotopique 37

II. Processus à l'origine de fractionnements isotopiques au sein des environnements miniers et des eaux de surface 38

III. Applications des isotopes stables de métaux pour le traçage des sources et des processus géochimiques dans les milieux aquatiques contaminés par les activités anthropiques et minières 45

3.a. Cadmium (Cd)..... 45

3.b. Sélénium (Se)..... 46

3.c. Chrome (Cr) 47

3.d. Antimoine (Sb)..... 48

Bibliographie..... 50

Chapitre 2 : Développement analytique d'une méthode de purification simplifiée de Sb pour la mesure précise du rapport isotopique $^{123}Sb/^{121}Sb$ par HG-MC-ICP-MS.....71

Introduction..... 72

A single-step purification method for the precise determination of antimony isotopic composition of environmental, geological and biological samples by HG-MC-ICP-MS 74

Chapitre 3 : Etude théorique et expérimentale du fractionnement isotopique de Sb.....91

Introduction..... 92

PARTIE A : Fractionnement isotopique dépendant de la masse à l'équilibre de l'antimoine entre la stibine et les minéraux secondaires de Sb : une étude basée sur la dynamique moléculaire *ab initio* (article 2) 93

PARTIE B : Fractionnement isotopique de l'antimoine lors de la sorption de Sb(V) et Sb(III) sur la schwertmannite etla ferrihydrite (article 3)..... 126

PARTIE C : Fractionnement isotopique de l'antimoine lors de l'oxydation de Sb(III) en Sb(V) : processus biotiques et abiotiques (article 4) 149

Chapitre 4 : Utilisation des isotopes de l'antimoine en contexte minier.....167

Introduction..... 168

Sb isotopes in surface waters of the mining and smelting city of Oruro, Bolivia..... 170

Conclusion générale.....191

Résumé 196

Abstract 196

Table des illustrations et des tableaux

Chapitre 1 : Synthèse bibliographique

Figure 1 : Minéraux principaux et secondaires de l'antimoine couramment rencontrés dans l'environnement. 18
Figure 2 : Schéma d'un drainage minier acide et de son impact sur la contamination des cours d'eau en aval. 19
Figure 3 : Aperçu du cycle de vie de l'antimoine et de ses principales sources lors de son utilisation industrielle..... 20
Figure 4 : Carte de la distribution globale des émissions atmosphériques d'antimoine pour l'année 2010. 24
Figure 5 : Structures de la forme dissoute trivalente et pentavalente de l'antimoine.. 26
Figure 6 : Diagramme Eh-pH de l'antimoine en phase dissoute pour les espèces Sb(III) et Sb(V) calculé d'après des modèles thermodynamiques. 27
Figure 7 : Tableau périodique des éléments tiré de Wiederhold 2015..... 34
Figure 8: Illustration schématique du fractionnement cinétique et à l'équilibre.. 35

Tableau 1 : Fractionnement isotopique de Cu, Zn et Fe lors de la dissolution abiotique de minéraux sulfurés à basse température……39
Tableau 2 : Fractionnements isotopiques de différents métaux lors de la précipitation de la phase aqueuse vers divers minéraux à faible température……43

Chapitre 2 : Développement analytique d'une méthode de purification simplifiée de Sb pour la mesure précise du rapport isotopique $^{123}Sb/^{121}Sb$ par HG-MC-ICP-MS

Article 1 :

Figure 1: $\delta^{123}Sb$ values for purified and unprocessed in-house SPEX isotopic standard analysed over a 3-day analytical session……81
Figure 2: Comparison of the $\delta^{123}Sb$ values (‰) for the in-house isotopic standard SPEX after $^{123}Sb/^{121}Sb$ outliers exclusion using methods A and B……81
Figure 3: $\delta^{123}Sb$ in studied biological, environmental, and geological CRM (‰)……82
Figure S1: Scheme of the procedure for the determination of Sb isotopic composition in environmental, biological and geological solid samples including sample digestion, antimony purification and antimony isotope analysis……88
Figure S2: Comparison of methods A and B for the exclusion of outlier values of measured $^{123}Sb/^{121}Sb$ ratio……89

Table 1: Synthesis of existing strategies for Sb purification and Sb isotope analyses by MC-ICP-MS….75
Table 2: Summary of the digestion procedures used for the different CRM type……76
Table 3: Elution scheme for purification of Sb using Thiol-functionalized Silica Powder……77
Table 4: Instrument parameter settings used for Sb isotope analysis by HG-MC-ICP-MS……79
Table 5: Extraction yield and purification recovery for the certified reference materials……80
Table 6: Average removal rates obtained from all CRM for the potential interfering elements and the

highest element:Sb ratios measured for each element in purified samples……80
Table S1: Instrument settings for ICP-MS and HG-ICP-MS analysis……86
Table S2: Residual Element:Sb ratios measured by ICP-MS in the purified samples after the purification process……87
Table S3: Comparison of the δ^{123}Sb values (‰) and their uncertainties (2 standard deviation, 2sd) obtained following the statistical treatment of isotope analysis data (outlier exclusion) using methods A and B……87
Table S4: Final δ^{123}Sb values of the different CRM with their uncertainties and the number of measurements of the purified solution……88

<u>Chapitre 3 : Etude théorique et expérimentale du fractionnement isotopique de Sb</u>

Article 2 :

Figure 1: Scheme of stibnite transformation process from Sb_2S_3 to Sb_2O_5 modelled in this study indicating the crystal system, the spacegroup of the minerals and Sb coordination number.. 96
Figure 2: Raman spectrum of valentinite calculated with the PBEsol functional compared with the experimental valentinite Raman spectrum measured at ambient temperature and pressure reproduced from Gonçalves et al. (2018) 101
Figure 3: a) Theoretical Raman spectrum of senarmontite calculated with the PBEsol functional compared with b) the experimental spectrum measured at ambient pressure, reproduced from Pereira et al. (2012). 101
Figure 4: Average Raman spectrum of cervantite calculated with the PBEsol functional. 102
Figure 5: Raman spectrum of Sb_2O_5 calculated in this study with the PBEsol functional. 103
Figure 6: β-factors (in ‰) of the different mineral phases during the oxidation process of the stibnite (Sb_2S_3) to the synthetic fully oxidized mineral phase Sb_2O_5 as a function of temperature (T)……104
Figure 7: Comparison of the β-factors calculated using different functionals (GGA (PBE, PBEsol) and LDA (PZ)) for stibnite (Sb_2S_3), valentinite (Sb_2O_3) and cervantite (Sb_2O_4). 105
Figure 8: Theoretical Raman frequencies (PBEsol functional) as a function of the experimental Raman frequencies of the different studied minerals……105
Figure S1: Contribution of the various frequencies to the β-factor (PBESOL_us calculation) of stibnite and valentinite……125

Table 1: Calculated cell parameters with the different functionals (PBE, PZ, PBEsol) determined in this study compared to the experimental data and calculations from other authors……99
Table 2: Recommended fits of the β-factors calculated for the PBEsol functional with us pseudopotentials and based on an equation of the type $ax^2 + bx^3$, with $x = 10^3/T$ (K)……103
Table 3: Raw and corrected β -factors for stibnite, valentinite, senarmontite and cervantite at 22 °C.106
Table 4. Estimates (Schauble 2013) of changes in effective electron density at the nucleus for various equilibria similar to Sb_2O_5-Sb_2O_3 (oxygen reductions Mn+On/2 -Mn(n-2)+O(n-2)/2) or to Sb_2O_3-Sb_2S_3 (O-S exchanges)……107
Table S1: Calculated Raman frequencies (in cm^{-1}) of stibnite for different symmetries compared with theoretical and experimental frequencies from Ibáñez et al. (2016)……117
Table S2: Calculated Raman frequencies (in cm^{-1}) and intensities of the valentinite compared with experimental data from Gonçalves et al. (2018)……118
Table S3: Calculated Raman frequencies (cm^{-1}) and Raman intensities of the senarmontite (cm^{-1})

compared with experimental results from Mestl et al., (1994) and Peirera et al. (2012) and other theoretical Raman frequencies (from Peirera et al., 2012) calculated with the CRYSTAL09 program package……119
Table S4: Calculated Raman frequencies (in cm^{-1}) and Raman intensities of the cervantite compared with previous literature data from Cody et al. (1979)……..120
Table S5: Calculated Raman frequencies (in cm^{-1}) of Sb_2O_5. These frequencies were calculated with PBESOL-dn-rrkjus as this functional proved its accuracy on the previous models. No exploitable experimental data was found as comparison for the validation of this structure……..122
Table S6: Values of β-factors in function of the temperature (in K and °C) based on the PBEsol functional for the different studied structures……123
Table S7: Values of β-factors in function of the temperature (in K and °C) based on the PBEsol functional for the two different Sb sites of the stibnite……124

Article 3 :

Figure 1: Freundlich sorption isotherms modelled for (a) Sb(V) and (b) Sb(III) on ferrihydrite at pH 6, 7 and 7.5 and for (c) Sb(V) and (d) Sb(III) on schwertmannite at pH 2.5 and 4.5……132
Figure 2: Sb isotope composition ($\delta^{123}Sb$) of dissolved and adsorbed during Sb(V) and Sb(III) adsorption on ferrihydrite……133
Figure 3: Sb isotope composition ($\delta^{123}Sb$) of dissolved and adsorbed during Sb(V) and Sb(III) adsorption on schwertmannite……133
Figure S1: XRD diffractograms of synthetized ferrihydrite and schwertmannite……..147
Figure S2: SEM images of the synthetized schwertmannite showing the “hedge-hog”-like structure characteristic of schwertmannite……147
Figure S3: Kinetic monitoring of the sorption of Sb(III) and Sb(V) on schwertmannite at pH 4.5 and of the sorption of Sb(V) on ferrihydrite at pH 6…… ……..147
Figure S4: Linear Freundlich sorption isotherms of Sb(III) on ferrihydrite and schwertmannite, and Sb(V) on ferrihydrite and schwertmannite calculated with Equation 4……148
Figure S5: Variation of the proportion of Sb(II) in the dissolved phase at equilibrium (48 h) as a function of Fe:Sb molar ratio and pH in sorption experiments with ferrihydrite and schwertmannite……..148

Table S1: Antimony isotope composition of dissolved Sb(III) and Sb(V) after 48 h and 96 h in sorption experiments on schwertmannite for initial Sb concentrations of 0.1 $mg.L^{-1}$ or 10 $mg.L^{-1}$ showing that isotopic equilibrium was reached after 48 h……145
Table S2: Hydride generation parameters used for Sb isotope ratio analysis by HG-MC-ICP-MS. These are optimized based on the ones indicated in Ferrari et al. (2021)……146

Article 4 :

Figure 1: Evolution of the oxidation of Sb(III) in biotic experiments RDB0, RDB1-3 and RDB4……155
Figure 2: Isotopic composition ($\delta^{123}Sb$) of Sb(III) and Sb(V) during biotic oxidation of Sb(III) by RDB at pH 6……..156
Figure 3: Oxidation kinetics of Sb(III) and isotopic composition ($\delta^{123}Sb$) of Sb(III) and Sb(V) during abiotic oxidation by H_2O_2……156
Figure S1: Optic Density measured at 600 nm for biotic, abiotic, and control batches……..166

Table 1:Elution scheme for the separation of the Sb(III) and Sb(V) species using thiol-functionalized silica powder……..154
Table S1: Evolution of the optical density and the bacterial cell concentration in biotic (RDB0, RDB1-3 and RDB4) and abiotic (Abio1-3 and Control1-3) experiments over time…….164
Table S2: Recovery rate of pure Sb(III) and pure Sb(V) solutions on TSP …….165
Table S3: Comparison between the percentage of oxidation calculated through HPLC and recovered through the physical separation of Sb(III) and Sb(V) on TSP ……..165
Table S4: δ^{123}Sb of the Sb(III) and Sb(V) species physically separated on TSP in the same H_2O_2, Sb and $NaNO_3$ concentrations than the online experiment described in 2.2.2 Chemical oxidation at pH 9…..166

<u>Chapitre 4 : Utilisation des isotopes de l'antimoine en contexte minier</u>

Article 5 :

Figure 1: Location of the sampling stations and of the main mining and industrial activities in the city of Oruro (Bolivia)……173
Figure 2: Distribution (in %) of Sb in the water column among the truly dissolved (<10 kDa), colloidal (> 10 kDa and < 0.22 µm) and particulate (> 0.22 µm) fractions. The colloidal fraction was calculated by the difference between Sb concentrations in the dissolved fraction filtrated at 0.22 µm and ultrafiltrated at 10 kDa……180
Figure 3: Variability of the Sb isotopic composition during the wet season (2019) and the dry season (2021) as a function of the distance to the San José mine gallery exit ……181

Table 1: Main physico-chemical parameters and concentrations of Sb, Fe, S, and DOC in water (< 0.22 µm), SPM, and sediments from the rivers at the end of the wet (March 2019) and dry (October 2021) seasons. Antimony isotopic composition (δ^{123}Sb ±- 2σ) are also reported……178
Table 2: Drinking water in the city of Vinto……..179
Table S1: Hydride generation parameters used for Sb isotope ratio analysis by HG-MC-ICP-MS. These are optimized based on the ones indicated in Ferrari et al. (2021)……190

<u>Conclusion générale</u>

Figure 36 : Schéma récapitulatif des processus étudiés et leur impact sur le fractionnement isotopique de l'antimoine……..193

Introduction générale

L'antimoine (Sb) est un métalloïde omniprésent dans l'environnement dû aux processus naturels et aux activités humaines. De nombreuses activités anthropiques sont responsables d'importants rejets d'antimoine dans l'environnement et plus particulièrement dans le milieu aquatique (mines, activités industrielles, réseaux routiers et urbains, terrains de tirs…). La production d'antimoine de ces dernières années a continué d'augmenter, en passant de 120000 tonnes d'antimoine produites en 2008 à plus de 160000 en 2016 (Brown et al. 2019). Souvent rencontré avec d'autres éléments et en particulier avec des métalloïdes et des métaux de transition (As, Fe, Pb, Zn, Cu…), il n'est pas évident de connaitre spécifiquement l'effet de l'antimoine sur les milieux aquatiques ainsi que sur les organismes. De plus, l'intérêt de la communauté scientifique pour l'antimoine a été limité jusqu'à récemment en comparaison à d'autres contaminants (e.g., As, Pb, Hg,…). De ce fait, le cycle géochimique de l'antimoine ainsi que son comportement dans le milieu aquatique sont assez peu connus.

Les zones les plus impactées par des contaminations en antimoine sont les zones minières, en activité ou historiques. Les plus grandes mines d'antimoine se trouvent en Chine (premier producteur mondial de Sb), avec en particulier la mine de Xikuangshan qui produit environ 40000 tonnes de Sb par an (Wang et al. 2011). D'autres sites miniers de plus ou moins grande envergure existent à travers le monde, notamment en Bolivie (ville minière d'Oruro, Goix 2012), ou en France par exemple (Cévennes, Resongles 2014). Une voie importante de transfert de l'antimoine des sites miniers vers l'environnement est la voie hydrique, et en particulier par la formation de drainages miniers acides qui peuvent contenir plusieurs milligrammes par litre d'antimoine, ou plus dans certains cas. Cependant, ces sites miniers sont souvent accompagnés de fonderies ou d'autres industries métallurgiques (Wang et al. 2011; Goix et al. 2013), créant d'autres sources de contamination et d'autres vecteurs de propagation (émissions atmosphériques de l'antimoine, via les fumées en particulier). Tous ces processus de transport et de transformation du minerai principal de l'antimoine (stibnite, Sb_2S_3), font des zones minières des terrains d'étude complexes, notamment lorsqu'il s'agit d'évaluer l'impact sur les populations ou sur les organismes (aquatiques et terrestres).

Plusieurs études effectuées sur le site minier d'Oruro (Altiplano bolivien) entre 2002 et 2019, et notamment des études impliquant des membres du laboratoire Hydrosciences Montpellier, ont permis de caractériser, d'une part la contamination d'origine minière ainsi que les différents paramètres physico-chimiques du drainage minier de San José et des cours d'eaux aux alentours, et d'autre part, les différents vecteurs de contaminations polymétalliques (plomb, arsenic et antimoine). Des études d'exposition ont montré des concentrations élevées en métaux et métalloïdes dans les cheveux des populations vivant près des zones minières et des fonderies à Oruro (Barbieri et al. 2011, 2014) ainsi que dans le lait maternel et le sang du cordon ombilical de femmes enceintes (Barbieri et al. 2016), avec une exposition importante des populations (particulièrement des enfants) à l'antimoine via les aérosols (Goix et al. 2011). Ces études ont montré que les principales sources de contamination des populations pour ces métaux étaient l'exposition par inhalation et/ou ingestion de particules contaminées issues des émissions de mines et fonderies, avec des taux d'exposition en antimoine 4 à 14 fois plus élevés pour les populations vivant aux alentours. Ces études ont motivé en partie l'objectif de cette présente thèse, à savoir le développement de l'utilisation des isotopes de l'antimoine pour améliorer le traçage des sources de contamination et des processus de transfert dans les milieux aquatiques. En effet, dans des environnements riches en antimoine avec des sources et des processus multiples, et des enjeux de santé publique, il est important de pouvoir discriminer les différentes

sources ainsi que les différents vecteurs de contamination à l'antimoine en développant de nouveaux outils de traçage.

C'est dans ce contexte qu'a été choisie la ville d'Oruro et le drainage minier acide de San José comme site d'étude pour cette thèse. Historiquement, le dôme volcanique qui borde cette ville située entre 3700 et 4200 m d'altitude est exploité depuis des siècles pour ses ressources minérales riches en Ag, Au, Pb, Sb, Sn et Zn (Cunningham et al. 1991). Une zone urbaine dense d'environ 250000 habitants s'est développée autour des activités minières à Oruro et d'environ 30000 habitants à Vinto (quelques kilomètres à l'est d'Oruro), où se situe la plus grande fonderie d'étain du pays (Goix et al. 2013). L'Altiplano bolivien est caractérisé par un climat semi-aride, avec une période humide allant de décembre jusqu'en mars. Lors de la saison sèche, les vents violents ainsi que la circulation sur les routes non goudronnées remettent en suspension des particules contaminées provenant des mines et des fonderies. Les différentes sources d'antimoine dans cette zone sont nombreuses (mines, fonderies, et possiblement le trafic urbain). Ainsi, le district minier et métallurgique d'Oruro, avec en son centre un drainage minier acide riche en Sb coulant de la mine de San José jusqu'au lac Uru-Uru, où l'antimoine subit différents processus de transformation (précipitation, adsorption sur des (oxy)hydroxydes de fer ou de la matière organique, oxydation…) constitue un site modèle pour étudier in-situ I) les différentes sources d'antimoine et leur signature isotopique et II) l'impact des processus sur le fractionnement isotopique de l'antimoine.

Les isotopes de métaux dits non-traditionnels ont démontré leur potentiel comme traceurs de sources et de processus depuis le développement de la spectrométrie de masse à multi-collection. L'isotopie de l'antimoine (^{121}Sb et ^{123}Sb) n'a été que très peu étudiée à ce jour, notamment du fait du verrou analytique que représente la mesure du rapport isotopique dans des échantillons environnementaux à faible teneur en Sb. Par ailleurs, les facteurs de fractionnement des isotopes de l'antimoine lors de processus biogéochimiques restent largement méconnus, limitant leur application comme traceurs géochimiques. Ainsi, cette thèse s'est d'abord attachée à valider une méthode de préparation et d'analyse des isotopes de l'antimoine dans diverses matrices environnementales puis à caractériser les fractionnements isotopiques de l'antimoine lors de processus clés de son cycle géochimique.

Ce manuscrit est organisé en 4 chapitres :

- <u>Le premier chapitre</u> présente une synthèse bibliographique divisée en deux parties. La première partie synthétise les connaissances actuelles sur les sources naturelles et anthropiques d'antimoine, ses utilisations dans l'industrie et ses effets sur la santé et les organismes, puis le cycle géochimique de l'antimoine est présenté et enfin son comportement dans les environnements miniers. La deuxième partie de ce chapitre sera consacrée à l'utilisation des isotopes stables de métaux comme traceurs de sources et de processus ; les rares études sur l'isotopie de l'antimoine y sont rassemblées.

- <u>Le deuxième chapitre</u> aborde la méthode analytique utilisée pour digérer, purifier et enfin analyser les isotopes de l'antimoine par génération d'hydrures couplée à la spectrométrie de masse multi-collection (HG-MC-ICP-MS). Plusieurs méthodes avaient été décrites dans la littérature pour l'analyse isotopique de l'antimoine, mais aucune n'était applicable et validée pour des matrices complexes variées présentant de faibles concentrations d'antimoine. Cette

nouvelle méthode de purification de l'antimoine utilisant la Thiol-Silice a été testée et validée pour un grand nombre de matrices différentes (roches, sédiments, sols, plantes, sang et urine, plastiques, poussières de routes…) afin d'avoir un protocole qui puisse être appliqué lors d'une étude environnementale complète. Ce chapitre a fait l'objet d'une publication au sein du *Journal of Analytical Adsorption Spectrometry* (JAAS) en 2021 et donne des valeurs de références (δ^{123}Sb) pour plusieurs matériaux de référence certifiés ainsi que pour plusieurs solutions standards mono-élémentaires de Sb.

- Le troisième chapitre se concentre sur les différents processus qui peuvent fractionner l'antimoine. Ce chapitre est essentiel afin de pouvoir comprendre le cycle isotopique de l'antimoine et de pouvoir interpréter les différentes signatures isotopiques mesurées dans l'environnement. Ce chapitre est séparé en deux. La première partie aborde l'étude de ces processus par des calculs théoriques utilisant la théorie de la fonctionnelle de la densité, en calculant les facteurs de fractionnement à l'équilibre entre la stibnite et ses produits d'oxydation, qui peuvent couramment se trouver au sein de cours d'eau impactés par l'activité minière.

  La seconde partie de ce chapitre aborde l'étude de processus par des méthodes expérimentales. Plusieurs processus couramment rencontrés dans l'environnement et plus particulièrement dans les drainages miniers acides ont été étudiés (oxydation biotique et abiotique ainsi que l'adsorption de l'antimoine sur des phases secondaires de fer), et s'appuient sur les résultats des calculs théoriques pour comprendre en partie ces fractionnements.

- Le quatrième chapitre, enfin, se focalise sur l'étude de l'antimoine dans les eaux, les matières en suspension et les sédiments du drainage minier d'Oruro, et vise à interpréter les changements de signature isotopique par la contribution de sources ou de processus différents, en s'appuyant sur la partie analytique pour les méthodes de purification et d'analyse ainsi que sur la partie expérimentale et théorique pour l'identification des différents processus.

Chapitre 1 :
Synthèse bibliographique

PARTIE A : L'antimoine, un polluant d'intérêt prioritaire

I. Généralités sur l'antimoine

1.a. Utilisation historique et moderne

L'antimoine est un élément connu et utilisé dès l'antiquité (Dardeniz 2020), dans l'artisanat (agent opacifiant de verre…), dans la cosmétique (khol, Anderson 2012) mais aussi en médecine (solution émétique, Lemery 1707). Son nom, sujet à de nombreuses hypothèses quant à son étymologie, proviendrait du grec ancien '*stibié*' (signifiant antimoine), puis d'un jeu singulier d'altération des langues en passant par les traductions arabes '*Ithmid*' puis '*Athmoud*' aurait résulté en '*Antimonium*' en latin Barbare (*Littré, 1877*).

L'antimoine est classé parmi les 50 matières premières critiques par les USA (U.S. Geological Survey 2022) et parmi les 20 matières premières critiques en 2020 identifiées par l'Union Européenne (COM(2020)474, 2020), sur la base de son importance économique et sa difficulté d'approvisionnement. La Chine est le principal producteur et exportateur d'antimoine depuis les années 1900, bien que ces dernières années sa production ait décliné de 90 % de la production mondiale en 2007 (163000 t) à 54 % (89000 t) en 2018 (Anderson 2012; Brown et al. 2019; He et al. 2019). Viennent ensuite la Russie (30000 t), le Tadjikistan (28881 t) et la Turquie (4000 t), et enfin, la Bolivie se place en cinquième position des pays producteurs d'antimoine avec près de 3100 tonnes produites en 2018 (Brown et al. 2019). Dans l'industrie moderne, cet élément est principalement utilisé dans les plastiques, comme retardateur de flammes sous forme de $NaSb(OH)_6$ (52 % de son utilisation), ou comme catalyseur dans la production de polyéthylène téréphtalate (PET) (Filella 2020; Filella et al. 2020), ainsi que dans certains matériaux électroniques. Certains plastiques ont besoin de 5 à 15 % de leur masse en antimoine pour être suffisamment ignifugés (Dupont et al. 2016). Il est également utilisé comme agent décolorant pour les lentilles optiques dans les caméras, les photocopieurs ou bien les tubes lumineux fluorescents (Dupont et al. 2016), sous forme d'antimoniate de sodium (Na_3O_4Sb). L'antimoine est utilisé dans le secteur automobile, où il a remplacé l'amiante dans les garnitures de frein, qui peuvent contenir entre 20 et 70 $g.kg^{-1}$ de Sb_2S_3 (Garg et al. 2000; Sternbeck, Sjödin, et Andréasson 2002; Hjortenkrans, Bergbäck, et Häggerud 2006; Mosleh et Khemet 2006); il est aussi utilisé comme alliage avec le plomb notamment dans les batteries des véhicules (augmentation de la résistance à la corrosion) et les munitions (He et al. 2019). Le recyclage de l'antimoine contenu dans les plastiques est difficilement envisageable du fait de la trop grande dispersion de l'antimoine au sein du produit, à la différence des alliages métalliques contenant Sb (Turner et Filella 2017), cependant aux Etats-Unis, environ 14 % de l'antimoine provient du recyclage (U.S. Geological Survey 2020).

1.b. Sources naturelles et anthropiques

Le cycle géochimique naturel de l'antimoine est fortement modifié par les activités humaines. En effet, il est estimé que plus de 80 % du flux d'antimoine à la surface terrestre est généré par les activités anthropiques (Sen et Peucker-Ehrenbrink 2012). Ainsi, les émissions de Sb dans l'environnement ont augmenté depuis le début de l'ère industrielle. Certains scénarios prévoient une augmentation par un facteur 2 des émissions atmosphériques de Sb entre 2010 et 2050 (Zhou et al. 2015).

2.1 Sources naturelles

Les sources naturelles de l'antimoine dans l'environnement (atmosphère, sols, milieux aquatiques) sont diverses. Les principales émissions naturelles de Sb vers l'atmosphère ont été estimées pour : le transport de poussières et de produits d'érosion des sols et de la croûte terrestre (entre 1000 et 3000 tonnes par an, valeur médiane de 800 tonnes par an), les activités volcaniques (de 10 à 1400 tonnes par an, valeur médiane de 700 tonnes par an), les feux de forêt (0 à 300 tonnes par an, valeur médiane de 200 tonnes par an), les sources biogéniques (émises à partir de la végétation, de 0 à 1200 tonnes par an) (Nriagu 1989). Au total, environ 2600 tonnes de Sb par an seraient émises naturellement dans l'atmosphère.

L'altération de minéraux riches en antimoine constitue la source naturelle principale de Sb dans les eaux de surface, les eaux souterraines et les sols. La minéralogie de l'antimoine est particulièrement diverse et on recense presque 200 minéraux qui contiennent de l'antimoine (Anthony et al. 1990; Roper, Williams, et Filella 2012), dont les plus courants sont reportés sur la Figure 1. L'antimoine étant un élément chalcophile, on le retrouve principalement sous forme de sulfures et sulfosels dans des minéraux primaires (Filella, Belzile, et Chen 2002; Roper, Williams, et Filella 2012). Sa forme la plus répandue et la plus exploitée, est la stibine (Sb_2S_3) (Lide 2005). L'antimoine est généralement associé à de nombreux métaux et métalloïdes, couramment rencontré sous forme de sulfosels Sb/métal tels que la boulangérite ($Pb_5Sb_4S_{11}$), la tétraédrite $(Cu,Fe)_{12}Sb_4S_{13}$ ou encore la chalcostibnite ($CuSbS_2$), mais peut aussi se rencontrer avec la plupart des métaux et métalloïdes (Ag, As, Au, Ba, Bi, Co, Cu, Cd, Fe, Hg, Ni, Pb, Se, Sn, Te,U, Zn…) ; l'arsenic est le métalloïde le plus fréquemment associé à l'antimoine (Herath, Vithanage, et Bundschuh 2017). Lorsque l'antimoine minéralise en l'absence de soufre, des phases oxydées ou silicatées sont formées comme la stibiotantalite ($SbTaO_4$), l'oxycalciorméite ($Ca_2Sb_2O_7$) ou la tripuhyite ($FeSbO_4$) (Roper, Williams, et Filella 2012). Ces phases sont généralement stables et peu solubles, à contrario des sulfures et des sulfosels, qui deviennent instables lorsqu'ils sont exposés à l'oxygène et à l'eau dans les conditions de surface. La dissolution oxydative des sulfures et des sulfosels libère Sb en phase aqueuse et peut conduire à la formation de minéraux secondaires de Sb. De nombreuses phases secondaires d'antimoine, principalement des oxydes et des oxyhydroxydes, ont été identifiées. Ainsi la chaîne d'oxydation stibine -> kermésite (Sb_2S_2O) -> sénarmontite (Sb_2O_3 cubique)/valentinite (Sb_2O_3 orthorhombique) -> cervantite (Sb_2O_4) est couramment observée (Roper, Williams, et Filella 2012). L'antimoine peut également s'associer à d'autres métaux pour former des oxydes et oxyhydroxydes tels que la bindheimite ($Pb_2Sb_2O_7$), la partzite ($Cu_2Sb_2(O,OH)_7$) ou la tripuhyite ($FeSbO_4$). Ces minéraux secondaires sont couramment rencontrés dans les environnements miniers à sulfures où ils jouent un rôle clé pour contrôler la mobilité de l'antimoine dans la zone critique (Roper, Williams, et Filella 2012; Anderson 2012).

D'autres sources naturelles plus singulières et avec un impact plus local peuvent exister, comme les sources géothermales. Les concentrations en Sb mesurées dans ces milieux sont variables mais peuvent dépasser 500 mg.L^{-1} (Filella, Belzile, et Chen 2001).

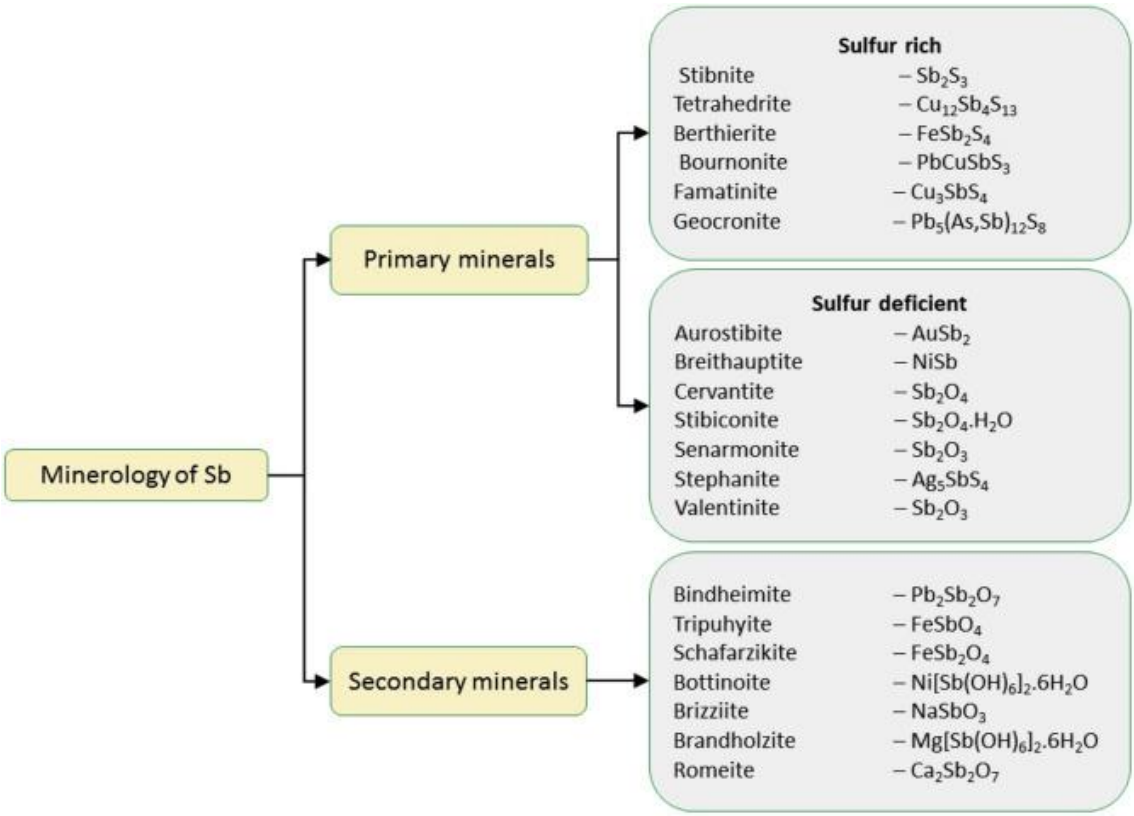

Figure 1: Minéraux principaux et secondaires de l'antimoine couramment rencontrés dans l'environnement. Issu de Herath et al., (2019).

2.2 Sources anthropiques de Sb

Du fait de son utilisation croissante dans l'industrie au cours des dernières décennies, l'antimoine est retrouvé en quantité grandissante dans l'environnement (Bolan et al. 2022), et notamment dans les cours d'eau. Les flux de matière totaux anthropiques d'antimoine à la surface de la Terre ont été estimés à 167 000 tonnes par an par Sen et Peucker-Ehrenbrink (2012) et l'activité minière représente le principal flux de Sb avec 155000 tonnes de Sb déplacées par an, soit environ 93 % des flux totaux anthropiques d'antimoine. Par conséquent, l'activité minière est la principale activité émettrice d'antimoine dans l'environnement. En effet, des concentrations élevées en Sb sont retrouvées dans certains stériles miniers, résidus de traitement de minerais ou encore dans les drainages miniers acides (DMA) (Filella, Belzile, et Chen 2002; Wen et al. 2017; Naidu et al. 2019, Figure 2). Citons par exemple le cas de la mine de Xikuangshan, en Chine, où pour la seule année 2007, 945000 tonnes d'effluents et 672000 tonnes de déchets et résidus miniers riches en Sb ont été produits (Tang et Liu 2009) ; les concentrations dans le DMA ont été mesurées à 38.3 mg.L^{-1} de Sb, soit 4 ordres de grandeur au-dessus des concentrations naturelles (Guo et al. 2018).

Ces drainages miniers acides proviennent de l'exploitation de sulfures métalliques, qui au contact de l'eau et de l'air s'oxydent et libèrent des sulfates, des protons et des métaux, notamment le fer (le

sulfure le plus répandu étant la pyrite, FeS_2, eq. 1) (Banks et al. 1997), mais également l'antimoine (oxydation de la stibine ou d'autres sulfures auxquels Sb est associé).

$$2FeS_2 + 2H_2O + 7O_2 = 2Fe^{2+} + 4SO_4^{2-} + 4H^+_{(aq)} \ (eq.\ 1)$$

Puis vient l'oxydation d'une partie des ions ferreux en ions ferriques via l'oxygène dissous :

$$4Fe^{2+} + 4H^+_{(aq)} + O_2 = 4Fe^{3+} + 2H_2O \ (eq.\ 2)$$

Les ions ferriques vont ensuite agir comme accepteur d'électrons, entrainant une oxydation de la pyrite, générant une acidification plus importante :

$$FeS_2 + 14Fe^{3+} + 8H_2O = 15Fe^{2+} + 2SO_4^{2-} + 16H^+_{(aq)} \ (eq.\ 3)$$

Le fer ferrique généré est hydrolysé, générant également de l'acidité :

$$Fe^{3+} + 3H_2O = Fe(OH)_3 + 3H^+_{(aq)} \ (eq.\ 4)$$

Ces drainages miniers acides sont caractérisés par des pH très bas et des concentrations en métaux dissous très élevées (Carlson et al. 2002; Casiot et al. 2007; Le Pape et al. 2017).

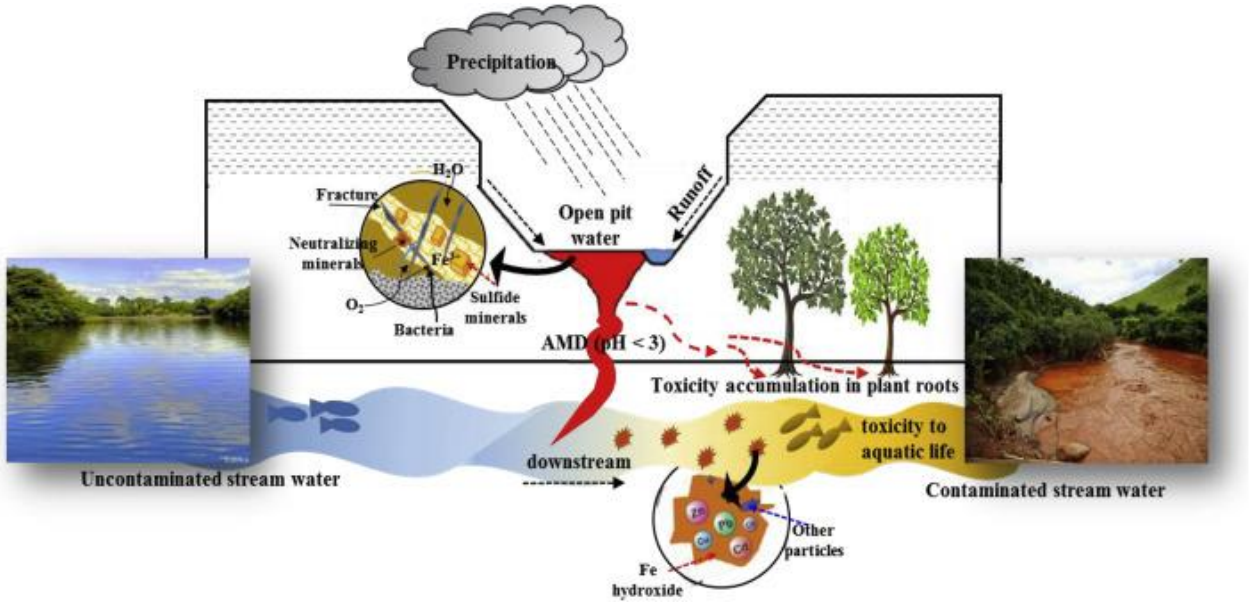

Figure 2: Schéma simplifié montrant la formation d'un drainage minier acide (AMD en anglais) au contact entre des sulfures, de l'eau, de l'oxygène et des bactéries, et l'accumulation de métaux vers les plantes terrestres et les particules riches en fer des cours d'eau en aval. Issu de Naidu et al., (2019).

Les fonderies, les raffineries de métaux ainsi que les incinérateurs de déchets ménagers constituent des sources majeures de contamination en Sb pour l'atmosphère (via les fumées et les aérosols), le sol (via les retombées de poussières et scories) et indirectement l'eau. La combustion des énergies fossiles, et en particulier du charbon (environ 6800 tonnes par an) est aussi une source importante d'antimoine dans l'environnement. Les réseaux routiers constituent des sources relativement importantes en villes et aux abords d'axes majeurs, en lien avec la combustion de pétrole (440 tonnes de Sb par an) et l'abrasion des plaquettes de frein (318 tonnes par an) (Thestorf et Makki 2021; Langner, Kull, et Endlicher 2011; Appleton et Cave 2018). A l'échelle globale, les émissions atmosphériques anthropogéniques de Sb ont atteint un pic à 2232 tonnes par an en 2005, pour ensuite

décliner faiblement et atteindre un peu plus de 1900 tonnes en 2010 (Tian et al. 2014) ; la source principale est liée à la production énergétique (combustion de charbon ou de pétrole, estimées entre 675 et 1011 tonnes en 2010), suivie par les activités minières (100 tonnes par an), et enfin les fonderies et incinérateurs de déchets (entre 171 et 1048 tonnes par an) (Figure 3).

Enfin, plus localement de nombreuses sources ponctuelles d'antimoine peuvent être présentes. On peut y compter par exemple parmi elles les stands de tirs, où l'antimoine est présent dans les munitions en alliage avec le plomb, et les effluents des décharges ménagères et industrielles car l'antimoine est présent dans de nombreux plastiques et composants (Turner et Filella 2017).

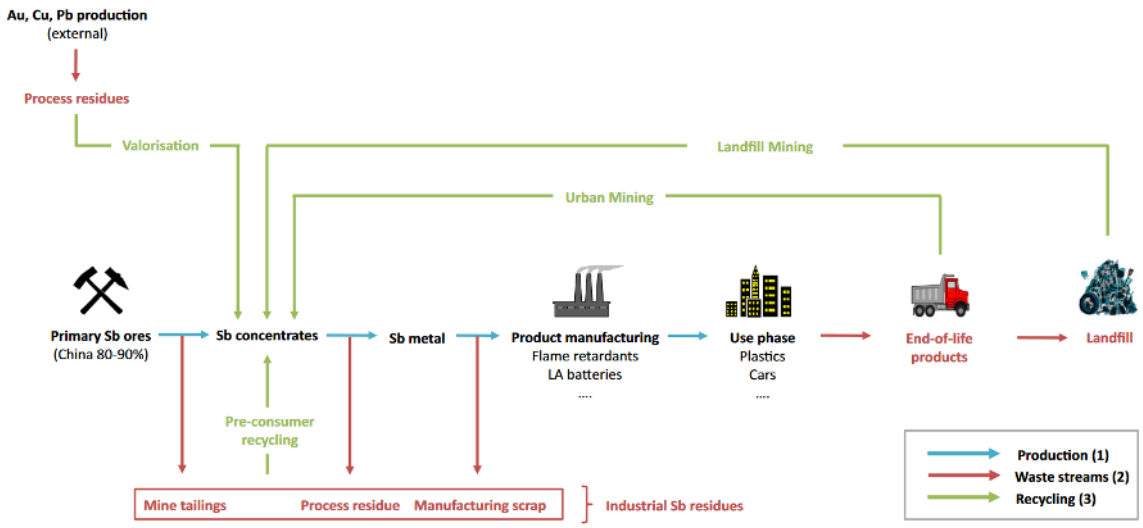

Figure 3: Aperçu du cycle de vie de l'antimoine et de ses principales sources lors de son utilisation industrielle. Issue de Dupont et al., (2016).

1.c. Concentrations dans l'environnement

Eaux de surface et souterraines continentales

Les concentrations en antimoine dissous dans les rivières et les nappes phréatiques non impactées par l'activité humaine se situent généralement entre quelques nanogrammes par litre et 1 $\mu g.L^{-1}$ (Filella, Belzile, et Chen 2002). Ces concentrations peuvent varier d'une région à une autre selon leur fond géochimique. Une collection de 3800 échantillons d'eaux de surface analysés par Udodov et Parilov en 1961 en Sibérie montraient par exemple une concentration en antimoine variant de 0.1 $ng.L^{-1}$ à 31.2 $ng.L^{-1}$. Gaillardet et al. (2003) ont estimé à 0.07 $\mu g.L^{-1}$ la moyenne mondiale de la concentration naturelle d'antimoine dans les eaux de rivière à partir d'une sélection de données issues de grands fleuves faiblement anthropisés. L'atlas géochimique de l'Europe (Salminen 2005) donne une valeur moyenne de fond géochimique pour les rivières de 0.109 ± 0.177 $\mu g.L^{-1}$ à partir de 807 valeurs d'eaux de surface. Pour les rivières chinoises non impactées par les activités humaines, les valeurs moyennes sont inférieures à 1 $\mu g.L^{-1}$, avec des valeurs comprises entre 0.070 et 4.92 $\mu g.L^{-1}$ (He et al. 2012). A l'échelle mondiale, le flux d'antimoine dissous transporté par les rivières vers les océans serait de l'ordre de 2600 tonnes par an (Gaillardet et al., 2003).

La concentration moyenne mondiale de Sb dans les matières en suspension est évaluée à 2.19 ± 2.41 $\mu g.g^{-1}$ d'après une compilation de 41 mesures sur des fleuves et rivières des différents continents

(Viers et al., 2009). La variabilité importante observée est principalement liée à la géologie locale, au niveau d'anthropisation et au climat des fleuves étudiés. Le flux particulaire d'antimoine transporté par les fleuves est estimé à 33000 (± 36000) tonnes par an (Viers et al. 2009) et représente environ 93 % du flux total de Sb exporté vers les océans.

La Chine renfermant de nombreux gisements exploités d'antimoine, les concentrations dans les eaux de surface au voisinage des sites miniers ont fait l'objet d'une attention particulière depuis de nombreuses années (He et al. 2012). Celles-ci varient entre 0.7 et 263 $\mu g.L^{-1}$ dans des cours d'eau en aval de mines (Zhang, Hu, et Zhao 2005), et jusqu'à 29423 $\mu g.L^{-1}$ pour des drainages miniers acides (Zhu et al. 2009; Guo et al. 2018; Hao et al. 2021). La forme particulaire est largement prédominante (He et al. 2012). En France, dans les Cévennes, certains cours d'eau drainant d'anciens sites miniers à stibine présentent des concentrations de l'ordre de quelques dizaines à quelques centaines de $\mu g.L^{-1}$ (Casiot et al. 2007; Resongles et al., 2015). A Oruro, sur l'Altiplano Bolivien, le DMA de la mine de San Jose atteint des concentrations de 8000 $\mu g.L^{-1}$; elles diminuent vers l'aval mais restent élevées (19 $\mu g.L^{-1}$) dans le lac Uru-Uru situé à une dizaine de kilomètres (Goix 2012).

Eaux de mer

Le développement de techniques analytiques pour les traces et ultra-traces entre les années 1980 et 2000 a permis l'analyse précise de l'antimoine dans les eaux de mer ; les concentrations étaient globalement surestimées entre les années 1960 et 1980, avec une gamme de variation entre 200 et 500 $ng.L^{-1}$. Les valeurs ont été finalement stabilisées après 1985 entre 150 et 250 $ng.L^{-1}$, avec une moyenne d'environ 184 (± 45) $ng.L^{-1}$ (valeurs compilées et calculées par Filella et al. 2002).

L'antimoine dans les roches, sédiments et sols

La concentration moyenne d'antimoine dans la croûte continentale supérieure (UCC) a été évaluée entre 0.2 et 0.4 $mg.kg^{-1}$ selon les études (Rudnick et Gao 2014), cette estimation étant réalisée (1) à partir de mesures de la composition de roches exposées à la surface, et (2), de minéraux insolubles trouvés dans certaines roches sédimentaires clastiques ou dépôts glaciaires (diorite, quartz, andésite) ainsi que des roches granitiques et basaltiques.

Les concentrations en antimoine dans les sols et les sédiments sont en moyenne de l'ordre de quelques $mg.kg^{-1}$ (Filella et al. 2001; Wilson et al. 2010). En Europe, la valeur moyenne pour les sols superficiels (n= 840) est de 1.04 ± 2.04 $mg.kg^{-1}$ et pour les sédiments de rivière non contaminées de 1.07 ± 1.88 $mg.kg^{-1}$ (n=848) (Salminen 2005). Des concentrations plus élevées résultent souvent d'un apport anthropique issu de mines, de fonderies, du trafic routier ou de sites industriels. Dans des cas plus rares, des concentrations élevées peuvent être liées à des contextes géologiques spécifiques (dépôt de cendres volcaniques, concrétions de sources géothermales…). Les fortes concentrations en antimoine dans les sédiments sont fortement corrélées aux concentrations de Sb dissous, et les environnements miniers montrent les concentrations en Sb dans les sédiments les plus élevées. Ainsi, dans la mine d'antimoine et de mercure de Qinling Orogen (Chine), les concentrations en antimoine dans les sédiments varient de 14 à 352 $mg.kg^{-1}$, avec une moyenne de 180.7 $mg.kg^{-1}$ (Qin et al. 2022). Ces valeurs relativement élevées, ne font pas exception dans les cours d'eau miniers. Ainsi, Asaoka et al. (2012) ont rapporté des concentrations en antimoine jusqu'à 531 $mg.kg^{-1}$ dans les sédiments en aval de la mine de Ichinokawa (Japon). Dans les sédiments à proximité de la plus grande mine d'antimoine du monde (Xikuangshan, Chine), des concentrations moyennes de plus de 1300 $mg.kg^{-1}$ ont été

mesurées, avec un maximum de plus de 7000 mg.kg^{-1} d'antimoine (He et al. 2012; Liang et al. 2018). Les sédiments à proximité de fonderies présentent également les concentrations en Sb parmi les plus élevées au monde (Nishad et Bhaskarapillai 2021). Ainsi, des concentrations entre 411 et 480 mg.kg^{-1} ont été mesurées dans les sédiments de la Manadas Creek (Etats-Unis) et jusqu'à 243 mg.kg^{-1} dans les sédiments d'Endeavour Inlet (Nouvelle-Zélande), près d'une fonderie d'antimoine (Baeza et al. 2010; Wilson et al. 2004).

Dans les sols, les concentrations les plus élevées en antimoine sont rencontrées, comme pour les sédiments, à proximité de mines et fonderies. Près de la mine d'antimoine de Xikuangshan (Chine), les concentrations en Sb dans les sols atteignent jusqu'à 5050 mg.kg^{-1} (Wang et al. 2011; He et al. 2012), et presque 750 mg.kg^{-1} pour les sols proches de la mine d'antimoine de Xunyang (Qin et al. 2022). A proximité de la mine d'antimoine de De'an (Chine), les concentrations en antimoine dans le sol varient entre 133 et 593 mg.kg^{-1}, avec une moyenne de 362 mg.kg^{-1}. Enfin, aux alentours de la fonderie d'antimoine de la province de Guizhou (Chine), les concentrations dans le sol avoisinent 35 mg.kg^{-1} (He et al. 2012). Des concentrations extrêmement élevées (jusqu'à 9619 mg.kg^{-1}) en Sb dans les sols ont été mesurées également aux alentours des mines abandonnées de la région des Carpates (Slovaquie) ; la plupart des valeurs sont comprises entre 10 et 3000 mg.kg^{-1} (Hiller et al. 2012). Dans cette région, les concentrations mesurées dans les sédiments de rivières (de 11 à 1360 mg.kg^{-1}) sont sensiblement plus faibles en moyenne que dans les sols, en lien avec une mobilisation potentielle de Sb du sédiment vers la colonne d'eau (Hiller et al. 2012).

Dans les sols urbains, les concentrations en antimoine sont également de l'ordre du mg.kg^{-1} mais une forte variabilité spatiale a été mise en évidence en fonction de la proximité et de la densité du trafic routier, en lien avec la présence d'antimoine dans les plaquettes de frein et les gaz d'échappement. D'autres facteurs, comme le type d'utilisation présente ou passée des terrains et les sites industriels aux alentours peuvent aussi impacter la concentration en antimoine dans les sols urbains (Appleton et Cave 2018; Thestorf et Makki 2021; Barbora Dousova et al. 2020; Földi et al. 2018). D'une manière générale, il a été relevé que le trafic automobile était un des facteurs les plus importants d'enrichissement en antimoine dans les sols urbains. Thestorf et Makki (2021) ont ainsi montré que dans la zone urbaine de Berlin, les concentrations en antimoine dans les sols superficiels étaient en moyenne de deux à six fois plus élevées que le fond géochimique de référence. Les concentrations moyennes dans les zones résidentielles étaient de 0.89 mg.kg^{-1} (maximum de 4.53 mg.kg^{-1}) alors que dans les zones industrielles ou à proximité des routes, les concentrations en antimoine étaient supérieures, avec des valeurs moyennes de 1.50 et 1.70 mg.kg^{-1} respectivement, et des maximums pouvant dépasser 170 mg.kg^{-1} pour une zone urbaine affectée par des activités industrielles. Des concentrations relativement similaires ont aussi été mesurées dans les sols londoniens, avec des concentrations maximales de 4.2 mg.kg^{-1} en moyenne mesurées dans les vieux quartiers de la ville. A Shanghai, des concentrations en antimoine similaires ont été mesurées dans les sols, entre 0.17 et 1.7 mg.kg^{-1}, avec une moyenne de 1.14 mg.kg^{-1} (He et al. 2012).

Plus localement, les sols des stands de tirs peuvent présenter de fortes concentrations en antimoine, généralement de plusieurs ordres de grandeur supérieures au fond géochimique, du fait de la présence de cet élément dans les munitions (Scheinost et al. 2006; Hockmann et al. 2015; Tandy et al. 2018; Barker et al. 2020; Sanderson et al. 2018). Ainsi, des concentrations entre 1000 et 17000 mg.kg^{-1} (Scheinost et al. (2006), et jusqu'à 29500 mg.kg^{-1} (Tandy et al. (2018) ; Hockmann et al. (2015)) ont été mesurées dans le sol de stands de tir en Suisse.

L'antimoine dans les plantes

D'une manière générale, la quantité d'antimoine incorporée dans les plantes est proportionnelle à la concentration d'antimoine soluble dans le sol (Tschan, Robinson, et Schulin 2009) mais ces valeurs restent généralement faibles car l'antimoine du sol est peu biodisponible du fait de sa sorption sur les hydroxydes de fer, de manganèse et d'aluminium (Lintschinger et al. 1998; Wilson et al. 2010). De nombreuses études démontrent que les concentrations en antimoine dans les plantes, même en contexte minier, sont généralement très inférieures à 1 $mg.kg^{-1}$ (Leduc et Gardou 1992; Pratas et al. 2005; Domínguez et al. 2008). L'antimoine n'a aucune fonction biologique connue et tend à être toxique pour les plantes. Une étude de Hammel, Debus, et Steubing (2000) a étudié le transfert de l'antimoine du sol vers les plantes sur des sols contaminés par des mines (concentrations en antimoine jusqu'à 500 $mg.kg^{-1}$). Les résultats ont montré que, sur 19 types de cultures étudiées, une concentration maximale de 0.09 mg Sb/kg a été mesurée dans les grains, de 0.34 mg Sb/kg dans les pousses et de 2.2 mg Sb/kg dans les feuilles. D'une manière générale, ces concentrations étaient similaires à celles mesurées dans des sols non contaminés ; ceci est expliqué par le fait que la fraction mobile de l'antimoine ne représentait que 0.06 à 0.59 % de l'antimoine total du sol. Cependant, des concentrations élevées en antimoine ont été mesurées dans certaines plantes. Par exemple, Baroni et al. (2000) a relevé jusqu'à 1367 $mg.kg^{-1}$ d'antimoine dans les feuilles d'une plante herbacée (*Achillea ageratum)* sur un ancien site minier où les concentrations en Sb dans le sol étaient de 9000 $mg.kg^{-1}$, témoignant d'une biodisponibilité importante. Cependant, les cas de très forte assimilation de l'antimoine par les plantes restent rares et ne relèvent pas de milieux cultivés. En milieu urbain, des concentrations faibles en antimoine (< 1 $mg.kg^{-1}$) ont été mesurées dans des plantes poussant près de routes très empruntées (Lehndorff et Schwark 2008).

L'antimoine dans l'atmosphère

Les concentrations en antimoine dans l'atmosphère sont très variables géographiquement, et dépendent principalement des activités humaines. Globalement, les concentrations en antimoine dans l'atmosphère ont augmenté depuis les années 1960, et on les retrouve dans les calottes antarctiques, où Sb montre une augmentation d'un facteur 4 du facteur d'enrichissement par rapport aux années 60, témoignant d'une dispersion globale de l'antimoine dans l'atmosphère due aux activités humaines, même sur les points les plus éloignés de la Terre (Hong et al. 2012). Des échantillons de tourbières dans les îles Féroé ont aussi montré une augmentation de l'antimoine dans l'atmosphère. Les taux de dépôt de Sb dans ces tourbières ont été mesurés à 0.33 $\mu g.m^{-2}.an^{-1}$ dont moins de 10 % provenaient d'aérosols marins (Shotyk, Chen, et Krachler 2005). Ainsi, les activités humaines auraient affecté le cycle atmosphérique de l'antimoine à une échelle similaire à celle du plomb (Shotyk, Chen, et Krachler 2005).

Dans les environnements industriels et miniers, les concentrations en antimoine dans les particules et aérosols atmosphériques peuvent être importantes. Goix et al. (2016) ont montré de fortes concentrations en antimoine dans l'atmosphère en analysant une plante épiphyte, *Tillandsia capillaris,* dans la ville minière d'Oruro en Bolivie. L'antimoine faisait partie des éléments les plus accumulés par cette plante, en particulier dans les quartiers miniers et industriels, où des fonderies sont présentes, avec des concentrations allant jusqu'à 90 $mg.kg^{-1}$. Dans le quartier des fonderies, les concentrations en antimoine dans les poussières atmosphériques atteignaient 101 ± 59 $ng.mg^{-3}$ et 114.3 ± 9.3 $ng.mg^{-3}$ pour les PM10 et PM2.5, respectivement, et jusqu'à 7863 $mg.kg^{-1}$ pour les particules inférieures à 2

µm, avec une fraction biodisponible de 35 à 60 % environ (Goix et al. 2016). Dans les milieux urbains hors contexte minier, Guéguen et al. (2012) ont noté que les concentrations les plus élevées en antimoine dans l'atmosphère étaient relevées à proximité des axes routiers et industriels. Dans la ville d'Addis Abeba (Ethiopie), des concentrations maximales en antimoine dans l'air ont été déterminées à 12 $\mu g.m^{-3}$ (via l'analyse des PM10) (Gebre, Feleke, et Sahle-Demissie 2010). Dans la ville de Saclay en banlieue parisienne, Ayrault et al. (2010) ont mesuré des concentrations en antimoine dans l'air de 4.53 $ng.m^{-3}$, avec un facteur d'enrichissement de près de 5000 dans les particules atmosphériques par rapport au bruit de fond géochimique.

A l'échelle globale, les principales sources d'antimoine dans l'atmosphère sont localisées dans les pays fortement développés ou industrialisés, comme l'Europe, l'Amérique du Nord, la Chine, l'Inde et l'Asie du Sud-Est (Tian et al. 2014, Figure 3).

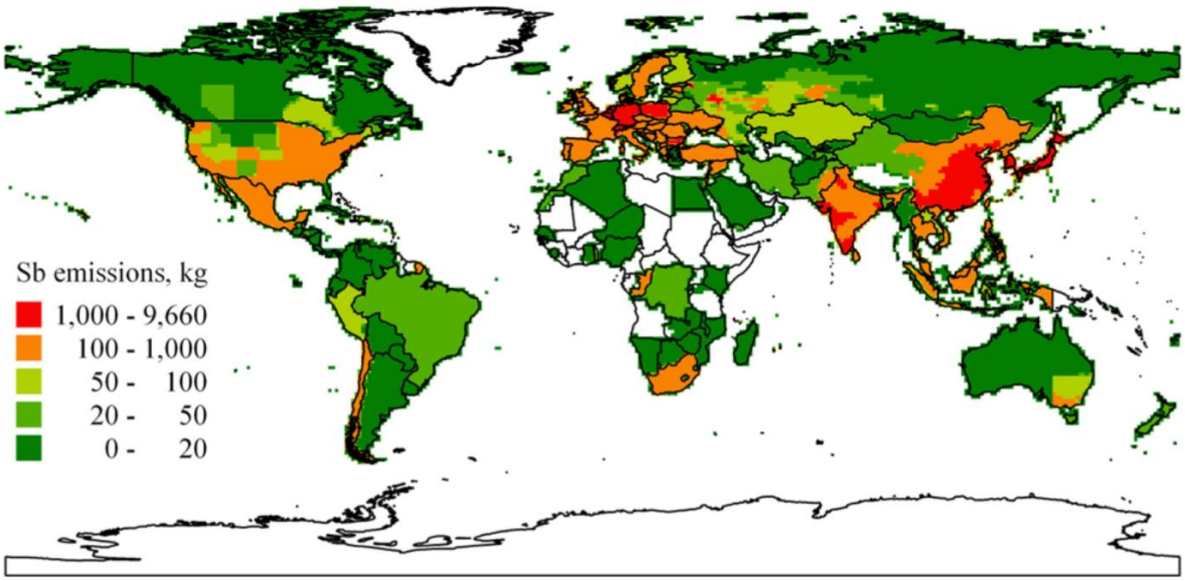

Figure 4: Carte de distribution globale des émissions atmosphériques d'antimoine pour l'année 2010. Issu de Tian et al., (2014).

1.d. Exposition et toxicité pour l'humain

Du fait de sa toxicité, l'antimoine est considéré par l'Agence de Protection de l'Environnement des Etats-Unis (US-EPA) comme un polluant d'intérêt prioritaire. L'Organisation Mondiale de la Santé définit le seuil de concentration en antimoine des eaux destinées à la consommation humaine à 20 $\mu g.L^{-1}$ (He et al. 2012). En France, la limite de potabilité est de 5 $\mu g.L^{-1}$ (Directive n° 98/83/CE du 03/11/98 relative à la qualité des eaux destinées à la consommation humaine). L'exposition des organismes vivants à l'antimoine est peu étudiée. De ce fait, les connaissances concernant la prise en charge physiologique de Sb, son cycle biochimique dans les organismes, ainsi que les effets des expositions environnementales à l'antimoine restent encore partielles à ce jour (Shtangeeva, Bali, et Harris 2011). A la différence d'autres métaux et métalloïdes (Se, Cu, Zn, Fe…), l'antimoine ne possède aucune fonction biologique connue. D'après l'étude de Gebel (1997), l'arsenic et l'antimoine présenteraient des similarités dans les effets toxiques qu'ils induisent chez les êtres vivants. De même que l'arsénite, l'antimoine trivalent serait la forme la plus toxique pour les organismes. Belyaeva (1967)

a étudié la reproduction d'une population de rats exposée à des taux de 209 mg de Sb/m^3, et a montré qu'à l'issue de 63 jours d'exposition, les deux tiers avaient été en incapacité de se reproduire. L'antimoine aurait ainsi un impact sur la capacité reproductive des organismes. L'antimoine a aussi un effet toxique neurocomportemental et induit des changements biochimiques chez les souris (dysfonctionnement des reins et altération bilan hépatique) (Tanu et al. 2018). Finalement, une étude menée par Asakura et al. en 2009 sur divers métaux et métalloïdes (Pb, Bi, In, Ag et Sb) a montré le caractère génotoxique de l'antimoine. Ces observations sont en accord avec celles de Cavallo et al. (2002) et plus récemment de El Shanawany et al. (2017), qui ont noté un endommagement de l'ADN chez une population de travailleurs exposés à du trioxyde d'antimoine (Sb_2O_3). Ceci a été par la suite contesté en pointant la qualité suspecte de ces études précédentes. En effet de fortes proportions d'aberrations chromosomiques (> 10% des cellules atteintes) ont été observées sur des cultures de cellules de mammifères, mais ces mécanismes *in vitro* ne semblent pas exprimés *in vivo* (Boreiko et Rossman 2020).

Plusieurs études ont documenté l'exposition professionnelle à Sb de travailleurs dans des contextes industriels riches en antimoine (fonderies, industries, mines… (Sundar et Chakravarty 2010; Huang et al. 2015; El Shanawany et al. 2017). Ces travaux ont mis en évidence, par l'analyse de différents biomarqueurs (urines et cheveux) une exposition et une assimilation plus importantes de l'antimoine chez les travailleurs par rapport aux populations non exposées (Huang et al. 2015; El Shanawany et al. 2017). Dans les mines, les fonderies et les usines, les particules fines d'antimoine ont un diamètre généralement inférieur à 1 µm, elles peuvent causer « un motif diffus de petites opacités dans chaque poumon », selon le constat des services de médecine du travail (Cooper et al. 1968), autrement appelé pneumoconioses (antimoniosis pour le cas spécifique de l'antimoine). Des études in-vitro montrent que la taille des particules inhalées influence le risque de cancer ; pour des particules de diamètre supérieur à 3.7 µm, aucun cancer n'a été diagnostiqué chez des populations de rats exposées (Schnorr et al. 1995). Toutefois, un risque accru de cancer du poumon ne saurait être exclut chez les travailleurs exposés à du trioxyde d'antimoine bien que la durée d'exposition ainsi que la dose n'aient pu être clairement définies (Saerens et al. 2019). Enfin, des études in vivo sur des travailleurs exposés ont montré que l'antimoine a également des effets toxiques sur les réponses immunitaires, en empêchant la phagocytose et en inhibant les protéases (Lobanova et al. 1996; Cooper et Harrison 2009).

Très peu d'études se sont intéressées à l'exposition environnementale à l'antimoine chez l'être humain et ses effets sur la santé. Des études autour des mines de Xikuangshan et Hunan en Chine ont montré que les habitants ont un apport quotidien en Sb très élevé (de l'ordre de 554 µg.j^{-1} à Xikuangshan, n=209), bien supérieur à l'apport quotidien toléré, principalement via la nourriture et l'eau (Wu et al. 2011; Liu et al. 2011, Ye et al. 2018). Il en résultait de fortes concentrations en Sb dans les cheveux (Wu et al. 2011). Une étude sur l'imprégnation des enfants dans la ville minière d'Oruro en Bolivie a montré que ceux vivant dans le quartier minier de la ville présentaient des concentrations en antimoine plus élevées que ceux vivant dans les quartiers périphériques (Barbieri et al. 2011; Barbieri et al. 2014). Fort et al. (2016) ont étudié l'exposition à l'antimoine chez les femmes enceintes en milieu urbain. Ils ont montré que la concentration en Sb dans les urines des femmes enceintes était corrélée avec la saison, leurs activités physiques et professionnelles et la présence ou non de grands axes routiers proches de leurs habitations. Ces résultats ont suggéré que l'inhalation de particules atmosphériques en milieu urbain pouvait constituer une source d'antimoine pour les femmes enceintes et la population d'une manière générale. Toutefois, les effets de cette exposition à long

terme à bas niveau sur la santé restaient à évaluer. A cet égard, les résultats de la cohorte NHANES aux Etats-Unis ont montré que dans la population générale américaine, les personnes ayant des concentrations plus élevées en antimoine dans les urines sont statistiquement plus touchées par les maladies cardiovasculaires, avec des attaques cardiaques plus fréquentes que pour le reste de la population (Guo et al. 2016).

En conclusion, malgré le peu de connaissances disponibles, il apparaît que la toxicité de l'antimoine pour les organismes humains ou animaux est avérée. Les effets de l'antimoine sur la santé sont multifactoriels et dépendent, entre autres, de la durée d'exposition à la pollution, de la dose, de la voie d'exposition, de paramètres biologiques (âge, sexe, hygiène de vie, nutrition…). L'exposition à d'autres éléments chimiques, auxquels l'antimoine est souvent associé, est aussi un facteur important à prendre en compte (Cooper et Harrison, 2009).

II. Comportement de l'antimoine en milieu aquatique

2.a. Spéciation en phase dissoute

L'antimoine, comme l'arsenic, possède les degrés d'oxydations suivants -III, 0, +III et +V. Son comportement dans l'environnement, et particulièrement dans les eaux, dépend fortement de son état d'oxydation. Il est principalement présent dans l'environnement sous les degrés d'oxydations +III et +V (Filella et al. 2001). L'antimoine a une configuration électronique $[Kr]4d^{10}5s^{2}5p^{3}$, ce qui explique la stabilité des degrés d'oxydation de la forme trivalente et pentavalente (perte de 3 ou 5 électrons de la couche extérieure, Scheinost et al. 2006). La forme dissoute trivalente est fortement asymétrique (Sb lié à trois atomes d'oxygène généralement) alors que la forme dissoute pentavalente se présente sous la forme d'un octaèdre (Sb lié à 6 atomes d'oxygène), comme illustré sur la Figure 5. La plus grande mobilité de l'antimoine relativement à l'arsenic est généralement attribuée au fait que Sb possède une couche électronique supplémentaire par rapport à celle de l'arsenic, augmentant ainsi la taille de l'atome ($4d^{10}$ vs $3d^{10}$, Johnston et al. 2020).

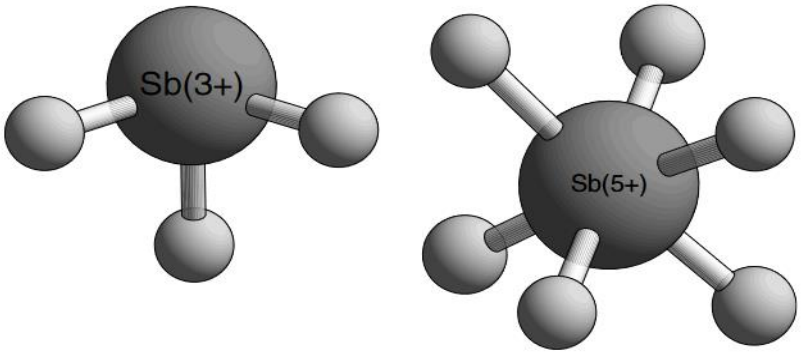

Figure 5: Structures des formes dissoutes trivalente (gauche) et pentavalente (droite) de l'antimoine. Issu de Scheinost et al., (2006).

Dans les eaux naturelles oxygénées, l'antimoine se trouve sous forme pentavalente, principalement sous forme de l'oxyanion $Sb(OH)_6^-$ (2.5 < pH < 14) (Widargo 2005). La forme trivalente ($Sb(OH)_3^0$) est présente dans des eaux fortement réductrices. Le diagramme Eh-pH (Figure 6) résume les principales formes dissoutes de l'antimoine dans le système Sb-O-H. En présence de soufre et dans des conditions neutres à alcalines fortement réductrices, l'antimoine est sous la forme de sulfure, principalement SbS_2^- , bien que la forme SbS_4^{3-} (forme pentavalente) ait été également observée dans des conditions anoxiques (Takayanagi et Cossa 1997; Filella, Belzile, et Chen 2002). La stibine, principal minerai sulfuré de Sb, présente la chaine de dissolution suivante (Roper, Williams, et Filella (2012) adaptée de Ashley et al. 2003) :

$$\mathrm{Sb_2S_3} + \mathrm{H_2O} + 2\mathrm{O_2} = \mathrm{SO_4}^{2-} + \mathrm{Sb_2S_2O} + 2\mathrm{H}^+ \ (eq.5)$$

Les deux atomes de soufre restants dans $\mathrm{Sb_2S_2O}$ sont ensuite remplacés par de l'oxygène pour former la valentinite (Sb_2O_3, structure orthorhombique) ou la sénarmontite (Sb_2O_3, structure cubique à 298 K). Il s'agit de la poursuite de la réaction 5 selon l'équation 6 :

$$Sb_2S_2O + 2\mathrm{H_2O} + 4\mathrm{O_2} = 2\mathrm{SO_4}^{2-} + \mathrm{Sb_2O_3} + 4\mathrm{H}^+ \ (eq.6)$$

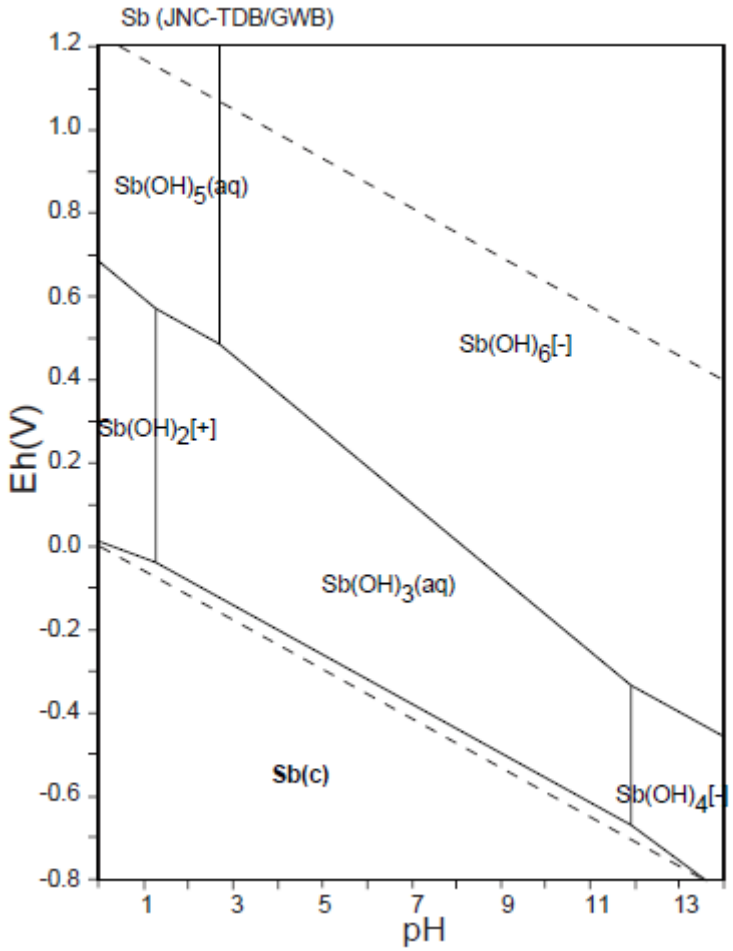

Figure 6: Diagramme Eh-pH de l'antimoine en phase dissoute dans le système Sb-O-H pour les espèces Sb(III) et Sb(V) calculée d'après des modèles thermodynamiques. Issu de Takeno, 2005.

Sb(III) semble s'oxyder à des valeurs de potentiel rédox (Eh) plus négatives que As(III). Ainsi, dans l'eau porale de sols, Mitsunobu, Harada, et Takahashi (2006) ont montré que pour une valeur de Eh de -140 mV, la grande majorité (99%) de l'arsenic a été réduite sous forme trivalente (As(III)), alors que la forme prédominante de Sb restait Sb(V). Cette différence de comportement peut s'expliquer par la différence de leurs propriétés RedOx. Ainsi, l'antimoine peut s'oxyder de manière plus rapide et dans des conditions plus réductrices que l'arsenic. Toutefois, Sb(V) s'est révélé moins stable dans les environnements réducteurs que précédemment rapporté, avec des vitesses de réduction de l'ordre de quelques semaines à quelques mois (Hockmann et al. 2014).

La présence de Sb(III) dans des eaux oxydantes où il serait normalement thermodynamiquement instable a été mise en évidence et expliquée par des vitesses d'oxydation très lentes (Filella, Nelson, et Yu-Wei 2002) ou bien par la stabilisation de Sb(III) par des ligands organiques, comme l'acide tartrique (Han-wen, Xiao-quan, et Zhe-ming 1982; Filella, Belzile, et Chen 2002). Sb(III) forme des complexes stables avec les acides polycarboxyliques et hydroxycarboxyliques sur une large gamme de pH typique des eaux naturelles (pH 3 à 9) (Tella et Pokrovski 2009) alors que Sb(V) forme des complexes stables avec les acides polycarboxyliques et hydroxycarboxyliques et avec les ligands aliphatiques et polyol aromatiques à pH acide uniquement (pH < 4) (Tella et Pokrovski 2012). Plusieurs études ont montré que la cinétique d'oxydation abiotique de Sb(III) par l'oxygène dissous ou le peroxyde d'hydrogène H_2O_2 dépendait fortement du pH, diminuant d'un facteur 100 entre pH 7 et pH 9 (Belzile, Chen, et Wang 2001; Quentel et al. 2004; Leuz et Johnson 2005). Ainsi, à pH 8.5 et avec une concentration d'O_2 dissous de 0.28×10^{-3} M, Leuz et Johnson (2005) estiment la durée de demi-vie de Sb(III) à 170 ans. Avec H_2O_2 présent aux concentrations naturelles (10^{-6} M), l'oxydation de Sb(III) est bien plus rapide, entre 3.2 (pH 7) ans et 11 jours (pH 9) pour la demi-vie de Sb(III) (Leuz et Johnson 2005). Toutefois, ces oxydants sont moins efficaces que les (oxyhydr)oxydes de fer et manganèse. En effet, Belzile, Chen, et Wang (2001) et Asta et al., (2012) ont montré que des oxyhydroxydes de fer et de manganèse de synthèse et naturels pouvaient oxyder rapidement Sb(III) en Sb(V), avec des temps de l'ordre de quelques jours sur une grande gamme de pH. Il a été cependant noté que l'oxydation était légèrement plus lente à pH acide (< 6.5) qu'à pH neutre ou basique (> 9) (Belzile, Chen, et Wang 2001).

Plusieurs études mentionnent la présence de Sb(III) dans des eaux de rivières impactées par l'activité minière. Par exemple, Guo et al. (2018) ont mesuré une concentration de 327 $\mu g.L^{-1}$ de Sb(III) en amont d'une zone minière, représentant 0.8% de l'antimoine total et l'ont attribuée à une oxydation incomplète due à un manque de temps et à une faible oxygénation de l'eau. Resongles et al. (2013) ont aussi mis en évidence la présence de Sb(III) dans une rivière impactée par l'activité minière, représentant entre 36 et 70 % de l'antimoine total dissous à la source du cours d'eau, au pied d'une digue à résidus minier. Dans ces deux cas, la concentration en Sb(III) dissous en solution diminue le long du cours d'eau, par oxydation de Sb(III) en Sb(V) mais aussi par adsorption de Sb(III) à la surface d'oxyhydroxydes de fer (Resongles et al., 2013 et Guo et al., 2018) .

2.b. Mécanismes de sorption

Dans les environnements miniers, l'altération des sulfures produit des lixiviats acides nommés drainages miniers acides (DMA) qui contiennent des concentrations élevées en éléments métalliques et en sulfates. Lors de la neutralisation des DMA avec des eaux de rivière à pH neutre, le fer précipite pour former des (oxy)hydroxydes et oxyhydroxysulfates de fer plus ou moins cristallisés tels que la schwertmannite, la magnétite ou la goethite à pH acide et la ferrihydrite et l'hématite à pH neutre (Bigham et al. 1996; Bigham, Schwertmann, et Pfab 1996; Roh et Moon 2001). La précipitation de ces phases secondaires de fer est souvent accompagnée par la précipitation d'autres oxydes tels que les oxydes de manganèse et d'aluminium. Ces solides contrôlent la mobilité de nombreux contaminants métalliques dans les milieux aquatiques en aval des mines à sulfures (Manaka et al. 2007; Fukushi et al. 2003). Les (oxy)hydroxydes de fer jouent un rôle important dans l'atténuation de l'antimoine dissous et son piégeage dans les sédiments de manière générale (Hiller et al. 2012). Ces phases solides ont une grande capacité d'adsorption des espèces anioniques tels que les oxyanions d'antimoine (Bagby et West 1995).

Plusieurs études se sont intéressées aux mécanismes d'adsorption de Sb à la surface d'oxyhydroxydes de fer tels que la ferrihydrite, la schwertmannite, l'hématite, la goethite, que ce soit par des approches expérimentales (Thanabalasingam et Pickering 1990; Leuz, Mönch, et Johnson 2006; McComb, Craw, et McQuillan 2007; Mitsunobu et al. 2010; Guo et al. 2014; Qiu et al. 2018) ou des observations de terrain (Scheinost et al. 2006; Manaka et al. 2007; Ritchie et al. 2013; Johnston et al. 2020). La plupart de ces études concernent l'adsorption de Sb(V). D'une manière générale, l'adsorption de Sb(V) sur les (oxy)hydroxydes de fer augmente lorsque le pH diminue, jusqu'à une valeur maximale pour un pH de 3. Ceci s'explique par le fait qu'à pH acide (< 3), Sb(V) forme l'espèce $Sb(OH)_5$ neutre, et donc moins attirée par les surfaces positives des oxydes de fer (McComb, Craw, et McQuillan 2007) et se désorbe à pH basique (> 6.5). A contrario, l'adsorption de Sb(III) sur la ferrihydrite est peu influencée par le pH sur une large gamme (de 4 à 10) (Qi et Pichler 2016) et sur une gamme encore plus élevée pour la goethite (de pH 3 à 12) (Leuz, Mönch, et Johnson 2006). Qi et Pichler (2016) ont montré que la présence en solution de Sb(V) n'avait pas d'influence sur l'adsorption de Sb(III) sur la ferrihydrite, mais que à contrario, Sb(III) inhibait la sorption de Sb(V). Au-delà de pH 8.5, la surface de la ferrihydrite devient neutre et n'a plus d'affinité particulière pour les oxyanions (Bagby et West 1995). Concernant les études de terrain, Resongles et al. (2013) ont noté une rétention plus importante de Sb(III) que de Sb(V) dans un environnement riche en schwertmannite, ce qui a aussi été rapporté et confirmé par Johnston et al. (2020) en contexte minier.

A travers l'étude de la spéciation solide de Sb par spectrométrie d'absorption des rayons X (analyses EXAFS et XANES), différents auteurs ont montré que Sb(V) s'adsorbe à la surface des minéraux secondaires de fer (ferrihydrite et goethite) par des complexes de sphères internes ; il se forme des liaisons Sb – O – Fe avec une configuration par partage de coins et d'arrêtes (« edge and corner sharing configuration ») (Scheinost et al. 2006; McComb, Craw, et McQuillan 2007), et une distance radiale Sb – Fe entre 3.10 et 3.56 Å. Cette observation a ensuite été confirmée par Mitsunobu et al. (2010) qui ont également mis en évidence la présence d'un complexe à double coin partagé (« double corner-sharing complex ») pour Sb(V) à la surface de la ferrihydrite et de la goethite.

Concernant l'adsorption de l'antimoine sur des oxydes d'aluminium (Zhou et al. 2022; Essington et Stewart 2016) ou de manganèse δ-MnO_2 (Sun et al. 2018; 2018; Zhang et al. 2020; Belzile, Chen, et Wang 2001), les mécanismes sont moins connus que pour les oxydes de fer. Il a été rapporté que quel que soit le pH ou la quantité initiale d'antimoine en solution, Sb(V) s'adsorbait selon des complexes de sphère externe à la surface des oxydes d'aluminium ϒ-AlO_3 (Zhou et al. 2022). Pour le cas particulier de $Al(OH)_3$, Essington et Stewart (2016) ont montré une dépendance au pH des modes d'adsorption de Sb(V) ; les complexes de sphère interne prédominent à pH acide (<5) tandis que les complexes de sphère externe prédominent à pH basique (>8). Comme pour les oxyhydroxydes de fer, l'adsorption de l'antimoine sur les oxydes de Al et Mn est plus efficace à pH acide qu'à pH neutre et basique (Wang et al. 2018; Sun et al. 2018).

L'adsorption de l'antimoine a été étudiée sur différentes argiles telles que les argiles Erzurum rouges et grises, de la ville turque d'Oltu (Targan, Tirtom, et Akkuş 2013), mais aussi des argiles utilisées pour la remédiation de l'antimoine dans l'eau, notamment la bentonite (Xi, He, et Lin 2011), la kaolinite et la montmorillonite (Biver, Krachler, et Shotyk 2011). Plusieurs résultats intéressants ressortent de ces études. Tout d'abord, à l'instar des oxydes de fer, l'adsorption de Sb(III) est plus importante que celle de Sb(V) et les cinétiques d'adsorption sont relativement rapides (24 h pour atteindre l'équilibre). De plus, il a été montré qu'en présence de différents anions compétitifs (NO_3^-, SO_4^{2-} et PO_4^{3-}), l'adsorption de Sb(V) était affectée mais pas celle de Sb(III) (Xi, He, et Lin 2011). Cela peut être expliqué par différents facteurs, notamment I) l'adsorption de Sb(III) à la surface de la bentonite s'effectue par des liaisons spécifiques différentes de celles de Sb(III) ou par des complexes de sphère interne, II) l'accumulation du phosphate en particulier et des autres oxyanions en général augmente les charges négatives de la surface des argiles et exerce une force de répulsion plus importante pour $Sb(OH)_6^-$, III) les sites de sorption sont les mêmes pour Sb(V) que pour les autres oxyanions étudiés.

Concernant les isothermes de sorption, l'adsorption de Sb sur la bentonite a été la mieux décrite par le modèle de Freundlich, ce qui peut signifier que l'adsorption de Sb s'effectue par couches successives sur la bentonite. A contrario, dans le cas de l'adsorption de l'antimoine sur les argiles rouges et grises, les meilleurs modèles d'adsorption de l'antimoine à sa surface étaient ceux décrits par Langmuir, supposant une adsorption monocouche sur une surface homogène et uniforme. Toutes ces études s'accordent à dire que l'adsorption de l'antimoine sur les argiles est plus efficace à pH acide (<6 avec un optimum à pH ~1.5), et que cette efficacité diminue lorsque le pH augmente, à l'instar des oxydes de fer.

L'antimoine a une forte affinité pour la matière organique. Il forme notamment lors de son adsorption des complexes avec les ligands présents à la surface des acides humiques (Dousova et al. 2015) à des vitesses remarquablement élevées en particulier pour Sb(III) (Ceriotti et Amarasiriwardena 2009). Les acides humiques jouent un rôle important dans l'oxydation de Sb(III) en Sb(V), par le biais de groupes fonctionnels quinones ($C_6H_4O_2$, transporteurs d'électrons) et disulfites ($S_2O_5^{2-}$) omniprésents (Ceriotti et Amarasiriwardena 2009). Pour la plupart des acides humiques, l'adsorption de Sb est optimale à pH égal ou inférieur à 6, et décroit ensuite lorsque le pH augmente (Buschmann et Sigg 2004). L'adsorption de Sb à la surface de l'acide humique peut être décrite par un isotherme de Langmuir, et suggère donc une adsorption monocouche et uniforme (Pilarski, Waller, et Pickering 1995). Enfin, les acides humiques ont la capacité de rétention de plusieurs formes de Sb, de la forme cationique (SbO^+), à la molécule neutre ($Sb(OH_3)$) ou anionique ($Sb(OH)_6^-$), avec différents groupes

fonctionnels mobilisés en fonction de la forme de Sb, et en particulier le groupe fonctionnel carboxyle pour la forme cationique (Pilarski, Waller, et Pickering 1995).

2.c. Interactions avec les micro-organismes

L'antimoine peut subir différentes biotransformations (adsorption, oxydation, réduction, méthylation) dans les milieux aquatiques et les sols sous l'effet de l'activité microbienne (Filella, Belzile, et Lett 2007). Certains micro-organismes ont développé la capacité d'oxyder Sb(III) en Sb(V) comme mécanisme de détoxification (Filella, Belzile, et Lett 2007; Lehr, Kashyap, et McDermott 2007; Li et al. 2013; Li et al. 2015; Wang et al. 2015; He et al. 2019) ou comme mécanisme de respiration, utilisant l'antimoine comme un donneur d'électron pour produire l'énergie requise pour leur croissance (Filella, Belzile, et Lett 2007). Depuis la première souche bactérienne (*Stibiobacter senarmontii*) isolée en 1974 ayant la capacité d'oxyder l'antimoine (Lialikova, 1974), de nombreuses souches ont depuis été identifiées, la plupart issues de sols ou d'environnements contaminés en antimoine, particulièrement au voisinage de sites miniers (Li et al. 2013; Li et al. 2015; Li et al. 2018; Nguyen et Lee 2015; Nguyen et al. 2017; Terry et al. 2015; Laroche 2019). La plupart des souches étudiées (*Acinetobacter* sp. JL7, *Comamonas* sp. JL25, *Comamonas* sp. JL40, *Comamonas* sp. S44, *Stenotrophomonas* sp. JL9, *Variovorax* sp. JL23 (Jie Li et al. 2013) *Agrobacterium tumefaciens* GW4 (Jingxin Li et al. 2015), *Shinella* sp. NLS1, *Ensifer* sp. NLS4 (Nguyen et al. 2017)), peuvent oxyder l'antimoine en conditions aérobies, mais peu d'entre elles le peuvent en conditions anaérobies, en utilisant les nitrates comme accepteurs d'élections (Nguyen et al. 2017). Concernant les gènes et protéines responsables de l'oxydation de Sb(III) en Sb(V), plusieurs voies ont été identifiées :

(1) AioA, il s'agit de la première protéine d'oxydation de l'antimoine identifiée (arsénite oxydase). Cette protéine est responsable de l'oxydation de Sb(III) dans le périplasme et empêche qu'une quantité trop importante de Sb(III) entre dans la cellule (Santini et al. 2002, Wang et al. 2015).
(2) Le second gène découvert a été AnoA, une oxydoréductase capable d'oxyder Sb(III) mais pas As(III). Li et al. 2015 ont découvert que ce gène était largement présent au sein des bactéries Sb(III) oxydantes *Agrobacterium tumefaciens* (Li et al. 2015; He et al. 2019).
(3) ArsV est une protéine dont le rôle a été récemment mis en évidence pour l'oxydation de Sb(III) par Zhang et al. (2022) identifiée chez *E. adhaerens* ST2 qui est capable d'oxyder Sb(III) en Sb(V) mais pas As(III) en As(V) (Li et al. 2016).

Certaines souches peuvent aussi, en conditions anaérobies, réduire Sb(V) en Sb(III) en utilisant par exemple le lactate ou l'acétate comme donneur d'électron et Sb(V) comme accepteur d'électron final dans des sols ou des sédiments miniers riches en stibnite (Hockmann et al. 2014; Kulp et al. 2014). Ces processus sont couplés à une respiration anaérobique hétérotrophe, c'est-à-dire l'utilisation d'une autre source d'énergie que l'oxygène (carbone organique, glycérol…). Quelques autres études ont aussi montré que le dihydrogène (H_2) pouvait être utilisé comme donneur d'électrons pour la réduction de Sb(V), ce processus conduisant à précipitation de Sb_2O_3 ; ce phénomène a été mis en évidence dans des puits de mine (Lai et al. 2016).

Certaines bactéries ont aussi développé comme moyen de détoxification de Sb(III) un processus de méthylation. Comme l'arsenic, l'antimoine méthylé peut se retrouver sous la forme de mono-, di- ou tri-méthyl d'antimoine (Dodd et al. 1992; Jenkins et al. 1998; Filella 2010). La méthylation de Sb a été observée dans beaucoup de milieux différents, et en particulier dans des sols, des eaux usées, des

sédiments, des eaux douces, des eaux de mer ou géothermales ainsi que dans des organismes (He et al. 2019) et semble provenir principalement de l'activité bactérienne ou fongique (Jenkins, Forster, et Craig 2002). La méthylation de Sb affecte sa mobilité, sa toxicité et ses caractéristiques de bioaccumulation (He et al. 2019). L'antimoine méthylé serait moins toxique que Sb(V) (Filella, Belzile, et Chen (2001)). Presque rien n'est connu du comportement des espèces méthylées de Sb dans les eaux (Filella, Belzile, et Chen 2002). Des études laissent à penser que la tri-méthylation de Sb(III) chez l'être humain pourrait le rendre plus mobile une fois oxydé (Jenkins et al. 1998).

Enfin, il est intéressant à noter que les micro-organismes peuvent avoir des effets indirects sur la spéciation de Sb en solution. Par exemple, des études ont montré que Sb(V) peut être réduit en Sb(III) par les sulfures générés lors de la réduction des sulfates par les bactéries sulfato-reductrices ; l'antimoine réduit est ensuite complexé avec les sulfures en excès et précipite pour former de la stibine (Wang et al. 2013 ; Zhang et al. 2016). Asta et al. (2012) ont aussi montré par des expérimentations de laboratoire que Sb(III) pouvait aussi être oxydé par le Fe(III) produit pas les bactéries ferro-oxydantes.

PARTIE B : Les isotopes stables des métaux comme traceurs de sources et de processus

I. Généralités sur les isotopes stables

Un grand nombre d'informations sur les isotopes stables de métaux et leur application au traçage de sources et de processus dans l'environnement présentées dans cette partie sont issus de l'excellent article de synthèse de Wiederhold (2015).

1.a Introduction

Sur près de 4000 nucléides connus (naturels et artificiels), seuls environ 287 sont stables ou ont une durée de vie très longue (^{130}Te par exemple a une demi-vie de l'ordre de 8.2×10^{20} ans (Meshik et Pravdivtseva 2017)), et ils correspondent à 118 éléments (Figure 7). Sont appelés « isotopes » les nucléides d'un même élément mais qui possèdent des masses différentes, dues à une variation du nombre de neutrons dans le noyau (le nombre de protons est identique). Isotope signifie littéralement « même place » et désigne donc les différents nucléides qui se situent à la même place sur le tableau périodique des éléments (Criss 1999). Le concept d'isotope est connu depuis 1913, où Thomson a utilisé un tube cathodique pour déterminer le ratio charge/masse (*q/m*) du Néon, et a découvert que les particules le composant avaient deux masses, une de 20 qui était connue et l'autre de 22 qu'il a tout d'abord confondu avec une molécule de CO_2 possédant deux charges (Münzenberg 2013). Il existe différents types d'isotopes (e.g. stable, radioactif, primordial, radiogénique…) ; dans le cadre de cette thèse, nous nous concentrerons exclusivement sur l'étude des isotopes stables de métaux et métalloïdes non-radiogéniques.

Les principes des propriétés et du fractionnement des isotopes stables ont été établis grâce à l'étude de systèmes isotopiques d'éléments légers dits traditionnels (H, C, O, N, S) (Fry 2006). Ils ont permis de mieux comprendre le cycle géochimique de ces éléments et ont été utilisés pour répondre à de nombreuses problématiques, notamment dans le domaine de la géochimie environnementale (Fry 2006; Hoefs, 2021). Par la suite, le développement de la spectrométrie de masse à multi-collection (MC-ICP-MS) dans les années 1990 a permis de mesurer précisément les rapports isotopiques de nombreux autres éléments et ainsi d'élargir le champ d'application de la géochimie des isotopes stables aux métaux (e.g. Cu, Zn, Cr, Cd, Ni…) métalloïdes (Ge, Se, Sb, Te…) et autres éléments (Li, B, Sr…) dits non-traditionnels (Weiss et al. 2008).

Différents mécanismes peuvent être à l'origine de variation de composition isotopique d'un élément lors de processus physiques ou (bio)-géochimiques. Ces mécanismes peuvent être dépendants de la masse ou indépendants de la masse des isotopes (effet de volume nucléaire NVE, effet isotopique magnétique, Wiederhold 2015). Il a été mis en évidence que le fractionnement indépendant de la masse lié à l'effet du volume nucléaire peut être plus important que le fractionnement dépendant de la masse pour les éléments lourds (Tl, Pb, U…) (Yang et Liu 2016) alors qu'il est négligeable pour les éléments légers et minoritaire pour les éléments intermédiaires (Edwin A. Schauble 2007; 2013; Fujii, Moynier, Telouk, et al. 2009; Fujii et al. 2013; 2014). Schauble (2007),

Fujii et al. (2009) et Schauble (2013) rapportent ainsi un fractionnement isotopique induit par le NVE à hauteur d'environ 1 ‰ pour le thallium et le mercure, d'environ 0.5 ‰ pour l'étain et enfin d'environ 0.038 ‰ pour le zinc. Dans la suite de ce travail, nous nous focaliserons sur le fractionnement isotopique dépendant de la masse. Les isotopes stables d'un élément réagissent de manière similaire lors des réactions chimiques, physiques et biologiques. Toutefois, la différence de masse entre les isotopes peut entrainer de faibles différences dans leur comportement au cours de certaines réactions (Wiederhold 2015).

Un fractionnement isotopique se caractérise par une différence de réactivité des isotopes lors d'une réaction chimique entrainant un rapport isotopique différent entre le produit et le réactif. Ces fractionnements causés par de nombreux processus (changement de degré d'oxydation, adsorption, évaporation…) sont souvent complexes à appréhender, décrire et prédire. L'étude des variations de compositions isotopiques de contaminants métalliques entre différents compartiments environnementaux peut permettre de renseigner sur l'origine de ces contaminant et/ou sur les processus qui les affectent lors de leur transport (Wiederhold 2015; Komárek et al. 2021).

1.b. Nomenclature

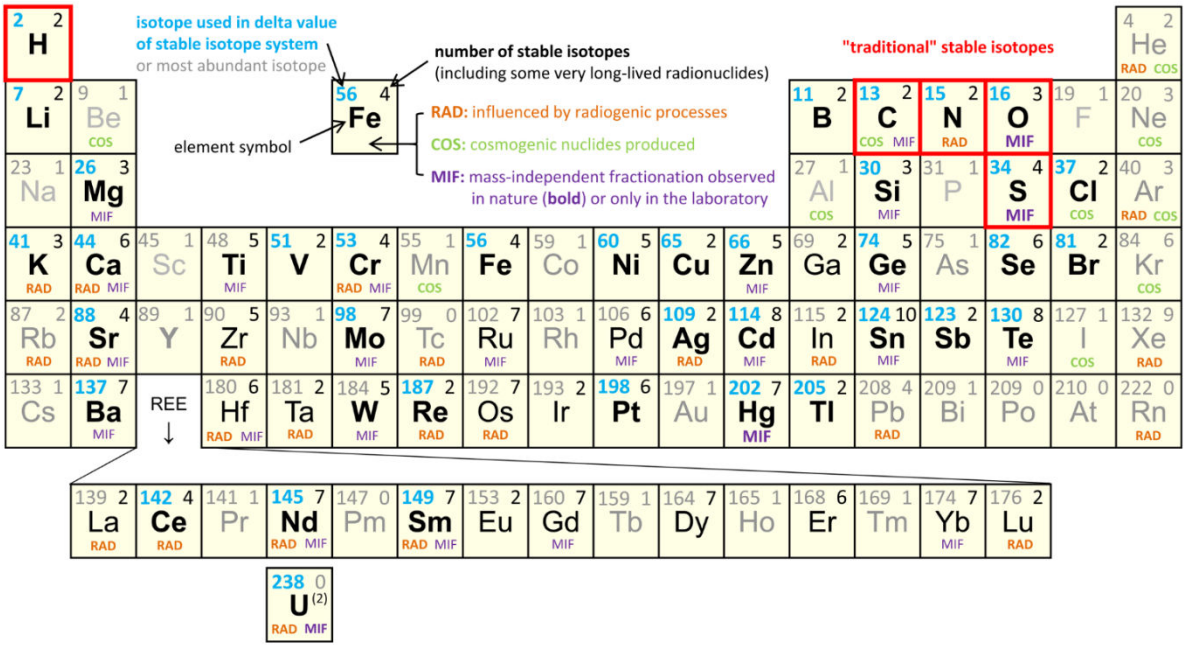

Figure 7: Tableau périodique des éléments tiré de Wiederhold 2015. Ce tableau montre les propriétés isotopiques des différents éléments. La masse d'un élément correspond à la moyenne des masses des différents isotopes pondérée par leurs abondances respectives (Criss 1999) : Masse atomique = $\Sigma_j A_j W_j$ (eq. 1), avec A_j et W_j les abondances relatives et les masses atomiques pour chaque isotope j (unité de masse atomique unifiée).

Les variations naturelles de rapports isotopiques des isotopes stables de métaux et métalloïdes sont faibles. Ainsi, leur composition isotopique est exprimée avec la notation δ (en ‰) qui correspond à la déviation du rapport isotopique d'un échantillon par rapport à celui d'une référence (Eq. 2).

$$\delta^x E = \left(\frac{({}^xE/{}^yE)_{échantillon}}{({}^xE/{}^yE)_{standard}} - 1\right) \times 1000 \; (eq.2)$$

Où *x* et *y* représentent deux isotopes de l'élément E, par convention, l'isotope lourd est généralement au numérateur et le léger au dénominateur.

Le facteur de fractionnement isotopique entre deux phases A et B est noté $\alpha_{B\text{-}A}$ (Eq. 3) :

$$\alpha_{B-A} = \frac{(\frac{{}^xE}{{}^yE})_B}{(\frac{{}^xE}{{}^yE})_A} = \frac{1000 + \delta_B}{1000 + \delta_A} = \frac{\beta_B}{\beta_A} \; (eq.3)$$

Où β_x est le facteur de partitionnement isotopique d'une molécule x comparé à un gaz atomique parfait. Le facteur d'enrichissement epsilon (ε en ‰) est également utilisé pour exprimer la différence de composition isotopique entre deux phases A et B (Eq. 4).

$$\varepsilon_{B-A} = \alpha_{B-A} - 1 \; (eq.4)$$

De plus, comme α est très proche de 1 (valable pour des δ < 10 ‰), le facteur de partitionnement isotopique peut être approximé comme décrit dans l'équation 5 (Schauble, Méheut, et Hill 2009; Sherman 2013; Wiederhold 2015), souvent noté $\Delta^x E_{A\text{-}B}$:

$$1000 \ln \alpha_{B-A} = 1000(\ln \beta_B - \ln \beta_A) \approx \delta\, {}^xE_B - \delta\, {}^xE_A \approx \varepsilon_{B-A} \; (eq.5)$$

1.c. Fractionnement cinétique vs fractionnement à l'équilibre

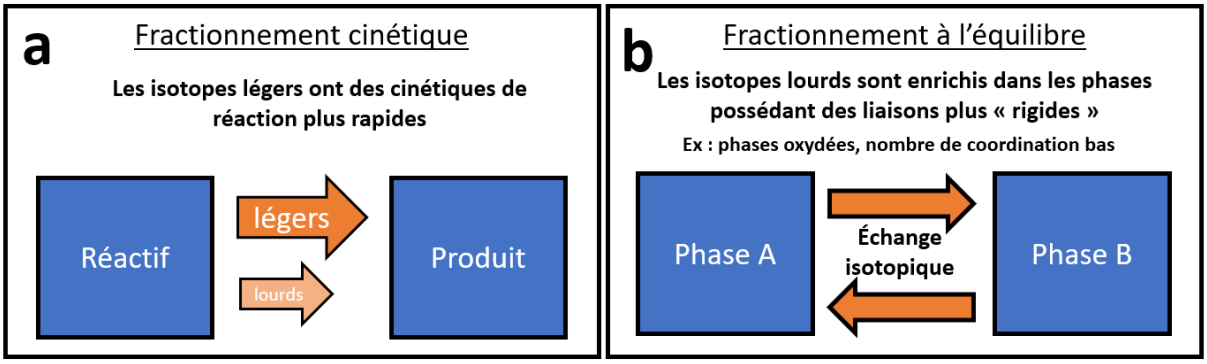

Figure 8: Illustration schématique du fractionnement cinétique (a) et à l'équilibre (b). Issu et traduit de Wiederhold (2015).

Le fractionnement isotopique dépendant de la masse peut avoir pour origine un effet cinétique ou bien refléter un fractionnement à l'équilibre (Figure 8).

Les fractionnements isotopiques cinétiques sont dus à des cinétiques de réactions différentes entre les isotopes lourds et légers d'un élément qui résultent de différences dans les énergies de dissociation des molécules qu'ils composent. La rupture des liaisons atomiques est plus facile pour des molécules contenant des isotopes légers qui possèdent des fréquences vibrationnelles plus hautes que celles contenant les isotopes lourds (Bigeleisen 1965; Criss 1999) ce qui conduit à un enrichissement

en isotopes légers dans le produit par rapport au réactif. Il est important de noter que les fractionnements cinétiques ne sont visibles et conservés que tant que la réaction demeure incomplète (Wiederhold 2015; Komárek et al. 2021). En effet, dès lors que la réaction est complète, et que tous les atomes sont passés de réactifs à produits, les compositions isotopiques initiale et finale sont les mêmes.

Le fractionnement isotopique unidirectionnel (sans échange isotopique entre le produit et le réactif) peut être décrit par le modèle de Rayleigh lorsque la réaction est incomplète en système clos. Ce modèle suit l'équation suivante (Rayleigh 1896; Wiederhold 2015) :

$$\frac{R_{St}}{R_{S0}} = f^{(\alpha-1)} \; (eq. 6)$$

Avec *R* le ratio isotopique d'un élément au sein de la molécule S lors de sa dégradation, à un temps *0* et *t* comme une fonction *f* de la fraction restante de la molécule *et* α le facteur de fractionnement isotopique entre la phase A et B, comme décrit plus haut.

Les fractionnements isotopiques à l'équilibre sont produits lorsque deux phases sont à l'équilibre isotopique l'une avec l'autre. Ils sont dus aux différences d'énergie des liaisons atomiques dans lesquelles les isotopes sont impliqués. L'équilibre isotopique peut être distinct de l'équilibre chimique (Komárek et al. 2021) et ne dépend que de la température et pas de la pression, ce qui peut être expliqué par le fait que la substitution isotopique ne provoque pas de variation du volume molaire des phases ; les fractionnements à l'équilibre décroient d'un facteur $1/T^2$ pour la plupart des éléments (Schauble 2004). De manière générale, à l'équilibre isotopique, les isotopes lourds sont enrichis dans les environnements à liaisons atomiques plus fortes, ce qui est expliqué thermodynamiquement par des énergies du point zéro plus faibles dans les molécules enrichies en isotopes lourds comparées aux liaisons avec des isotopes légers d'un même élément (Criss 1999; Wiederhold et al. 2010). O'Neil en 1986 a montré que le fractionnement isotopique à l'équilibre n'est pas seulement fonction de la différence de masse relative entre deux isotopes ou de la robustesse des liaisons atomiques, mais aussi du type de liaison. Les liaisons covalentes, qui sont des liaisons présentant des mouvements vibratoires et rotationnels vigoureux sont plus fortement sensibles aux différences de masses et donc vont avoir tendance à générer des fractionnements isotopiques plus importants, à la différence des liaisons métalliques ou ioniques, qui sont, elles, principalement influencées par des forces électrostatiques qui dépendent de la charge mais très peu de la masse (O'Neil 1986; Criss 1999). Ceci peut être observé pour les isotopes ^{12}C et ^{13}C du carbone, qui, malgré une différence relative de masse bien moins importante qu'entre le ^{40}Ca et ^{48}Ca, fractionnent beaucoup plus, du fait de leurs liaisons covalentes. Les principes de la mécanique quantique peuvent s'appliquer pour prédire l'amplitude et le sens de ces fractionnements à l'équilibre (Criss 1999; Schauble 2004; Burke 2007; Méheut-Le Quéau 2008).

1.d. Principes généraux du fractionnement isotopique

Avant de rentrer plus en détail sur chacun des processus qui fractionnent les éléments métalliques, des observations générales sur le sens et l'amplitude des fractionnements isotopiques à l'équilibre sont présentées ici, bien qu'elles puissent varier d'un système isotopique à un autre. Elles sont issues

à la fois d'études théoriques et expérimentales (Criss 1999; Schauble, Rossman, et Taylor 2001; Schauble 2004; Fry 2006; Balistrieri et al. 2008; Wiederhold 2015; Johnson, Beard, et Albarède 2018; Hoefs 2021; Komárek et al. 2021) :

- Les liaisons atomiques courtes sont plus robustes et énergétiques et favorisent préférentiellement les isotopes lourds ; c'est le cas généralement lorsque le degré de coordination est faible. Par exemple, les espèces oxydées auront tendance à s'enrichir en isotopes lourds par rapport aux espèces réduites.
- Les fractionnements isotopiques sont généralement plus élevés pour les éléments légers que pour les éléments lourds, étant donné qu'un neutron de plus ou de moins provoque une différence de masse, en proportion, plus importante.
- Le fractionnement isotopique lié à un processus donné décroît lorsque la température augmente, d'un facteur en général proportionnel à $1/T^2$.

1.e. Méthodes d'étude du fractionnement isotopique

Trois approches complémentaires peuvent être mises en œuvre afin d'appréhender les fractionnements isotopiques (Wiederhold 2015; Fujii et al. 2014; Schauble, Méheut, et Hill 2009; Sherman 2013):

- **Les études de laboratoire** permettent de reproduire des processus physico-chimiques de manière isolée et contrôlée afin de quantifier leur impact sur le fractionnement isotopique de l'élément ciblé. Ces expériences se déroulent en conditions contrôlées et permettent notamment d'étudier le fractionnement d'équilibre ou cinétique au cours de processus comme les changements de degré d'oxydation, l'adsorption, la précipitation, la dissolution…

- **Les études théoriques** de fractionnement à l'équilibre entre deux phases, permettent d'estimer le sens et les amplitudes de fractionnements isotopiques de manière non empirique en se basant sur des modèles théoriques de mécanique quantique. Ces fractionnements sont généralement dus à des différences d'énergies associées aux fréquences vibrationnelles des liaisons atomiques ainsi qu'au type de liaison. Ces modèles théoriques se basent sur des équations du début et du milieu du siècle dernier (Schrödinger de par ses travaux concernant l'évolution dans le temps d'une particule massique non relativiste, Born et Oppenheimer 1927 de par leurs travaux résultant aux approximations adiabatiques, Urey, 1947 pour les équations simplifiées des ratios des fonctions de partitions isotopiques des molécules, et Kieffer 1982 pour son extension aux phases condensées) mais elles se sont popularisées avec l'essor de l'informatique et des moyens de calculs depuis les années 1990, et en particulier avec la théorie de la fonctionnelle de la densité (DFT), qui permet d'avoir le meilleur compromis entre la précision des résultats et les temps de calculs (Burke 2007; 2012; Burke et Wagner 2013). Ces méthodes de calcul nécessitent une bonne connaissance des environnements atomiques des éléments dans les minéraux étudiés et se déroulent la plupart du temps dans des cas idéaux (sans impuretés, avec deux ou

plusieurs phases à l'équilibre). Elles permettent de mieux comprendre et d'expliquer les fractionnements isotopiques observés lors des expérimentations de laboratoire ou les études de terrain.

- **Les études de terrain** permettent de mesurer la composition isotopique d'échantillons naturels. Cette composition découle des différentes sources de l'élément ainsi que des processus biogéochimiques qu'il subit lors de son transport. En croisant les données isotopiques avec d'autres informations géochimiques (concentrations, spéciation dissoute) et minéralogiques (spéciation solide de l'élément), il est possible d'identifier les processus dans lequel l'élément est impliqué et d'évaluer des facteurs de fractionnements isotopiques apparents associés.

II. Processus à l'origine de fractionnements isotopiques au sein des environnements miniers et des eaux de surface

La connaissance du fractionnement isotopique associé aux processus biogéochimiques est essentielle afin de pouvoir tracer les sources et processus qu'ont subi les éléments. Dans cette partie, le fractionnement isotopique produit par les processus majeurs contrôlant le devenir des métaux et des métalloïdes dans les environnements miniers sont présentés avec un focus sur les milieux aquatiques. Ces processus sont principalement l'oxydation ou la réduction des éléments, la dissolution de minéraux sulfurés, la re-précipitation de minéraux secondaires et l'adsorption sur les oxydes et (oxy)hydroxydes de Fe, Al et Mn.

2.a. Processus géochimiques à l'origine de fractionnement isotopique au sein des environnements miniers

1. Dissolution des minéraux sulfurés

La dissolution des minéraux sulfurés joue un rôle important dans la libération de métaux au sein des cours d'eaux impactés par l'activité minière, c'est le processus responsable de la formation de drainages miniers acides (DMA) (Banks et al. 1997).

Les changements de plus proches voisins sont à l'origine de fractionnement isotopique, ainsi que le changement de degré d'oxydation de l'élément (Blanchard et al. 2009; Schauble, Méheut, et Hill 2009; Ducher, Blanchard, et Balan 2016). Lorsqu'un atome de soufre est substitué par un atome d'oxygène, la nature des liaisons que possède l'élément change, et devient plus robuste, courte, énergétique et avec des fréquences vibrationnelles plus hautes, ce qui implique un enrichissement en isotopes lourds du composé lié à l'oxygène. Cela a été rapporté par des travaux théoriques pour Zn, Fe, Cu (Fujii et al. 2014; Ducher, Blanchard, et Balan 2016; Liu et al. 2021) mais également par des résultats expérimentaux et des observations de terrain (Matthies, Krahé, et Blowes 2014; Fernandez et Borrok 2009; Little et al. 2019; Kimball et al. 2009; Mathur et al. 2005) (Tableau 1). Pour les trois

éléments présentés dans le Tableau 1, le processus de dissolution de la phase sulfurée vers la phase aqueuse ou liée à des oxydes provoque dans la majorité des cas un fractionnement isotopique favorisant les isotopes lourds dans la phase formée/le produit.

Les processus de dissolution impliqués dans les études expérimentales et de terrain sont complexes car ils peuvent faire l'objet de plusieurs étapes et sous-processus (oxydation, re-précipitation…) et les mécanismes à l'origine des fractionnements observés font l'objet d'hypothèses. Cependant, les études ab-initio de prédiction du fractionnement isotopique sont cohérentes à la fois dans le sens et l'amplitude de ces fractionnements. Pour le cuivre ($\delta^{65}Cu$), un fractionnement de l'ordre de 0 à +2 ‰ est observé (Tableau 1) dans les études expérimentales et de terrain (Kimball et al. 2009; Mathur et al. 2005; Little et al. 2019; Fernandez et Borrok 2009), corroborant les valeurs de +1,2 à +2 ‰ obtenues dans les études théoriques, selon les minéraux (Liu et al. 2021). D'un point de vue théorique et lorsque les deux phases sont à l'équilibre thermodynamique, ces fractionnements peuvent être expliqués par les différences de nature (liaisons plus énergétiques et plus courtes notamment) des liaisons -S et -O sans changement de degré d'oxydation. Dans le cas des études de terrain ou expérimentales, plusieurs autres processus peuvent entrer en jeu et générer un fractionnement isotopique. Trois hypothèses principales ressortent de ces différentes études. Selon l'étude de Little et al. (2019), la libération préférentielle de l'isotope lourd de Cu vers la phase aqueuse pourrait être due à l'incorporation de l'isotope léger dans des phases secondaires d'oxydes de fer aluminique ou alors à une complexation avec des ligands organiques dans la phase aqueuse. Mathur et al. (2005), quant à eux, écartent les hypothèses d'adsorption du cuivre sur des (oxy)hydroxydes de fer ou d'un fractionnement lors de la dissolution de la chalcopyrite ($CuFeS_2$), mais explique le fractionnement observé par la précipitation d'un nouveau minéral après libération de Cu en solution, la covellite (CuS), et par la différence de coordination du cuivre entre la chalcopyrite et la covellite. Kimball et al. (2009) a proposé que le fractionnement observé pourrait être dû à une oxydation du cuivre à la surface du minéral. Fernandez et Borrok (2009) précisent que ce fractionnement serait généré par la formation de fines couches de sulfate de cuivre enrichies en isotope lourd de Cu à la surface de la chalcopyrite.

Pour le cadmium, des études sur le site minier de la province de Yunnan (Chine) ont montré que les processus de dissolution des minéraux sulfurés de cadmium provoquaient un fractionnement $\Delta^{114/110}Cd_{solution\text{-}CdS}$ de +0.33 ‰ (Zhu et al. 2018). Zhang et al. (2016) avaient, en conditions expérimentales, déjà montré des résultats similaires, avec un $\Delta^{114/110}Cd_{solution\text{-}CdS}$ de +0.40 à 0.50 ‰, et sur le terrain avec des $\Delta^{114/110}Cd_{solution\text{-}sol}$ qui pouvaient aller jusqu'à +0.50 ‰.

Concernant le zinc, les études environnementales (Matthies, Krahé, et Blowes 2014; Fernandez et Borrok 2009) n'ont pas montré de fractionnements isotopiques aussi importants que ceux déterminés par les calculs théoriques (Ducher, Blanchard, et Balan 2016) ou ceux observés pour Cu et Fe. Ceci pourrait être expliqué par le fait que le zinc ne change pas de degré d'oxydation dans l'environnement ; les changements redox associés à la dissolution des sulfures de Cu et de Fe ne jouent donc aucun rôle dans le cas du Zn (Fernandez et Borrok 2009).

Tableau 1:Fractionnement isotopique de Cu, Zn et Fe lors de la dissolution abiotique de minéraux sulfurés à basse température. Des études théoriques, expérimentales (*) et de terrain (**) sont présentées, avec le $\Delta ln(\beta)_{O\text{-}S}$ comme étant la différence de

fractionnement isotopique entre la phase liée à l'oxygène et celle liée au soufre (cf équation 5). Modifié et complété à partir de Resongles, 2014.

Etudes	Elément	Rapport isotopique	Minéraux	$\Delta\ln(\beta)_{O-S}$ (‰) à 22 °C	Référence
Théoriques	Zn	$^{66}Zn/^{64}Zn$	Zincite (ZnO) - Sphalérite (ZnS)	+0.77	Ducher et al. 2016
			Zincite (ZnO) - Wurtzite (ZnS)	+0.80	
			Zincite (ZnO) - Gunningite ($ZnSO_4$)	+0.50	
	Fe	$^{56}Fe/^{54}Fe$	$FeOH(H_2O)_5^+$ - $Fe_2S_2(H_2O)_4$	+0.64	Fujii et al. 2014
			$FeOH(H_2O)_5^+$ - $FeSO_4(H_2O)_5^+$	+0.09	
	Cu	$^{65}Cu/^{63}Cu$	Cuprite (Cu_2O) - Chalcocite (Cu_2S)	+1.90	Liu et al. 2021
			Cuprite (Cu_2O) - Covelite (CuS)	+1.20	
			Cuprite (Cu_2O) - Villamaninite (CuS_2)	+2.00	
Expérimentales (*) ou observations de terrain (**)	Zn	$^{66}Zn/^{64}Zn$	$Zn(III)_{aq}$ - Sphalérite (ZnS)	X à +0.32	Matthies et al. 2014**
			$Zn(II)_{aq}$ - Sphalérite (ZnS)	0.00 à +0.20	Fernandez & Borrok 2009*
			$Zn(II)_{aq}$ - Sulfures de Zinc (n.p.)	+0.55	Little et al. 2019**
	Cu	$^{65}Cu/^{63}Cu$	$Cu(III)_{aq}$ - Sulfures de Cuivre (n.p.)	+0.91	Little et al. 2019**
			$Cu(II)_{aq}$ - roche riche en chalcopyrite	0.00 à +2.00	Fernandez & Borrok 2009*
			$Cu(II)_{aq}$ - Enargite (Cu_3AsS_5)	+0.98 à +1.60	Kimball et al. 2009**
			$Cu(II)_{aq}$ - Chalcopyrite ($CuFeS_2$)	+1.37 à +1.43	
			$Cu(II)_{aq}$ - Chalcopyrite ($CuFeS_2$)	+1.32	Mathur et al. 2005*
	Fe	$^{56}Fe/^{54}Fe$	$Fe(II)_{aq}$ - Pyrite (FeS_2)	-1.75 à +1	Fernandez & Borrok 2009*

2. Changements de degré d'oxydation

Les changements de degré d'oxydation d'un élément sont souvent accompagnés par des fractionnements importants des isotopes stables (Criss 1999; Schauble 2004; Wiederhold 2015), dus à la différence de robustesse et de longueur des liaisons (Asael et al. 2007). Ces processus rédox sont omniprésents dans les environnements miniers.

Les minéraux de cuivre qui ont connu de nombreux cycles oxydation/réduction montrent de très grandes variations isotopiques, de l'ordre de 20 ‰ environ (Maréchal, Télouk, et Albarède 1999; Larson et al. 2003; Mason et al. 2005; Mathur et al. 2005; 2009; 2010; Asael et al. 2007). Pour le cas du fer, Schauble, Rossman, et Taylor (2001) ont montré par des calculs théoriques que le degré d'oxydation provoquait des fractionnements importants, $\Delta^{56}Fe_{ox-red}$ de l'ordre de +3 à +5 ‰ entre les

deux degrés d'oxydation (Fe(II) et Fe(III)) pour un même ligand et une température de 25 °C, conduisant à un enrichissement en isotopes lourds de la phase oxydée. Lors de la dissolution oxydative des minéraux riches en $Cr(III)_s$ vers le $Cr(VI)_{aq}$, Gilleaudeau et al. (2016) ont noté un enrichissement de la phase aqueuse en isotopes lourds jusqu'à +1.77 ‰. Cette observation avait été également faite par Ellis et al. (2008) qui avaient relevé un fractionnement isotopique de +1 ‰ lors de l'oxydation de $Cr(III)_s$ en $Cr(VI)_{aq}$. Celui-ci ne suivait pas un fractionnement de Rayleigh ou cinétique mais plutôt un fractionnement à l'équilibre, observé aussi par Wang et al. (2010). Dans un article de synthèse sur l'isotopie du sélénium ($^{80}Se/^{76}Se$), Johnson (2004) a montré que la réduction de Se(VI) et Se(IV) est le processus principal fractionnant les isotopes du sélénium; les fractionnements varient de -7 à -12 ‰ (de -3 à -5 ‰ pour la réaction biotique) pour la réduction du Se(VI) en Se(IV) et de -6 à -12 ‰ (-6 à -9 ‰ pour la réaction biotique) pour la réduction du Se(IV) en Se(0). Par contre la réduction de Se(0) en Se(-II) ne génèrerait pas ou très peu de fractionnement apparent, comme l'oxydation de S(-II) vers S(0), qui est très faible (Fry et al. 1988; Johnson 2004).

Les processus biologiques peuvent modifier voire inverser le fractionnement observé pour les changements rédox abiotiques, en formant des phases oxydées plus légères. C'est le cas par exemple du cuivre, pour lequel, lors d'une oxydation de sulfure de Cu en présence de bactéries oxydantes, un fractionnement $\Delta^{65}Cu_{ox\text{-}red}$ variant de – 1‰ à -4.4‰ est observé alors que pour une oxydation abiotique, un fractionnement de +1 à +4 ‰ est mis en évidence (Moynier et al. 2017). Ceci corrobore les observations antérieures de Kimball et al. (2009), démontrant que l'activité bactérienne de *Acidithiobacillus ferroxidans* oxydant le sulfure de cuivre ($CuS + 2O_2 \rightarrow CuSO_4$, Torma et Habashi (1972)) favorise les isotopes légers ($\Delta^{65}Cu_{ox\text{-}red}$ = -0.57 ± 0.14 ‰).

Concernant l'antimoine, très peu d'études ont abordé l'effet de l'oxydation de Sb sur son fractionnement isotopique. Tanimizu et al. (2011) ont montré que le Sb(V) dissous dans un drainage minier acide était enrichi préférentiellement en isotope lourd comparé à la stibnite présente dans les déchets miniers ($\Delta^{123}Sb_{dissous\text{-}solide}$ = +0.35 ‰). La contribution des processus de dissolution, d'adsorption et d'oxydation dans ce fractionnement apparent n'a pas été évaluée. Une étude expérimentale de Rouxel, Ludden, et Fouquet (2003) a montré que la réduction abiotique de Sb(V) en Sb(III) entrainait un fractionnement isotopique $\Delta^{123}Sb_{Sb(III)\text{-}Sb(V)}$ de l'ordre de -0.9 ‰. Mackinney (2016) a également observé un fractionnement isotopique important ($\Delta^{123}Sb_{Sb(III)\text{-}Sb(V)}$ de -1.45 ‰) lors de la réduction de Sb(V) par des sulfures pour former une phase solide $Sb(III)_2S_3$. Cependant, d'autres effets se superposent à ceux liés aux changements redox, en particulier les effets associés à des différences de ligand (Sb-Cl et Sb-S…).

3. Adsorption sur les (oxy)hydroxydes de Fe, Al et Mn

Dans les environnements miniers, l'adsorption des éléments métalliques sur les (oxy)hydroxydes de fer, d'aluminium et de manganèse est un processus important contrôlant la mobilité des contaminants (voir partie I. 2.b mécanismes de sorption). De façon générale, l'adsorption des métaux présents sous forme cationique (Cu, Tl, Zn…) dans les eaux semble privilégier les isotopes lourds à la surface des (oxy)hydroxydes de fer, d'aluminium et de manganèse, alors que pour les éléments sous forme anionique (Ge, Se, Mo, Sb), l'adsorption semble privilégier les isotopes légers (Balistrieri et al. 2008; Barling et Anbar 2002; Kuhn et al. 2003; Pokrovsky et al. 2006). Ceci peut être expliqué par le fait que lorsque les cations sont adsorbés à la surface des (oxy)hydroxydes, leur nombre de

coordination décroit ainsi que la longueur des liaisons métal-oxygène. Par exemple, le cuivre en phase aqueuse a un nombre de coordination de 6 avec une longueur de liaison Cu-O moyenne de 2.10 Å (Fulton, Hoffmann, et Darab 2000) alors que le Cu(II) adsorbé sur différents (oxy)hydroxydes possède un nombre de coordination de 4 avec des distances Cu-O comprises entre 1.85 et 2.05 Å (Peacock et Sherman 2004). Très récemment, des observations similaires ont été faites pour le zinc ; le nombre de coordination et les distances atomiques sont apparus comme les principaux paramètres contrôlant le fractionnement isotopique lors de l'adsorption du zinc à la surface de la todorokite, un oxyde de manganèse (Wang et al. 2022). Dans le cas des oxyanions, la phase adsorbée possède en général un nombre de coordination plus important et des longueurs de liaisons plus grandes qu'en phase aqueuse, comme c'est la cas par exemple avec le germanium Ge(IV) ; en solution, Ge(IV) possède un nombre de coordination de 4 alors qu'adsorbé sur des oxydes de fer, son nombre de coordination augmente jusqu'à 6 (Pokrovsky et al. 2006). Pour le germanium, il a aussi été rapporté que l'apparition du fer ou d'un autre élément comme second voisin le plus proche pouvait entrainer une distorsion de la première sphère de coordination et une perte de symétrie, fragilisant les liaisons atomiques en privilégiant les isotopes légers à la surface du solide (Pokrovsky et al. 2014).

Les fractionnements observés ne sont pas toujours uniquement expliqués par ces variations d'environnement atomique. Lorsque l'élément existe sous plusieurs formes chimiques en solution (par exemple MoO_4^{2-} et MoO_3) et que ces espèces chimiques ne possèdent pas le même rapport isotopique et n'ont pas la même affinité avec les oxydes de fer, cela peut générer un fractionnement qui ne relève pas uniquement de l'environnement atomique global de Mo (Tossell 2005).

D'une manière générale, il est rare que les processus d'adsorption fractionnent avec des facteurs supérieurs à 1 ‰. Pour les isotopes du zinc, les fractionnements liés à l'adsorption ($\Delta^{66}Zn_{aq\text{-}adsorbé}$) ont été rapportés entre +0.17 et -0.8 ‰ selon les phases minérales concernées (Cacaly et al. 2004; Juillot et al. 2008; Pokrovsky, Viers, et Freydier 2005; Balistrieri et al. 2008; Wang et al. 2022). Les valeurs relevées pour le cuivre sont relativement similaires, avec des fractionnements allant de -0.35 à -1 ‰ (Clayton, Hudson-Edwards, et Houghton 2005; Balistrieri et al. 2008; Pokrovsky et al. 2008; Liu et al. 2022). Pour le cadmium, des valeurs de $\Delta^{114/110}Cd_{aq\text{-}adsorbé}$ sont rapportées entre +0.12 et +0.55 ‰ selon les phases d'oxydes de fer et de manganèse observées (Wasylenki et al. (2014); Yan et al. (2021)) Des fractionnements importants lors de l'adsorption de Se ont été observés par Mitchell et al. (2013), de l'ordre de +3 ‰ (avec un maximum de +9.7 ‰) et cela a été attribué au fait que l'oxydation de Se(IV) se surimposait à son adsorption à la surface des (oxy)hydroxydes de fer. Ellis, Johnson, et Bullen (2004) ont, quant à eux, montré que l'adsorption du chrome à l'équilibre sur un oxyde d'aluminium et sur la goethite provoquait un fractionnement isotopique négligeable (< 0.04 ‰), mais que les fractionnements cinétiques générés avant d'atteindre cet équilibre pourraient ne pas être négligeables dans l'environnement. Plus récemment, Xu et al. (2020) ont observé un fractionnement de Se similaire à celui observé par Mitchell et al. (2013) lors de son adsorption sur des oxydes de fer (de l'ordre de 3 ‰). Ce fractionnement important avait en réalité une origine cinétique ; lors de l'équilibre isotopique, l'adsorption de Se induisait un fractionnement de l'ordre +0.87 à +1.24 ‰ pour les oxydes de fer et de manganèse et de +0.05 à +0.08 ‰ pour les oxydes d'aluminium. Enfin, les isotopes du molybdène ont montré un fractionnement compris entre +0.55 et +1.8 ‰ ($\Delta^{97}Mo_{aq\text{-}adsorbé}$) lors de leur adsorption sur des oxyhydroxydes de fer (Barling et Anbar 2004; Wasylenki et al. 2008; Goldberg et al. 2009).

Récemment, Zhou et al. (2022) ont étudié le fractionnement isotopique de l'antimoine lors de son adsorption sur des oxydes d'aluminium ($\Upsilon\text{-}Al_2O_3$) et ont montré l'existence d'un fractionnement

cinétique entre la phase aqueuse et la phase adsorbée en début de réaction ($\delta^{123}Sb_{adsorbé\text{-}aqueux}$ = -0.25 ‰). A l'équilibre isotopique, le fractionnement n'est plus significatif ($\Delta^{123}Sb_{adsorbé\text{-}aqueux}$ = 0 ± 0.08 ‰). Cette absence de fractionnement isotopique entre la phase aqueuse et la phase solide à l'équilibre a été attribuée au fait que Sb formait des complexes de sphères externes à la surface de l'oxyde d'aluminium Υ-Al_2O_3.

4. Précipitations de minéraux

La précipitation de minéraux est un processus de fractionnement couramment rencontré dans les environnements de surface (Wiederhold 2015). C'est particulièrement le cas dans les environnements miniers où les processus de dissolution et de re-précipitation sont un important contrôle de la mobilité des contaminants métalliques. La plupart du temps, le fractionnement isotopique lors de la précipitation dépend d'un processus cinétique, mais il n'est pas toujours évident de faire la distinction entre le fractionnement cinétique et celui à l'équilibre (DePaolo 2011). D'une manière générale, le lien entre la cinétique de précipitation et l'amplitude du fractionnement, ainsi que la précipitation préférentielle des isotopes légers durant la précipitation tendent à montrer que ces fractionnements sont surtout d'origine cinétique (Skulan, DePaolo, et Owens 1997; Skulan et DePaolo 1999; Tang, Köhler, et Dietzel 2008).

*Tableau 2: Fractionnements isotopiques de différents métaux lors de la précipitation de la phase aqueuse vers divers minéraux à faible température, adapté et complété de Resongles (2014). * précipitations biotiques ; [e] fractionnement à l'équilibre.*

Rapport isotopique	Espère aqueuse - Phase minérale	$\Delta_{solution\text{-}solide}$ (‰)	Référence
$^{66}Zn/^{64}Zn$	$Zn(II)_{aq}$ - sphalérite (ZnS)	+0.36 ± 0.09	Archer et al. (2004)
	$Zn(II)_{aq}$ - Zincite (ZnO)	+0.52	Cacaly et al. (2004)
	$Zn(II)_{aq}$ - hydrozincite ($Zn_5(CO_3)_2(OH)_6$)*	-0.35 ± 0.05	Wanty et al. (2013)
	$Zn(II)_{aq}$ - smithonite ($ZnCO_3$)	+0.04 à +0.11	Marechal et Sheppard (2002)
$^{65}Cu/^{63}Cu$	$Cu(II)_{aq}$ - malachite ($CuCO_3.Cu(OH)_2$)	+0.20 à +0.38	
	$Cu(II)_{aq}$-covelite (CuS)	+3.06 ± 0.14	Ehrlich et al. (2004)
	Cu(II)aq -$Cu(OH)_2$	+0.28 ± 0.02	
$^{202}Hg/^{198}Hg$	$Hg(II)_{aq}$ - metacinnabar (β-HgS)	-0.63	Smith et al. (2015)
	$Hg(II)_{aq}$ - Montroydite (HgO)	-0.32	
$^{60}Ni/^{58}Ni$	$Ni(II)_{aq}$ - $Ni(OH)_2$	-0.40 ± 0.04	Parigi et al. (2022)
	$Ni(II)_{aq}$ - $Ni_4Co_3(OH)_6(H_2O)_4$	-0.50 ± 0.02	
	$Ni(II)_{aq}$ - NiS	-0.73 ± 0.08	
	$Ni(II)_{aq}$ - NiS*	-1.99	Parigi, et al. (2022)
$^{98}Mo/^{95}Mo$	$Mo(VI)_{aq}$ - powellite ($CaMoO_4$)	+0.82 ± 0.12	Skierszkan et al. (2019)
	$Mo(VI)_{aq}$ - wulfénite ($PbMoO_4$)	+0.25 ± 0.10	
	$Mo(VI)_{aq}$ - wulfénite ($PbMoO_4$)[e]	+0.75 ± 0.07	

Les phénomènes de précipitation d'un élément étant courants dans l'environnement, plusieurs études, reportées dans le Tableau 2, ont porté sur les fractionnements isotopiques associés à ces réactions. Pour le cuivre et le zinc, lors de la précipitation, les phases solides sont préférentiellement enrichies en isotopes légers, avec des facteurs de fractionnements $\Delta_{solution\text{-}solide}$ pouvant aller de +0.04 à +0.52 ‰ pour le zinc, et de +0.20 à +3.06 ‰ pour le cuivre (Archer et al. 2004; Cacaly et al. 2004; Wanty et al. 2013; Marechal et Sheppard 2002; Ehrlich et al. 2004). Le Molybdène présente lui aussi un enrichissement préférentiel en isotopes légers dans la phase solide (Skierszkan et al. 2019). L'exception reportée dans le Tableau 2 pour un enrichissement préférentiel en isotopes lourds de la phase solide du zinc correspond à un processus biotique. Les deux autres éléments étudiés (Hg et Ni) présentent tous des phases solides préférentiellement enrichies en isotopes lourds, avec des $\Delta_{solution\text{-}solide}$ pouvant aller jusqu'à -0.73 ‰ dans le cas du nickel et jusqu'à -1.99 ‰ pour ce même processus, mais via des processus biotiques (Smith, Wiederhold, et Kretzschmar 2015; Parigi, Pakostova, et al. 2022; Parigi, Chen, et al. 2022).

Il est important de noter que lorsque qu'il n'y a pas de re-dissolution ou d'échange isotopique entre phase dissoute et phase solide, ces fractionnements peuvent être décrits par un modèle de Rayleigh, avec une phase dissoute qui va s'enrichir progressivement en isotopes lourds au fur et à mesure que les isotopes légers sont entraînés vers la phase solide (Wiederhold 2015). La plupart des facteurs de fractionnements reportés dans le Tableau 2 ont suivi un modèle de Rayleigh, à l'exception du fractionnement entre $Mo(VI)_{aq}$ et la wulfénite, pour lequel des échanges isotopiques entre la phase aqueuse et précipitée ont eu lieu (Skierszkan et al. 2019).

En ce qui concerne la précipitation de sulfures d'antimoine, dans une mine de Zhaxikang au sud du Tibet, qui possède un important gisement riche en Sb, Pb, Zn et Ag, Wang et al. (2021) ont attribué les variations isotopiques de la stibnite (Sb_2S_3), de la bournonite ($PbCuSbS_3$) et de la boulangérite ($Pb_5Sb_4S_{11}$) observées dans les filons au fractionnement résultant de la réduction progressive de Sb(V) par les sulfures dans les fluides hydrothermaux et de la précipitation de Sb(III) qui a suivi, avec un facteur de fractionnement $\Delta^{123}Sb_{fluide\text{-}stibnite}$ entre +0.6 et +0.9 ‰. Zhai et al. (2021) ont aussi étudié la formation d'un gisement riche en stibnite dans le sud de la Chine, et ont trouvé une gamme de variation de 1.13 ‰ le long de l'ancien système hydrothermal ($\delta^{123}Sb$ de -0.27 à +0.86 ‰). Ces variations ont été attribuées à une augmentation progressive de la composition isotopique de Sb au cours de la circulation du fluide hydrothermal à l'origine de la formation de la stibnite. Le fractionnement entre le fluide et la stibnite précipitée a quant à lui été évalué à environ 0.45 ‰ et a été expliqué par un effet cinétique. Beaucoup d'incertitudes demeurent encore quant aux mécanismes à l'origine du fractionnement isotopique lors de la formation de ces gisements sulfurés riches en Sb.

III. Applications des isotopes stables de métaux pour le traçage des sources et des processus géochimiques dans les milieux aquatiques contaminés par les activités anthropiques et minières

Les éléments étudiés dans cette partie seront principalement des contaminants peu étudiés, à l'instar de l'antimoine. De récentes et très bonnes revues ont été faites pour l'isotopie du cuivre (Wang, Chen, et Zhang 2017), du zinc (Desaulty et Petelet-Giraud 2020; Li et al. 2019) et du mercure (Yin et al. 2014; Tsui, Blum, et Kwon 2020). Pour ce chapitre, une présentation détaillée sera faite de l'isotopie du cadmium, du sélénium, du chrome et enfin, de l'antimoine.

3.a. Cadmium (Cd)

Les signatures isotopiques du cadmium dans les environnements naturels non contaminés et les sources anthropiques sont généralement différentes. Ces dernières années, plusieurs études se sont penchées sur l'isotopie du cadmium, les processus de fractionnement et l'utilisation potentielle de la signature isotopique du cadmium comme traceur de source de contamination (Cloquet et al. 2006; Horner, Rickaby, et Henderson 2011; Gao et al. 2013; Wasylenki, Swihart, et Romaniello 2014; Chrastný et al. 2015; Yang et al. 2018; Yang et al. 2019; Zhong et al. 2020; Ratié et al. 2021; Yin et al. 2021; Fang et al. 2022).

Les fractionnements isotopiques du cadmium par des processus métallurgiques ont été caractérisés pour la première fois dans une étude de Cloquet et al. (2006). Cette étude a montré que la signature isotopique singulière du cadmium dans les sols aux alentours des fonderies pouvait être attribuée au fractionnement lors du processus de raffinage, avec une corrélation entre la composition isotopique et la distance aux cheminées de la fonderie. Deux autres sources de contamination ont pu être identifiées grâce aux isotopes du cadmium : (1) les scories minières, enrichies en isotopes lourds, et (2) l'agriculture locale, bien qu'elle constitue une source minoritaire (Cloquet et al. 2006). Ces résultats ont par la suite été corroborés par Shiel, Weis, et Orians (2010) qui ont montré que certains processus de fonderie pouvaient enrichir les résidus de Cd de l'ordre de +1 ‰. Gao et al. (2013) ont étudié les relations entre les concentrations et les rapports isotopiques de Cd dans les sédiments d'une rivière contaminée par l'activité minière, métallurgique et industrielle. Ces sédiments, significativement enrichis en isotopes légers (jusqu'à -0.35 ‰) ont finalement montré que la source principale de contamination provenait des scories d'une fonderie de Pb-Zn, mais que l'utilisation des isotopes du cadmium permettait aussi d'identifier les apports d'une usine de recyclage électronique ($^{114/110}$Cd > 0) et du fond géochimique (Gao et al. 2013). Wen et al. (2015) ont utilisé les isotopes du cadmium pour tracer différentes sources de cadmium dans des échantillons de sols contaminés et ont mesuré la composition isotopique de minéraux oxydés, sulfurés et de scories ; ils ont montré que toutes les signatures isotopiques mesurées dans ces échantillons pouvaient être expliquées par des lois de mélanges binaires entre ces minéraux de signature distincte et le fond géochimique, suggérant que la contamination des sols provenait principalement de l'émission de poussières générées par les

activités anthropiques (Wen et al. 2015). Toutefois, une autre étude a montré que les différences de signature isotopique entre deux profils de sol situés à proximité de mines de Pb et Zn étaient probablement associées à des processus de mobilisation du Cd au sein du sol et non à l'influence des sources anthropiques, limitant l'utilisation des isotopes du cadmium pour l'identification de sources industrielles dans ce contexte (Chrastný et al. 2015).

Finalement, Yang et al. (2019) ont étudié la composition isotopique du cadmium au sein d'un drainage minier acide (montagne Dabao, Chine) et son évolution le long de ce DMA. Le $\delta^{114/110}$Cd dissous variait de 0.21 à 1.03 ‰ le long du DMA, avec un facteur de fractionnement entre l'eau et le sédiment $\Delta^{114/110}Cd_{eau\text{-}sédiment}$ mesuré jusqu'à 1.61 ‰ au plus près de la source, et dont la grande amplitude a été attribuée à un fractionnement cinétique de Cd lors de la dissolution rapide des déchets miniers (avant de diminuer plus en aval jusqu'à 0.91 ‰). Les variations de composition isotopique vers l'aval témoignent de l'influence de différents processus (adsorption, complexation, coprécipitation de Cd avec des (hydr)oxydes…) qui fractionnent les isotopes du Cd. Plus en aval, la hausse soudaine du $\delta^{114/110}$Cd près des terres agricoles suggère la présence d'une source secondaire de cadmium dans les eaux. Cette étude montre que les processus naturels peuvent influencer fortement les signatures isotopiques du Cd dans les milieux aquatiques impactés par l'activité minière (Yang et al. 2019).

3.b. Sélénium (Se)

Comme il a été évoqué dans le chapitre précédent, les processus redox sont les processus qui fractionnent le plus les isotopes du sélénium (Johnson 2004; 2012; Weiss et al. 2008). Etant donné que le sélénium est présent sous quatre états d'oxydation dans l'environnement, ses isotopes sont relativement complexes à utiliser comme traceurs géochimiques. Johnson, Bullen, et Zawislanski (2000) ont étudié les processus et les sources affectant les signatures isotopiques du sélénium dans la baie de San-Francisco (USA). Ils ont relevé que les sédiments étaient préférentiellement enrichis en isotopes légers par rapport aux eaux de la baie et aux effluents d'une raffinerie de pétrole, avec un fractionnement d'environ 2 ‰. Ce fractionnement étant relativement faible par rapport à ceux rapportés lors de la réduction de Se(VI) vers Se(IV) ou de Se(IV) vers Se(0), ces auteurs ont conclu que la réduction n'était pas le processus dominant par lequel Se s'incorporait dans les sédiments. Herbel et al. (2002) ont mesuré une amplitude de fractionnement similaire à celle mesurée par Johnson et al (2000) entre la phase dissoute et la phase adsorbée sur les sédiments au sein du lac Tulare et d'une zone humide aux alentours, affectés par une contamination au sélénium provenant d'eaux usées de raffineries.

Une étude de terrain a montré de faibles variations de la signature isotopique (entre +1.14 et +2.40 ‰) du sélénium $\delta^{80/76}$Se dans la phase dissoute, sédimentaire et liée à la matière organique du lac Sweitzer (Colorado, USA), alimenté par deux canaux provenant de deux bassins versants différents (sans sources de contaminations spécifiques) malgré la mise en évidence de processus de réduction. L'absence d'influence de la réduction du sélénium sur les signatures isotopiques a été expliquée par l'absence d'échange entre les sites de réduction au sein des sédiments et les eaux du lac. L'étude a conclu que dans ce type de contexte, l'utilisation des isotopes de Se comme traceur de changements redox (biotiques ou abiotiques) n'était pas efficace (Clark et Johnson 2010).

Les signatures isotopiques de trois gisements de schistes riches en Se ont été déterminées afin de tracer les différents processus à l'origine de la formation des gisements (Wen et Carignan (2011)). Un des trois gisements montrait de faibles variations isotopiques (-1.6‰ à +2.4‰) alors que les deux autres présentaient de plus grandes variations (de -3.8 à +5.4‰ et de -12.7 à 7.5‰). L'absence de variation isotopique importante au sein du premier gisement a été attribuée à une origine hydrothermale du sélénium ; le sélénium dissous aurait été transporté avec H_2S sous forme de H_2Se et aurait directement précipité sous forme de séléniure ou de sulfure. Les deux autres gisements présentant de fortes disparités dans leur composition isotopique, auraient été formés en suivant des changements redox importants, induisant un fractionnement cinétique (Wen et Carignan 2011). Zhu et al. (2014) ont utilisé les isotopes du sélénium comme traceurs de processus au sein de formations de schiste du Permien, pour le fractionnement du sélénium lors des processus d'érosion. Ils ont montré que les grandes variations de $\delta^{82/76}Se$ observées (-14.20 à +11.37‰) découlaient de nombreux cycles d'oxydation, de mobilisation et de réduction, avec de très grandes variations à l'échelle du décimètre, indiquant que les conditions redox sont très variables d'un point à un autre et sont contrôlées par les fractures et les interstices dans la roche (Zhu et al. 2014).

3.c. Chrome (Cr)

L'isotopie du chrome a été principalement utilisée pour le traçage de processus dans l'environnement. En effet, le $\delta^{53}Cr$ a été identifié comme étant un outil très efficace pour détecter la réduction du Cr(VI), en particulier dans les systèmes mixtes fluviaux/aquifères, pour distinguer les processus de mélange du processus de réduction (Izbicki et al. 2008; 2012; Heikoop et al. 2014; Novak et al. 2014; D'Arcy et al. 2016; Qin et Wang 2017).

Izbicki et al. (2008) ont étudié les variations du $\delta^{53}Cr$ dans les aquifères alluviaux du désert du Mojave (USA). Dans les eaux non contaminées, les valeurs de $\delta^{53}Cr$ variaient de +0.7 à +5.1 ‰, avec une gamme allant de +1.2 à +2.3 ‰ pour les zones de recharge ayant de faibles concentrations en Cr, ce qui est cohérent avec un fractionnement se produisant entre l'eau et les minéraux composant l'aquifère, lié aux processus d'adsorption à la surface des minéraux. Les fractionnements les plus importants sont associés aux zones qui possèdent de faibles concentrations en O_2, en lien avec la réduction partielle de Cr(VI) en Cr(III), et la précipitation du Cr(III). Enfin, ces auteurs ont montré qu'il était possible de quantifier l'étendue de la contamination anthropique de Cr sur le site (agriculture et industrie chimique), en utilisant les valeurs de $\delta^{53}Cr$ conjointement avec les éléments majeurs et la composition isotopique de l'eau ($\delta^{18}O$ et δD). Izbicki et al. (2012) ont effectué une autre étude dans le désert du Mojave, sur trois sites de contamination différents (pollution au niveau d'une conduite de gaz, d'une station de compression et d'un ancien site de fraisage chimique de pièces d'avions militaires). Les gammes de rapports isotopiques du fond géochimique et des contaminations en $\delta^{53}Cr$ se superposant, il a été difficile d'utiliser le $\delta^{53}Cr$ pour délimiter les zones de pollution anthropique au chrome. Cependant, trois processus différents ont pu être identifiés grâce aux signatures isotopiques $\delta^{53}Cr$: (1) la réduction du Cr(VI) par des agents réducteurs naturellement présents dans la nappe phréatique, (2) le mélange entre les eaux réduites anthropiques et naturelles aux limites des panaches et (3) le mélange au centre des panaches (Izbicki et al. 2012). De même, Heikoop et al. (2014) ont utilisé l'isotopie du chrome afin de quantifier la réduction du chrome dans les nappes phréatiques et les effets de mélange dans les eaux souterraines de Los Alamos (USA) impactées par l'utilisation du dichromate de potassium comme agent anti-corrosif dans des centrales électriques. Cette étude souligne que le

traçage des différentes sources de chrome au sein d'un environnement hydrologique complexe est possible, mais que l'interprétation de données peut être délicate. Novak et al. (2014) et Economou-Eliopoulos, Frei, et Atsarou (2014) ont montré que pour l'utilisation du $\delta^{53}Cr$ comme traceur de processus ou de sources dans les eaux souterraines, il est impératif de prendre en compte la lithologie et les sources géogéniques, qui peuvent avoir des signatures $\delta^{53}Cr$ très positives. Une étude récente de Bolaños-Benítez et al. (2021) dans un environnement minier a montré que les différences entre les signatures $\delta^{53}Cr$ pouvaient être utilisées afin de tracer le lessivage de Cr contenu dans les sols contaminés vers les eaux souterraines et de surface. Ces auteurs précisent que les enrichissements en isotopes lourds (^{53}Cr) dans les eaux de surfaces et souterraines sont reliés à l'oxydation dans les phases solides. Une partie de ces enrichissements est due à l'érosion naturelle, mais les activités minières jouent un rôle important dans l'accélération de cette érosion.

Concernant les eaux de surface, Paulukat et al. (2015) ont révélé une pollution importante au chrome liée à l'activité minière au sein du cours d'eau Damsal (Inde) ; cette contamination est associée à une baisse significative de la signature isotopique du chrome $\delta^{53}Cr$ ($\Delta^{53}Cr_{naturel\text{-}contaminé}$ varie de -0.65 à -0.27‰), entre l'amont et l'aval du cours d'eau. La signature $\delta^{53}Cr$ positive observée dans l'estuaire Brahmani, situé en aval du site précédent, et dans les eaux marines de la baie du Bengale indique que la signature générée par des processus conduisant à un enrichissement en isotope lourd dans l'eau de l'estuaire est conservée lors du transport du chrome en mer.

3.d. Antimoine (Sb)

A ce jour, il existe très peu d'études portant sur l'utilisation des isotopes stables de l'antimoine pour le traçage de sources de contamination ou de processus de transfert dans l'environnement. Rouxel, Ludden, et Fouquet (2003) furent les premiers à s'intéresser au potentiel de l'isotopie de l'antimoine comme traceur géochimique. Ils ont mesuré les rapports isotopiques de l'antimoine dans un certain nombre de matrices environnementales et géologiques (roches basaltiques et silicatées, sulfures hydrothermaux, eaux de mer, sols, sédiments, minéraux, matériaux d'origine anthropique…) et ont mis en évidence une gamme de variation naturelle de la composition isotopique de Sb d'environ 1.8 ‰ ; de plus, ces auteurs ont montré que la réduction abiotique de Sb(V) en Sb(III) fractionnait d'environ -0.9‰ les isotopes de l'antimoine.

Plus récemment, d'autres études ont porté sur l'isotopie de l'antimoine dans les milieux naturels et dans les eaux impactées par l'activité minière (Tanimizu et al. 2011; Resongles et al. 2015; Li et al. 2021). Ainsi, Tanimizu et al. (2011) ont d'abord analysé la composition isotopique de l'antimoine dans deux échantillons de minéraux de stibnite et dans un échantillon d'eau d'un DMA de la zone minière et métallurgique de Ichinokawa au Japon. Les résultats ont montré que les eaux du DMA étaient isotopiquement plus lourdes que la stibnite (Tanimizu et al. 2011). Resongles et al. (2015) ont mesuré la composition isotopique des rivières de l'Orb ($\delta^{123}Sb$ de -0.06 à +0.11 ‰) et du Gardon ($\delta^{123}Sb$ de +0.27 à +0.83 ‰) dans le Sud de la France, toutes deux affectées par une contamination liée à la présence d'anciennes mines d'antimoine. Plusieurs hypothèses ont été émises quant à l'origine des différences de signatures : une signature variable des sources primaires de Sb dans les différents gisements ((stibnite, boulangérite $Pb_5Sb_4S_{11}$, plagionite $Pb_5Sb_8S_{17}$ et tétraédrite $Cu_{10}(FeZn)_2Sb_4S_{13}$), une signature contrastée produite par le traitement du minerai (fonderie), une signature héritée d'une combinaison de processus (dissolution, oxydation précipitation, adsorption…) affectant le devenir de

l'antimoine lors de son transport dans les rivières (Resongles et al. 2015). Enfin, Li et al. (2021) ont analysé quelques échantillons d'eaux issus de la mine de Lengshuijiang (Chine) et ont trouvé des variations du rapport isotopique allant de -0.20 à +0.27 ‰, soulignant une fois de plus, le potentiel de l'isotopie de l'antimoine comme traceur de sources de contamination.

Outre ces applications environnementales de l'isotopie de l'antimoine, une série d'études archéologiques a été menée afin de tracer les anciennes routes commerciales de verres antiques (Lobo et al. 2012; 2013; 2014; Degryse et al. 2015; 2020; Reguera-Galan et al. 2019). Les auteurs ont mesuré l'isotopie de l'antimoine dans la stibnite provenant de différentes régions, ainsi que dans des verres romains et des objets d'art de l'âge de bronze. La stibnite provenant de différents endroits du monde ont montré des gammes de variation de signature δ^{123}Sb de l'ordre de 1 ‰. Dillis et al. (2019) ont également tenté d'étudier les fractionnements liés aux processus métallurgiques utilisés à l'âge de bronze pour traiter le minerai de Sb ; l'objectif était de mieux corréler la signature isotopique des objets d'art à un site d'extraction des minéraux, en tentant d'établir un « facteur de correction » lié au processus de traitement du minerai. Ils ont montré que pour la production du verre ou des éléments métalliques, les processus d'oxydation à haute température de la stibnite en oxydes d'antimoine (Sb(V)) fractionnaient les isotopes de l'antimoine d'environ +0.25‰.

Les études portant sur les méthodes de purification et d'analyse des isotopes stables de l'antimoine s'étant grandement développées ces trois dernières années (Liu et al. 2020; Ferrari et al. 2021; Kaufmann et al. 2021; Li et al. 2021; Sun et al. 2021), la purification d'échantillons environnementaux à faible teneur en Sb est désormais possible. Ainsi, de nombreuses avancées sont attendues sur l'isotopie de Sb dans les milieux aquatiques, et plus particulièrement dans les environnements miniers. Toutefois, la littérature récente montre aussi qu'il est nécessaire de mieux caractériser les facteurs de fractionnement isotopiques associés aux processus biogéochimiques pour pouvoir interpréter les signatures isotopiques de Sb dans l'environnement.

Bibliographie

Almoukhalalati, Adel, Avijit Shee, et Trond Saue. 2016. « Nuclear Size Effects in Vibrational Spectra ». *Physical Chemistry Chemical Physics* 18 (22): 15406-17. https://doi.org/10.1039/C6CP01913G.

Anderson, Corby G. 2012. « The Metallurgy of Antimony ». *Geochemistry*, Antimony, 72 (juillet): 3-8. https://doi.org/10.1016/j.chemer.2012.04.001.

Angeli, I., et K. P. Marinova. 2013. « Table of Experimental Nuclear Ground State Charge Radii: An Update ». *Atomic Data and Nuclear Data Tables* 99 (1): 69-95. https://doi.org/10.1016/j.adt.2011.12.006.

Anthony, John W., Richard A. Bideaux, Kenneth W. Bladh, et Monte C. Nichols. 1990. *Handbook of Mineralogy*. Mineralogical Society of America, Chantilly, VA 20151-1110, USA.

Appleton, J. D., et M. R. Cave. 2018. « Variation in Soil Chemistry Related to Different Classes and Eras of Urbanisation in the London Area ». *Applied Geochemistry* 90 (mars): 13-24. https://doi.org/10.1016/j.apgeochem.2017.12.024.

Archer, C., D. Vance, I. B. Butler, et Ian Butler. 2004. « Abiotic Zn Isotope Fractionations Associated with ZnS Precipitation ». In *Geochimica et Cosmochimica Acta*, 68: A325-A325. Elsevier. https://www.research.ed.ac.uk/en/publications/abiotic-zn-isotope-fractionations-associated-with-zns-precipitati.

Asael, Dan, Alan Matthews, Miryam Bar-Matthews, et Ludwik Halicz. 2007. « Copper Isotope Fractionation in Sedimentary Copper Mineralization (Timna Valley, Israel) ». *Chemical Geology* 243 (3): 238-54. https://doi.org/10.1016/j.chemgeo.2007.06.007.

Asakura, Keiko, Hiroshi Satoh, Momoko Chiba, Masahide Okamoto, Koji Serizawa, Makiko Nakano, et Kazuyuki Omae. 2009. « Genotoxicity Studies of Heavy Metals: Lead, Bismuth, Indium, Silver and Antimony ». *Journal of Occupational Health* 51 (6): 498-512. https://doi.org/10.1539/joh.L9080.

Asaoka, Satoshi, Yoshio Takahashi, Yusuke Araki, et Masaharu Tanimizu. 2012. « Comparison of Antimony and Arsenic Behavior in an Ichinokawa River Water–Sediment System ». *Chemical Geology* 334 (décembre): 1-8. https://doi.org/10.1016/j.chemgeo.2012.09.047.

Ashley, P. M., D. Craw, B. P. Graham, et D. A. Chappell. 2003. « Environmental Mobility of Antimony around Mesothermal Stibnite Deposits, New South Wales, Australia and Southern New Zealand ». *Journal of Geochemical Exploration* 77 (1): 1-14. https://doi.org/10.1016/S0375-6742(02)00251-0.

Asta, Maria P., D. Kirk Nordstrom, et R. Blaine McCleskey. 2012. « Simultaneous Oxidation of Arsenic and Antimony at Low and Circumneutral PH, with and without Microbial Catalysis ». *Applied Geochemistry* 27 (1): 281-91. https://doi.org/10.1016/j.apgeochem.2011.09.002.

Ayrault, Sophie, Abderrahmane Senhou, Mélanie Moskura, et André Gaudry. 2010. « Atmospheric Trace Element Concentrations in Total Suspended Particles near Paris, France ». *Atmospheric Environment* 44 (30): 3700-3707. https://doi.org/10.1016/j.atmosenv.2010.06.035.

Baeza, Marcia, Jianhong Ren, Sushma Krishnamurthy, et Thomas C. Vaughan. 2010. « Spatial Distribution of Antimony and Arsenic Levels in Manadas Creek, an Urban Tributary of the Rio Grande in Laredo, Texas ». *Archives of Environmental Contamination and Toxicology* 58 (2): 299-314. https://doi.org/10.1007/s00244-009-9357-0.

Bagby, E. Lee, et Charles M. West. 1995. « Treatment of an Anionic Metal by Adsorption on Iron Oxides ». In *Emerging Technologies in Hazardous Waste Management V*, 607:64-73. ACS Symposium Series 607. American Chemical Society. https://doi.org/10.1021/bk-1995-0607.ch006.

Balistrieri, Laurie S., David M. Borrok, Richard B. Wanty, et W. Ian Ridley. 2008. « Fractionation of Cu and Zn Isotopes during Adsorption onto Amorphous Fe(III) Oxyhydroxide: Experimental Mixing of Acid Rock Drainage and Ambient River Water ». *Geochimica et Cosmochimica Acta* 72 (2): 311-28. https://doi.org/10.1016/j.gca.2007.11.013.

Banks, David, Paul L. Younger, Rolf-Tore Arnesen, Egil R. Iversen, et S. B. Banks. 1997. « Mine-Water Chemistry: The Good, the Bad and the Ugly ». *Environmental Geology* 32 (3): 157-74. https://doi.org/10.1007/s002540050204.

Barbieri, Enio, Francisco E. Fontúrbel, Cristian Herbas, Flavia L. Barbieri, et Jacques Gardon. 2014. « Indoor Metallic Pollution and Children Exposure in a Mining City ». *Science of The Total Environment* 487 (juillet): 13-19. https://doi.org/10.1016/j.scitotenv.2014.03.136.

Barbieri, Flavia L., Jacques Gardon, María Ruiz-Castell, Pamela Paco V., Rebecca Muckelbauer, Corinne Casiot, Rémi Freydier, et al. 2016. « Toxic trace elements in maternal and cord blood and social determinants in a Bolivian mining city ». *International Journal of Environmental Health Research* 26 (2): 158-74. https://doi.org/10.1080/09603123.2015.1061114.

Barbieri, Flavia Laura, Amandine Cournil, Jorge Eduardo Souza Sarkis, Eric Bénéfice, et Jacques Gardon. 2011. « Hair Trace Elements Concentration to Describe Polymetallic Mining Waste Exposure in Bolivian Altiplano ». *Biological Trace Element Research* 139 (1): 10-23. https://doi.org/10.1007/s12011-010-8641-1.

Barker, Amanda J., L. E. Mayhew, T. A. Douglas, A. G. Ilgen, et T. P. Trainor. 2020. « Lead and Antimony Speciation Associated with the Weathering of Bullets in a Historic Shooting Range in Alaska ». *Chemical Geology* 553 (octobre): 119797. https://doi.org/10.1016/j.chemgeo.2020.119797.

Barling, J., et A. D Anbar. 2002. « Mo scavenging by manganese oxyhydroxides and the seawater Mo isotope record in oxic sediments ». *Geochimica et Cosmochimica Acta* 66 (15A).

Barling, J., et A. D. Anbar. 2004. « Molybdenum Isotope Fractionation during Adsorption by Manganese Oxides ». *Earth and Planetary Science Letters* 217 (3): 315-29. https://doi.org/10.1016/S0012-821X(03)00608-3.

Baroni, F, A Boscagli, G Protano, et F Riccobono. 2000. « Antimony Accumulation in Achillea Ageratum, Plantago Lanceolata and Silene Vulgaris Growing in an Old Sb-Mining Area ». *Environmental Pollution* 109 (2): 347-52. https://doi.org/10.1016/S0269-7491(99)00240-7.

Belyaeva, AP. 1967. « The effect of antimony on reproduction ». *Gigiena Truda i Professional'nye Zabolevaniia* 11 (32).

Belzile, Nelson, Yu-Wei Chen, et Zijian Wang. 2001. « Oxidation of Antimony (III) by Amorphous Iron and Manganese Oxyhydroxides ». *Chemical Geology* 174 (4): 379-87. https://doi.org/10.1016/S0009-2541(00)00287-4.

Benjamin Kaufmann, Andreas, Marina Lazarov, Stefan Kiefer, Juraj Majzlan, et Stefan Weyer. 2021. « In-Situ Determination of Antimony Isotope Ratios in Sb Minerals by Femtosecond LA-MC-ICP-MS ». *Journal of Analytical Atomic Spectrometry*. https://doi.org/10.1039/D1JA00089F.

Bigeleisen, Jacob. 1965. « Chemistry of Isotopes ». *Science* 147 (3657): 463-71. https://doi.org/10.1126/science.147.3657.463.

Bigham, J. M., U. Schwertmann, et G. Pfab. 1996. « Influence of PH on Mineral Speciation in a Bioreactor Simulating Acid Mine Drainage ». *Applied Geochemistry* 11 (6): 845-49. https://doi.org/10.1016/S0883-2927(96)00052-2.

Bigham, J. M., U. Schwertmann, S. J. Traina, R. L. Winland, et M. Wolf. 1996. « Schwertmannite and the Chemical Modeling of Iron in Acid Sulfate Waters ». *Geochimica et Cosmochimica Acta* 60 (12): 2111-21. https://doi.org/10.1016/0016-7037(96)00091-9.

Biver, Marc, Michael Krachler, et William Shotyk. 2011. « The Desorption of Antimony(V) from Sediments, Hydrous Oxides, and Clay Minerals by Carbonate, Phosphate, Sulfate, Nitrate, and Chloride ». *Journal of Environmental Quality* 40 (4): 1143-52. https://doi.org/10.2134/jeq2010.0503.

Blanchard, Marc, Franck Poitrasson, Merlin Méheut, Michele Lazzeri, Francesco Mauri, et Etienne Balan. 2009. « Iron Isotope Fractionation between Pyrite (FeS_2), Hematite (Fe_2O_3) and Siderite ($FeCO_3$): A First-Principles Density Functional Theory Study ». *Geochimica et Cosmochimica Acta* 73 (21): 6565-78. https://doi.org/10.1016/j.gca.2009.07.034.

Bolan, Nanthi, Manish Kumar, Ekta Singh, Aman Kumar, Lal Singh, Sunil Kumar, S. Keerthanan, et al. 2022. « Antimony Contamination and Its Risk Management in Complex Environmental Settings:

A Review ». *Environment International* 158 (janvier): 106908. https://doi.org/10.1016/j.envint.2021.106908.

Bolaños-Benítez, Viviana, Eric D. van Hullebusch, Jean-Louis Birck, Jérémie Garnier, Piet N. L. Lens, Mickaël Tharaud, Cécile Quantin, et Yann Sivry. 2021. « Chromium Mobility in Ultramafic Areas Affected by Mining Activities in Barro Alto Massif, Brazil: An Isotopic Study ». *Chemical Geology* 561 (février): 120000. https://doi.org/10.1016/j.chemgeo.2020.120000.

Boreiko, Craig J., et Toby G. Rossman. 2020. « Antimony and Its Compounds: Health Impacts Related to Pulmonary Toxicity, Cancer, and Genotoxicity ». *Toxicology and Applied Pharmacology* 403 (septembre): 115156. https://doi.org/10.1016/j.taap.2020.115156.

Born, M., et R. Oppenheimer. 1927. « Zur Quantentheorie Der Molekeln ». *Annalen Der Physik* 389 (20): 457-84. https://doi.org/10.1002/andp.19273892002.

Brown, T J, N E Idoine, C E Wrighton, E R Raycraft, S F Hobbs, R A Shaw, P Everett, C Kresse, E A Deady, et T Bide. 2019. « World Mineral Production, 2014-18 ». British Geological Survey.

Burke, Kieron. 2007. *The ABC of DFT*. Department of Chemistry, University of California, Irvine, CA 92697. https://dft.uci.edu/doc/g1.pdf.

Burke, Kieron. 2012. « Perspective on density functional theory ». *The Journal of Chemical Physics* 136 (15): 150901. https://doi.org/10.1063/1.4704546.

Burke, Kieron, et Lucas O. Wagner. 2013. « DFT in a Nutshell ». *International Journal of Quantum Chemistry* 113 (2): 96-101. https://doi.org/10.1002/qua.24259.

Buschmann, Johanna, et Laura Sigg. 2004. « Antimony(III) Binding to Humic Substances: Influence of pH and Type of Humic Acid ». *Environmental Science & Technology* 38 (17): 4535-41. https://doi.org/10.1021/es049901o.

Cacaly, S., C Marechal, F. Juillot, F. Guyot, et M. Benedetti. 2004. « Zn isotopes fractionation upon sorption and precipitation ». *Geochimica et Cosmochimica Acta* 68 (11): A366-A366.

Carlson, L., J. M. Bigham, U. Schwertmann, A. Kyek, et F. Wagner. 2002. « Scavenging of As from Acid Mine Drainage by Schwertmannite and Ferrihydrite: A Comparison with Synthetic Analogues ». *Environmental Science & Technology* 36 (8): 1712-19. https://doi.org/10.1021/es0110271.

Casiot, C., M. Ujevic, M. Munoz, J. L. Seidel, et F. Elbaz-Poulichet. 2007. « Antimony and Arsenic Mobility in a Creek Draining an Antimony Mine Abandoned 85 Years Ago (Upper Orb Basin, France) ». *Applied Geochemistry* 22 (4): 788-98. https://doi.org/10.1016/j.apgeochem.2006.11.007.

Cavallo, Delia, Ivo Iavicoli, Andrea Setini, Alessandro Marinaccio, Barbara Perniconi, Giovanni Carelli, et Sergio Iavicoli. 2002. « Genotoxic Risk and Oxidative DNA Damage in Workers Exposed to Antimony Trioxide ». *Environmental and Molecular Mutagenesis* 40 (3): 184-89. https://doi.org/10.1002/em.10102.

Ceriotti, Gabriel, et Dulasiri Amarasiriwardena. 2009. « A Study of Antimony Complexed to Soil-Derived Humic Acids and Inorganic Antimony Species along a Massachusetts Highway ». *Microchemical Journal* 91 (1): 85-93. https://doi.org/10.1016/j.microc.2008.08.010.

Chrastný, Vladislav, Eva Čadková, Aleš Vaněk, Leslaw Teper, Jerzy Cabala, et Michael Komárek. 2015. « Cadmium Isotope Fractionation within the Soil Profile Complicates Source Identification in Relation to Pb–Zn Mining and Smelting Processes ». *Chemical Geology* 405 (juin): 1-9. https://doi.org/10.1016/j.chemgeo.2015.04.002.

Clark, Scott K., et Thomas M. Johnson. 2010. « Selenium Stable Isotope Investigation into Selenium Biogeochemical Cycling in a Lacustrine Environment: Sweitzer Lake, Colorado ». *Journal of Environmental Quality* 39 (6): 2200-2210. https://doi.org/10.2134/jeq2009.0380.

Clayton, R. E., K. A. Hudson-Edwards, et S. L. Houghton. 2005. « Isotopic effects during Cu sorption onto goethite ». *Geochimica et Cosmochimica Acta Supplement* 69 (mai): A216.

Cloquet, C., J. Carignan, G. Libourel, T. Sterckeman, et E. Perdrix. 2006. « Tracing Source Pollution in Soils Using Cadmium and Lead Isotopes ». *Environmental Science & Technology* 40 (8): 2525-30. https://doi.org/10.1021/es052232+.

Cody, C. A., L. Dicarlo, et R. K. Darlington. 1979. « Vibrational and Thermal Study of Antimony Oxides ». *Inorganic Chemistry* 18 (6): 1572-76. https://doi.org/0020-1669/79/1318-1572$01.00/0.

« Communication From The Commission To The European Parliament, The Council, The European Economic And Social Committee And The Committee Of The Regions Critical Raw Materials Resilience: Charting a Path towards greater Security and Sustainability ». 2020. Communication COM(2020)474.

Cooper, David A., Eugene P. Pendergrass, Arthur J. Vorwald, Robert L. Mayock, et Heinrich Brieger. 1968. « Pneumoconiosis among workers in an antimony industry ». *American Journal of Roentgenology* 103 (3): 495-508. https://doi.org/10.2214/ajr.103.3.495.

Cooper, Ross G., et Adrian P. Harrison. 2009. « The exposure to and health effects of antimony ». *Indian Journal of Occupational and Environmental Medicine* 13 (1): 3-10. https://doi.org/10.4103/0019-5278.50716.

Criss, Robert E. 1999. *Principles of Stable Isotope Distribution*. Oxford University Press, USA.

Cunningham, Charles G., James McNamee, Jose Pinto Vasquez, et George E. Ericksen. 1991. « A model of volcanic dome-hosted precious metal deposits in Bolivia ». *Economic Geology* 86 (2): 415-21. https://doi.org/10.2113/gsecongeo.86.2.415.

D'Arcy, Joan, Michael G. Babechuk, Lasse Nørbye Døssing, Claudio Gaucher, et Robert Frei. 2016. « Processes Controlling the Chromium Isotopic Composition of River Water: Constraints from Basaltic River Catchments ». *Geochimica et Cosmochimica Acta* 186 (août): 296-315. https://doi.org/10.1016/j.gca.2016.04.027.

Dardeniz, Gonca. 2020. « Why Did the Use of Antimony-Bearing Alloys in Bronze Age Anatolia Fall Dormant after the Early Bronze Age?: A Case from Resuloğlu (Çorum, Turkey) ». *PLOS ONE* 15 (7): e0234563. https://doi.org/10.1371/journal.pone.0234563.

Degryse, P., L. Lobo, A. Shortland, F. Vanhaecke, A. Blomme, J. Painter, D. Gimeno, et al. 2015. « Isotopic Investigation into the Raw Materials of Late Bronze Age Glass Making ». *Journal of Archaeological Science* 62 (octobre): 153-60. https://doi.org/10.1016/j.jas.2015.08.004.

Degryse, Patrick, Andrew J. Shortland, Sarah Dillis, Alicia van Ham-Meert, Frank Vanhaecke, et Peter Leeming. 2020. « Isotopic Evidence for the Use of Caucasian Antimony in Late Bronze Age Glass Making ». *Journal of Archaeological Science* 120 (août): 105195. https://doi.org/10.1016/j.jas.2020.105195.

DePaolo, Donald J. 2011. « Surface Kinetic Model for Isotopic and Trace Element Fractionation during Precipitation of Calcite from Aqueous Solutions ». *Geochimica et Cosmochimica Acta* 75 (4): 1039-56. https://doi.org/10.1016/j.gca.2010.11.020.

Desaulty, Anne-Marie, et Emmanuelle Petelet-Giraud. 2020. « Zinc Isotope Composition as a Tool for Tracing Sources and Fate of Metal Contaminants in Rivers ». *Science of The Total Environment* 728 (août): 138599. https://doi.org/10.1016/j.scitotenv.2020.138599.

Dillis, Sarah, Alicia Van Ham-Meert, Peter Leeming, Andrew Shortland, Gela Gobejishvili, Mikheil Abramishvili, et Patrick Degryse. 2019. « Antimony as a raw material in ancient metal and glass making: provenancing Georgian LBA metallic Sb by isotope analysis ». *STAR: Science & Technology of Archaeological Research* 0 (0): 1-15. https://doi.org/10.1080/20548923.2019.1681138.

Dodd, Matthew, Stephen L Grundy, Kenneth J Reimer, et William R Cullen. 1992. « Methylated Antimony(V) Compounds: Synthesis, Hydride Generation Properties and Implications for Aquatic Speciation ». *Applied Organometallic Chemistry* 6 (2): 207-11. https://doi.org/10.1002/aoc.590060215.

Domínguez, María T., Teodoro Marañón, José M. Murillo, Rainer Schulin, et Brett H. Robinson. 2008. « Trace Element Accumulation in Woody Plants of the Guadiamar Valley, SW Spain: A Large-Scale Phytomanagement Case Study ». *Environmental Pollution* 152 (1): 50-59. https://doi.org/10.1016/j.envpol.2007.05.021.

Dousova, B., F. Buzek, L. Herzogova, V. Machovic, et M. Lhotka. 2015. « Effect of Organic Matter on Arsenic(V) and Antimony(V) Adsorption in Soils ». *European Journal of Soil Science* 66 (1): 74-82. https://doi.org/10.1111/ejss.12206.

Dousova, Barbora, Miloslav Lhotka, Frantisek Buzek, Bohuslava Cejkova, Iva Jackova, Vaclav Bednar, et Pavel Hajek. 2020. « Environmental Interaction of Antimony and Arsenic near Busy Traffic

Nodes ». *Science of The Total Environment* 702 (février): 134642. https://doi.org/10.1016/j.scitotenv.2019.134642.

Ducher, Manoj, Marc Blanchard, et Etienne Balan. 2016. « Equilibrium Zinc Isotope Fractionation in Zn-Bearing Minerals from First-Principles Calculations ». *Chemical Geology* 443 (décembre): 87-96. https://doi.org/10.1016/j.chemgeo.2016.09.016.

Dupont, David, Sander Arnout, Peter Tom Jones, et Koen Binnemans. 2016. « Antimony Recovery from End-of-life Products and Industrial Process Residues: A critical Review ». *J. Sustain. Metall.* 2: 79-103. https://doi.org/10.1007/s40831-016-0043-y.

Economou-Eliopoulos, Maria, Robert Frei, et Cathy Atsarou. 2014. « Application of Chromium Stable Isotopes to the Evaluation of Cr(VI) Contamination in Groundwater and Rock Leachates from Central Euboea and the Assopos Basin (Greece) ». *CATENA* 122 (novembre): 216-28. https://doi.org/10.1016/j.catena.2014.06.013.

Ehrlich, S., I. Butler, L. Halicz, D. Rickard, A. Oldroyd, et Alan Matthews. 2004. « Experimental Study of the Copper Isotope Fractionation between Aqueous Cu(II) and Covellite, CuS ». *Chemical Geology* 209 (3): 259-69. https://doi.org/10.1016/j.chemgeo.2004.06.010.

El Shanawany, Safaa, Nermine Foda, Doaa I. Hashad, Naglaa Salama, et Zahraa Sobh. 2017. « The Potential DNA Toxic Changes among Workers Exposed to Antimony Trioxide ». *Environmental Science and Pollution Research* 24 (13): 12455-61. https://doi.org/10.1007/s11356-017-8805-z.

Ellis, A., T. Johnson, A. Villalobos-Aragon, et T. Bullen. 2008. « Environmental Cycling of Cr Using Stable Isotopes: Kinetic and Equilibrium Effects » 2008 (décembre): H53F-08.

Ellis, Andre S., Thomas M. Johnson, et Thomas D. Bullen. 2004. « Using Chromium Stable Isotope Ratios To Quantify Cr(VI) Reduction: Lack of Sorption Effects ». *Environmental Science & Technology* 38 (13): 3604-7. https://doi.org/10.1021/es0352294.

Essington, Michael E., et Melanie A. Stewart. 2016. « Adsorption of Antimonate by Gibbsite: Reversibility and the Competitive Effects of Phosphate and Sulfate ». *Soil Science Society of America Journal* 80 (5): 1197-1207. https://doi.org/10.2136/sssaj2016.04.0129.

Fang, Ting, Hui Wang, Yangyang Liang, Kai Cui, Kun Yang, Wenxuan Lu, Jing Li, et al. 2022. « Source Tracing with Cadmium Isotope and Risk Assessment of Heavy Metals in Sediment of an Urban River, China ». *Environmental Pollution* 305 (juillet): 119325. https://doi.org/10.1016/j.envpol.2022.119325.

Fernandez, Alvaro, et David M. Borrok. 2009. « Fractionation of Cu, Fe, and Zn Isotopes during the Oxidative Weathering of Sulfide-Rich Rocks ». *Chemical Geology* 264 (1): 1-12. https://doi.org/10.1016/j.chemgeo.2009.01.024.

Ferrari, Colin, Eleonore Resongles, Remi Freydier, et Corinne Casiot. 2021. « A Single-Step Purification Method for the Precise Determination of Antimony Isotopic Composition of Environmental, Geological and Biological Samples by HG-MC-ICP-MS ». *Journal of Analytical Atomic Spectrometry* 36 (Issue 4): 776-85. https://doi.org/10.1039/D0JA00452A.

Filella, Montserrat. 2010. « 8:Alkyl Derivatives of Antimony in the Environment ». In *Organometallics in Environment and Toxicology*, 267-301. https://doi.org/10.1039/9781849730822-00267.

Filella, Montserrat. 2010. 2020. « Antimony and PET Bottles: Checking Facts ». *Chemosphere* 261 (décembre): 127732. https://doi.org/10.1016/j.chemosphere.2020.127732.

Filella, Montserrat, Nelson Belzile, et Yu-Wei Chen. 2001. « Antimony in the environment: a review focused on natural waters. I. Occurence ». *Earth-Sciences Reviews* 57: 125-76.

Filella, Montserrat, Nelson Belzile, et Yu-Wei Chen. 2002. « Antimony in the environment: a review focused on natural waters. II. Relevant solution chemistry ». *Earth-Sciences Reviews* 59: 265-85.

Filella, Montserrat, Nelson Belzile, et Marie-Claire Lett. 2007. « Antimony in the environment: a review focused on natural waters. III. Microbial relevant interactions ». *Earth Sciences Reviews* 80: 195-217. https://doi.org/10.1016/j.earscirev.2006.09.003.

Filella, Montserrat, Pierre Hennebert, Gudny Okkenhaug, et Andrew Turner. 2020. « Occurrence and Fate of Antimony in Plastics ». *Journal of Hazardous Materials* 390 (mai): 121764. https://doi.org/10.1016/j.jhazmat.2019.121764.

Földi, Corinna, Simon Sauermann, Reiner Dohrmann, et Tim Mansfeldt. 2018. « Traffic-Related Distribution of Antimony in Roadside Soils ». *Environmental Pollution* 237 (juin): 704-12. https://doi.org/10.1016/j.envpol.2017.10.112.

Fort, Marta, Joan O. Grimalt, Xavier Querol, Maribel Casas, et Jordi Sunyer. 2016. « Evaluation of Atmospheric Inputs as Possible Sources of Antimony in Pregnant Women from Urban Areas ». *Science of The Total Environment* 544 (février): 391-99. https://doi.org/10.1016/j.scitotenv.2015.11.095.

Fry, Brian. 2006. *Stable Isotope ecology*. Springer.

Fry, Brian, William Ruf, Howard Gest, et J. M. Hayes. 1988. « Sulfur Isotope Effects Associated with Oxidation of Sulfide by O_2 in Aqueous Solution ». *Chemical Geology: Isotope Geoscience Section* 73 (3): 205-10. https://doi.org/10.1016/0168-9622(88)90001-2.

Fujii, Toshiyuki, Frédéric Moynier, Arnaud Agranier, Emmanuel Ponzevera, Minori Abe, Akihiro Uehara, et Hajimu Yamana. 2013. « Nuclear Field Shift Effect in Isotope Fractionation of Thallium ». *Journal of Radioanalytical and Nuclear Chemistry* 296 (1): 261-65. https://doi.org/10.1007/s10967-012-2181-4.

Fujii, Toshiyuki, Frédéric Moynier, Janne Blichert-Toft, et Francis Albarède. 2014. « Density Functional Theory Estimation of Isotope Fractionation of Fe, Ni, Cu, and Zn among Species Relevant to Geochemical and Biological Environments ». *Geochimica et Cosmochimica Acta* 140 (septembre): 553-76. https://doi.org/10.1016/j.gca.2014.05.051.

Fujii, Toshiyuki, Frédéric Moynier, Philippe Telouk, et Francis Albarède. 2009. « Nuclear Field Shift Effect in the Isotope Exchange Reaction of Cadmium Using a Crown Ether ». *Chemical Geology*, Advances in experimental and theoretical isotope geochemistry, 267 (3): 157-63. https://doi.org/10.1016/j.chemgeo.2008.12.004.

Fujii, Toshiyuki, Frédéric Moynier, Akihiro Uehara, Minori Abe, Qing-Zhu Yin, Takayuki Nagai, et Hajimu Yamana. 2009. « Mass-Dependent and Mass-Independent Isotope Effects of Zinc in a Redox Reaction ». *The Journal of Physical Chemistry A* 113 (44): 12225-32. https://doi.org/10.1021/jp904882d.

Fukushi, Keisuke, Miwa Sasaki, Tsutomu Sato, Nobuyuki Yanase, Hikaru Amano, et Hodaka Ikeda. 2003. « A Natural Attenuation of Arsenic in Drainage from an Abandoned Arsenic Mine Dump ». *Applied Geochemistry* 18 (8): 1267-78. https://doi.org/10.1016/S0883-2927(03)00011-8.

Fulton, John L., Markus M. Hoffmann, et John G. Darab. 2000. « An X-Ray Absorption Fine Structure Study of Copper(I) Chloride Coordination Structure in Water up to 325°C ». *Chemical Physics Letters* 330 (3): 300-308. https://doi.org/10.1016/S0009-2614(00)01110-6.

Gaillardet, J., J. Viers, et B. Dupré. 2003. « Trace Elements in River Waters ». *Treatise on Geochemistry* 5 (décembre): 605. https://doi.org/10.1016/B0-08-043751-6/05165-3.

Gao, Bo, Haidong Zhou, Xirong Liang, et Xianglin Tu. 2013. « Cd Isotopes as a Potential Source Tracer of Metal Pollution in River Sediments ». *Environmental Pollution* 181 (octobre): 340-43. https://doi.org/10.1016/j.envpol.2013.05.048.

Gao, Caihong, et Yun Liu. 2021. « First-Principles Calculations of Equilibrium Bromine Isotope Fractionations ». *Geochimica et Cosmochimica Acta* 297 (mars): 65-81. https://doi.org/10.1016/j.gca.2021.01.010.

Garg, Bhagwan D., Steven H. Cadle, Patricia A. Mulawa, Peter J. Groblicki, Chris Laroo, et Graham A. Parr. 2000. « Brake Wear Particulate Matter Emissions ». *Environmental Science & Technology* 34 (21): 4463-69. https://doi.org/10.1021/es001108h.

Gebel, T. 1997. « Arsenic and Antimony: Comparative Approach on Mechanistic Toxicology ». *Chemico-Biological Interactions* 107 (3): 131-44. https://doi.org/10.1016/S0009-2797(97)00087-2.

Gebre, G., Z. Feleke, et E. Sahle-Demissie. 2010. « Mass Concentrations and Elemental Composition of Urban Atmospheric Aerosols in Addis Ababa, Ethiopia ». *Bulletin of the Chemical Society of Ethiopia* 24 (3). https://doi.org/10.4314/bcse.v24i3.60787.

Gilleaudeau, G.J., R. Frei, A.J. Kaufman, L.C. Kah, K. Azmy, J.K. Bartley, P. Chernyavskiy, et A.H. Knoll. 2016. « Oxygenation of the mid-Proterozoic atmosphere: clues from chromium isotopes in

carbonates ». *Geochemical Perspectives Letters* 2 (2): 178-87. https://doi.org/10.7185/geochemlet.1618.

Goix, Sylvaine. 2012. « Origine et impact des pollutions liées aux activités minières sur l'environnement et la santé, cas de Oruro (Bolivie) ». Université de Toulouse. https://tel.archives-ouvertes.fr/tel-00781152/file/Goix_these.pdf.

Goix, Sylvaine, David Point, Priscia Oliva, Mireille Polve, Jean Louis Duprey, Hubert Mazurek, Ludivine Guislain, Carlos Huayta, Flavia L. Barbieri, et Jacques Gardon. 2011. « Influence of Source Distribution and Geochemical Composition of Aerosols on Children Exposure in the Large Polymetallic Mining Region of the Bolivian Altiplano ». *Science of The Total Environment* 412-413 (décembre): 170-84. https://doi.org/10.1016/j.scitotenv.2011.09.065.

Goix, Sylvaine, Eléonore Resongles, David Point, Priscia Oliva, Jean Louis Duprey, Erika de la Galvez, Lincy Ugarte, et al. 2013. « Transplantation of Epiphytic Bioaccumulators (Tillandsia Capillaris) for High Spatial Resolution Biomonitoring of Trace Elements and Point Sources Deconvolution in a Complex Mining/Smelting Urban Context ». *Atmospheric Environment* 80 (décembre): 330-41. https://doi.org/10.1016/j.atmosenv.2013.08.011.

Goix, Sylvaine, Gaëlle Uzu, Priscia Oliva, Fiorella Barraza, Aude Calas, Sylvie Castet, David Point, et al. 2016. « Metal Concentration and Bioaccessibility in Different Particle Sizes of Dust and Aerosols to Refine Metal Exposure Assessment ». *Journal of Hazardous Materials* 317 (novembre): 552-62. https://doi.org/10.1016/j.jhazmat.2016.05.083.

Goldberg, Tatiana, Corey Archer, Derek Vance, et Simon Poulton. 2009. « Mo isotope fractionation during adsorption to Fe (oxyhydr)oxydes ». *Geochimica et Cosmochimica Acta* 73: 6502-16. https://doi.org/10.1016/j.gca.2009.08.004.

Gonçalves, Rosana Alves, Maurício Ribeiro Baldan, Adenilson José Chiquito, et Olivia Maria Berengue. 2018. « Synthesis of Orthorhombic Sb_2O_3 Branched Rods by a Vapor–Solid Approach ». *Nano-Structures & Nano-Objects* 16 (octobre): 127-33. https://doi.org/10.1016/j.nanoso.2018.05.008.

Guéguen, Florence, Peter Stille, Majdi Lahd Geagea, et René Boutin. 2012. « Atmospheric Pollution in an Urban Environment by Tree Bark Biomonitoring – Part I: Trace Element Analysis ». *Chemosphere* 86 (10): 1013-19. https://doi.org/10.1016/j.chemosphere.2011.11.040.

Guo, Jing, Liling Su, Xinyuan Zhao, Zhengping Xu, et Guangdi Chen. 2016. « Relationships between Urinary Antimony Levels and Both Mortalities and Prevalence of Cancers and Heart Diseases in General US Population, NHANES 1999–2010 ». *Science of The Total Environment* 571 (novembre): 452-60. https://doi.org/10.1016/j.scitotenv.2016.07.011.

Guo, Wenjing, Zhiyou Fu, Hao Wang, Fanhao Song, Fengchang Wu, et John P. Giesy. 2018. « Environmental Geochemical and Spatial/Temporal Behavior of Total and Speciation of Antimony in Typical Contaminated Aquatic Environment from Xikuangshan, China ». *Microchemical Journal* 137 (mars): 181-89. https://doi.org/10.1016/j.microc.2017.10.010.

Guo, Xuejun, Zhijun Wu, Mengchang He, Xiaoguang Meng, et Xin Jin. 2014. « Adsorption of antimony onto iron oxyhydroxides: Adsorption behavior and surface structure ». *Journal of Hazardous Materials* 276: 339-45. http://dx.doi.org/10.1016/j.jhazmat.2014.05.025.

Hammel, Wolfram, Reinhard Debus, et Lore Steubing. 2000. « Mobility of Antimony in Soil and Its Availability to Plants ». *Chemosphere* 41 (11): 1791-98. https://doi.org/10.1016/S0045-6535(00)00037-0.

Han-wen, Sun, Shan Xiao-quan, et Ni Zhe-ming. 1982. « Selective Separation and Differential Determination of Antimony(III) and Antimony(V) by Solvent Extraction with N-Benzoyl-N-Phenylhydroxylamine and Graphite-Furnace Atomic-Absorption Spectrometry Using a Matrix-Modification Technique ». *Talanta* 29 (7): 589-93. https://doi.org/10.1016/0039-9140(82)80007-6.

Hao, Chunming, Herong Gui, Linlin Sheng, Jie Miao, et Huiqing Lian. 2021. « Contrasting Water–Rock Interaction Behaviors of Antimony and Arsenic in Contaminated Rivers around an Antimony Mine, Hunan Province, China ». *Geochemistry* 81 (2): 125748. https://doi.org/10.1016/j.chemer.2021.125748.

He, Mengchang, Ningning Wang, Xiaojing Long, Chengjun Zhang, Congli Ma, Qianyun Zhong, Aihua Wang, Aneesa Pervaiz, et Jun Shan. 2019. « Antimony speciation in the environment: Recent advances in understanding the biogeochemical processes and ecological effects ». *Journal of Environmental Sciences* 75: 14-39. https://doi.org/10.1016/j.jes.2018.05.023.

He, Mengchang, Xiangqin Wang, Fengchang Wu, et Zhiyou Fu. 2012. « Antimony Pollution in China ». *Science of The Total Environment*, Special Section: Reviews of Trace Metal Pollution in China, 421-422 (avril): 41-50. https://doi.org/10.1016/j.scitotenv.2011.06.009.

Heikoop, Jeffrey M., Thomas M. Johnson, Kay H. Birdsell, Patrick Longmire, Donald D. Hickmott, Elaine P. Jacobs, David E. Broxton, et al. 2014. « Isotopic Evidence for Reduction of Anthropogenic Hexavalent Chromium in Los Alamos National Laboratory Groundwater ». *Chemical Geology* 373 (mai): 1-9. https://doi.org/10.1016/j.chemgeo.2014.02.022.

Herath, Indika, Meththika Vithanage, et Jochen Bundschuh. 2017. « Antimony as a global dilemma: Geochemistry, mobility, fate and transport ». *Environmental Pollution*, 1-15. http://dx.doi.org/10.1016/j.envpol.2017.01.057.

Herbel, Mitchell J., Thomas M. Johnson, Kenneth K. Tanji, Suduan Gao, et Thomas D. Bullen. 2002. « Selenium Stable Isotope Ratios in California Agricultural Drainage Water Management Systems ». *Journal of Environmental Quality* 31 (4): 1146-56. https://doi.org/10.2134/jeq2002.1146.

Hiller, Edgar, Bronislava Lalinská, Martin Chovan, Ľubomír Jurkovič, Tomáš Klimko, Michal Jankulár, Róbert Hovorič, et al. 2012. « Arsenic and Antimony Contamination of Waters, Stream Sediments and Soils in the Vicinity of Abandoned Antimony Mines in the Western Carpathians, Slovakia ». *Applied Geochemistry* 27 (3): 598-614. https://doi.org/10.1016/j.apgeochem.2011.12.005.

Hjortenkrans, David, Bo Bergbäck, et Agneta Häggerud. 2006. « New Metal Emission Patterns in Road Traffic Environments ». *Environmental Monitoring and Assessment* 117 (1-3): 85-98. https://doi.org/10.1007/s10661-006-7706-2.

Hockmann, Kerstin, Markus Lenz, Susan Tandy, Maarten Nachtegaal, Markus Janousch, et Rainer Schulin. 2014. « Release of Antimony from Contaminated Soil Induced by Redox Changes ». *Journal of Hazardous Materials* 275 (juin): 215-21. https://doi.org/10.1016/j.jhazmat.2014.04.065.

Hockmann, Kerstin, Susan Tandy, Markus Lenz, René Reiser, Héctor M. Conesa, Martin Keller, Björn Studer, et Rainer Schulin. 2015. « Antimony Retention and Release from Drained and Waterlogged Shooting Range Soil under Field Conditions ». *Chemosphere* 134 (septembre): 536-43. https://doi.org/10.1016/j.chemosphere.2014.12.020.

Hoefs, Jochen. 2021. *Stable Isotope Geochemistry*. Ninth Edition. Springer.

Hong, Sungmin, Tseren-Ochir Soyol-Erdene, Hee Jin Hwang, Sang Bum Hong, Soon Do Hur, et Hidaeki Motoyama. 2012. « Evidence of Global-Scale As, Mo, Sb, and Tl Atmospheric Pollution in the Antarctic Snow ». *Environmental Science & Technology* 46 (21): 11550-57. https://doi.org/10.1021/es303086c.

Horner, Tristan J., Rosalind E. M. Rickaby, et Gideon M. Henderson. 2011. « Isotopic Fractionation of Cadmium into Calcite ». *Earth and Planetary Science Letters* 312 (1): 243-53. https://doi.org/10.1016/j.epsl.2011.10.004.

Huang, Yue, Wenqing Ni, Yaowen Chen, Xiaoling Wang, Jingwen Zhang, et Kusheng Wu. 2015. « Levels and Risk Factors of Antimony Contamination in Human Hair from an Electronic Waste Recycling Area, Guiyu, China ». *Environmental Science and Pollution Research* 22 (9): 7112-19. https://doi.org/10.1007/s11356-014-3941-1.

Ibáñez, J., J. A. Sans, C. Popescu, J. López-Vidrier, J. J. Elvira-Betanzos, V. P. Cuenca-Gotor, O. Gomis, F. J. Manjón, P. Rodríguez-Hernández, et A. Muñoz. 2016. « Structural, Vibrational, and Electronic Study of Sb_2S_3 at High Pressure ». *The Journal of Physical Chemistry C* 120 (19): 10547-58. https://doi.org/10.1021/acs.jpcc.6b01276.

Izbicki, John A., James W. Ball, Thomas D. Bullen, et Stephen J. Sutley. 2008. « Chromium, Chromium Isotopes and Selected Trace Elements, Western Mojave Desert, USA ». *Applied Geochemistry* 23 (5): 1325-52. https://doi.org/10.1016/j.apgeochem.2007.11.015.

Izbicki, John A., Thomas D. Bullen, Peter Martin, et Brian Schroth. 2012. « Delta Chromium-53/52 Isotopic Composition of Native and Contaminated Groundwater, Mojave Desert, USA ». *Applied Geochemistry* 27 (4): 841-53. https://doi.org/10.1016/j.apgeochem.2011.12.019.

Jenkins, Richard O., Peter J. Craig, Walter Goessler, David Miller, Naaman Ostah, et Kurt J. Irgolic. 1998. « Biomethylation of Inorganic Antimony Compounds by an Aerobic Fungus: Scopulariopsis brevicaulis ». *Environmental Science & Technology* 32 (7): 882-85. https://doi.org/10.1021/es970824p.

Jenkins, Richard O., Sarah N. Forster, et Peter J. Craig. 2002. « Formation of Methylantimony Species by an Aerobic Prokaryote: Flavobacterium Sp. » *Archives of Microbiology* 178 (4): 274-78. https://doi.org/10.1007/s00203-002-0456-9.

Johnson, Clark M., Brian L. Beard, et Francis Albarède. 2018. *Geochemistry of Non-Traditional Stable Isotopes*. Walter de Gruyter GmbH & Co KG.

Johnson, Thomas M. 2004. « A Review of Mass-Dependent Fractionation of Selenium Isotopes and Implications for Other Heavy Stable Isotopes ». *Chemical Geology*, Applications of Stable Isotope Techniques to Geological and Environmental Problems, 204 (3): 201-14. https://doi.org/10.1016/j.chemgeo.2003.11.015.

Johnson, Thomas M. 2012. « Stable Isotopes of Cr and Se as Tracers of Redox Processes in Earth Surface Environments ». In *Handbook of Environmental Isotope Geochemistry: Vol I*, édité par Mark Baskaran, 155-75. Advances in Isotope Geochemistry. Berlin, Heidelberg: Springer. https://doi.org/10.1007/978-3-642-10637-8_9.

Johnson, Thomas M., Thomas D. Bullen, et Peter T. Zawislanski. 2000. « Selenium Stable Isotope Ratios as Indicators of Sources and Cycling of Selenium: Results from the Northern Reach of San Francisco Bay ». *Environmental Science & Technology* 34 (11): 2075-79. https://doi.org/10.1021/es990187y.

Johnston, Scott G., William W. Bennett, Nicholas Doriean, Kerstin Hockmann, Niloofar Karimian, et Edward D. Burton. 2020. « Antimony and Arsenic Speciation, Redox-Cycling and Contrasting Mobility in a Mining-Impacted River System ». *Science of The Total Environment* 710 (mars): 136354. https://doi.org/10.1016/j.scitotenv.2019.136354.

Juillot, F., C. Maréchal, M. Ponthieu, S. Cacaly, G. Morin, M. Benedetti, J. L. Hazemann, O. Proux, et F. Guyot. 2008. « Zn Isotopic Fractionation Caused by Sorption on Goethite and 2-Lines Ferrihydrite ». *Geochimica et Cosmochimica Acta* 72 (19): 4886-4900. https://doi.org/10.1016/j.gca.2008.07.007.

Kieffer, Susan Werner. 1982. « Thermodynamics and Lattice Vibrations of Minerals: 5. Applications to Phase Equilibria, Isotopic Fractionation, and High-Pressure Thermodynamic Properties ». *Reviews of Geophysics* 20 (4): 827-49. https://doi.org/10.1029/RG020i004p00827.

Kimball, B. E., R. Mathur, A. C. Dohnalkova, A. J. Wall, R. L. Runkel, et S. L. Brantley. 2009. « Copper Isotope Fractionation in Acid Mine Drainage ». *Geochimica et Cosmochimica Acta* 73 (5): 1247-63. https://doi.org/10.1016/j.gca.2008.11.035.

Komárek, Michael, Gildas Ratié, Zuzana Vaňková, Adéla Šípková, et Vladislav Chrastný. 2021. « Metal isotope complexation with environmentally relevant surfaces: Opening the isotope fractionation black box ». *Critical Reviews in Environmental Science and Technology*, juillet, 1-31. https://doi.org/10.1080/10643389.2021.1955601.

Kuhn, T., B. C. Bostick, A. Koschinsky, P. Halbach, et S. Fendorf. 2003. « Enrichment of Mo in Hydrothermal Mn Precipitates: Possible Mo Sources, Formation Process and Phase Associations ». *Chemical Geology* 199 (1): 29-43. https://doi.org/10.1016/S0009-2541(03)00054-8.

Kulp, Thomas R., Laurence G. Miller, Franco Braiotta, Samuel M. Webb, Benjamin D. Kocar, Jodi S. Blum, et Ronald S. Oremland. 2014. « Microbiological Reduction of Sb(V) in Anoxic Freshwater

Sediments ». *Environmental Science & Technology* 48 (1): 218-26. https://doi.org/10.1021/es403312j.

Lai, Chun-Yu, Li-Lian Wen, Yin Zhang, Shan-Shan Luo, Qing-Ying Wang, Yi-Hao Luo, Ran Chen, Xiaoe Yang, Bruce E. Rittmann, et He-Ping Zhao. 2016. « Autotrophic Antimonate Bio-Reduction Using Hydrogen as the Electron Donor ». *Water Research* 88 (janvier): 467-74. https://doi.org/10.1016/j.watres.2015.10.042.

Langner, Marcel, Martin Kull, et Wilfried R. Endlicher. 2011. « Determination of PM10 Deposition Based on Antimony Flux to Selected Urban Surfaces ». *Environmental Pollution*, Selected papers from the conference Urban Environmental Pollution: Overcoming Obstacles to Sustainability and Quality of Life (UEP2010), 20-23 June 2010, Boston, USA, 159 (8): 2028-34. https://doi.org/10.1016/j.envpol.2011.01.017.

Laroche, Elia. 2019. « Acteurs et mécanismes des bio-transformations de l'arsenic, de l'antimoine et du thallium pour la mise en place d'éco-technologies appliquées à la gestion d'anciens sites miniers ». Thèse de doctorat.

Larson, Peter B, Kierran Maher, Frank C Ramos, Zhaoshan Chang, Miguel Gaspar, et Lawrence D Meinert. 2003. « Copper Isotope Ratios in Magmatic and Hydrothermal Ore-Forming Environments ». *Chemical Geology* 201 (3): 337-50. https://doi.org/10.1016/j.chemgeo.2003.08.006.

Le Pape, Pierre, Fabienne Battaglia-Brunet, Marc Parmentier, Catherine Joulian, Cindy Gassaud, Lidia Fernandez-Rojo, Jean-Michel Guigner, et al. 2017. « Complete Removal of Arsenic and Zinc from a Heavily Contaminated Acid Mine Drainage via an Indigenous SRB Consortium ». *Journal of Hazardous Materials* 321 (janvier): 764-72. https://doi.org/10.1016/j.jhazmat.2016.09.060.

Leduc, C., et C. Gardou. 1992. « Biogeochemical prospecting for antimony: results of an orientation study on the Brouzils deposit (Vendee, France) ». In *Bulletin de la Societe Botanique de France Actualites Botaniques (France)*.

Lehndorff, E., et L. Schwark. 2008. « Accumulation Histories of Major and Trace Elements on Pine Needles in the Cologne Conurbation as Function of Air Quality ». *Atmospheric Environment* 42 (5): 833-45. https://doi.org/10.1016/j.atmosenv.2007.10.025.

Lehr, Corinne R., Des R. Kashyap, et Timothy R. McDermott. 2007. « New Insights into Microbial Oxidation of Antimony and Arsenic ». *Applied and Environmental Microbiology* 73 (7): 2386-89. https://doi.org/10.1128/AEM.02789-06.

Lemery, Nicolas (1645-1715) Auteur du texte. 1707. *Traité de l'antimoine, contenant l'analyse chymique de ce minéral et un recueil d'un grand nombre d'opérations rapportées à l'Académie royale des sciences par Nicolas Lemery.* https://gallica.bnf.fr/ark:/12148/bpt6k96175592.

Leuz, Ann-Kathrin, et C. Annette Johnson. 2005. « Oxidation of Sb(III) to Sb(V) by O_2 and H_2O_2 in Aqueous Solutions ». *Geochimica et Cosmochimica Acta* 69 (5): 1165-72. https://doi.org/10.1016/j.gca.2004.08.019.

Leuz, Ann-Kathrin, Hermann Mönch, et Annette Johnson. 2006. « Sorption of Sb(III) and Sb(V) to Goethite: Influence on Sb(III) Oxidation and Mobilization ». *Environement Sciences and Technologies* 40 (23): 7277-82. https://doi.org/10.1021/es061284b.

Li, Jiaokun, Huang Yu, Xueling Wu, Li Shen, Yuandong Liu, Guanzhou Qiu, Wenmin Zeng, et Runlan Yu. 2018. « Novel Hyper Antimony-Oxidizing Bacteria Isolated from Contaminated Mine Soils in China ». *Geomicrobiology Journal* 35 (8): 713-20. https://doi.org/10.1080/01490451.2018.1454556.

Li, Jie, Qian Wang, Shengzhe Zhang, Dong Qin, et Gejiao Wang. 2013. « Phylogenetic and Genome Analyses of Antimony-Oxidizing Bacteria Isolated from Antimony Mined Soil ». *International Biodeterioration & Biodegradation*, Geomicrobial Ecotoxicology, 76 (janvier): 76-80. https://doi.org/10.1016/j.ibiod.2012.06.009.

Li, Jingxin, Qian Wang, Mingshun Li, Birong Yang, Manman Shi, Wei Guo, Timothy R. McDermott, Christopher Rensing, et Gejiao Wang. 2015. « Proteomics and Genetics for Identification of a Bacterial Antimonite Oxidase in Agrobacterium tumefaciens ». *Environmental Science & Technology* 49 (10): 5980-89. https://doi.org/10.1021/es506318b.

Li, Jingxin, Qian Wang, Ronald S. Oremland, Thomas R. Kulp, Christopher Rensing, et Gejiao Wang. 2016. « Microbial Antimony Biogeochemistry: Enzymes, Regulation, and Related Metabolic Pathways ». *Applied and Environmental Microbiology* 82 (18): 5482-95. https://doi.org/10.1128/AEM.01375-16.

Li, Shuyang, Yanli Deng, Hongtao Zheng, Xing Liu, Peidong Tang, Jianwei Zhou, et Zhenli Zhu. 2021. « A New Purification Method Based on a Thiol Silica Column for High Precision Antimony Isotope Measurements ». *Journal of Analytical Atomic Spectrometry* 36: 157-64. https://doi.org/10.1039/D0JA00367K.

Li, Wei, Wenxian Gou, Weiqiang Li, Tuoya Zhang, Ben Yu, Qian Liu, et Jianbo Shi. 2019. « Environmental Applications of Metal Stable Isotopes: Silver, Mercury and Zinc ». *Environmental Pollution* 252 (septembre): 1344-56. https://doi.org/10.1016/j.envpol.2019.06.037.

Lialikova, N. N. 1974. « Stibiobacter Senarmontii--a New Microorganism Oxidizing Antimony. » *Mikrobiologiia* 43 (6): 941-48.

Liang, Zhi-wei, Zheng-shuan Hua, Pu Jia, Jun Liu, Zhen-hao Luo, Wen-ce Chen, Jia-liang Kuang, Bin Liao, Wen-sheng Shu, et Jin-tian Li. 2018. « Strong Associations Between Biogeochemical Factors and Sb Species in Sediments of the World's Largest Sb Mine (Xikuangshan) in China ». *Journal of Geophysical Research: Biogeosciences* 123 (5): 1548-56. https://doi.org/10.1029/2018JG004481.

Lide, David R. 2005. *CRC Handbook of Chemistry and Physics, Internet Version 2005*. CRC Press. http://www.hbcpnetbase.com.

Lintschinger, Joseph, Bernhard Michalke, Sigurd Schulte-hostede, et Peter Schramel. 1998. « Studies on Speciation of Antimony in Soil Contaminated by Industrial Activity ». *International Journal of Environmental Analytical Chemistry* 72 (1): 11-25. https://doi.org/10.1080/03067319808032641.

Little, Susan H., Sophie Munson, Julie Prytulak, Barry J. Coles, Samantha J. Hammond, et Mike Widdowson. 2019. « Cu and Zn Isotope Fractionation during Extreme Chemical Weathering ». *Geochimica et Cosmochimica Acta* 263 (octobre): 85-107. https://doi.org/10.1016/j.gca.2019.07.057.

Liu, Bijun, Fengchang Wu, Xingliang Li, Zhiyou Fu, Qiujing Deng, Changli Mo, Jing Zhu, Yuanrong Zhu, et Haiqing Liao. 2011. « Arsenic, Antimony and Bismuth in Human Hair from Potentially Exposed Individuals in the Vicinity of Antimony Mines in Southwest China ». *Microchemical Journal*, Antimony: Emerging Global Contaminant in the Environment, 97 (1): 20-24. https://doi.org/10.1016/j.microc.2010.07.008.

Liu, Jianfeng, Jiubin Chen, Ting Zhang, Yina Wang, Wei Yuan, Yunchao Lang, Chenglong Tu, Liangzhi Liu, et Jean-Louis Birck. 2020. « Chromatographic Purification of Antimony for Accurate Isotope Analysis by MC-ICP-MS ». *Journal of Analytical Atomic Spectrometry* 35: 1360-67. https://doi.org/10.1039/D0JA00136H.

Liu, Jin-Hua, Jie Cheng, Lian Zhou, Lan-Ping Feng, Ya-Ting Hu, et Thomas J. Algeo. 2022. « Copper and Gallium Isotopic Behavior in Highly Weathered Soils ». *Chemical Geology* 594 (avril): 120757. https://doi.org/10.1016/j.chemgeo.2022.120757.

Liu, Shanqi, Yongbing Li, Jie Liu, Zhiming Yang, Jianming Liu, et Yaolin Shi. 2021. « Equilibrium Cu Isotope Fractionation in Copper Minerals: A First-Principles Study ». *Chemical Geology* 564 (mars): 120060. https://doi.org/10.1016/j.chemgeo.2021.120060.

Lobanova, EA, LA Ivanova, TA Pavlova, et II Prosina. 1996. « Clinical and pathogenetic features of exposure of workers to antimonate ore ». *Meditsina Truda i Promyshlennaia Ekologiia* 4.

Lobo, Lara, Patrick Degryse, Andrew Shortland, Katherine Eremin, et Frank Vanhaecke. 2014. « Copper and Antimony Isotopic Analysis via Multi-Collector ICP-Mass Spectrometry for Provenancing Ancient Glass ». *Journal of Analytical Atomic Spectrometry* 29 (1): 58-64. https://doi.org/10.1039/C3JA50303H.

Lobo, Lara, Patrick Degryse, Andrew Shortland, et Frank Vanhaecke. 2013. « Isotopic analysis of antimony using multi-collector ICP-mass spectrometry for provenance determination of

Roman glass ». *Journal of Analytical Atomic Spectrometry* 28: 1213-19. https://doi.org/10.1039/c3ja50018g.

Lobo, Lara, Veerle Devulder, Patrick Degryse, et Frank Vanhaecke. 2012. « Investigation of natural isotopic variation of Sb in stibnite ores via multi-collector ICP-mass spectrometry - perspectives for Sb isotopic analysis of Roman glass ». *Journal of Analytical Atomic Spectrometry* 27: 1304-10. https://doi.org/10.1039/c2ja30062a.

Mackinney, Joel Stephen. 2016. « Antimony Isotopes as Indicator of RedOx Reactions in Aqueous Systems: Fractionation during Sb(V) Reduction by Sulfide and Isotope Exchange Kinetics between Dissolved Sb(III) and Sb(V) ». Thesis, University of Illinois at Urbana-Champaign. https://www.ideals.illinois.edu/bitstream/handle/2142/90949/MACKINNEY-THESIS-2016.pdf?sequence=1&isAllowed=y.

Manaka, Mitsuo, Nobuyuki Yanase, Tsutomu Sato, et Keisuke Fukushi. 2007. « Natural attenuation of antimony in mine drainage water ». *Geochemical Journal* 41 (1): 17-27. https://doi.org/10.2343/geochemj.41.17.

Marechal, C, et S. M. F. Sheppard. 2002. « Isotopic fractionation of Cu and Zn between chloride and nitrate solutions and malachite or smithsonite at 30° and 50°C ». *Goldschmidt Conference. Geochim. Cosmochim. Acta* 66: A484.

Maréchal, Chloé Nadia, Philippe Télouk, et Francis Albarède. 1999. « Precise Analysis of Copper and Zinc Isotopic Compositions by Plasma-Source Mass Spectrometry ». *Chemical Geology* 156 (1): 251-73. https://doi.org/10.1016/S0009-2541(98)00191-0.

Mason, Thomas F. D., Dominik J. Weiss, John B. Chapman, Jamie J. Wilkinson, Svetlana G. Tessalina, Baruch Spiro, Matthew S. A. Horstwood, John Spratt, et Barry J. Coles. 2005. « Zn and Cu Isotopic Variability in the Alexandrinka Volcanic-Hosted Massive Sulphide (VHMS) Ore Deposit, Urals, Russia ». *Chemical Geology* 221 (3): 170-87. https://doi.org/10.1016/j.chemgeo.2005.04.011.

Mathur, Ryan, Molly Dendas, Spencer Titley, et Allison Phillips. 2010. « Patterns in the Copper Isotope Composition of Minerals in Porphyry Copper Deposits in Southwestern United States ». *Economic Geology* 105 (8): 1457-67. https://doi.org/10.2113/econgeo.105.8.1457.

Mathur, Ryan, Joaquin Ruiz, Spencer Titley, Laura Liermann, Heather Buss, et Susan Brantley. 2005. « Cu Isotopic Fractionation in the Supergene Environment with and without Bacteria ». *Geochimica et Cosmochimica Acta* 69 (22): 5233-46. https://doi.org/10.1016/j.gca.2005.06.022.

Mathur, Ryan, Spencer Titley, Fernando Barra, Susan Brantley, Marc Wilson, Allison Phillips, Francisco Munizaga, Victor Maksaev, Jeff Vervoort, et Garret Hart. 2009. « Exploration Potential of Cu Isotope Fractionation in Porphyry Copper Deposits ». *Journal of Geochemical Exploration* 102 (1): 1-6. https://doi.org/10.1016/j.gexplo.2008.09.004.

Matthies, R., L. Krahé, et D. W. Blowes. 2014. « Zinc Stable Isotope Fractionation upon Accelerated Oxidative Weathering of Sulfidic Mine Waste ». *Science of The Total Environment* 487 (juillet): 97-101. https://doi.org/10.1016/j.scitotenv.2014.04.020.

McComb, Kiri A., Dave Craw, et A. James McQuillan. 2007. « ATR-IR Spectroscopic Study of Antimonate Adsorption to Iron Oxide ». *Langmuir* 23 (24): 12125-30. https://doi.org/10.1021/la7012667.

Méheut-Le Quéau, Merlin. 2008. « Calcul prédictif du facteur de partage isotopique entre minéraux dans le cadre de la théorie de la fonctionnelle de la densité ». Phdthesis, Université Pierre et Marie Curie - Paris VI. https://tel.archives-ouvertes.fr/tel-00231076.

Meshik, Alex, et Olga Pravdivtseva. 2017. « Weak Decay of Tellurium and Barium Isotopes in Geological Samples: Current Status ». In *Proceedings of the 14th International Symposium on Nuclei in the Cosmos (NIC2016)*. Vol. 14. JPS Conference Proceedings 14. Journal of the Physical Society of Japan. https://doi.org/10.7566/JPSCP.14.020702.

Mitchell, Kristen, Raoul-Marie Couture, Thomas M. Johnson, Paul R. D. Mason, et Philippe Van Cappellen. 2013. « Selenium Sorption and Isotope Fractionation: Iron(III) Oxides versus Iron(II) Sulfides ». *Chemical Geology* 342 (mars): 21-28. https://doi.org/10.1016/j.chemgeo.2013.01.017.

Mitsunobu, Satoshi, Teppei Harada, et Yoshio Takahashi. 2006. « Comparison of Antimony Behavior with that of Arsenic under Various Soil Redox Conditions ». *Environmental Science & Technology* 40 (23): 7270-76. https://doi.org/10.1021/es060694x.

Mitsunobu, Satoshi, Yoshio Takahashi, Yasuko Terada, et Masahiro Sakata. 2010. « Antimony(V) Incorporation into Synthetic Ferrihydrite, Goethite, and Natural Iron Oxyhydroxides ». *Environmental Science & Technology* 44 (10): 3712-18. https://doi.org/10.1021/es903901e.

Mosleh, Mohsen, et Bomani A. Khemet. 2006. « A Surface Texturing Approach for Cleaner Disc Brakes ». *Tribology Transactions* 49 (2): 279-83. https://doi.org/10.1080/05698190600639913.

Moynier, Frédéric, Derek Vance, Toshiyuki Fujii, et Paul Savage. 2017. « The Isotope Geochemistry of Zinc and Copper ». *Reviews in Mineralogy and Geochemistry* 82 (1): 543-600. https://doi.org/10.2138/rmg.2017.82.13.

Münzenberg, G. 2013. « Development of Mass Spectrometers from Thomson and Aston to Present ». *International Journal of Mass Spectrometry*, 100 years of Mass Spectrometry, 349-350 (septembre): 9-18. https://doi.org/10.1016/j.ijms.2013.03.009.

Naidu, Gayathri, Seongchul Ryu, Ramesh Thiruvenkatachari, Youngkwon Choi, Sanghyun Jeong, et Saravanamuthu Vigneswaran. 2019. « A Critical Review on Remediation, Reuse, and Resource Recovery from Acid Mine Drainage ». *Environmental Pollution* 247 (avril): 1110-24. https://doi.org/10.1016/j.envpol.2019.01.085.

Nguyen, Van Khanh, Wonyoung Choi, Jaecheul Yu, et Taeho Lee. 2017. « Microbial Oxidation of Antimonite and Arsenite by Bacteria Isolated from Antimony-Contaminated Soils ». *International Journal of Hydrogen Energy*, Special Issue on The Asia Biohydrogen and Biorefinery Symposium (ABBS 2016), 5-8 October 2016, Jeju Island, South Korea, 42 (45): 27832-42. https://doi.org/10.1016/j.ijhydene.2017.08.056.

Nguyen, Van Khanh, et Jong-Un Lee. 2015. « Antimony-Oxidizing Bacteria Isolated from Antimony-Contaminated Sediment – A Phylogenetic Study ». *Geomicrobiology Journal* 32 (1): 50-58. https://doi.org/10.1080/01490451.2014.925009.

Nishad, Padala Abdul, et Anupkumar Bhaskarapillai. 2021. « Antimony, a Pollutant of Emerging Concern: A Review on Industrial Sources and Remediation Technologies ». *Chemosphere* 277 (août): 130252. https://doi.org/10.1016/j.chemosphere.2021.130252.

Novak, Martin, Vladislav Chrastny, Eva Cadkova, Juraj Farkas, Thomas D. Bullen, Jiri Tylcer, Zdenka Szurmanova, et al. 2014. « Common Occurrence of a Positive δ^{53}Cr Shift in Central European Waters Contaminated by Geogenic/Industrial Chromium Relative to Source Values ». *Environmental Science & Technology* 48 (11): 6089-96. https://doi.org/10.1021/es405615h.

Nriagu, Jerome O. 1989. « A Global Assessment of Natural Sources of Atmospheric Trace Metals ». *Nature* 338 (6210): 47-49. https://doi.org/10.1038/338047a0.

O'Neil, James R. 1986. « Theoretical And Experimental Aspects of Isotopic Fractionation. » *Reviews in Mineralogy*.

Parigi, Roberta, Ning Chen, Joel W. Reid, Carol J. Ptacek, et David W. Blowes. 2022. « Nickel Isotope Fractionation during Precipitation of Ni Secondary Minerals and Synchrotron-Based Analysis of the Precipitates ». *Geochimica et Cosmochimica Acta* 317 (janvier): 91-105. https://doi.org/10.1016/j.gca.2021.10.027.

Parigi, Roberta, Eva Pakostova, Joel W. Reid, Emily M. Saurette, Joyce M. McBeth, Carol J. Ptacek, et David W. Blowes. 2022. « Nickel Isotope Fractionation As an Indicator of Ni Sulfide Precipitation Associated with Microbially Mediated Sulfate Reduction ». *Environmental Science & Technology* 56 (12): 7954-62. https://doi.org/10.1021/acs.est.2c00523.

Paulukat, Cora, Lasse N. Døssing, Sisir K. Mondal, Andrea R. Voegelin, et Robert Frei. 2015. « Oxidative Release of Chromium from Archean Ultramafic Rocks, Its Transport and Environmental Impact – A Cr Isotope Perspective on the Sukinda Valley Ore District (Orissa, India) ». *Applied Geochemistry* 59 (août): 125-38. https://doi.org/10.1016/j.apgeochem.2015.04.016.

Peacock, Caroline L., et David M. Sherman. 2004. « Copper(II) Sorption onto Goethite, Hematite and Lepidocrocite: A Surface Complexation Model Based on Ab Initio Molecular Geometries and

EXAFS Spectroscopy1 1Associate Editor: D. L. Sparks ». *Geochimica et Cosmochimica Acta* 68 (12): 2623-37. https://doi.org/10.1016/j.gca.2003.11.030.

Pilarski, Janette, Pamela Waller, et William Pickering. 1995. « Sorption of Antimony Species by Humic Acid ». *Water, Air, and Soil Pollution* 84 (1): 51-59. https://doi.org/10.1007/BF00479588.

Pokrovsky, O. S., G. S. Pokrovski, J. Schott, et A. Galy. 2006. « Experimental Study of Germanium Adsorption on Goethite and Germanium Coprecipitation with Iron Hydroxide: X-Ray Absorption Fine Structure and Macroscopic Characterization ». *Geochimica et Cosmochimica Acta* 70 (13): 3325-41. https://doi.org/10.1016/j.gca.2006.04.012.

Pokrovsky, O. S., J. Viers, E. E. Emnova, E. I. Kompantseva, et R. Freydier. 2008. « Copper Isotope Fractionation during Its Interaction with Soil and Aquatic Microorganisms and Metal Oxy(Hydr)Oxides: Possible Structural Control ». *Geochimica et Cosmochimica Acta* 72 (7): 1742-57. https://doi.org/10.1016/j.gca.2008.01.018.

Pokrovsky, O. S., J. Viers, et R. Freydier. 2005. « Zinc Stable Isotope Fractionation during Its Adsorption on Oxides and Hydroxides ». *Journal of Colloid and Interface Science* 291 (1): 192-200. https://doi.org/10.1016/j.jcis.2005.04.079.

Pokrovsky, Oleg S., Albert Galy, Jacques Schott, Gleb S. Pokrovski, et Samia Mantoura. 2014. « Germanium Isotope Fractionation during Ge Adsorption on Goethite and Its Coprecipitation with Fe Oxy(Hydr)Oxides ». *Geochimica et Cosmochimica Acta* 131 (avril): 138-49. https://doi.org/10.1016/j.gca.2014.01.023.

Pratas, J., M. N. V. Prasad, H. Freitas, et L. Conde. 2005. « Plants Growing in Abandoned Mines of Portugal Are Useful for Biogeochemical Exploration of Arsenic, Antimony, Tungsten and Mine Reclamation ». *Journal of Geochemical Exploration* 85 (3): 99-107. https://doi.org/10.1016/j.gexplo.2004.11.003.

Qi, Pengfei, et Thomas Pichler. 2016. « Sequential and Simultaneous Adsorption of Sb(III) and Sb(V) on Ferrihydrite: Implications for Oxidation and Competition ». *Chemosphere* 145 (février): 55-60. https://doi.org/10.1016/j.chemosphere.2015.11.057.

Qin, Liping, et Xiangli Wang. 2017. « Chromium Isotope Geochemistry ». *Reviews in Mineralogy and Geochemistry* 82 (1): 379-414. https://doi.org/10.2138/rmg.2017.82.10.

Qin, Zemin, Shuting Zhao, Taoran Shi, Fengyang Zhang, Ziru Pei, Yuheng Wang, et Yanru Liang. 2022. « Accumulation, Regional Distribution, and Environmental Effects of Sb in the Largest Hg–Sb Mine Area in Qinling Orogen, China ». *Science of The Total Environment* 804 (janvier): 150218. https://doi.org/10.1016/j.scitotenv.2021.150218.

Qiu, Canrong, Frantisek Majs, Thomas A. Douglas, Moritz Schmidt, et Thomas P. Trainor. 2018. « In Situ Structural Study of Sb(V) Adsorption on Hematite (1$\bar{1}$02) Using X-ray Surface Scattering ». *Environmental Science & Technology* 52 (19): 11161-68. https://doi.org/10.1021/acs.est.8b03903.

Quentel, François, Montserrat Filella, Catherine Elleouet, et Christian-Louis Madec. 2004. « Kinetic Studies on Sb(III) Oxidation by hydrogen Peroxide in Aqueous Solution ». *Environement Science and Technology* 38 (10): 2843-48. https://doi.org/10.1021/es035019r.

Ratié, Gildas, Vladislav Chrastný, Damien Guinoiseau, Rémi Marsac, Zuzana Vaňková, et Michael Komárek. 2021. « Cadmium Isotope Fractionation during Complexation with Humic Acid ». *Environmental Science & Technology* 55 (11): 7430-44. https://doi.org/10.1021/acs.est.1c00646.

Rayleigh, Lord. 1896. « L. Theoretical considerations respecting the separation of gases by diffusion and similar processes ». *The London, Edinburgh, and Dublin Philosophical Magazine and Journal of Science* 42 (259): 493-98. https://doi.org/10.1080/14786449608620944.

Reguera-Galan, A., T. Barriero-Grille, M. Moldovan, L. Lobo, M. A. De Blas Cortina, et J. I. Garcia Alonso. 2019. « A provenance study of early bronze age artefacts found in Asturias (Spain) by means of metal impurities and lead, copper and antimony isotopic compositions ». *Archaeometry* 61 (3): 683-700. https://doi.org/10.1111/arcm.12445.

Resongles, Eléonore. 2014. « Etude de la contamination par les métaux et les métalloïdes d'origine minière sur le bassin des Gardons : approches élémentaires (As, Cd, Hg, Pb, Sb, Tl, Zn) et isotopique (Sb, Zn). » Bibliothèque Universitaire de Montpellier.

Resongles, Eléonore, Corinne Casiot, Françoise Elbaz-Poulichet, Rémi Freydier, Odile Bruneel, Christine Piot, Sophie Delpoux, Aurélie Volant, et Angélique Desoeuvre. 2013. « Fate of Sb(V) and Sb(III) species along a gradient of pH and oxygen concentration in the Canoulès mine waters (Southern France) ». *Environmental Science Processes and Impacts* 15: 1536-44. https://doi.org/10.1039/c3em00215b.

Resongles, Eléonore, Rémi Freydier, Corinne Casiot, Jérôme Viers, Jérôme Chmeleff, et Françoise Elbaz-Poulichet. 2015. « Antimony isotopic composition in river waters affected by ancient mining activity ». *Talanta* 144: 851-61. http://dx.doi.org/10.1016/j.talanta.2015.07.013.

Ritchie, Vanessa J., Anastasia G. Ilgen, Seth H. Mueller, Thomas P. Trainor, et Richard J. Goldfarb. 2013. « Mobility and Chemical Fate of Antimony and Arsenic in Historic Mining Environments of the Kantishna Hills District, Denali National Park and Preserve, Alaska ». *Chemical Geology* 335 (janvier): 172-88. https://doi.org/10.1016/j.chemgeo.2012.10.016.

Roh, Yul, et Hi-Soo Moon. 2001. « Iron Reduction by a Psychrotolerant Fe(III)-Reducing Bacterium Isolated from Ocean Sediment ». *Geosciences Journal* 5 (3): 183-90. https://doi.org/10.1007/BF02910302.

Roper, Adam J., Peter A. Williams, et Montserrat Filella. 2012. « Secondary Antimony Minerals: Phases That Control the Dispersion of Antimony in the Supergene Zone ». *Geochemistry*, Antimony, 72 (juillet): 9-14. https://doi.org/10.1016/j.chemer.2012.01.005.

Rouxel, Olivier, John Ludden, et Yves Fouquet. 2003. « Antimony isotope variations in natural systems and implications for their use as geochemical tracers ». *Chemical Geology* 200: 25-40. https://doi.org/10.1016/S0009-2541(03)00121-9.

Rudnick, R. L., et S. Gao. 2014. « 4.1 - Composition of the Continental Crust ». In *Treatise on Geochemistry (Second Edition)*, édité par Heinrich D. Holland et Karl K. Turekian, 1-51. Oxford: Elsevier. https://doi.org/10.1016/B978-0-08-095975-7.00301-6.

Saerens, Anton, Manosij Ghosh, Jelle Verdonck, et Lode Godderis. 2019. « Risk of Cancer for Workers Exposed to Antimony Compounds: A Systematic Review ». *International Journal of Environmental Research and Public Health* 16 (22): 4474. https://doi.org/10.3390/ijerph16224474.

Salminen, R. 2005. *Geochemical Atlas of Europe. Part 1: Background Information, Methodology and Maps.* Geological Survey of FInland, Espoo.

Sanderson, Peter, Fangjie Qi, Balaji Seshadri, Ayanka Wijayawardena, et Ravi Naidu. 2018. « Contamination, Fate and Management of Metals in Shooting Range Soils—a Review ». *Current Pollution Reports* 4 (2): 175-87. https://doi.org/10.1007/s40726-018-0089-5.

Santini, J. M., R. N. Vanden Hoven, J. M. Macy, et W. T. Frankenberger. 2002. « Characteristics of newly discovered arsenite-oxydizing bacteria ». *Environmental chemistry of arsenic*, 329-42.

Schauble, E. A., G. R. Rossman, et H. P. Taylor. 2001. « Theoretical Estimates of Equilibrium Fe-Isotope Fractionations from Vibrational Spectroscopy ». *Geochimica et Cosmochimica Acta* 65 (15): 2487-97. https://doi.org/10.1016/S0016-7037(01)00600-7.

Schauble, E. A. 2004. « Applying Stable Isotope Fractionation Theory to New Systems ». *Reviews in Mineralogy and Geochemistry* 55 (1): 65-111. https://doi.org/10.2138/gsrmg.55.1.65.

Schauble, E. A. 2007. « Role of Nuclear Volume in Driving Equilibrium Stable Isotope Fractionation of Mercury, Thallium, and Other Very Heavy Elements ». *Geochimica et Cosmochimica Acta* 71 (9): 2170-89. https://doi.org/10.1016/j.gca.2007.02.004.

Schauble, E. A. 2013. « Modeling nuclear volume isotope effects in crystals ». *Proceedings of the National Academy of Sciences* 110 (44): 17714-19. https://doi.org/10.1073/pnas.1216216110.

Schauble, Edwin A., Merlin Méheut, et Pamela S. Hill. 2009. « Combining Metal Stable Isotope Fractionation Theory with Experiments ». *Elements* 5 (6): 369-74. https://doi.org/10.2113/gselements.5.6.369.

Scheinost, Andreas C., Andre Rossberg, Delphine Vantelon, Irene Xifra, Ruben Kretzschmar, Ann-Kathrin Leuz, Harald Funke, et C. Annette Johnson. 2006. « Quantitative Antimony Speciation in Shooting-Range Soils by EXAFS Spectroscopy ». *Geochimica et Cosmochimica Acta* 70 (13): 3299-3312. https://doi.org/10.1016/j.gca.2006.03.020.

Schnorr, Teresa M., Kyle Steenland, Michael J. Thun, et Robert A. Rinsky. 1995. « Mortality in a Cohort of Antimony Smelter Workers ». *American Journal of Industrial Medicine* 27 (5): 759-70. https://doi.org/10.1002/ajim.4700270510.

Sen, Indra S., et Bernhard Peucker-Ehrenbrink. 2012. « Anthropogenic Disturbance of Element Cycles at the Earth's Surface ». *Environmental Science & Technology* 46 (16): 8601-9. https://doi.org/10.1021/es301261x.

Sherman, David M. 2013. « Equilibrium Isotopic Fractionation of Copper during Oxidation/Reduction, Aqueous Complexation and Ore-Forming Processes: Predictions from Hybrid Density Functional Theory ». *Geochimica et Cosmochimica Acta* 118 (octobre): 85-97. https://doi.org/10.1016/j.gca.2013.04.030.

Shiel, Alyssa E., Dominique Weis, et Kristin J. Orians. 2010. « Evaluation of Zinc, Cadmium and Lead Isotope Fractionation during Smelting and Refining ». *Science of The Total Environment* 408 (11): 2357-68. https://doi.org/10.1016/j.scitotenv.2010.02.016.

Shotyk, William, Bin Chen, et Michael Krachler. 2005. « Lithogenic, Oceanic and Anthropogenic Sources of Atmospheric Sb to a Maritime Blanket Bog, Myrarnar, Faroe Islands ». *Journal of Environmental Monitoring* 7 (12): 1148-54. https://doi.org/10.1039/B509928P.

Shtangeeva, Irina, Roza Bali, et Andrew Harris. 2011. « Bioavailability and toxicity of antimony ». *Journal of Geochemical Exploration* 110: 40-45. https://doi.org/10.1016/j.gexplo.2010.07.003.

Skierszkan, E. K., K. U. Mayer, D. Weis, J. Roberston, et R. D. Beckie. 2019. « Molybdenum Stable Isotope Fractionation during the Precipitation of Powellite ($CaMoO_4$) and Wulfenite ($PbMoO_4$) ». *Geochimica et Cosmochimica Acta* 244 (janvier): 383-402. https://doi.org/10.1016/j.gca.2018.09.030.

Skulan, Joseph, et Donald J. DePaolo. 1999. « Calcium isotope fractionation between soft and mineralized tissues as a monitor of calcium use in vertebrates ». *Proceedings of the National Academy of Sciences* 96 (24): 13709-13. https://doi.org/10.1073/pnas.96.24.13709.

Skulan, Joseph, Donald J. DePaolo, et Thomas L. Owens. 1997. « Biological Control of Calcium Isotopic Abundances in the Global Calcium Cycle ». *Geochimica et Cosmochimica Acta* 61 (12): 2505-10. https://doi.org/10.1016/S0016-7037(97)00047-1.

Smith, Robin S., Jan G. Wiederhold, et Ruben Kretzschmar. 2015. « Mercury Isotope Fractionation during Precipitation of Metacinnabar (β-HgS) and Montroydite (HgO) ». *Environmental Science & Technology* 49 (7): 4325-34. https://doi.org/10.1021/acs.est.5b00409.

Sternbeck, John, Åke Sjödin, et Kenth Andréasson. 2002. « Metal Emissions from Road Traffic and the Influence of Resuspension—Results from Two Tunnel Studies ». *Atmospheric Environment* 36 (30): 4735-44. https://doi.org/10.1016/S1352-2310(02)00561-7.

Sun, Guangyi, Yunjie Wu, Xinbin Feng, Xian Wu, Xinyu Li, Qianwen Deng, Feiyue Wang, et Xuewu Fu. 2021. « Precise Analysis of Antimony Isotopic Composition in Geochemical Materials by MC-ICP-MS ». *Chemical Geology*, juillet, 120459. https://doi.org/10.1016/j.chemgeo.2021.120459.

Sun, Qian, Cun Liu, Marcelo Eduardo Alves, Syed Tahir Ata-Ul-Karim, Dong-Mei Zhou, Jian-Zhou He, Pei-Xin Cui, et Yu-Jun Wang. 2018. « The Oxidation and Sorption Mechanism of Sb on δ-MnO2 ». *Chemical Engineering Journal* 342 (juin): 429-37. https://doi.org/10.1016/j.cej.2018.02.091.

Sundar, Shyam, et Chakravarty. 2010. « Antimony Toxicity ». *International Journal of Environmental Research and Public Health* 7: 4267-77. https://doi.org/10.3390/ijerph7124267.

Takayanagi, Kazufumi, et Daniel Cossa. 1997. « Vertical Distributions of Sb(III) and Sb(V) in Pavin Lake, France ». *Water Research* 31 (3): 671-74. https://doi.org/10.1016/S0043-1354(96)00285-0.

Tandy, Susan, Kerstin Hockmann, Martin Keller, Björn Studer, Andreas Papritz, et Rainer Schulin. 2018. « Antimony Mobility during Prolonged Waterlogging and Reoxidation of Shooting Range Soil:

A Field Experiment ». *Science of The Total Environment* 624 (mai): 838-44. https://doi.org/10.1016/j.scitotenv.2017.12.193.

Tang, B, et S Liu. 2009. « Severe pollution of Xikuangshan antimony mine constitutes great environmental risk to local inhabitants ». *Chinese environment*.

Tang, Jianwu, Stephan Jürgen Köhler, et Martin Dietzel. 2008. « Sr^{2+}/Ca^{2+} and $^{44}Ca/^{40}Ca$ fractionation during inorganic calcite formation: I. Sr incorporation. » *Geochimica* 72: 3718-32.

Tanimizu, Masaharu, Yusuke Araki, Satoshi Asaoka, et Yoshio Takahashi. 2011. « Determination of natural isotopic variation in antimony using inductively coupled plasma mass spectrometry for an uncertainty estimation of the standard atomic weight of antimony ». *Geochemical Journal* 45: 27-32.

Tanu, Tanzina, Adiba Anjum, Momotaj Jahan, Farjana Nikkon, Mominul Hoque, Apurba Kumar Roy, Azizul Haque, Seiichiro Himeno, Khaled Hossain, et Zahangir Alam Saud. 2018. « Antimony-Induced Neurobehavioral and Biochemical Perturbations in Mice ». *Biological Trace Element Research* 186 (1): 199-207. https://doi.org/10.1007/s12011-018-1290-5.

Targan, Şerif, Vedia Nüket Tirtom, et Birsen Akkuş. 2013. « Removal of Antimony(III) from Aqueous Solution by Using Grey and Red Erzurum Clay and Application to the Gediz River Sample ». *ISRN Analytical Chemistry* 2013 (septembre): e962781. https://doi.org/10.1155/2013/962781.

Tella, Marie, et Gleb S. Pokrovski. 2009. « Antimony(III) Complexing with O-Bearing Organic Ligands in Aqueous Solution: An X-Ray Absorption Fine Structure Spectroscopy and Solubility Study ». *Geochimica et Cosmochimica Acta* 73 (2): 268-90. https://doi.org/10.1016/j.gca.2008.10.014.

Tella, Marie, et Gleb S. Pokrovski. 2012. « Stability and Structure of Pentavalent Antimony Complexes with Aqueous Organic Ligands ». *Chemical Geology* 292-293 (janvier): 57-68. https://doi.org/10.1016/j.chemgeo.2011.11.004.

Terry, Lee R., Thomas R. Kulp, Heather Wiatrowski, Laurence G. Miller, et Ronald S. Oremland. 2015. « Microbial Oxidation of Antimony(III) with Oxygen or Nitrate by Bacteria Isolated from Contaminated Mine Sediments ». *Applied and Environmental Microbiology* 81 (24): 8478-88. https://doi.org/10.1128/AEM.01970-15.

Thanabalasingam, P., et W. F. Pickering. 1990. « Specific Sorption of Antimony (III) by the Hydrous Oxides of Mn, Fe, and Al ». *Water, Air, and Soil Pollution* 49 (1): 175-85. https://doi.org/10.1007/BF00279519.

Thestorf, Kolja, et Mohsen Makki. 2021. « Pseudo-Total Antimony Content in Topsoils of the Berlin Metropolitan Area ». *Journal of Soils and Sediments* 21 (5): 2102-17. https://doi.org/10.1007/s11368-020-02742-9.

Tian, Hezhong, JunRui Zhou, Chuanyong Zhu, Dan Zhao, Jiajia Gao, Jiming Hao, Mengchang He, Kaiyun Liu, Kun Wang, et Shenbing Hua. 2014. « A Comprehensive Global Inventory of Atmospheric Antimony Emissions from Anthropogenic Activities, 1995–2010 ». *Environmental Science & Technology* 48 (17): 10235-41. https://doi.org/10.1021/es405817u.

Torma, Arpad E., et Fathi Habashi. 1972. « Oxidation of Copper (II) Selenide by Thiobacillus Ferrooxidans ». *Canadian Journal of Microbiology*. https://doi.org/10.1139/m72-278.

Tossell, J. A. 2005. « Calculating the Partitioning of the Isotopes of Mo between Oxidic and Sulfidic Species in Aqueous Solution ». *Geochimica et Cosmochimica Acta* 69 (12): 2981-93. https://doi.org/10.1016/j.gca.2005.01.016.

Tschan, Martin, Brett H. Robinson, et Rainer Schulin. 2009. « Antimony in the Soil–Plant System – a Review ». *Environmental Chemistry* 6 (2): 106-15. https://doi.org/10.1071/EN08111.

Tsui, Martin Tsz-Ki, Joel D. Blum, et Sae Yun Kwon. 2020. « Review of Stable Mercury Isotopes in Ecology and Biogeochemistry ». *Science of The Total Environment* 716 (mai): 135386. https://doi.org/10.1016/j.scitotenv.2019.135386.

Turner, Andrew, et Montserrat Filella. 2017. « Field-portable-XRF reveals the ubiquity of antimony in plastic consumer products ». *Science of the Total Environment* 584: 982-89. http://dx.doi.org/10.1016/j.scitotenv.2017.01.149.

Udodov, P.A., et Yu. S. Parilov. 1961. « Certain regularities of migration of metals in natural waters ». *Geochemistry* 8: 763-71.

Urey, Harold C. 1947. « The Thermodynamic Properties of Isotopic Substances ». *Journal of the Chemical Society (Resumed)*, n° 0 (janvier): 562-81. https://doi.org/10.1039/JR9470000562.

U.S. Geological Survey. 2020. « Mineral Commodity Summaries ».

U.S. Geological Survey. 2022. « 2022 Final List of Critical Minerals ». Notices Federal Register / Vol. 87, No. 37.

Wang, D. T., D. C. Fregoso, A. S. Ellis, T. M. Johnson, et T. D. Bullen. 2010. « Stable Isotope Fractionation during Chromium(III) Oxidation by δ-MnO_2 » 2010 (décembre): H53F-1109.

Wang, Da, Ryan Mathur, Youye Zheng, Kunfeng Qiu, et Hongjie Wu. 2021. « Redox-Controlled Antimony Isotope Fractionation in the Epithermal System: New Insights from a Multiple Metal Stable Isotopic Combination Study of the Zhaxikang Sb–Pb–Zn–Ag Deposit in Southern Tibet ». *Chemical Geology* 584 (décembre): 120541. https://doi.org/10.1016/j.chemgeo.2021.120541.

Wang, Huawei, Fulong Chen, Shuyong Mu, Daoyong Zhang, Xiangliang Pan, Duu-Jong Lee, et Jo-Shu Chang. 2013. « Removal of Antimony (Sb(V)) from Sb Mine Drainage: Biological Sulfate Reduction and Sulfide Oxidation–Precipitation ». *Bioresource Technology* 146 (octobre): 799-802. https://doi.org/10.1016/j.biortech.2013.08.002.

Wang, Huawei, Ya-nan Wang, Yingjie Sun, Xiangliang Pan, Daoyong Zhang, et Yiu Fai Tsang. 2018. « Differences in Sb(V) and As(V) Adsorption onto a Poorly Crystalline Phyllomanganate (δ-MnO_2): Adsorption Kinetics, Isotherms, and Mechanisms ». *Process Safety and Environmental Protection* 113 (janvier): 40-47. https://doi.org/10.1016/j.psep.2017.09.015.

Wang, Qian, Thomas P. Warelow, Yoon-Suk Kang, Christine Romano, Thomas H. Osborne, Corinne R. Lehr, Brian Bosthner, Timothy R. McDermott, Joanne M. Santini, et Gejiao Wang. 2015. « Arsenite Oxidase Alsop Functions as an Antimonite Oxidase ». *Applied and Environmental Microbiology* 81 (6). https://doi.org/10.1128/AEM.02981-14.

Wang, Wenzhong, Tian Qin, Chen Zhou, Shichun Huang, Zhongqing Wu, et Fang Huang. 2017. « Concentration Effect on Equilibrium Fractionation of Mg-Ca Isotopes in Carbonate Minerals: Insights from First-Principles Calculations ». *Geochimica et Cosmochimica Acta* 208 (juillet): 185-97. https://doi.org/10.1016/j.gca.2017.03.023.

Wang, Xiangqin, Mengchang He, Jianhong Xi, et Xiaofei Lu. 2011. « Antimony Distribution and Mobility in Rivers around the World's Largest Antimony Mine of Xikuangshan, Hunan Province, China ». *Microchemical Journal*, Antimony: Emerging Global Contaminant in the Environment, 97 (1): 4-11. https://doi.org/10.1016/j.microc.2010.05.011.

Wang, Zhao, Kideok D. Kwon, Caroline Peacock, Xinxin Mo, Wenxian Gou, Xionghan Feng, et Wei Li. 2022. « Zn Stable Isotope Fractionation during Adsorption onto Todorokite: A Molecular Perspective from X-Ray Absorption Spectroscopy and Density Functional Theory ». *Geochimica et Cosmochimica Acta* 327 (juin): 116-36. https://doi.org/10.1016/j.gca.2022.04.016.

Wang, Zhuhong, Jiubin Chen, et Ting Zhang. 2017. « Cu Isotopic Composition in Surface Environments and in Biological Systems: A Critical Review ». *International Journal of Environmental Research and Public Health* 14 (5): 538. https://doi.org/10.3390/ijerph14050538.

Wanty, R. B., F. Podda, G. De Giudici, R. Cidu, et P. Lattanzi. 2013. « Zinc Isotope and Transition-Element Dynamics Accompanying Hydrozincite Biomineralization in the Rio Naracauli, Sardinia, Italy ». *Chemical Geology* 337-338 (janvier): 1-10. https://doi.org/10.1016/j.chemgeo.2012.11.010.

Wasylenki, Laura E., Bryan A. Rolfe, Colin L. Weeks, Thomas G. Spiro, et Ariel D. Anbar. 2008. « Experimental Investigation of the Effects of Temperature and Ionic Strength on Mo Isotope Fractionation during Adsorption to Manganese Oxides ». *Geochimica et Cosmochimica Acta* 72 (24): 5997-6005. https://doi.org/10.1016/j.gca.2008.08.027.

Wasylenki, Laura E., Jared W. Swihart, et Stephen J. Romaniello. 2014. « Cadmium Isotope Fractionation during Adsorption to Mn Oxyhydroxide at Low and High Ionic Strength ». *Geochimica et Cosmochimica Acta* 140 (septembre): 212-26. https://doi.org/10.1016/j.gca.2014.05.007.

Weiss, Dominik J., Mark Rehkdmper, Ronny Schoenberg, Mike McLaughlin, Jason Kirby, Peter G. C. Campbell, Tim Arnold, John Chapman, Kate Peel, et and Simone Gioia. 2008. « Application of Nontraditional Stable-Isotope Systems to the Study of Sources and Fate of Metals in the

Environment ». *Environmental Science & Technology* 42 (3): 655-64. https://doi.org/10.1021/es0870855.

Wen, Bing, Jianwei Zhou, Aiguo Zhou, Cunfu Liu, et Ligang Li. 2017. « A review of antimony (Sb) isotopes analytical methods and application in environmental systems ». *International Bioteterioration & Biodegradation* XXX: 1-8. http://dx.doi/10.1016/j.ibiod.2017.01.008.

Wen, Hanjie, et Jean Carignan. 2011. « Selenium Isotopes Trace the Source and Redox Processes in the Black Shale-Hosted Se-Rich Deposits in China ». *Geochimica et Cosmochimica Acta* 6 (75): 1411-27. https://doi.org/10.1016/j.gca.2010.12.021.

Wen, Hanjie, Yuxu Zhang, Christophe Cloquet, Chuanwei Zhu, Haifeng Fan, et Chongguang Luo. 2015. « Tracing Sources of Pollution in Soils from the Jinding Pb–Zn Mining District in China Using Cadmium and Lead Isotopes ». *Applied Geochemistry* 52 (janvier): 147-54. https://doi.org/10.1016/j.apgeochem.2014.11.025.

Widargo, Dito. 2005. « Atlas of Eh-pH diagrams Intercomparison of thermodynamic databases Geological Survey of Japan Open File ». https://www.academia.edu/9502204/Atlas_of_Eh_pH_diagrams_Intercomparison_of_thermodynamic_databases_Geological_Survey_of_Japan_Open_File.

Wiederhold, Jan G. 2015. « Metal Stable Isotope Signatures as Tracers in Environmental Geochemistry ». *Environmental Science & Technology* 49 (5): 2606-24. https://doi.org/10.1021/es504683e.

Wiederhold, Jan G., Christopher J. Cramer, Kelly Daniel, Ivan Infante, Bernard Bourdon, et Ruben Kretzschmar. 2010. « Equilibrium Mercury Isotope Fractionation between Dissolved Hg(II) Species and Thiol-Bound Hg ». *Environmental Science & Technology* 44 (11): 4191-97. https://doi.org/10.1021/es100205t.

Wilson, N. J., D. Craw, et K. Hunter. 2004. « Antimony Distribution and Environmental Mobility at an Historic Antimony Smelter Site, New Zealand ». *Environmental Pollution* 129 (2): 257-66. https://doi.org/10.1016/j.envpol.2003.10.014.

Wilson, Susan C., Peter V. Lockwood, Paul M. Ashley, et Matthew Tighe. 2010. « The Chemistry and Behaviour of Antimony in the Soil Environment with Comparisons to Arsenic: A Critical Review ». *Environmental Pollution (Barking, Essex: 1987)* 158 (5): 1169-81. https://doi.org/10.1016/j.envpol.2009.10.045.

Wu, Fengchang, Zhiyou Fu, Bijun Liu, Changli Mo, Bin Chen, Warren Corns, et Haiqing Liao. 2011. « Health Risk Associated with Dietary Co-Exposure to High Levels of Antimony and Arsenic in the World's Largest Antimony Mine Area ». *Science of The Total Environment* 409 (18): 3344-51. https://doi.org/10.1016/j.scitotenv.2011.05.033.

Xi, Jianhong, Mengchang He, et Chunye Lin. 2011. « Adsorption of Antimony(III) and Antimony(V) on Bentonite: Kinetics, Thermodynamics and Anion Competition ». *Microchemical Journal*, Antimony: Emerging Global Contaminant in the Environment, 97 (1): 85-91. https://doi.org/10.1016/j.microc.2010.05.017.

Xu, Wenpo, Jian-Ming Zhu, Thomas M. Johnson, Xiangli Wang, Zhi-Qing Lin, Decan Tan, et Haibo Qin. 2020. « Selenium Isotope Fractionation during Adsorption by Fe, Mn and Al Oxides ». *Geochimica et Cosmochimica Acta* 272 (mars): 121-36. https://doi.org/10.1016/j.gca.2020.01.001.

Yan, Xinran, Mengqiang Zhu, Wei Li, Caroline L. Peacock, Jingyuan Ma, Hanjie Wen, Fan Liu, Zhengbing Zhou, Chuanwei Zhu, et Hui Yin. 2021. « Cadmium Isotope Fractionation during Adsorption and Substitution with Iron (Oxyhydr)oxides ». *Environmental Science & Technology* 55 (17): 11601-11. https://doi.org/10.1021/acs.est.0c06927.

Yang, Sha, et Yun Liu. 2016. « Nuclear Field Shift Effects on Stable Isotope Fractionation: A Review ». *Acta Geochimica* 35 (3): 227-39. https://doi.org/10.1007/s11631-016-0109-3.

Yang, Shun-Chung, Jing Zhang, Yoshiki Sohrin, et Tung-Yuan Ho. 2018. « Cadmium Cycling in the Water Column of the Kuroshio-Oyashio Extension Region: Insights from Dissolved and Particulate Isotopic Composition ». *Geochimica et Cosmochimica Acta* 233 (juillet): 66-80. https://doi.org/10.1016/j.gca.2018.05.001.

Yang, Wen-Jun, Keng-Bo Ding, Peng Zhang, Hao Qiu, Christophe Cloquet, Han-Jie Wen, Jean-Louis Morel, Rong-Liang Qiu, et Ye-Tao Tang. 2019. « Cadmium Stable Isotope Variation in a Mountain Area Impacted by Acid Mine Drainage ». *Science of The Total Environment* 646 (janvier): 696-703. https://doi.org/10.1016/j.scitotenv.2018.07.210.

Ye, Li, Shixin Qiu, Xinhai Li, Yuxuan Jiang, et Chuanyong Jing. 2018. « Antimony Exposure and Speciation in Human Biomarkers near an Active Mining Area in Hunan, China ». *Science of The Total Environment* 640-641 (novembre): 1-8. https://doi.org/10.1016/j.scitotenv.2018.05.267.

Yin, Runsheng, Xinbin Feng, Xiangdong Li, Ben Yu, et Buyun Du. 2014. « Trends and Advances in Mercury Stable Isotopes as a Geochemical Tracer ». *Trends in Environmental Analytical Chemistry* 2 (mai): 1-10. https://doi.org/10.1016/j.teac.2014.03.001.

Yin, Xiuzhen, Rongfei Wei, Huadong Chen, Chuanwei Zhu, Yizhang Liu, Hanjie Wen, Qingjun Guo, et Jie Ma. 2021. « Cadmium Isotope Constraints on Heavy Metal Sources in a Riverine System Impacted by Multiple Anthropogenic Activities ». *Science of The Total Environment* 750 (janvier): 141233. https://doi.org/10.1016/j.scitotenv.2020.141233.

Zhai, Degao, Ryan Mathur, Sheng-Ao Liu, Jiajun Liu, Linda Godfrey, Kexin Wang, Junwei Xu, et Jeffery Vervoort. 2021. « Antimony Isotope Fractionation in Hydrothermal Systems ». *Geochimica et Cosmochimica Acta*, mai. https://doi.org/10.1016/j.gca.2021.05.031.

Zhang, Chengjun, Mengchang He, Wei Ouyang, Chunye Lin, et Xitao Liu. 2020. « Influence of Fe(II) on Sb(III) Oxidation and Adsorption by MnO2 under Acidic Conditions ». *Science of The Total Environment* 724 (juillet): 138209. https://doi.org/10.1016/j.scitotenv.2020.138209.

Zhang, Guoping, Xiaoxue Ouyang, Haixia Li, Zhiping Fu, et Jingjing Chen. 2016. « Bioremoval of Antimony from Contaminated Waters by a Mixed Batch Culture of Sulfate-Reducing Bacteria ». *International Biodeterioration & Biodegradation* 115 (novembre): 148-55. https://doi.org/10.1016/j.ibiod.2016.08.007.

Zhang, Jun, Jian Chen, Yi-Fei Wu, Zi-Ping Wang, Ji-Guo Qiu, Xiao-Long Li, Feng Cai, et al. 2022. « Oxidation of Organoarsenicals and Antimonite by a Novel Flavin Monooxygenase Widely Present in Soil Bacteria ». *Environmental Microbiology* 24 (2): 752-61. https://doi.org/10.1111/1462-2920.15488.

Zhang, X, MA Hu, et B Zhao. 2005. « A survey of heavy metals pollution in Daye Tieshan Area ». *Environement Sciences and Technologies (China)*.

Zhang, Yuxu, Hanjie Wen, Chuanwei Zhu, Haifeng Fan, Chongguang Luo, Jie Liu, et Christophe Cloquet. 2016. « Cd Isotope Fractionation during Simulated and Natural Weathering ». *Environmental Pollution* 216 (septembre): 9-17. https://doi.org/10.1016/j.envpol.2016.04.060.

Zhong, Qiaohui, Yuchen Zhou, Daniel C. W. Tsang, Juan Liu, Xiao Yang, Meiling Yin, Shijun Wu, Jin Wang, Tangfu Xiao, et Zhaofeng Zhang. 2020. « Cadmium Isotopes as Tracers in Environmental Studies: A Review ». *Science of The Total Environment* 736 (septembre): 139585. https://doi.org/10.1016/j.scitotenv.2020.139585.

Zhou, Junrui, Hezhong Tian, Chuanyong Zhu, Jiming Hao, Jiajia Gao, Yong Wang, Yifeng Xue, Shenbin Hua, et Kun Wang. 2015. « Future Trends of Global Atmospheric Antimony Emissions from Anthropogenic Activities until 2050 ». *Atmospheric Environment* 120 (novembre): 385-92. https://doi.org/10.1016/j.atmosenv.2015.09.018.

Zhou, Weiqing, Aiguo Zhou, Bing Wen, Peng Liu, Zhenli Zhu, Zou Finfrock, et Jianwei Zhou. 2022. « Antimony Isotope Fractionation during Adsorption on Aluminum Oxides ». *Journal of Hazardous Materials* 429 (mai): 128317. https://doi.org/10.1016/j.jhazmat.2022.128317.

Zhu, Chuanwei, Hanjie Wen, Yuxu Zhang, Runsheng Yin, et Christophe Cloquet. 2018. « Cd Isotope Fractionation during Sulfide Mineral Weathering in the Fule Zn-Pb-Cd Deposit, Yunnan Province, Southwest China ». *Science of The Total Environment* 616-617 (mars): 64-72. https://doi.org/10.1016/j.scitotenv.2017.10.293.

Zhu, J, F-C Wu, Q-J Deng, S-X Shao, C-L Mo, X-L Pan, W Li, et R-Y Zhang. 2009. « Environmental characteristics of water near the Xikuangshan antimony mine. » *Acta Scientiae Circumstantiae* 29.

Zhu, Jian-Ming, Thomas M. Johnson, Scott K. Clark, Xiang-Kun Zhu, et Xiang-Li Wang. 2014. « Selenium Redox Cycling during Weathering of Se-Rich Shales: A Selenium Isotope Study ». *Geochimica et Cosmochimica Acta* 126 (février): 228-49. https://doi.org/10.1016/j.gca.2013.11.004.

Chapitre 2 :
Développement analytique d'une méthode de purification simplifiée de Sb pour la mesure précise du rapport isotopique $^{123}Sb/^{121}Sb$ par HG-MC-ICP-MS

Introduction

Ce chapitre est consacré au développement d'une méthode de séparation de l'antimoine dans des matrices diverses et complexes (matrices environnementales, géologiques, biologiques, anthropiques…) afin de pouvoir réaliser des analyses du rapport isotopique $^{123}Sb/^{121}Sb$ par couplage HG-MC-ICP-MS (Génération d'Hydrures – Spectromètre de masse à source plasma et Multi-collection).

Lors de ce développement de méthode indispensable pour réaliser les analyses isotopiques de la suite de la thèse, deux points principaux ont été étudiés (1) la préparation des échantillons depuis la minéralisation jusqu'à la séparation de l'antimoine des autres éléments contenus dans la matrice et, (2) l'optimisation de la mesure par HG-MC-ICP-MS et le traitement de données permettant d'obtenir la meilleure précision, justesse et reproductibilité sur les rapports isotopiques. L'enjeu de cette partie était de développer une méthode de purification de l'antimoine en une seule étape qui puisse être utilisée sur un grand nombre de matrices complexes avec de faibles teneurs en antimoine mais également d'optimiser au mieux les paramètres instrumentaux qui influencent la précision, la justesse et la reproductibilité des analyses.

Dans un premier temps, la méthode de séparation de Sb par adsorption sur Thiol-silice a été optimisée, notamment quant à la quantité minimale d'antimoine requise pour la procédure, le taux de récupération de l'antimoine après la séparation ainsi que le taux d'abattement des éléments chimiques qui peuvent interférer lors de la mesure (As, Cd, Co, Cr, Cu, Fe, Ni, Pb, Se et Sn). Toutes ces vérifications ont été réalisées sur un total de 14 matériaux de références certifiés très divers quant à leur nature et concentration en antimoine, dont la grande majorité n'avaient jamais été analysés pour le rapport $^{123}Sb/^{121}Sb$.

La seconde partie de ce travail a porté sur la mesure du rapport isotopique $^{123}Sb/^{121}Sb$ par HG-MC-ICP-MS. La génération d'hydrures a été choisie comme système d'introduction de l'antimoine (par rapport à d'autres systèmes plus classiques de nébulisation liquide) pour 2 raisons principales :
1/ elle est très sensible, l'antimoine étant introduit sous forme gazeuse, le rendement d'ionisation est beaucoup plus élevé que pour les systèmes d'introduction classique avec nébulisation liquide. Une concentration d'antimoine autour de 1 $\mu g.L^{-1}$ et 10 ml d'échantillon suffisent.
2/ L'hydruration étant très sélective (seuls quelques éléments s'hydrurent), de nombreux éléments qui pourraient être présents dans l'échantillon et qui pourraient créer des interférences isobariques ou polyatomiques dans le plasma ne sont pas introduits dans l'ICP-MS multicollecteur.

Le principe de la génération d'hydrure utilisée dans cette thèse est de créer des hydrides volatiles de l'antimoine(III) via l'ajout d'un réducteur (dans notre cas, le tétrahydruroborate de sodium ($NaBH_4$) dans une solution d'hydroxyde de sodium (NaOH)).

L'ensemble des résultats de deux parties de ce chapitre sont présentés sous forme d'un article publié dans *Journal of Analytical Atomic Spectrometry* :
https://doi.org/10.1039/D0JA00452A">10.1039/D0JA00452A.

Résumé en français

Les isotopes de l'antimoine ont été récemment utilisés comme traceurs géochimiques à des fins archéologiques ou environnementales. La purification de l'antimoine dans des échantillons à faible concentration en Sb et à matrice complexe est une étape critique pour mesurer le rapport $^{123}Sb/^{121}Sb$ par génération d'hydrure couplée à un spectromètre de masse à couplage inductif multi-collecteurs (HG-MC-ICP-MS). Une méthode de purification en une seule étape basée sur l'utilisation de poudre de silice mésoporeuse fonctionnalisée avec des groupements thiol (TSP pour « Thiol-Silica Powder ») a été développée pour séparer l'antimoine des autres éléments. Une faible quantité d'antimoine (de 40 à 100 ng) est nécessaire grâce à de faibles blancs de procédure (< 1 ng Sb) et à une élimination efficace (98,7 % en moyenne) des éléments interférents potentiels (y compris As, Cd, Co, Cr, Cu, Fe, Ni, Pb, Se, Sn).

La méthode a été validée sur quatorze Matériaux de Référence Certifiés (CRM) comprenant des matériaux environnementaux (sédiments, poussières de route, sols), des matériaux biologiques (plantes, sang et urine humains), des roches et des matériaux manufacturés (cendres d'incinérateurs, polyéthylène). L'antimoine a été récupéré à 100 ± 7 % et aucun fractionnement isotopique ne s'est produit au cours de la procédure. La composition isotopique de Sb ($\delta^{123}Sb$) dans l'ensemble des CRM variait entre -0,52 ± 0,06 ‰ (2 sd) et 0,40 ± 0,03 ‰ (2 sd) par rapport à une solution étalon isotopique interne (SPEX). La reproductibilité externe a été évaluée à 0, 05 ‰ (2 sd) pour le $\delta^{123}Sb$, sur la base de mesures répliquées de CRM digéré et purifié indépendamment. Les CRM GSD-3, SDO-1 et BCR-176R ont présenté une valeur de $\delta^{123}Sb$ similaire aux mesures précédentes de Rouxel et al. (2003)[1]. De plus, trois solutions étalons pures de Sb ont été mesurées par rapport à la solution étalon isotopique interne. Deux d'entre elles étaient isotopiquement similaires ($\delta^{123}Sb$ = 0,00 ± 0,05‰, Sb Fisher Scientific® et PlasmaCAL-1, SCP Science®) tandis qu'une valeur de $\delta^{123}Sb$ de 0,62 ± 0,02‰ a été mesurée pour la troisième (PlasmaCAL-2, SCP Science®). Cela soulève l'importance de choisir une solution standard isotopique unique et commune pour comparer les données isotopiques de Sb déjà publiées et futures.

A single-step purification method for the precise determination of antimony isotopic composition of environmental, geological and biological samples by HG-MC-ICP-MS

Ferrari Colin,*[a] Resongles Eléonore, [a] Freydier Rémi[a] and Casiot Corinne [a]

Antimony isotopes have been recently used as geochemical tracers for archeological or environmental purposes. The purification of antimony in samples with a low Sb concentration and a complex matrix is a critical step to measure $^{123}Sb/^{121}Sb$ ratio by hydride generation coupled to a multi-collector inductively coupled plasma mass spectrometer (HG-MC-ICP-MS). A single-step purification method based on the use of Thiol-functionalized mesoporous Silica Powder (TSP) was developed to separate antimony from other elements. Low amount of Sb (40-100 ng) is required thanks to low procedural blanks (< 1 ng Sb) and an efficient removal (98.7% on average) of potential interfering elements (including As, Cd, Co, Cr, Cu, Fe, Ni, Pb, Se, Sn). The method was validated on fourteen Certified Reference Materials (CRM) including environmental materials (sediments, road dust, soils), biological materials (plants, human blood and urine), rocks and manufactured materials (fly ash, polyethylene). Antimony was recovered at 100 ± 7% and no isotopic fractionation occurred during the procedure. The isotopic composition of Sb ($\delta^{123}Sb$) in the CRM ranged between -0.52 ± 0.06‰ (2 sd) and 0.40 ± 0.03‰ (2 sd) relative to an in-house isotopic standard solution (SPEX). The external reproducibility was evaluated at 0.05‰ (2 sd) for $\delta^{123}Sb$, based on replicated measurements of independently digested and purified CRM. CRM GSD-3, SDO-1 and BCR-176R exhibited $\delta^{123}Sb$ value similar to previous measurements by Rouxel et al. (2003)[1]. In addition, three pure standard solutions of Sb were measured against the in-house isotopic standard solution. Two of them were isotopically similar ($\delta^{123}Sb$ = 0.00 ± 0.05‰, Sb Fisher Scientific® and PlasmaCAL-1, SCP Science®) while a $\delta^{123}Sb$ value of 0.62 ± 0.02‰ was measured for the third one (PlasmaCAL-2, SCP Science®). This raises the importance of chosing a common isotopic standard solution to compare already published and future Sb isotope data.

1. Introduction

Antimony is a pollutant of emerging concern due to recent increase of anthropogenic emissions from various sources (waste incineration, road traffic, mining and metallurgical activities)[2].

Antimony has two stable isotopes, ^{121}Sb (57.21%) and ^{123}Sb (42.79%)[3]. As for other trace metal contaminants, the isotopic composition of Sb might be used to track the sources of this element and investigate the processes involved in its transport in the environment[4,5]. However, there is still a considerable amount of work before this new tool being validated for a broad range of applications. Pioneer work by Rouxel et al. (2003)[1] showed that natural Sb isotopic variation is wide enough to apply this tool as geochemical tracer. More recently, several studies focused on the application of Sb isotopes in archaeology and attempted to identify the provenance of antimony ores used to manufacture ancient Roman glass and bronze age artefacts and to trace ancient trade routes [6–12]. Resongles et al. (2015)[13] showed that Sb isotopic composition in surface waters contaminated by ancient Sb mines varied over a wide range (-0.06‰ < $\delta^{123}Sb$ < +0.83‰) allowing to determine the contribution of two sub-watersheds to the total dissolved Sb load.

Precise measurement of $^{123}Sb/^{121}Sb$ isotope ratio may be carried out by multi-collector inductively coupled plasma mass spectrometry (MC-ICP-MS) after purification of Sb from the sample matrix and pre-concentration using solid-phase extraction (SPE). Different strategies for Sb purification have been developed depending on antimony concentration in samples and matrix types (Table 1). For solid matrices, a two-step procedure was generally used with either a combination of cation- and anion-exchange resins[6–8,10,14] or a combination of cation-exchange resin and thiol-functionalized cotton fibres[1]. A single-step procedure using thiol-functionalized material (cotton fibres or cellulose powder) was sufficient for the purification of water samples even at low Sb concentration (river water, groundwater)[13,15,16] or for solid samples highly concentrated with Sb (stibnite)[16]. However, we faced major drawbacks using these materials such as extended processing times and clogging due to the low permeability of cotton fibres or cellulose, as well as uncomplete Sb recovery for geologic and

Table 1: Synthesis of existing strategies for Sb purification and Sb isotope analyses by MC-ICP-MS

Sample type (number of samples)	Antimony pre-concentration and purification				Antimony isotope analysis by MC-ICP-MS		Reference
	Sorbent used for Sb purification		Mass of Sb processed (ng)	Purification yield (%)	Sample introduction system	Concentration of the sample introduced in MC-ICP-MS	
	Step 1	Step 2					
Seawater (n=17), geological, environmental and anthropogenic samples (n=14)	Biorad AG50-X8 (cation removal)	Thiol cotton fiber (TCF)	50 – 100	n.s.	Dry plasma (Hydride Generation)	2 - 10 µg L^{-1}	Rouxel et al. (2003)[1]
River water (n=2)	Milled TCF		150 – 350	> 95	Wet plasma	n.s.	Asaoka et al. (2011)[15]
Stibnite (n=2), mine drainage water (n=1)	TCF		150 – 350	> 95	Wet plasma	50 µg L^{-1}	Tanimizu et al. (2011)[16]
Stibnite (n=10), ancient glass (n=69)	Dowex AG50-X8 (cation removal)	Amberlite IRA 743 (removal of S, Al and As)	100000	> 84	Wet plasma (Cyclonic/Scott dual spray chamber)	n.s.	Lobo et al. (2012, 2013, 2014)[6–8], Degryse et al. (2015)[9]
River waters (n=14)	Thiol-cellulose Powder (TCP)		100	96 ± 2	Dry plasma (Hydride Generation)	1 µg L^{-1}	Resongles et al. (2015)[13]
Stream sediment (n=1) and soil (n=1)	AG 1-X4 (Sb pre-concentration)	AG 50W-X8 (cation removal)	> 300	> 94.8	Wet plasma (Cyclonic/Scott dual spray chamber)	200 µg L^{-1}	Liu et al. (2020)[14]
Contaminated river and groundwater samples (n=8)	Thiol-silica		1000 - 2000	> 95.2	Dry plasma (Desolvation system)	75 - 100 µg L^{-1}	Li et al. (2021)[17]

n.s. not specified

environmental samples (unpublished data). Recently, Li et al. (2021)[17] proposed a new single-step purification method based on thiol-functionalized silica. Antimony was successfully purified (Sb recovery of 95.2%) from water samples contaminated by the Xikuangshan antimony mine (China) that presented extremely high Sb concentrations (up to 30 mg L^{-1}).

However, thiol-functionalized silica has never been applied to the separation of Sb from complex solid matrices with low Sb content using a single-step procedure.

Depending on the Sb concentration in purified samples, different sample introduction techniques have been applied for MC-ICP-MS analysis (Table 1). For high Sb concentration (> 50 µg L^{-1}), wet plasma conditions[14–16] or a desolvation system[17] can be used. For low Sb concentrations, Hydride Generation (HG)-MC-ICP-MS is required. This technique, due to its highly efficient sample transport, has the advantage to increase sensitivity and thus decrease the Sb concentration required in analysed samples compared to other introduction systems (wet plasma, desolvation) (Table 1). In addition, even though the purification step remains essential to remove hydride forming elements (e.g. As, Pb, Se, Sn)[18] and transition metals (e.g. Cd, Co, Cr, Cu, Fe, Ni) which may inhibit Sb hydride formation[19–21], hydride generation separates Sb from the matrix; thus, hydride non-forming elements do not reach the plasma, avoiding to create potential non-spectral interferences.

In the present study, we tested Thiol-functionalized mesoporous Silica Powder (TSP) for a single-step purification procedure of Sb in various environmental, geological and biological Certified Reference Materials (CRM) having a large range of Sb concentrations and matrix types. This material, synthesised by the French company Sikémia®, is a mesoporous material; it has a high porosity and is calibrated in size and specific surface area, which is 10^4 times larger than cellulose used in our previous study[13]. Thiol-functionalized silica has a high adsorption capacity for various metals (Pb, Pd, Hg, Cd…)[22–25] including for Sb[17]. TSP can be easily packed in disposable cartridges connected to a peristaltic pump to provide continuous flow processing at a constant rate. The purification procedure adapted from previous studies[1,13,26] was applied on fourteen geological (ore and rocks), environmental (soils, sediments, road dust, fly ash, polyethylene) and biological (plants, human blood and urine) Certified Reference Materials. The reproducibility and efficiency of the purification method were assessed and the Sb isotopic composition of the CRM was determined by HG-MC-ICP-MS.

Table 2: Summary of the digestion procedures used for the different CRM type.

CRM type	CRM name	Amount of CRM digested	Acid mixture
Biological fluids	Clinchek® Urine control level II, Seronorm™ whole blood II	3 mL	Analpure HNO_3 (3 mL)
Low-density polyethylene	ERM-EC680m	50 mg	
Soils	NIST 2711a	150 mg	Analpure HNO_3 (3 mL) + Suprapur® HF (1 mL) + Suprapur® HCl (1 mL)
Plants	NCS-DC-73349, BCR-482	500 mg	
Sediments	NCS-DC-70317, PACS-3, GSD-3	50 mg	
Ore and rocks	GXR-4, SDO-1	50 mg	
Fly ash, road dust	BCR-176R, BCR-723	50 mg	

2. Material and methods

2.1. Chemical reagents and materials

Sample preparation was carried out in a class 10,000 cleanroom facility equipped with a class 100 laminar-flow clean bench. Ultrapure water (Milli-Q®, resistivity > 18.2 MΩ cm, Q-POP Element system, Millipore) was used for all experiments and reagent preparations. All material (e.g. sample bottles, tubes, SPE cartridges, pipette tips…) was soaked in 10% w/w analytical grade HCl for 48 h and rinsed three times with ultrapure water before use. Purification of antimony was carried out using 0.2 g (± 10%) of Thiol-functionalized Silica Powder (hereafter referred to as TSP) filled in 1 mL polypropylene SPE cartridges fitted with polyethylene frits (Supelco®). TSP was purchased from Sikémia® (Montpellier, France) after being prepared on special request from commercial silica powder (Geduran® Si 60, Merck, grain size 40-63 µm). Brunauer–Emmett–Teller (BET) analysis made by Sikémia® showed that TSP has a specific surface of 416 $m^2\ g^{-1}$ versus 0.04 $m^2\ g^{-1}$ for the thiol cellulose powder used previously[13]. The functionalisation rate was roughly estimated by Sikémia at one thiol function per nm^2 based on thermogravimetric analysis and assuming that the weight loss is due to grafted silanes. Both the grain size and specific surface area are similar with the thiol-functionalized silica used by Li and al. (2021)[17].

Suprapur® ≥ 30% w/w HCl (Merck), Analpure 65 – 69 % w/w HNO_3 (Analityka®), and Suprapur® ≥ 40% w/w HF (Merck®) were used for sample digestion, sample preparation, and analysis. A reducing solution was prepared daily by dissolving analytical grade ascorbic acid (Sigma-Aldrich®) and Suprapur potassium iodide (Merck®) at 10% w/v each in ultrapure water. A solution of sodium borohydride (1% w/v) stabilised with 0.05% w/v sodium hydroxide (both 99.99% trace metal basis, Sigma-Aldrich) was prepared daily by dissolving the appropriate amount of compounds in ultrapure water and filtrated. The pure Sb standard solution used as in-house isotopic standard was purchased from SPEX CertiPrep (Sb 1000 µg mL^{-1} in 20% w/w HCl, batch number 24-175SBX, hereafter named "SPEX"). This solution was preferred to previously used PlasmaCAL-1 (SCP Science®)[13], chosen for its appropriate matrix for hydride generation (20% w/w HCl) and its promiscuity with the isotopic standard used in Resongles et al. (2015)[13] ($\delta^{123}Sb$ = 0.04 ± 0.08‰, 2 sd, n=6). Three other pure Sb standard solutions were measured for their isotopic ratio and named "*Fisher*" (Sb 1001.2 µg mL^{-1} in 20% w/w HCl, lot number 682785, Fisher Scientific®), "*PlasmaCAL-1*" and "*PlasmaCAL-2*" (PlasmaCAL ICP/ICPMS Standard-Antimony 1000 µg mL^{-1} in 4% w/w HNO_3, lot number SC0108283 and S170206013, respectively, SCP Science®).

2.2. Certified Reference Materials

A series of fourteen Certified Reference Materials (CRM) was used to evaluate the quality of the Sb purification procedure for different types of environmental, geological, and biological materials of interest in environmental studies. Environmental CRM consisted of plants (*NCS-DC-73349, BCR-482*), soils (*NIST SRM 2711a*), river water (*NIST 1643f*), stream sediments (*NCS-DC-70317, GSD-3*), marine sediment (*PACS-3*) and anthropogenic materials including incinerator fly ash (*BCR-176R*), road dust (*BCR-723*), low-density polyethylene (*ERM-EC680m*). The geological CRM were composed of copper mill-head (*GXR-4*) and shale (*SDO-1*). Finally, biological fluids include human urine (*Clincheck® Urine control level II*) and human blood (*Seronorm™ whole blood II*).

NIST 2711a and NIST 1643f were bought from the National Institute of Standards and Technologies (NIST®, USA); BCR-176R, BCR-482, BCR-723 and ERM-EC680m were obtained from the European Institute for Reference Material and Measurements (IRMM, Belgium); NCS-DC-73349 and NCS-DC-70317 were bought to the NCS Testing Technologies Company (China); PACS-3 was purchased from the National Research Council of Canada (NRCC, Canada). Clincheck® Urine control level II was bought to Recipe company (Germany); Seronorm™ whole blood II was obtained from SERO AS (Norway). SDO-1, GXR-4 (USGS, USA) and GSD-3 (alias GBW07303, IGGE, China) are no longer marketed; they were kindly provided by the CRPG (Nancy, France).

2.3. Sample digestion

All CRM were digested using microwave-assisted acid digestion (UltraWAVE, Milestone®) and with different acid mixtures depending on their nature (Table 2). Three millilitres of urine (Clincheck® Urine control level II) and blood (Seronorm™ whole blood II), and 0.05 g of polyethylene (*ERM-EC 680m*) were weighed in PTFE microwave tubes and digested with 3 mL of concentrated HNO_3. Fifty milligrams of sediments (*NCS-DC-70317, PACS-3,* and *GSD-3*), rocks (*GXR-4, SDO-1*), fly ash (BCR-176R) and road dust (BCR-723), 150 mg of soil (*NIST 2711a*) and 500 mg of plants (*NCS-DC-73349*, *BCR-482*) were weighed in PTFE microwave tubes and digested with 3 mL of concentrated HNO_3, 1 mL of concentrated HF and 1 mL of concentrated HCl. Triplicates were made for *GXR-4*, *GSD-3, BCR-723,* and *BCR-482* to evaluate the reproducibility of the digestion method. Digestion blanks for both digestion procedures were performed as well.

The samples were heated from ambient temperature to 200 °C in 25 min and maintained at 200 °C for 10 min. Once the samples had cooled, they were transferred in 30 mL PTFE vials. Next, all samples were evaporated at 75 °C maximum to prevent antimony volatilisation due to high temperature[15]. Finally, the dry residue was re-dissolved in 5 mL of 1.5 M HNO_3, vials were placed in an ultrasound bath for one hour and then heated hermetically closed at 80 °C for one night.

Only *BCR-723* (road dust) showed dark particles in the final digest solution probably consisting of black carbon. These solutions were filtrated with 0.22 µm PVDF filters previously rinsed with 1.5 M HNO_3. A filtration blank (1.5 M HNO_3) was performed and showed that no significant amount of Sb was released from the filter.

2.4. Antimony purification

The procedure for antimony purification was adapted from Resongles et al. (2015)[13]. An aliquot of the digest solutions containing 120 ng of Sb, when possible, was evaporated at 75 °C in PTFE vials. Residues were dissolved in 10 mL of 0.5 M HCl, an aliquot of the solution was kept to check Sb concentration.

Water sample (NIST 1643f) did not undergo through the digestion process, it was directly acidified to 0.5 M HCl. Sb(V) was reduced into Sb(III) by adding 10% w/v of KI-ascorbic acid (KI/AA) solution to obtain a final concentration of 0.5% w/v and allowing a 3 h reduction time[15]. The elution scheme is summarised in Table 3. The TSP cartridges (0.2 g or 0.7 mL TSP) were set on a Gilson® peristaltic pump with 1.02 mm i.d. Tygon® tubing allowing to run six samples simultaneously (Figure S1). The pump speed was set at 8 rpm, corresponding to a flow rate of 1.0 mL min^{-1}. First, the system was cleaned by delivering successively 10 mL of ultrapure water, 5 mL of 6 M HCl and 10 mL of ultrapure water. TSP was then conditioned with 10 mL of 0.5 M HCl. Next, the samples were loaded in 0.5 M HCl, 0.5% w/v KI/AA. One hundred ng of Sb were loaded except for *Seronorm™ Whole Blood level II* (80 ng), and *NCS-DC-73349* (37 ng). Antimony was adsorbed on the TSP while major elements and metals passed through with no interaction or weaker interaction. Next, TSP was washed successively with 5 mL of 0.5 M HCl and 6 mL of 2.5 M HCl to desorb all the elements which are weakly retained. Finally, Sb was eluted with 6 mL of 6 M HCl. Purified solution was collected and stored at 4 °C until Sb concentration determination, isotopic analyses and interferent concentration measurements.

Five procedural blanks were performed to ensure that no Sb contamination occurred at each step: three blanks underwent the purification step only; two other blanks underwent both the digestion and the purification steps. The peristaltic pump tubing used for the purification procedure was changed every five sets of six purified samples to prevent any Sb contamination which could occur due to tubing degradation.

Table 3: Elution scheme for purification of Sb using Thiol-functionalized Silica Powder.

	Step	Volume (mL)	Eluent
1	Cleaning	10	Ultrapure water
	Cleaning	5	6 M HCl
	Cleaning	10	Ultrapure water
2	Conditioning	10	0.5 M HCl
3	Sample loading	10	0.5 M HCl, 0.5% w/v KI-AA
4	Washing	5	0.5 M HCl
5	Washing	6	2.5 M HCl
6	Sb elution (collection of purified sample)	6	6 M HCl

2.5. Analysis

All the analyses (ICP-MS, HG-ICP-MS and HG-MC-ICP-MS) were performed on the AETE-ISO Platform (OSU OREME, Université de Montpellier).

Antimony and trace element concentration measurement by ICP-MS: ICP-MS iCAP TQ (ThermoScientific®) was used to measure the concentration of antimony and other elements (As, Cd, Co, Cr, Cu, Fe, Ni, Pb, Se, Sn, Zn) in the digest solutions of CRM. Concentrations of residual elements in Sb purified samples were also determined after evaporating an aliquot (one mL at 75 °C) and residue dissolution in 5 mL of 1.5 M HNO_3. Instrument settings are presented in Supplementary Information (Table S1). A collision cell, using He as collision gas, and the KED Mode (Kinetic Energy Discrimination) were used to eliminate polyatomic interferences created in the plasma. Isobaric interferences between two different elements were corrected using mathematical equations based on natural abundance ratios of the interfering elements (routine corrections preset in the instrument software). Element concentrations were determined using an external calibration curve analysed every 20-30 samples. A solution, containing Be, Sc, Ge, Rh and Ir was added on-line to the samples to correct changes in sensitivity (internal standard correction) due to matrix effect and instrument drift. Samples were diluted in 0.15 M HNO_3 and SLRS-6 certified material was systematically analysed to check the accuracy of the measurement. Typically, the SLRS-6 was measured at 0.331 ± 0.004 µg L^{-1} of Sb (n=6, RSD = 1.2%) within 2% of the certified Sb value (average accuracy better than 6% for the other elements).

Antimony concentration measurement by HG-ICP-MS: Hydride generation (MP2 hydride ICP, Elemental Scientific®) coupled with ICP-MS iCAP Q (ThermoScientific®) was used to determine the recovery rate of antimony after the purification step[13]. Antimony (^{121}Sb) was measured in the unpurified samples and in purified samples after an adequate dilution in 3 M HCl with 0.5% w/v of KI/AA at least three hours before analysis. Complete instrument settings for HG-ICP-MS are summarised in Supplementary Information (Table S1). An external calibration curve was analysed and internal standard correction (^{128}Te) was applied to correct sensitivity drifts. Average detection limit for Sb was 0.008 ± 0.001 µg L^{-1}. Accuracy was assessed by analysing two certified reference freshwaters. Antimony concentration was on average within 1.5% of the certified value for NIST 1643f (55.7 ± 1.8 µg L^{-1}, n=3) and within 5.8% of the certified value for SLRS-6 (0.319 ± 0.005 µg L^{-1}, n=3).

Antimony recovery (in %) after the purification step was calculated according to equation 1.

$$Sb_{recovery} = \frac{(m_F)}{(m_I)} \cdot 100 \qquad \text{Eq. 1}$$

with m_I the mass of Sb in unpurified sample loaded on the TSP cartridge and m_F the mass of Sb recovered in the purified sample (in ng). m_I and m_F were calculated using Sb concentrations measured by HG-ICP-MS. We estimated the uncertainty associated with the calculation of the purification recovery rate at ± 7% (relative standard deviation) using the uncertainty of HG-ICP-MS measurement and conventional error propagation equations[27]. In addition, the external reproducibility of the purification step, evaluated on four different CRM (n=3), was better than 5%.

Antimony isotope ratio measurement by HG-MC-ICP-MS: Antimony stable isotope measurements were performed with a MC-ICP-MS (Neptune Plus, ThermoScientific®) coupled with a hydride generation system (MP2 hydrideICP, Elemental Scientific®) introducing the sample at 475 µL min^{-1}. All instrumental settings are summarised in Table 4. Hydrides are formed by reacting the sample (1 µg L^{-1} of Sb in 3 M HCl and 0.5% w/v of KI/AA) with sodium borohydride (1% w/v $NaBH_4$, 0.05% w/v NaOH). A Quartz Stable Sample Introduction Cyclonic/Scott dual spray chamber (Elemental Scientific®) was used to stabilise the signal.

Every measurement was composed of one block of 80 cycles of 4.194 seconds. The 1 µg L^{-1} Sb concentration resulted in a signal of 1.8-2 V for the ^{121}Sb isotope (with a background noise under 2%). ^{126}Te has been measured to correct ^{123}Te isobaric interferences on the ^{123}Sb. However, the average signal intensity on the ^{126}Te (0.01 to 0.1 mV) did not made necessary the correction on the ^{123}Sb intensity (difference of 7.10^{-5}‰ on the final $^{123}Sb/^{121}Sb$ ratio).

SnH and SbH_2 interferences for ^{121}Sb (^{120}SnH) and ^{123}Sb (^{122}SnH, $^{121}SbH_2$) was not significant. Indeed, literature showed that the formation of ^{120}SnH is negligible (less than 0.1% of the ^{121}Sb signal intensity)[1]. The intensity for ^{120}Sn (isotope abundance of 32.6%) remained constant for all the samples and did not exceed 100 mV. In addition, no increase in ^{122}Sn intensity in SPEX solution with 1 µg L^{-1} Sb was observed compared to blank solutions showing that formation of ^{121}SbH was not detectable. Thus, no corrections were made on ^{121}Sb and ^{123}Sb from the ^{120}SnH, ^{122}SnH and $^{121}SbH_2$ interferences .

A conventional external correction with the sample-standard bracketing approach was used to correct the mass bias[28]. An in-house isotopic Sb standard solution (SPEX) was analysed before and after every sample as no certified isotopic standard exists for antimony yet. The isotopic composition of Sb was expressed as $\delta^{123}Sb$ (Equation 2) which represents the deviation between the isotope ratio measured for the sample $\left(\frac{^{123}Sb}{^{121}Sb}\right)_{sample}$ and the mean isotope ratio of the in-house isotopic standard (SPEX) measured before and after the sample $\left(\frac{^{123}Sb}{^{121}Sb}\right)_{mean\ std}$. Each $\delta^{123}Sb$ result is the average value for three different isotopic measurements (n=3), if not specified otherwise.

$$\delta^{123}Sb(‰) = \left(\frac{\left(\frac{^{123}Sb}{^{121}Sb}\right)_{sample} - \left(\frac{^{123}Sb}{^{121}Sb}\right)_{mean\ std}}{\left(\frac{^{123}Sb}{^{121}Sb}\right)_{mean\ std}}\right) \times 1000 \qquad \text{Eq 2.}$$

Table 4: Instrument parameter settings used for Sb isotope analysis by HG-MC-ICP-MS.

Hydride Generation Parameters	
System	MP2 HydrideICP - Elemental Scientific
Peristaltic Pump Speed	25 rpm
Reducing agent medium	$NaBH_4$ 1% w/v in NaOH 0.05% w/v
Acid medium	HCl 3M
Flow rate (mL min^{-1}); tubing colour code – Internal Diameter ID (mm)	
Waste	1.28; Yellow/Blue - 1.52 ID
Sample	0.48; Black/Black - 0.76 ID
$NaBH_4$ =	0.24; Orange/Yellow - 0.51 ID
HCl	0.12; Orange/Green - 0.38 ID
Gas flow (Ar) (L min^{-1})	
Sample gas	0.31
Additional Gas	0.45
Instrument Settings	
Instrument	Neptune Plus - Thermo Scientific
Forward power	1275 W
Skimmer Cone	X version
Sample Cone	Jet version
Measured isotopes	^{120}Sn, ^{121}Sb, ^{122}Sn, ^{123}Sb (^{123}Te), ^{126}Te
Cups	L1, C, H1, H2, H3
Sensitivity ^{121}Sb (V/ppb)	1.8 – 2
Resolution	Low resolution (M/ΔM = 400)
Acquisition Parameters	
Uptake time (s)	140
Number of block	1
Number of cycles per block	80
Integration Time (s)	4.194

3. Results and discussion

3.1. Efficiency of the purification method

Sb recovery after CRM digestion: For most certified materials, Sb extraction yield after digestion was within 100 ± 10% (Table 5). Only the low-density polyethylene (*ERM-EC680m*) showed a relatively low antimony extraction yield (83%) despite the complete dissolution of PET pellets. This might be due to Sb content heterogeneity between pellets (only two pellets digested). GSD-3 showed an extraction yield between 113 and 147% (n=3), based on different indicative data[29–31]. Considering the uncertainty associated with these indicative concentrations and the age of this certified material, it was decided to pursue the purification step with GSD-3 despite this inconsistency.

Antimony recovery after the purification step: Blank samples that have undergone both digestion and TSP purification contained less than 1 ng of Sb (Sb was lower than detection limit in blanks) which accounted for a maximum of 0.3 to 2% of the amount of Sb in processed samples (37-100 ng of Sb). For most CRM, the recovery rate was within 100 ± 7% (Table 5). These recovery values are similar to the ones found in the recent literature (Table 1) that used a two-step procedure with anion- and cation-exchange resins combining either AG 1-X4 and AG 50W-X8 (recovery of Sb > 98% for Liu et al. 2020[14]) or Dowex AG50-X8 and Amberlite IRA 743 resin (recovery > 94% for Lobo et al. 2014[8]). For the CRM *NCS-DC-73349* and *GXR-4*, the recovery rates were 79%, and 84 ± 3%, respectively. These lower recovery rates could be related to the high ionic strength in the sample solution loaded on the TSP cartridge; indeed these two CRM exhibited the highest matrix:Sb concentration ratio considering the sum of all measured elements by ICP-MS. Investigation of the nature of interactions between matrix elements, antimony and thiol moieties would require further research. We recommend to systematically check Sb recovery rate and concentrations of potential interfering elements in the purified samples before performing Sb isotope measurement on a particular new type of material. Indeed, peculiar sample matrix may lead to unexpected incomplete recovery; in particular, Fe-rich sample (Fe:Sb > 50000) may still need a pre-treatment as observed by Rouxel et al. 2003[1]. Nevertheless, the isotopic composition for these CRM is further presented as indicative values to be confirmed in future works.

Elimination of potential interfering elements: Two main groups of elements may interfere with antimony hydride formation. On one hand, transient metals such as Cd, Cr, Cu Fe, Ni can produce a matrix effect during hydride generation[19]. The matrix effect mainly originates from the precipitation of metal borides which affects the release efficiency of hydrides and decomposition of the reducing agent. Besides, iron can decrease the efficiency of Sb hydride formation by oxidizing Sb(III) into Sb(V), which prevents further hydride formation (since Sb(V) forms hydrides more slowly than Sb(III))[32]. On the other hand, hydride-forming elements including As, Pb, Se, Sn, Ge, Bi and Te may compete with Sb for its reduction[19] with $NaBH_4$ but also may cause matrix effect during the analysis by MC-ICP-MS. Selenium may also induce Sb signal suppression prior to hydride formation by precipitating Sb in the form of Sb_3Se_3[19]. Finally, non-hydride forming elements can interfere with Sb isotopes measurement by MC-ICP-MS by being transported to the plasma as fine aerosols[21] with the excess of H_2 gas[33].

Average removal rates for interfering elements in all CRM were ≥ 97% (Table 6). The concentrations of these elements in the purified samples analysed by HG-MC-ICP-MS were systematically lower than the Sb concentration (metal:Sb ratios < 1, Table 6), except for iron and copper. For iron, there is a body of evidence which suggests that no interference can occur from Fe in the purified CRM: 1) Sb signal suppression related to the oxidation of Sb(III) into Sb(V) by Fe(III) was only evidenced at

Table 5: Extraction yield and purification recovery for the certified reference materials.

	Digestion				Purification	
CRM	**Measured concentration (µg g^{-1})**	**Certified value (µg g^{-1})**	**Sb extraction yield (%)**	**n**	**Sb purification recovery (%)**	**n**
SDO-1	4.58	4.45 ± 0.35	102.9	1	98	1
GXR-4	4.50 ± 0.01	4.4 ± 0.8	102.8 ± 0.8	3	84 ± 3	3
ERM-EC680m	8.0	9.6 ± 0.7	83.3	1	103	1
BCR 176R	836	850 ± 50	98.3	1	94	1
BCR 723	26.4 ± 0.3	28.2 ± 2.3[a]	93.6 ± 0.9	3	97 ± 3	3
NIST 2711a	25.3	23.8 ± 1.4	107.3	1	97 ± 2	3
NCS-DC-70317	4.82	4.44 ± 0.44	108.5	1	89	1
GSD-3	7.4	5.02 ± 0.12[b], 5.4[c], 6.52[d]	147.4 [b], 137.0 [c], 113.5 [d]	1	97	1
PACS-3	14.1	14.6 ± 2.4	96.6	1	98	1
NCS-DC-73349	0.106	0.095 ± 0.027	112.0	1	79	1
BCR 482	0.35 ± 0.01	0.35[a]	99 ± 3	3	95 ± 4	3
Whole blood trace elements II	0.026*	0.026 ± 0.005*	99.0	1	99	1
Urines Control Clincheck® level II	0.051*	0.0475 ± 0.0095*	107.1	1	99	1

[a,b]Indicative values : [a]Institute for Reference Materials and Measurements ; [b]Hall and Pelchat (1997)[30], [c]Govindaraju (1994)[29], [d]Fadda et al. (1995)[31] ; *µg mL^{-1}.

Fe(III):Sb mass ratio greater than 22[32] whereas the highest Fe:Sb value in our purified CRM was 13.4 (Table 6), 2) precipitation of iron borides was evidenced only for high Fe:Sb ratios, in the range 1000 to 10,000 (50 to 100 mg L^{-1} of Fe)[30,34,35] and 3) the amount of Fe transported to the plasma during the hydride generation process was estimated to be less than 0.001%[33], and thus would be negligible considering the measured residual Fe concentrations in purified samples.

Cu:Sb ratio was lower than 1 in all the samples, except for GXR-4 (Cu:Sb = 4.7, Table 6), and Seronorm™ Whole blood level II in a lesser extent (Cu:Sb = 2.3, Table S2). GXR-4 has a high copper concentration (6500 µg g^{-1}) and despite a good abatement rate (> 99.7%), the residual concentration of Cu in the purified sample analysed by HG-MC-ICP-MS was 4.7 µg L^{-1}. However, potential interference from Cu might be masked by precipitation of CuI when using potassium iodide as reductant for hydride generation[36]. Furthermore, Cu transportation in the gas phase to the plasma with hydride generation in 3 M HCl was reported to be 0.38% of Cu present in solution[21]. Thus, interference from Cu in GXR-4 and Seronorm™ Whole Blood Level II might be negligible.

However, no investigation of Fe and Cu effects at these concentrations and configurations for Sb hydride generation was reported in the literature, so further tests have been carried out to ensure that these residual concentrations of Fe and Cu did not have an impact on the formation of Sb hydrides and isotopic measurement. Antimony standard solution at 1 µg L^{-1} (in-house isotope standard SPEX) was spiked with 50 µg L^{-1} of Fe, or Cu and measured by HG-MC-ICP-MS. Results showed that there was no influence of Fe or Cu for metal:Sb mass ratios of 50 on Sb isotope measurement ($\delta^{123}Sb_{Fe}$ = 0.02 ± 0.07, 2 sd, $\delta^{123}Sb_{Cu}$ = -0.02 ± 0.02, 2 sd) compared with a pure SPEX solution. ^{121}Sb intensities were also not influenced by the presence of these elements. This demonstrates that Fe

Table 6: Average removal rates obtained from all CRM for the potential interfering elements and the highest element:Sb ratios measured for each element in purified samples. The uncertainties were calculated as the standard deviation obtained from all CRM for each element. Residual element:Sb ratios for individual CRM are given in Supplementary Information, Table S2.

	Element	**Percentage removed (%)**	**Highest Element:Sb ratio in purified samples**
Transition metals	**Cd**	99.7 ± 0.5	0.00
	Co	98 ± 3	0.1
	Cr	97 ± 3	0.9
	Cu	99 ± 1	4.7
	Fe	99.9 ± 0.2	13.4
	Ni	97 ± 4	0.3
Hydride-forming elements	**As**	99.8 ± 0.3	0.03
	Pb	100.0 ± 0.1	0.2
	Se	> 89	< 0.1
	Sn	97 ± 3	0.05

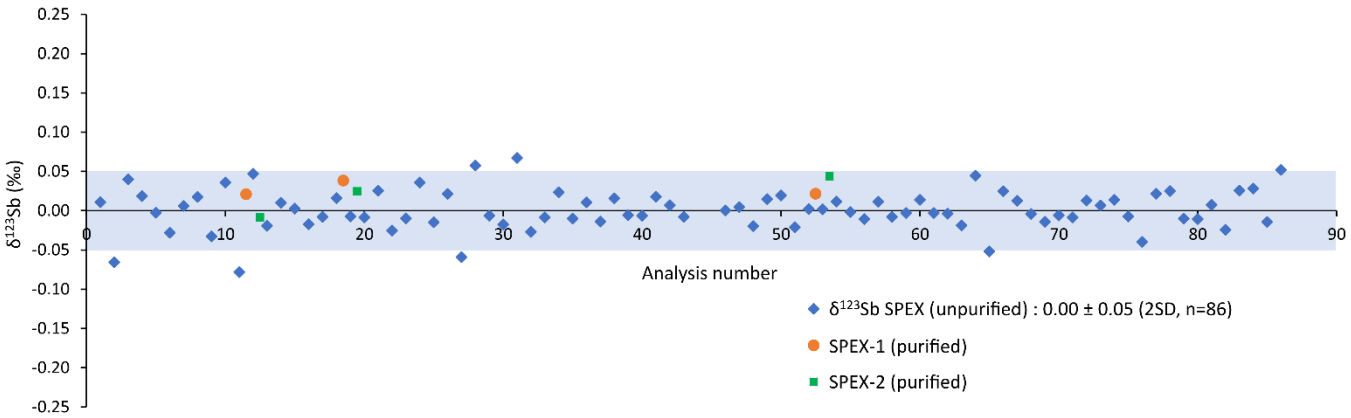

Figure 1: δ^{123}Sb values for purified and unprocessed in-house SPEX isotopic standard analysed over a 3-day analytical session.

and Cu do not interfere at any step of the HG-MC-ICP-MS analysis of Sb (i.e. reduction, hydride formation, ionisation, extraction and focusing steps) for metal:Sb mass ratio lower than 50.

3.2. Precision and statistical data treatment of Sb isotope measurement

Sb signal intensity (^{121}Sb and ^{123}Sb) measured in blanks (3 M HCl, 0.5% v/v KI/AA) did not exceed 2% of the Sb signal intensity in standards and samples, resulting in an average difference of 0.01‰ for δ^{123}Sb. No correction was therefore made to account for the blank contribution.

The long-term external precision obtained for the repeated measurement of purified and unpurified Sb SPEX solution corrected with the sample-standard bracketing method is presented in Figure 1. The precision was 0.05‰ (2 sd) for the unprocessed in-house isotopic standard SPEX measured over 3 days. The drift over time of the ^{123}Sb/^{121}Sb ratio (data not shown) did not have an impact on the δ^{123}Sb of the in-house isotopic standard SPEX (Figure 1).

Despite the relatively stable ^{121}Sb signal (standard deviation < 0.1 V (RSD < 5%)), short-term instabilities randomly occurred (up to an increase of 20% of ^{121}Sb and ^{123}Sb signal over less than 30 seconds). These short-term instabilities caused a simultaneous drop in the ^{123}Sb/^{121}Sb ratio (up to 0.1%) and affected the internal standard error on ^{123}Sb/^{121}Sb ratio (10 to 25 ppm). Such instabilities were also observed in other studies[37], and are probably due to an over pressure in the hydride generation system. Two methods for excluding outliers values from the eighty cycle values of ^{123}Sb/^{121}Sb ratio were compared to limit the impact of the short-term instabilities and determine how heavily it impacts the final δ^{123}Sb value (Figure S2). The first treatment (method A) is routinely used (preset in the instrument software) and consists in excluding values of ^{123}Sb/^{121}Sb ratio overpassing two standard deviations from the calculation of ^{123}Sb/^{121}Sb ratio average (i.e. excluding ratios outside the confidence interval of 95%). The second method (method B) consists in excluding the values of ^{123}Sb/^{121}Sb ratios measured during the short-term instability period based on the variation in ^{121}Sb intensity (i.e. cycles with ^{121}Sb intensity exceeding 5% of the average signal intensity are excluded, with two cycles before and after the disruption) (Figure S2). The method A did not efficiently remove outlier values of ^{123}Sb/^{121}Sb ratio; only four impacted cycles over the ten visually identified were removed (Figure S2). On the other hand, method B removed efficiently all the impacted cycles. δ^{123}Sb values for the

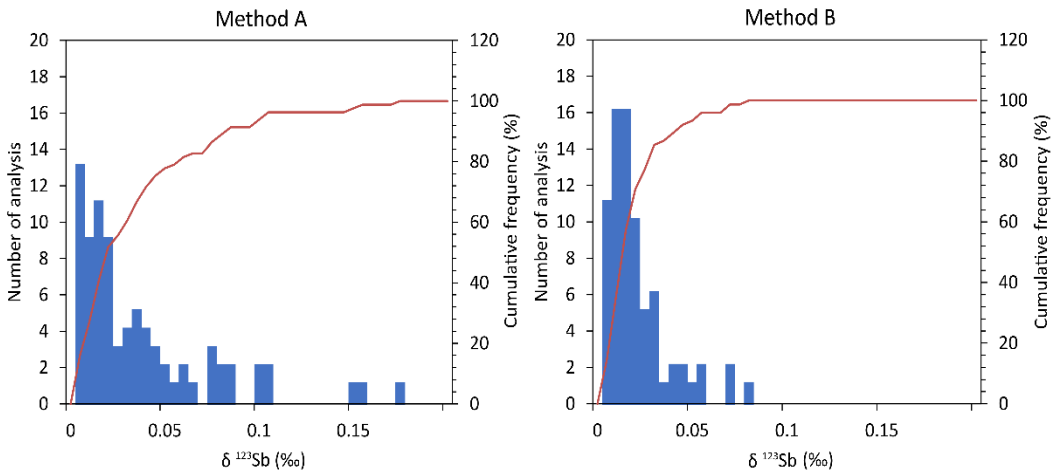

Figure 2: Comparison of the δ^{123} Sb values (‰) for the in-house isotopic standard SPEX after ^{123}Sb/^{121}Sb outliers exclusion using methods A and B.

in-house isotopic standard SPEX were more gathered around 0 using method B (85% of the δ^{123}Sb values exceeded 0.03‰) than method A (85% of the δ^{123}Sb values are below or equal to 0.07‰) (Figure 2). Average values of δ^{123}Sb calculated for CRM with both methods were not significantly different but the precision is improved with method B (Table S3). Therefore, method B was selected to further process isotope data.

Two aliquots of the in-house isotopic standard SPEX (named SPEX-1 and SPEX-2) were processed using the purification procedure and analysed by HG-MC-ICP-MS to ensure that the protocol did not cause isotope fractionation. For SPEX-2, the first millilitre of the Sb elution step was collected independently to check whether Sb isotopes were fractionated due to incomplete Sb elution from TSP. δ^{123}Sb measured for the two aliquots of the purified in-house isotopic standard SPEX (SPEX-1 and SPEX-2, Figure 1) did not show a significant difference with the unpurified SPEX. Results of the purified SPEX-1 (purification recovery of 94%) showed that no fractionation occurred during the purification (δ^{123}Sb = 0.03 ± 0.02‰, 2 sd, n=3). For SPEX-2, 92% of the total Sb was recovered, δ^{123}Sb was identical to unpurified in-house isotopic standard SPEX (δ^{123}Sb = 0.02 ± 0.05‰, 2 sd, n=3). Thus, partial Sb elution did not induce fractionation of Sb isotopes. A reduction of the volume of Sb elution from 6 mL to 1 mL in the purification procedure could be considered in future work.

3.3. Sb isotopic composition in pure Sb standard solutions

The isotopic composition of PlasmaCAL-1 and Fisher pure Sb standard solutions were similar to the in-house isotopic standard SPEX, with δ^{123}Sb values of 0.04 ± 0.08‰ (n=6) and 0.01 ± 0.04‰ (n=3), respectively (Figure 3). Only PlasmaCAL-2 showed a contrasted isotopic composition (δ^{123}Sb = 0.62 ± 0.02‰ (n=4)). All these standards were prepared from antimony(III) oxide. The similarities between in-house isotopic standards SPEX, Fisher, and PlasmaCAL-1 could indicate a common source of supply of antimony(III) oxide. Conversely, a different source or a different standard preparation procedure might explain different δ^{123}Sb signature observed for PlasmaCAL-2. This point deserves further research.

3.4. Sb isotopes in certified reference materials (CRM)

Isotopic composition of Sb in studied CRM are presented in Figure 3 and in Supplementary Information (Table S4). δ^{123}Sb values ranged between -0.52 ± 0.06‰ and 0.40 ± 0.03‰ (Figure 3). However, most of the CRM had a δ^{123}Sb value within a narrower range, between -0.20 and 0.20‰. A few CRM had a slightly negative δ^{123}Sb value including *BCR-176R* (-0.03 ± 0.03‰, 2 sd), *NCS-DC-70317* (-0.11 ± 0.03‰, 2 sd) and *NIST 1643f* (-0.08 ± 0.09‰, 2 sd). The slightly positive δ^{123}Sb values were: *BCR-482* (0.05 ± 0.05‰, 2 sd, n=3), *Clincheck® Urines level II* (0.17 ± 0.04‰, 2 sd), *Seronorm™ whole blood level II* (0.09 ± 0.02‰, 2 sd), *GSD-3* (0.15 ± 0.05‰, 2 sd), *PACS-3* (0.16 ± 0.02‰, 2 sd), *NIST 2711a* (0.06 ± 0.02‰, 2 sd) and *BCR-723* (0.03 ± 0.05 ‰, 2 sd). The greatest deviations from these narrow range of δ^{123}Sb values were observed for *ERM-EC680m* (0.40 ± 0.03‰, 2 sd), *GXR-4* (0.35 ± 0.04‰, 2 sd, n=3), *SDO-1* (0.22 ± 0.03‰, 2 sd) and *NCS-DC-73349* (-0.52 ± 0.04‰, 2 sd).

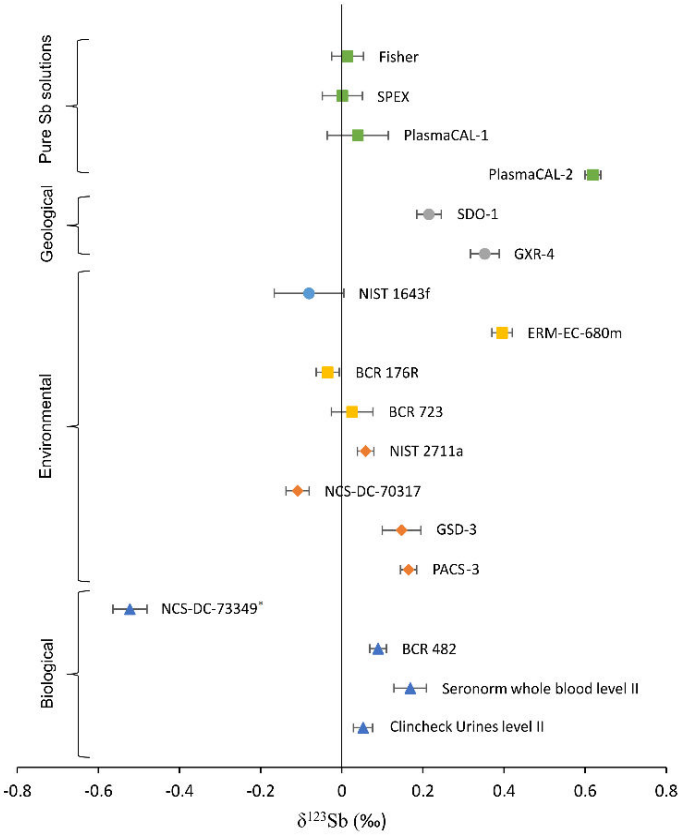

Figure 3: δ^{123}Sb in studied biological, environmental, and geological CRM (‰). *Indicative value, to be confirmed in future works.

Some of the CRM (*NIST 1643f*, *ERM-EC680m*, *Seronorm™ Whole blood level II*, *Clincheck® Urines level II*) were artificially enriched with Sb while others (*SDO-1*, *GRX-4*, *BCR 176R*, *BCR 723*, *NIST 2711a*, *NCS-DC-70317*, *GSD-3*, *PACS-3*, *NCS-DC-73349*, *BCR-482*) originally contained Sb. Among the first group, all these standards exhibited different δ^{123}Sb values. This could be explained by Sb enrichment from different sources. *Clincheck® urine control level II* was enriched with Sb using Sb standard prepared from $SbCl_3$. Conversely, *ERM-EC680m* was artificially enriched using the Sb pigment Sb_2O_3, it exhibited a different δ^{123}Sb signature. *NIST 1643f* was enriched using antimony(III) trinitrate and also exhibited a different δ^{123}Sb signature.

The other CRM had a natural Sb content; they are likely more representative of the δ^{123}Sb isotopic range which could be found in the environment. Among these CRM, Tibet sediments (*NCS-DC-70317*) had a distinct δ^{123}Sb compared to the other river and marine sediments (*GSD-3* and *PACS-3*). Such difference might reflect different geographic provenance (Tibet for *NCS-DC-70317*, mixture of several Chinese river sediments for *GSD-3*, marine sediments from Esquimalt harbour, British Columbia for *PACS-3*). *NCS-DC-73349* and *BCR-482*, both vegetal samples have a highly different δ^{123}Sb signature. *NCS-DC-73349* was branches and leaves of bushes from China while *BCR-482* was lichen collected from pines in Switzerland. Geographic location and vegetal species have probably influenced δ^{123}Sb

signature. However, many processes may have left their own δ^{123}Sb imprint and the origin of different isotopic signatures deserves further research. The external reproducibility of the whole procedure (i.e. including the digestion and purification steps) was assessed for two CRM (*GXR-4* and *BCR-482*). Three independent digested solutions were purified and analysed for Sb isotope ratio. The errors associated to δ^{123}Sb values were comparable to the other CRM (δ^{123}Sb = 0.05 ± 0.05‰ for *BCR-482*, and δ^{123}Sb = 0.35 ± 0.04‰ for *GXR-4*), which demonstrated the good external reproducibility of the method.

Four CRM (*GXR-4*, *GSD-3*, *BCR-176R* and *SDO-1*) had been previously analysed by Rouxel et al. (2003)[1]. Compared to previous δ^{123}Sb data obtained by these authors, we found a δ^{123}Sb difference of -0.13‰ for *GXR-4*, -0.02‰ for *GSD-3*, -0.06‰ for *BCR-176R* and -0.01‰ for *SDO-1*. These differences were not significant for *GSD-3*, *SDO-1* and *BCR-176R*. This suggests that the in-house isotopic standard used by Rouxel et al. (2003)[1] had a similar isotopic composition than the Sb SPEX solution used in this study. However, a slight difference was observed for *GXR-4*, which could be explained by a significant heterogeneity between the bottles of *GXR-4*, as reported by Kane et al. (1992)[38] or uncomplete Sb recovery (Table 5). Overall, the δ^{123}Sb variation range in geological and environmental CRM reported in Rouxel et al. (2003)[1] (from -0.05 ± 0.04‰ to 0.48 ± 0.03‰, 2 sd) is similar to the ones measured in this paper for additional environmental and biological CRM.

4. Conclusions

A single-step purification method for antimony was developed to analyse isotopic composition by HG-MC-ICP-MS in samples with low Sb concentration and complex solide matrices. The purification method has been tested and validated over a wide range of CRM with various matrices (geological, environmental, and biological). The good recovery rates (100 ± 7%) for Sb and abatement rates for interfering elements (Fe > 99%, Ti > 99%, Cu > 99%, Cr > 97%, Ni > 97%, Cd > 99%, As > 99%, Sn > 96%) allowed the precise measurement of Sb isotope ratio. This validates the efficiency of the TSP protocol to isolate Sb from complex and diverse matrices, to be analysed by HG-MC-ICP-MS without a pre-treatment step to eliminate metals as previously reported[1,14], with a maximal Fe:Sb initial mass ratio of 50,000. Due to its high affinity with Sb and its high specific surface area with an important thiol density per nm², TSP is efficient to purify antimony in samples containing from 0.026 µg mL^{-1} (*Seronorm™ whole blood II*) to 850 µg g^{-1} (*BCR-176R*) of Sb. Purification recovery rates were similar to the ones found in the literature for environmental samples[13,14,17].

Extreme isotopic values were found to be -0.52 ± 0.06‰ (2 sd) for the branches and leaves of bush originally containing Sb (*NCS-DC-73349*) and 0.40 ± 0.03‰ (2 sd) for polyethylene artificially enriched with Sb (*ERM-EC680m*) while most of the CRM had an isotopic composition between -0.2 and +0.2‰. These data give an overview of the δ^{123}Sb isotopic variation in CRM which may be analysed during future study using Sb isotopes as environmental tracer.

To date, there is no internationally shared isotopic standard for Sb isotopes. The community should make efforts to inter-calibrate the different in-house isotopic standards and if possible to use the same standard solution in the future to be able to compare Sb isotope data.

Conflicts of interest

There are no conflicts of interest to declare.

Acknowledgments

This work received funding support from CNRS INSU EC2CO program (Project AntiBol).
We thank Sikémia (Franck Martin, Céline Schmitt) for fruitful discussions and for kindly providing custom-made TSP.
We would like to thank Sophie Delpoux and Léa Causse for assistance in laboratory analysis. We would like to thank the CRPG to have provided us some Certified Reference Materials.

References

1 O. Rouxel, J. Ludden and Y. Fouquet, *Chemical Geology*, 2003, **200**, 25–40.
2 H. Tian, J. Zhou, C. Zhu, D. Zhao, J. Gao, J. Hao, M. He, K. Liu, K. Wang and S. Hua, *Environ. Sci. Technol.*, 2014, **48**, 10235–10241.
3 T.-L. Chang, Q.-Y. Qian, M.-T. Zhao and J. Wang, *International Journal of Mass Spectrometry and Ion Processes*, 1993, **123**, 77–82.
4 F.-Z. Teng, N. Dauphas and J. M. Watkins, *Reviews in Mineralogy and Geochemistry*, 2017, **82**, 1–26.
5 J. G. Wiederhold, *Environ. Sci. Technol.*, 2015, **49**, 2606–2624.
6 L. Lobo, V. Devulder, P. Degryse and F. Vanhaecke, *Journal of Analytical Atomic Spectrometry*, 2012, **27**, 1304–1310.
7 L. Lobo, P. Degryse, A. Shortland and F. Vanhaecke, *Journal of Analytical Atomic Spectrometry*, 2013, **28**, 1213–1219.
8 L. Lobo, P. Degryse, A. Shortland, K. Eremin and F. Vanhaecke, *Journal of Analytical Atomic Spectrometry*, 2014, **29**, 58–64.
9 P. Degryse, L. Lobo, A. Shortland, F. Vanhaecke, A. Blomme, J. Painter, D. Gimeno, K. Eremin, J. Greene, S. Kirk and M. Walton, *Journal of Archaeological Science*, 2015, **62**, 153–160.
10 P. Degryse, A. J. Shortland, S. Dillis, A. van Ham-Meert, F. Vanhaecke and P. Leeming, *Journal of Archaeological Science*, 2020, **120**, 105195.
11 A. Reguera-Galan, T. Barriero-Grille, M. Moldovan, L. Lobo, M. A. De Blas Cortina and J. I. Garcia Alonso, *Archaeometry*, 2019, **61**, 683–700.
12 S. Dillis, A. V. Ham-Meert, P. Leeming, A. Shortland, G. Gobejishvili, M. Abramishvili and P. Degryse, *STAR: Science & Technology of Archaeological Research*, 2019, **5**, 1–15.
13 E. Resongles, R. Freydier, C. Casiot, J. Viers, J. Chmeleff and F. Elbaz-Poulichet, *Talanta*, 2015, **144**, 851–861.

14 J. Liu, J. Chen, T. Zhang, Y. Wang, W. Yuan, Y. Lang, C. Tu, L. Liu and J.-L. Birck, *J. Anal. At. Spectrom.*, 2020, **35**, 1360–1367.

15 S. Asaoka, Y. Takahashi, Y. Araki and M. Tanimizu, *Analytical Sciences*, 2011, **27**, 25–28.

16 M. Tanimizu, Y. Araki, S. Asaoka and Y. Takahashi, *Geochemical Journal*, 2011, **45**, 27–32.

17 S. Li, Y. Deng, H. Zheng, X. Liu, P. Tang, J. Zhou and Z. Zhu, *J. Anal. At. Spectrom.*, , DOI:10.1039/D0JA00367K.

18 T. J. Hosick, R. L. Ingamells and S. D. Machemer, *Analytica Chimica Acta*, 2002, **456**, 263–269.

19 A. R. Kumar and P. Riyazuddin, *TrAC Trends in Analytical Chemistry*, 2010, **29**, 166–176.

20 P. Pohl, *TrAC Trends in Analytical Chemistry*, 2004, **23**, 87–101.

21 P. Pohl and W. Zyrnicki, *Analytica Chimica Acta*, 2001, **429**, 135–143.

22 M. O. Ahmed, A. Shrpip and M. Mansoor, *Processes*, 2020, **8**, 246.

23 J.-S. Lim, S.-M. Kim, S.-Y. Lee, E. A. Stach, J. N. Culver and M. T. Harris, *Journal of Colloid and Interface Science*, 2011, **356**, 31–36.

24 Z. Wang, G. Wu and C. He, *Microchim Acta*, 2009, **165**, 151–157.

25 R. Rostamian, M. Najafi and A. A. Rafati, *Chemical Engineering Journal*, 2011, **171**, 1004–1011.

26 M.-Q. Yu, G.-Q. Liu and Q. Jin, *Talanta*, 1983, **30**, 265–270.

27 S. L. R. Ellison and A. Williams, *Eurachem/CITAC guide: Quantifying uncertainty in Analytical Measurement*, Third edition., 2012.

28 V. Devulder, L. Lobo, K. Van Hoecke, P. Degryse and F. Vanhaecke, *Spectrochimica Acta Part B: Atomic Spectroscopy*, 2013, **89**, 20–29.

29 K. Govindaraju, *Geostandards Newsletter*, 1994, **18**, 1–158.

30 G. E. M. Hall and J.-C. Pelchat, *Geostandards Newsletter*, 1997, **21**, 85–91.

31 S. Fadda, A. Rivoldini and I. Cau, *Geostandards Newsletter*, 1995, **19**, 41–54.

32 J. Sanz, M. T. Martínez, J. Galbán and J. R. Castillo, *Journal of Analytical Atomic Spectrometry*, 1990, **5**, 651–655.

33 T. Wickstrøm, W. Lund and R. Bye, *Analyst*, 1996, **121**, 201–204.

34 A. Risnes and W. Lund, *Journal of Analytical Atomic Spectrometry*, 1996, **11**, 943–948.

35 B. Welz and M. Melcher, *Spectrochimica Acta*, 1981, **36B**, 439–462.

36 C. Schmidt and M. Bahadir, *Fresenius J Anal Chem*, 1993, **346**, 683–685.

37 M.-L. Pons, M.-A. Millet, G. N. Nowell, S. Misra and H. M. Williams, *Journal of Analytical Atomic Spectrometry*, 2020, **35**, 320–330.

38 J. S. Kane, D. F. Siems and B. F. Arbogast, *Geostandards Newsletter*, 1992, **16**, 45–54.

Supplementary Information to article 1:

A single-step purification method for the precise determination of antimony isotopic composition of environmental, geological and biological samples by HG-MC-ICP-MS

Ferrari Colin,*[a] Resongles Eléonore, [a] Freydier Rémi[a] and Casiot Corinne [a]

[a]*HydroSciences Montpellier, Univ. Montpellier, CNRS, IRD, Montpellier, France*

*Corresponding author:

Mailing address : Université de Montpellier – CC 57
163, rue Augyste Broussonnet,
34090 Montpellier, France
Email : colin.ferrari@umontpellier.fr

This file includes:

Tables S1 to S4

Figures S1 to S2

Additional Tables and Figures

Table S1: Instrument settings for ICP-MS and HG-ICP-MS analysis (adapted from Resongles et al. 2015[1]).

Instrument settings	ICP-MS	HG-ICP-MS
Instrument	iCAP TQ, Thermo Scientific	iCAP Q, Thermo Scientific
RF Power (W)	1550	1550
Cooling (L min^{-1})	14.0	14
Auxiliary (L min^{-1})	0.8	0.8
Sample (L min^{-1})	1.03	/
Data acquisition parameters		
Wash time (s)		120
Uptake time (s)		90
Number of blocks		3
Number of cycles per block		/
Dwell time (ms)		100
Integration time per cycle (s)	/	/
Hydride generation parameters		
System	/	ESI HydrideICP
Reducing agent	/	1% w/v NaBH4 in 0.05% w/v NaOH
Sample	/	3 M HCl, 0.5 % (w/v) KI/AA
Internal standard	/	3 M HCl + 4 µg L^{-1} Te
Gas flow (L min^{-1})		
Sample gas	/	0.2
Add gas	/	0.7
Reagent flow (ml.min^{-1})		
Reducing agent	/	0.24
Sample	/	0.48
Internal standard	/	0.12

[1]E. Resongles, R. Freydier, C. Casiot, J. Viers, J. Chmeleff and F. Elbaz-Poulichet, *Talanta*, 2015, **144**, 851–861.

Table S2: Residual Element:Sb ratios measured by ICP-MS in the purified samples after the purification process.

CRM	Residual Cd:Sb ratio	Residual Co:Sb ratio	Residual Cr:Sb ratio	Residual Cu:Sb ratio	Residual Fe:Sb ratio	Residual Ni:Sb ratio	Residual As:Sb ratio	Residual Pb:Sb ratio	Residual Sn:Sb ratio
NCS-DC-73349	0.0026	0.02	1	0.1	10.9	0.35	0.01	0.245	0.06
PACS-3	0.0002	0.03	0.3	0.2	3.4	0.09	0.004	0.03	0.02
NCS-DC-70317	0.0001	0.03	0.2	0.2	13.4	0.05	0.004	0.002	0.02
SDO-1	0.001	0.02	0.3	0.1	2.3	0.1	0.003	0.002	0.02
GSD-3	0.0005	0.01	0.2	0.1	3.1	0.08	0.004	0.01	0.02
Urine Control Clincheck II	0.0003	0.01	0.1	< 0.0004	1.1	0.03	0.003	< 0.001	0.01
Whole blood trace elements II	0.0003	0.03	0.001	2.3	3.6	0.1	0.005	0.006	0.03
BCR-176R	0.0002	0.02	0.2	< 0.0025	1.6	0.05	0.004	0.007	0.02
ERM-EC680m	0.0001	0.001	0.01	0.004	0.10	0.005	0.0002	0.007	0.004
Average BCR 482 (n=3)	0.0003	0.02 ± 0.001	0.2 ± 0.02	0.3 ± 0.2	1.6 ± 0.3	0.05 ± 0.01	0.003 ± 0.000	0.008 ± 0.001	0.02 ± 0.002
Average NIST 2711a (n=3)	0.0004 ± 0.0002	0.01 ± 0.01	0.2 ± 0.1	0.04 ± 0.02	1.8 ± 0.7	0.05 ± 0.02	0.003 ± 0.000	0.006 ± 0.002	0.02 ± 0.002
Average BCR 723 (n=3)	0.0002 ± 0.0001	0.01 ± 0.001	0.2 ± 0.1	0.17 ± 0.03	3.5 ± 3.3	0.05 ± 0.02	0.003 ± 0.000	0.012 ± 0.004	0.02 ± 0.002
Average GXR4 (n=3)	0.0012 ± 0.0002	0.02 ± 0.01	0.2 ± 0.1	3 ± 3	2.9 ± 1.0	0.07 ± 0.03	0.003 ± 0.001	0.004 ± 0.003	0.03 ± 0.02

Table S3: Comparison of the δ^{123}Sb values (‰) and their uncertainties (2 standard deviation, 2sd) obtained following the statistical treatment of isotope analysis data (outlier exclusion) using methods A and B.

	Method A		Method B		
CRM	**δ^{123}Sb (‰)**	**2sd**	**δ^{123}Sb (‰)**	**2sd**	**n**
NCS-DC-73341	-0.52	0.08	-0.52	0.06	2
PACS-3	0.16	0.07	0.16	0.02	4
NCS-DC-70317	-0.10	0.01	-0.11	0.03	3
SDO-1	0.23	0.05	0.22	0.03	3
GSD-3	0.13	0.10	0.15	0.05	4
Urines Control Clincheck II	0.19	0.12	0.17	0.04	3
Whole blood trace elements II	0.09	0.02	0.09	0.02	3
BCR-176R	-0.03	0.07	-0.03	0.03	4
ERM EC680m	0.40	0.03	0.40	0.03	3
BCR-482	0.07	0.10	0.05	0.02	9
NIST 2711a	0.06	0.03	0.06	0.02	3
BCR 723	0.03	0.05	0.03	0.05	3
GXR4	0.36	0.09	0.35	0.04	9
NIST 1643f	-0.03	0.13	-0.08	0.09	3

Table S4: Final δ^{123}Sb values (data processed using method B for the statistical treatment) of the different CRM with their uncertainties (2 standard deviation, 2sd) and the number of measurements of the purified solution (n).

CRM	δ^{123}Sb (‰)	2sd	n
NCS-DC-73349	-0.52	0.06	2
PACS-3	0.16	0.02	4
NCS-DC-70317	-0.11	0.03	3
SDO-1	0.22	0.03	3
GSD-3	0.15	0.05	4
Urine Control Clincheck II	0.17	0.04	3
Whole blood trace elements II	0.09	0.02	3
BCR - 176R	-0.03	0.03	4
ERM-EC680m	0.40	0.03	3
BCR 482	0.05	0.05	9*
NIST 2711a	0.06	0.02	3
BCR 723	0.03	0.05	3
GXR4	0.35	0.04	9*
NIST 1643f	-0.08	0.09	3

*CRM with 3 measurements for each triplicate (digestion and purification step) showing external reproducibility of the complete method

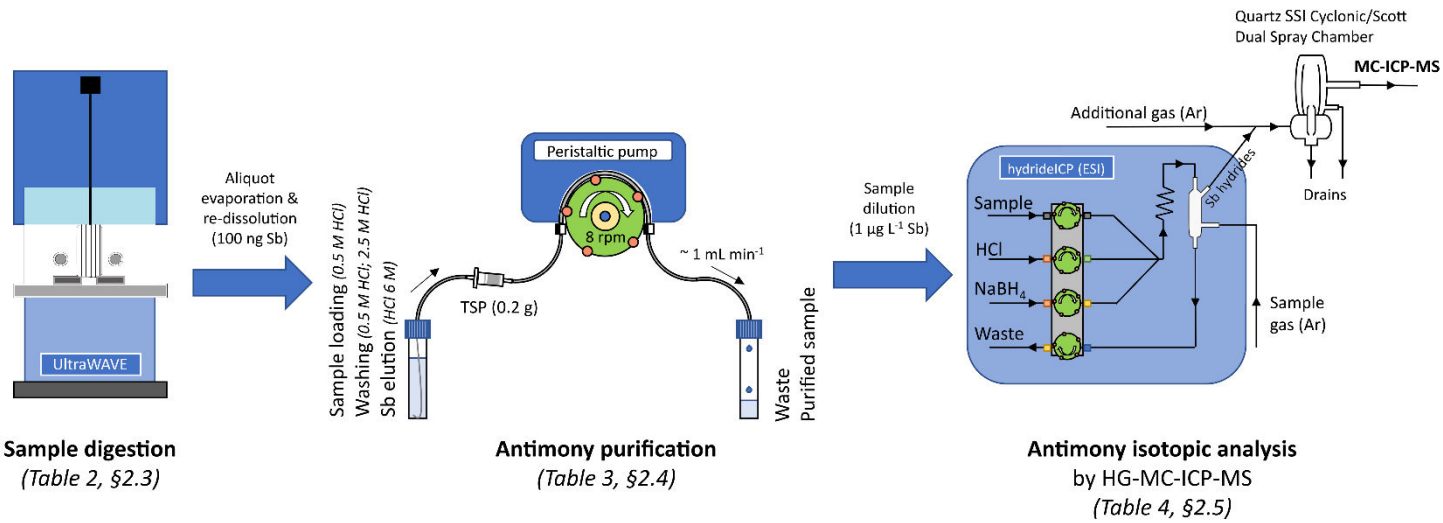

Figure S1: Scheme of the procedure for the determination of Sb isotopic composition in environmental, biological and geological solid samples including sample digestion, antimony purification and antimony isotope analysis. For the purification step, a 6-channel Gilson® peristaltic pump (at 8 rpm) with 1.02 mm i.d. Tygon® tubing allowed to run six samples simultaneously at a flow rate of ~ 1 mL min^{-1}.

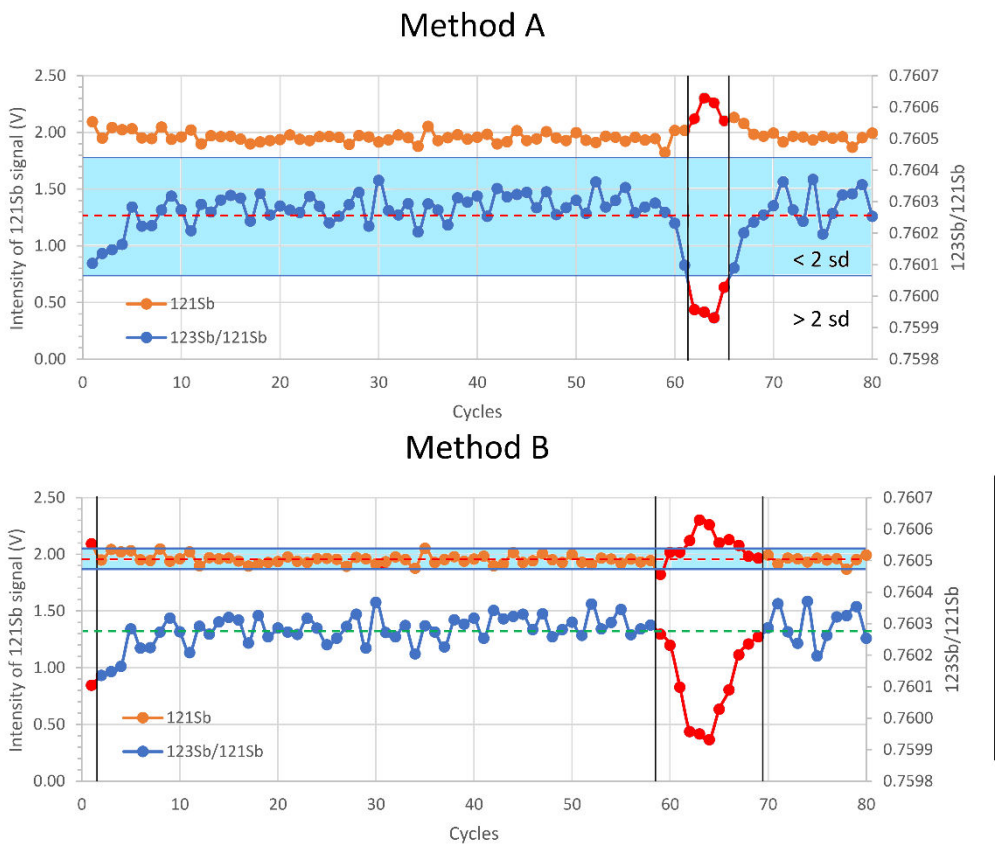

Figure S2: Comparison of methods A and B for the exclusion of outlier values of measured $^{123}Sb/^{121}Sb$ ratio. The blue area represents the 2 standard deviation area from the mean $^{123}Sb/^{121}Sb$ ratio (method A) or the mean ^{121}Sb intensity ± 5 % (method B). Dashed lines represent the mean values of signal intensity and isotope ratio.

Chapitre 3 :
Etudes théorique et expérimentales du fractionnement isotopique de Sb

Introduction

Ce chapitre est consacré à différentes études théoriques et expérimentales visant à caractériser et mieux comprendre le sens et l'amplitude des fractionnements isotopiques de l'antimoine résultants de processus couramment rencontrés dans l'environnement (oxydation, adsorption, changement d'environnement atomique…) sous la forme de trois articles publiés ou en préparation.

Dans ce chapitre, deux approches complémentaires ont été utilisées, comme vu dans le chapitre 1, partie B et section 1.d. Dans un premier temps, une approche théorique de l'étude du fractionnement isotopique dans le cadre de la théorie de la fonctionnelle de la densité (DFT) a été utilisée, afin de caractériser les fractionnements produits lors de l'oxydation de la stibnite en minéraux secondaires, et, dans un deuxième temps, deux études expérimentales ont été menées afin de mesurer l'amplitude et le sens du fractionnement isotopique de l'antimoine lors des processus d'adsorption et d'oxydation biotique et abiotique.

Dans la première partie de ce chapitre, le fractionnement isotopique de l'antimoine lors de l'oxydation de la stibnite en minéraux secondaires a été calculé pour plusieurs phases minérales (la stibnite, la valentinite, la sénarmontite, la cervantite et Sb_2O_5), couramment rencontrées en aval des sites miniers. Cette étude a servi à comprendre le sens et l'amplitude du fractionnement isotopique à l'équilibre entre les différentes phases minérales, mais aussi à les hiérarchiser et à en comprendre les origines. Pour les minéraux comportant plusieurs sites d'antimoine (la stibnite et la cervantite), le fractionnement isotopique pour chaque site a été calculé séparément afin d'identifier les contributions des différentes longueurs de liaisons atomiques ou encore du degré d'oxydation sur ce fractionnement à l'équilibre. Cette étude théorique est précurseur pour la quantification du fractionnement à l'équilibre de l'antimoine entre différentes phases minérales, contribuant de ce fait à la compréhension du cycle isotopique global de l'antimoine. Ces résultats ont été publiés dans la revue *Chemical Geology*.

La seconde partie de ce chapitre vise à caractériser expérimentalement le fractionnement de l'antimoine résultant de processus couramment rencontrés dans l'environnement. Dans un premier temps, l'étude du fractionnement de l'antimoine a été étudiée lors de son adsorption (sous forme tri- et pentavalente) sur des oxyhydroxydes et oxyhydroxysulfates de fer (ferrihydrite et schwertmannite). Ces processus d'adsorption sont des processus clés contrôlant la mobilité de l'antimoine en aval des drainages miniers acides, lors de la précipitation des oxydes de fer avec le soufre présent en solution. Dans un second temps, le fractionnement isotopique lors de l'oxydation biotique et abiotique de Sb(III) en Sb(V) a été étudié. Les différences de fractionnements entre les processus biotiques et abiotiques ont été mises en lumière lors de cette expérience, avec un fractionnement privilégiant les isotopes légers pour la phase oxydée lors de l'intervention de bactéries, alors qu'une absence de fractionnement a été observée dans le cas de l'oxydation abiotique dans les conditions expérimentales étudiées. Ces deux sous-parties sont présentées sous forme de deux articles en préparation pour *Chemical Geology*.

PARTIE A : Fractionnement isotopique dépendant de la masse à l'équilibre de l'antimoine entre la stibine et les minéraux secondaires Sb : une étude basée sur la dynamique moléculaire *ab initio* (article 2)

Colin Ferrari, Merlin Méheut, Eléonore Résongles, Rémi Freydier, Corinne Casiot

Article publié dans *Chemical Geology* (https://doi.org/10.1016/j.chemgeo.2022.121115).

Résumé en français

Les isotopes de l'antimoine (Sb) suscitent un intérêt croissant pour leur potentiel en tant que traceurs géochimiques dans les études géologiques, environnementales et archéologiques. Cependant, peu de connaissances existent sur les paramètres contrôlant le fractionnement isotopique de l'antimoine, ce qui est essentiel pour interpréter les variations de la signature isotopique dans les systèmes naturels. Dans cette étude, des facteurs de fractionnement isotopique dépendant de la masse à l'équilibre (facteur β) ont été calculés entre différents minéraux d'antimoine couramment trouvés dans les environnements miniers, dont le sulfure d'antimoine (stibine Sb_2S_3) et ses produits d'oxydation (valentinite Sb_2O_3, sénarmontite Sb_2O_3, cervantite Sb_2O_4) et du pentoxyde d'antimoine synthétique Sb_2O_5.

Les calculs *ab initio* dans le cadre de la théorie fonctionnelle de la densité (DFT) ont été effectués avec différentes fonctionnelles pour tester la robustesse de la méthode. Parmi les minéraux étudiés, la stibine a le facteur β le plus bas (ln(β) = 0,71 ‰ à 22 °C), puis les facteurs β augmentent progressivement de la valentinite (ln(β) = 1,64 ‰ à 22 °C) à la sénarmontite (ln(β) = 1,80 ‰ à 22 °C), la cervantite (ln(β) = 2,20 ‰ à 22 °C) et le pentoxyde d'antimoine (ln(β) = 3,03 ‰ à 22 °C).

Les facteurs qui fractionnent le plus les isotopes de Sb sont i) le changement d'état d'oxydation de Sb (le rapport des isotopes de Sb dans les minéraux contenant du Sb(V) est plus élevé que dans les minéraux contenant du Sb(III)), ii) le changement du premier voisin de Sb (le rapport isotopique Sb dans les liaisons Sb - O est plus élevé que dans les liaisons Sb - S) et iii) la distorsion des polyèdres atomiques Sb - O.

Les différences négligeables dans les facteurs β obtenus avec différentes fonctionnelles ont montré la robustesse de l'approche pour le calcul des facteurs β, malgré les différences dans le réseau minéral calculé et les fréquences Raman. Les résultats de cette étude fournissent une base théorique pour interpréter les variations isotopiques naturelles de Sb. Les résultats suggèrent qu'un enrichissement significatif en isotope lourd pourrait se produire lors de la dissolution oxydative de la stibine et de la précipitation subséquente des oxydes de Sb(III) et Sb(V) dans les environnements sulfurés. Plus généralement, ce travail soutient fortement que les isotopes de Sb peuvent être un traceur utile des processus de transformation de Sb dans la nature.

Equilibrium mass-dependent isotope fractionation of antimony between stibnite and Sb secondary minerals: a first-principles study

Colin Ferrari *[a], Merlin Méheut [b], Eléonore Resongles [a], Rémi Freydier [a] and Corinne Casiot [a]

[a]*HydroSciences Montpellier, Univ. Montpellier, CNRS, IRD, Montpellier, France*

[b]*Géosciences Environnement Toulouse, CNRS-UPS-OMP, 14 av. Edouard Belin, 31400 Toulouse, France*

*Corresponding author

Mailing address : Université de Montpellier – CC 57
163, rue Auguste Broussonnet,
34090 Montpellier, France
Email : colin.ferrari@umontpellier.fr

Abstract

Antimony (Sb) isotopes are gaining increasing interest for their potential as geochemical tracers in geological, environmental, and archaeological studies. However, little is known about the parameters controlling Sb isotope fractionation, which is essential to interpret variations of isotopic signature in natural systems. In this study, equilibrium mass-dependent isotope fractionation factors (β-factor) were calculated between different Sb-bearing minerals commonly found in mining environments including primary Sb sulphide (stibnite Sb_2S_3) and its oxidation products (valentinite Sb_2O_3, senarmontite Sb_2O_3, cervantite Sb_2O_4) and synthetic antimony pentoxide Sb_2O_5. First-principles calculations within the Density Functional Theory (DFT) were performed with different functionals to test the robustness of the method. Among the studied minerals, stibnite has the lowest β-factor (ln(β) = 0.71 ‰ at 22 °C), then β-factors progressively increase from valentinite (ln(β) = 1.64 ‰ at 22 °C), to senarmontite (ln(β) = 1.80 ‰ at 22 °C), cervantite (ln(β) = 2.20 ‰ at 22 °C) and antimony pentoxide (ln(β) = 3.03 ‰ at 22 °C). The factors that most fractionate Sb isotopes are found to be i) the change of Sb oxidation state (Sb isotope ratio in Sb(V)-bearing minerals is higher than in Sb(III)-bearing minerals), ii) the change of first neighbour of Sb (Sb isotope ratio in Sb – O bonds is higher than in Sb – S bonds) and iii) distortion of the atomic Sb - O polyhedrons. The negligible differences in the β-factors obtained with different functionals showed the robustness of the approach for the calculation of β-factors, despite differences in the calculated mineral lattice and Raman frequencies. The results of this study provide a theoretical basis to interpret natural Sb isotope variations. The results suggest that a significant enrichment in the heavy isotope could occur during oxidative dissolution of stibnite and subsequent precipitation of Sb(III) and Sb(V) oxides in sulphide environments. More generally, this work strongly supports that Sb isotopes may be a useful tracer of Sb transformation processes in nature.

Keywords: Antimony, Equilibrium isotope fractionation, Density Functional Theory (DFT), Sb minerals, Ab initio calculations.

1. Introduction

Antimony (Sb) is toxic for organisms and considered as a possible human carcinogen (Sundar and Chakravarty, 2010). Global anthropogenic Sb emissions have dramatically increased during the 20th century and a further two-fold increase is expected between 2010 and 2050 (Zhou et al., 2015). Anthropogenic sources of antimony emission include mining and metallurgical industries, coal and fuel combustion, waste incineration and road traffic (He et al., 2019; Tian et al., 2014). As a result, environmental contamination with Sb has been reported in various urban, industrial and mining contexts (He et al., 2019). In particular, the mining of Sb- or base metals-sulphide ores is a major cause of high environmental Sb concentrations (Hiller et al., 2012; Liu et al., 2010). However, compared to other toxic metal(loid)s, the behaviour of Sb in the environment is poorly known.

Metal(loid) stable isotopes are useful geochemical tracers for tracking the sources and fate of metals in the environment (Wiederhold, 2015). While some isotopic systems are relatively well-known (e.g. Cu, Zn (Moynier et al., 2017)), only few studies have focused on antimony stable isotopes (^{121}Sb (57.21%) and ^{123}Sb (42.79%), Chang et al., 1993). Rouxel et al. (2003) first showed that natural variations of the isotopic composition (δ^{123}Sb) were wide enough to be applied as a geochemical tracer and the potential of Sb isotopes as archaeological and environmental tracers has been confirmed afterwards (Degryse et al., 2020, 2015; Dillis et al., 2019; Lobo et al., 2014, 2013; Resongles et al., 2015). As for other stable isotope systems, Sb isotopes may be fractionated during (bio-)geochemical processes controlling Sb fate in surface environments (e.g. change of redox state, adsorption, precipitation…) (Wiederhold, 2015). Documenting the direction and intensity of Sb isotope fractionation during these processes is of primary importance to interpret Sb isotope signatures in complex environmental systems (Komárek et al., 2021).

Metal isotope fractionation factors have been acquired from field observations, laboratory experimentations, or theoretical calculations (Fujii et al., 2014; Schauble et al., 2009; Sherman, 2013; Wiederhold, 2015) but investigations of Sb isotope fractionation are scarce. Rouxel et al. (2003) showed a large fractionation of Sb isotopes during the abiotic reduction of aqueous Sb(V) to Sb(III). A recent experimental study showed no significant equilibrium isotope fractionation due to adsorption of Sb on aluminium oxides while a kinetic fractionation was observed in the first stage of the reaction (Zhou et al., 2022). Wang et al. (2021) and Zhai et al. (2021) showed large δ^{123}Sb range of 0.75 ‰ and 1.13 ‰, respectively, among stibnite ores or Sb sulfosalts in the epithermal system but the origin of Sb isotope fractionation during the precipitation of Sb-bearing minerals from the hydrothermal fluid is still under debate (Wang et al., 2021; Zhai et al., 2021). To date, no theoretical study has been made to predict the extend of Sb isotopic fractionation at equilibrium among various Sb minerals and different bonding environments, and the current knowledge of Sb isotope fractionation caused by physical and biogeochemical processes is very limited.

This study aims to determine mass-dependent equilibrium isotopic fractionation factors between various Sb minerals to provide a theoretical basis for the interpretation of Sb isotopic signatures in natural systems. For this, Sb isotopic partitions at equilibrium were calculated between stibnite (Sb_2S_3), the main Sb primary ore and selected Sb secondary minerals (senarmontite, valentinite, cervantite (Figure 1)) (Roper et al., 2012). The methodology is based on the Density Functional Theory (DFT); it involves determining theoretically the vibrational properties of these structures. The theoretical and quantum approach of DFT aims at estimating the relationship between fractionation properties and interatomic bond strengths (Sb-S bond or Sb-O bond), or Sb redox change. In this work, we modelled the oxidation steps of stibnite (orthorhombic $Sb(III)_2S_3$) towards a fully oxidized and synthetic Sb_2O_5 phase, via valentinite (orthorhombic $Sb(III)_2O_3$), senarmontite (cubic $Sb(III)_2O_3$) and cervantite (orthorhombic α-$Sb(V)Sb(III)O_4$) by calculating their isotopic partition ^{123}Sb β-factor. To quantify the extent of Sb isotopic fractionation associated with the different parameters controlling the isotopic fractionation, each site of cervantite has then been studied and calculated separately to observe the effect of trivalent/pentavalent antimony and its oxygen bonds on the β-factor. The site-by-site calculation has also been made for the two Sb sites in stibnite, where their coordination number and average bond length are significantly different. This oxidation process, described by Roper et al. (2012), commonly occurs in sulphide mining environments and plays an important role in Sb attenuation in the supergene environments (Ashley

et al., 2003; Filella et al., 2009). Computations have been made using two different functionals (Local Density Approximation (LDA) and Generalized Gradient Approximation (GGA)). At all steps of the calculation (relaxation, phonon dispersion; Infra-Red (IR) and Raman spectrum), results have been compared with experimental values, when available (Cody et al., 1979; Mestl et al., 1994.; Sereni et al., 2010). The results are expected to provide information on the direction and magnitude of Sb isotope fractionation factors, to help interpretation of future field or experimental observations.

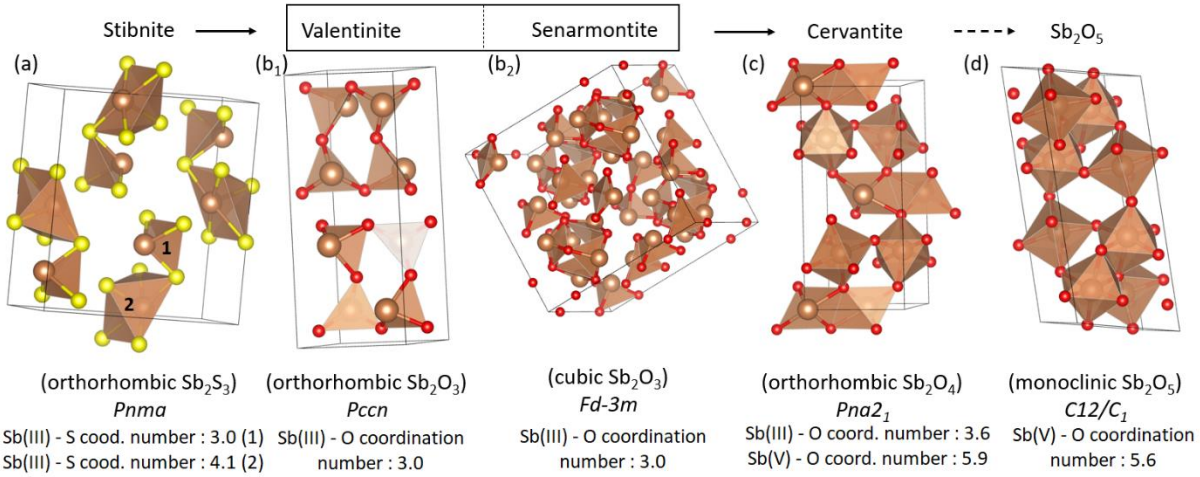

Figure 1: Scheme of stibnite transformation process from Sb_2S_3 to Sb_2O_5 modelled in this study indicating the crystal system, the spacegroup of the minerals and Sb coordination number. The atomic structures were drawn with VESTA software as well as the coordination number determination (Momma et al., (2011)).

2. Method

2.1 β-factors

The equilibrium isotope fractionation factor α_{B-A} between two mineral phases A and B corresponds to the ratio of Sb isotope ratios in these minerals and can be expressed as:

$$\alpha_{B-A} = \frac{\left(\frac{^{123}Sb}{^{121}Sb}\right)_B}{\left(\frac{^{123}Sb}{^{121}Sb}\right)_A} = \frac{\beta_B}{\beta_A} \quad (1)$$

Where β_X is the isotopic partition factor of a mineral X relative to an ideal atomic gas. As α is very close to 1, the isotopic fractionation factor can be expressed as (Schauble et al., 2009; Sherman, 2013):

$$1000 \ln \alpha_{B-A} = 1000(\ln \beta_B - \ln \beta_A) \approx \delta^{123}Sb_B - \delta^{123}Sb_A \quad (2)$$

$$\text{With } \delta^{123}Sb = \frac{(^{123}Sb/^{121}Sb)sample}{(^{123}Sb/^{121}Sb)standard} - 1 \quad (3)$$

Equilibrium mass-dependent isotope fractionation results from the effect of atomic mass on bond energy (Bigeleisen and Mayer, 1947; Urey, 1947). If A is a crystalline solid, and Y the element of interest, The β-factor of phase A for the Y/Y* substitution can be written as:

$$\beta(AY_n, Y) = \left[\frac{Q(AY_n^*)}{Q(AY_n)}\right]^{\frac{1}{n}} \left[\frac{m_Y}{m_{Y^*}}\right]^{\frac{3}{2}} \quad (4)$$

where Y^* is the heavier isotope and Y the main isotope, m_Y and m_{Y^*} are the respective mass of the isotopes Y and Y^* and n is the total number of sites. $Q(AY_n^*)$ denotes the partition function of the system having all the Y isotopes substituted with Y^*(Méheut-Le Quéau, 2008).

When the crystal structure presents two types of sites with significantly different environments, such as the Sb(III) and Sb(V) sites in cervantite, it is interesting to consider the local β-factor, relative to one type of site only. In this case, if the system is written $AY_{1,i}Y_{2,j}$, with i and j the number of sites 1 and 2, the β-factor of site 1 is:

$$\beta(AY_1, Y) = \left[\frac{Q\left(AY_{1,i}^* Y_{2,j}\right)}{Q\left(AY_{1,i} Y_{2,j}\right)}\right]^{\frac{1}{T}} \left[\frac{m_Y}{m_{Y^*}}\right]^{\frac{3}{2}} \quad (5)$$

The partition function Q can then be computed from the vibrational properties of the system:

$$Q = \left[\prod_{i=1}^{3N^{at}} \prod_{\{q\}} \frac{exp(-\frac{hv_{q,i}}{(2kT)})}{1 - \exp(\frac{-hv_{q,i}}{(kT)})}\right]^{\frac{1}{N_q}} \quad (6)$$

Where $v_{q,i}$ are the frequencies of the phonon with the wavevector **q** and branch index i=1.3N^{at}. N^{at} is the number of atoms in the unit cell, *N* is the number of sites for the *Y* atom in the unit cell, *T* is the temperature (K), k is the Boltzmann constant and *h* is Plank's constant. In the product of Eq. (6) the three translational ***q***=0 modes with $v_{q,i} = 0$ are not considered.

2.2 Computational methods

In this paper, electronic and vibrational properties are calculated within the first-principles plane waves method based on DFT through the Quantum espresso suite (version 6.4 (Giannozzi et al., 2017, 2009)). The starting structures are those experimentally determined for stibnite in orthorhombic *Pnma* symmetry (Kyono and Kimata, 2004), senarmontite in cubic *Fd-3m* symmetry (Whitten et al., 2004), valentinite in *Pccn* symmetry (Whitten et al., 2004), cervantite in *Pna2₁* symmetry (Gopalakrishnan et al., 1975) and Sb_2O_5 in monoclinic *C12/c1* symmetry (Jansen, 1979). For stibnite, valentinite and cervantite, several functionals were used, namely the local approximation of Perdew and Zunger (PZ) (Perdew and Zunger, 1981), the generalized-gradient approximations to the exchange-correlation functional of Perdew, Burke and Ernzerhoff (PBE) (Perdew et al., 1996) and the recent PBEsol functional (Perdew et al., 2008). Previous models have shown good results for stibnite using the PZ (Filip et al., 2013) and PBESOL (Ibáñez et al., 2016) pseudopotentials. However, no model tested the PBE functional, it is then interesting to compare the results obtained using these three different functionals. For senarmontite and Sb_2O_5, only the PBEsol functional is used as it appears to be the most reliable. Ionic cores of each atom are described by either ultrasoft (us) or norm conserving pseudopotentials (nc). The pseudopotential for O is nc and is generated for PZ, PBE, or PBEsol with the same characteristics as described in the electronic annexes of Méheut et al. (2007). For S, the pseudopotential is from the PSLibrary (Dal Corso, 2014). For Sb, two types of pseudopotentials from the PSLibrary are considered: the "ultrasoft" (e.g. pseudopotential file Sb.pz-dn-rrkjus_psl.1.0.0.UPF for PZ functional) and the "norm-conserving" (e.g. Sb-pz-n-nc.UPF for PZ functional). The first one is in principle very accurate (due to the account of semicore states). This permits an accurate calculation at a reasonable computational cost, due to the ultrasoft approach. However, the computation of Raman intensities is not implemented for this type of pseudopotentials in the Quantum Espresso software package. In order to compute Raman intensities and compare more precisely calculated gamma-point frequencies with experiment, nc pseudopotentials only should be used. Calculations using the us or nc pseudopotentials for Sb will be thereafter called us or nc, respectively. For both types of calculations, electronic wave-functions are expanded in plane-waves up to an energy cutoff ε_{cut}=80 Ry (1088 eV) and the charge density cut-off is set to 4 ε_{cut}. Electronic integration is done by sampling the Brillouin zone with a 4×2×4 k-point grid for valentinite, a

2×6×2 grid for stibnite, a 3×4×2 grid for cervantite, a 2×2×2 grid for senarmontite and a 2×3×3 grid for Sb_2O_5 (Monkhorst and Pack, 1976).

Phonon frequencies are computed using linear response theory (Baroni et al., 2001), with the Quantum Espresso package (Giannozzi et al., 2009). Interatomic force-constants are obtained from the dynamical matrices computed exactly (within DFT) on a n × m × p grid of vectors (where n, m and p are equal to the numbers used for electronic integration). Long-range effects are taken into account by computing Born effective-charges and static dielectric constants (Baroni et al., 2001). Dynamical matrices and thus phonon frequencies can be obtained in any point of the reciprocal space by Fourier-interpolation of the force constants. For all materials, the vibrational partition function (Eq. (5)) is converged with a 6×6×6 interpolation grid.

To help correlate calculated frequencies at gamma-point with experimental spectroscopic Raman data, the intensities (Raman cross-sections) of each mode are computed for PBEsol calculations. For Raman-active modes, non-resonant Raman cross-sections are computed using second- order response as in Lazzeri and Mauri (2003).

2.3 Raman spectra

To directly compare the calculations with the experiment, Raman spectrum configurations of all the structures are modelled for a 300 K temperature (as this temperature was the reference in the experimental valentinite study (Gonçalves et al., 2018)). Two light polarisations are considered: parallel-polarized “xyyx” geometry, with incoming and outcoming polarisation in the same direction (giving A_g modes) and cross-polarized “xyzx” geometry, with incoming and outcoming polarisations perpendicular to each other, giving B_g modes. As the Raman spectra found in the literature are always measured on mineral powders for the cases considered here, the spectra are averaged over several grain orientations (80) and broadened by Gaussian convolution. However, these experimental methods generally give information on anharmonic frequencies at the Brillouin zone centre (Méheut-Le Quéau, 2008). So, these comparisons could be biased, but remain the best point of comparison between theoretical and experimental data. Calculated IR frequencies will not be compared for validation of the models with experimental data, as for most of these structures, they do not exist or are incomplete.

3. Results

3.1. Structural predictions

The structures of stibnite, valentinite and cervantite are relaxed at the PBE, PBEsol (GGA) and PZ (LDA) levels using the us Sb pseudopotential (Table 1). The calculations using the nc pseudopotential performed for valentinite and cervantite at the PZ and PBESOL levels hold slightly smaller cell parameters (typically by 0.7 %). The results of the us calculations show good agreement with experimental data and previous computations, with global differences under 5 % (Allen et al., 2013; Gopalakrishnan and Manohar, 1975; Kyono and Kimata, 2004; Svensson, 1975). PBE relaxation shows the worst lattice reproduction, with a 8 % deformation along the *a*-axis for stibnite and valentinite, resulting in an important lattice volume difference. This elongation is not found with the other functionals and particularly for PBEsol, which presents the best agreement with experimental data for each structure, with an average difference of 1 % in the cell parameters for the 3 structures. The comparison between experimental and theoretical data is reported in Table 1 as well as other studies working with similar PBEsol (Ibáñez et al., 2016) and PZ (calculated with semicore, Filip et al., 2013) functionals. Both PBEsol pseudopotentials showed similar lattice values. For the PZ functional, our calculation is reasonably close to the calculation using the pseudopotential w/o semicore (Table 1) while there are significant differences between the two PZ pseudopotentials used in Filip et al. (2013) and this study (Table 1).

The Sb-S and Sb-O distances are slightly longer after the relaxation step for all the structures, as in other models (Allen et al., 2013) where the bond elongation ranked between 1 to 4.1 %. No extreme dilatation was reported for the

different bonds in the valentinite structure. Despite these small elongations, the bond distances obtained through the calculations are close to measured values and the reproduction of these structures is satisfying to proceed with the next calculation steps.

The structures of senarmontite and Sb_2O_5 are calculated at the PBEsol level only (Table 1), based on the conclusion that this functional is the most accurate (see discussion in 3.2).

Table 1: Calculated cell parameters with the different functionals (PBE, PZ, PBEsol, us calculations only) determined in this study compared to the experimental data (Expce) and calculations from other authors. Bracketed values are the percentage differences with the experimental data ([‡]Kyono et al., 2001, [Φ]Whitten et al., 2004, [†]Svensson et al., 1974, [⁂]Gopalakrishnan et al., 1975, [X]Jansen 1979) and are compared with other theoretical studies ([ϑ]Ibáñez et al., 2016 (PBESOL), [ω]Filip et al. 2013 (PZ), , [Θ]Allen et al., 2013 (PBE)).

Material	Properties	PBE	PZ	PBESOL	Expce	Other calculations		
						PBESOL	PZ	PBE
Sb_2S_3[‡] (Stibnite)	a (Å)	12.199 (+8.1)	10.927 (-3.2)	11.271 (-0.1)	11.282	11.2746[ϑ]	11.087[ω]	
	b (Å)	3.879 (+1.3)	3.786 (-1.1)	3.832 (+0.1)	3.83	3.8306[ϑ]	3.838[ω]	
	c (Å)	11.257 (+0.3)	10.727 (-4.4)	10.916 (-2.8)	11.225	10.8941[ϑ]	10.834[ω]	
	α (°)	90 (0)	90 (0)	90 (0)	90			
	β (°)	90 (0)	90 (0)	90 (0)	90			
	ɣ (°)	90 (0)	90 (0)	90 (0)	90			
	|Sb1-S1| (Å)	2.553 (+1.5)	2.561 (+1.8)	2.590 (+1.8)	2.514			
	|Sb1-S2| (Å)	2.574 (+1.4)	2.564 (+1.1)	2.570 (+1.3)	2.537			
	|Sb1-S3| (Å)	3.156 (+1.6)	2.979 (-4.1)	3.014 (-3.0)	3.106			
	S2-Sb1-S3 (°)	88.587 (+1.1)	84.183 (-3.9)	85.440 (-2.4)	87.581			
	Vol (A^3)	532.6 (+9.8)	443.8 (-8.5)	471.4 (-2.8)	485			
α-Sb_2O_3[Φ] Senarmontite	a (Å)	-	-	11.130 (+0.1)	11.116			
	α (°)	-	-	90 (0)	90			
	β (°)	-	-	90 (0)	90			
	ɣ (°)	-	-	90 (0)	90			
	|Sb1-O1| (Å)	-	-	2.0195 (+2.0)	1.98			
	|Sb1-O2| (Å)	-	-	2.0195 (+2.0)	1.98			
	|Sb1-O3| (Å)	-	-	2.0195 (+2.0)	1.98			
	O2-Sb1-O3 (°)	-	-	96.77 (+0.9)	95.87			
	Vol ($Å^3$)	-	-	1378.78 (+0.3)	1373.55			
β-Sb_2O_3[†] (Valentinite)	a (Å)	5.323 (+8.6)	4.803 (-2.0)	4.941 (+0.8)	4.9			5.008[Θ]
	b (Å)	12.722 (+2.2)	12.190 (-2.1)	12.296 (-1.2)	12.449			12.654[Θ]
	c (Å)	5.570 (+2.9)	5.372 (-0.7)	5.418 (+0.1)	5.41			5.527[Θ]
	α (°)	90 (0)	90 (0)	90 (0)	90			
	β (°)	90 (0)	90 (0)	90 (0)	90			
	ɣ (°)	90 (0)	90 (0)	90 (0)	90			
	|Sb1-$O1_a$| (Å)	2.034 (+2.5)	2.008 (+1.2)	2.0228 (+2.0)	1.984			
	|Sb1-$O1_b$| (Å)	2.059 (+1.9)	2.054 (+1.65)	2.0762 (+2.7)	2.021			
	|Sb1-O2| (Å)	2.074 (+2.5)	2.068 (+2.2)	2.0624 (+1.9)	2.024			
	Vol ($Å^3$)	377.2 (+14.3)	314.5 (-4.7)	329.2 (-0.25)	330			350.25[Θ]

	a (Å)	5.623 (+3.4)	5.455 (+0.4)	5.489 (+1.0)	5.436	5.558[Θ]
	b (Å)	4.940 (+2.7)	4.819 (+0.2)	4.868 (+1.2)	4.81	4.912[Θ]
	c (Å)	12.030 (+2.3)	11.735 (-0.2)	11.819 (+0.5)	11.76	11.943[Θ]
	α (°)	90.0 (0)	90.0 (0)	90.0 (0)	90	
	β (°)	90.0 (0)	90.0 (0)	90.0 (0)	90	
α-Sb_2O_4[*,**] (Cervantite)	ɣ (°)	90.0 (0)	90.0 (0)	90.0 (0)	90	
	|Sb1-O1| (Å)	2.030 (+5.3)	1.992 (+3.3)	2.009 (+4.2)	1.929	
	|Sb1-O2| (Å)	2.002 (+2.4)	1.965 (+0.5)	1.982 (+1.4)	1.954	
	|Sb1-O3| (Å)	2.060 (+1.7)	2.026 (+0.1)	2.042 (+0.8)	2.024	
	O2-Sb1-O3 (°)	88.5 (-2.3)	89.1 (-1.7)	88.9 (-1.9)	90.7	
	Vol (Å^3)	334.2 (+8.7)	308.5 (+0.3)	315.8 (+2.7)	307.5	326.05[Θ]
	a (Å)	-	-	12.762 (+0.9)	12.646	
	b (Å)	-	-	3.963 (-17.1)	4.782	
	c (Å)	-	-	3.926 (-27.6)	5.4247	
Sb_2O_5[X]	α (°)	-	-	87.8 (-2.4)	90	
	β (°)	-	-	101.85 (-2.0)	103.91	
	ɣ (°)	-	-	91 (+1.1)	90	
	Vol (Å^3)	-	-	194.7 (-38.9)	318.429	

3.2 Vibrational predictions

To assess the validity of the phonon calculation on the structures, the calculated vibrational frequencies can be compared with results from conventional spectroscopic studies (IR and Raman spectra). On classical and well-known materials commonly used in industries such as stibnite, plenty of experimental and theoretical data are available on the Raman spectrum (Cai et al., 2018; Ibáñez et al., 2016; Sereni et al., 2010). However, data are not available or incomplete for rarer materials with no industrial applications, such as senarmontite, cervantite or Sb_2O_5. For these minerals, the whole spectrum and frequencies are given to provide, for the first time, full calculated vibrational spectra with their symmetries and they are discussed with previous existing data. PBEsol is the functional which best suits the experimental frequencies (R^2 = 0.993 for all structures). On the other hand, the error of PBE on frequencies is more variable, especially around the 300 – 600 cm^{-1} frequencies. The average ~ 4 % underestimation of the Raman frequencies calculated with PBE observed by Méheut et al. (2007), Scheurer et al. (2014) and Ducher et al. (2016) is found as well in this study. However, uncertainties on the cervantite assignation remain high due to the incompleteness of experimental data. The detailed frequencies and their assignations are discussed below in details for each mineral considered. Frequencies calculated through nc and us pseudopotentials are close enough to be associated with each other and to use the Raman intensity calculated with nc to attribute experimental frequencies to us. All the Raman spectra are calculated with nc pseudopotentials.

3.2.1. Stibnite Raman frequencies

The calculated Raman frequencies of stibnite are compared to the experimental study from Ibáñez et al. (2016) and are reported in Table S1. Overall, the theoretical and experimental values are similar, with errors calculated at 0.3 % with a linear regression between the experimental and theoretical (PBEsol) frequencies. PBEsol best reproduces the Raman frequencies obtained experimentally (peak positions and symmetries). Frequencies calculated with PZ and PBEsol show more similarities between each other than with PBE. As stibnite is the most documented Sb mineral phase and since the experimental and theoretical Raman frequencies have a good correspondence and do not present

any ambiguity, the Raman spectrum of stibnite is not calculated to validate the model nor attribute the experimental and theoretical frequencies. Calculated Raman frequencies in this study are also compared with theoretical Raman frequencies from Ibáñez et al., (2016) where PBEsol was used, with a good similarity of lattice parameters (Table 1). The two theoretical studies show very similar calculated frequencies (Table S1).

3.2.2. Valentinite Raman frequencies

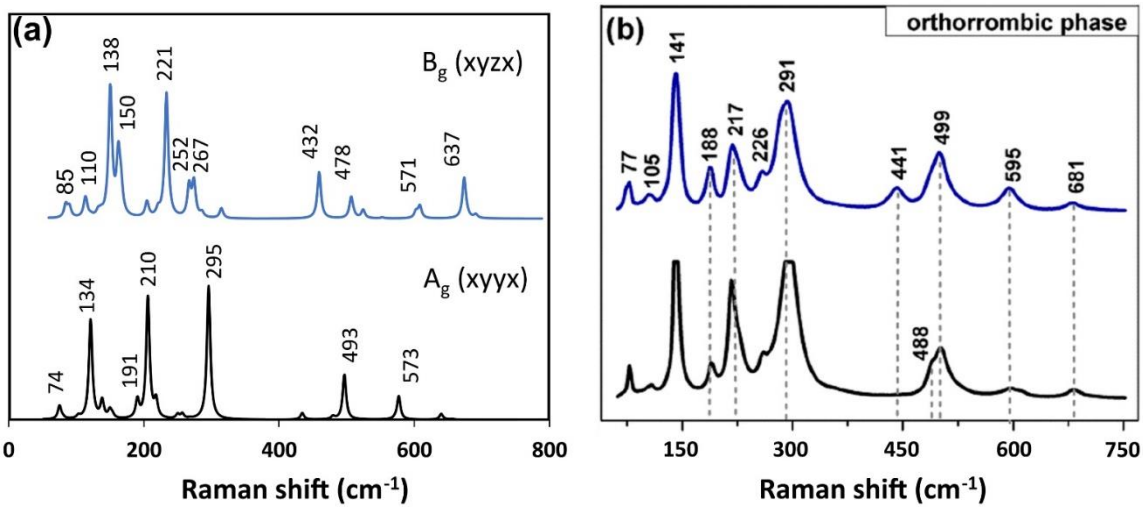

Figure 2: a) Raman spectrum of valentinite calculated with the PBEsol functional compared with b) the experimental valentinite Raman spectrum measured at ambient temperature and pressure reproduced from Gonçalves et al. (2018) with permission from Elsevier. Blue lines represent the Bg symmetry while the black represent the Ag symmetry.

The calculated Raman frequencies of valentinite are compared with experimental data from the study of Gonçalves et al. (2018). The full list of frequencies and symmetries is reported in Table S2 and compared with the experiment. Then, the Raman spectrum of valentinite is calculated to make the best possible correspondences between the theoretical and experimental Raman frequencies. For this, the pseudopotential PBEsol_nc is used, as PBEsol gives the best results for the lattice reproduction. The calculated spectrum is compared with the experimental one in Figure 2. Some of the experimental frequencies did not find an experimental correspondence (Table S2), however, it concerns relatively low intensities frequencies (< 100 a.u.) and all the major peaks are attributed to an experimental equivalent. The errors are acceptable, with -4.4 % for PBEsol compared with the experimental data through linear regression. As previously seen for lattice parameters, the PBE model is less efficient than the others for Raman frequencies.

3.2.3 Senarmontite Raman frequencies

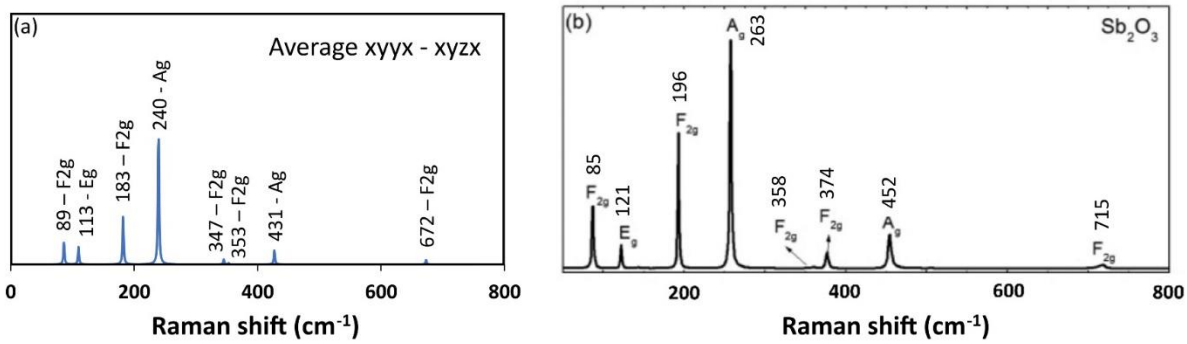

Figure 3: a) theoretical Raman spectrum of senarmontite calculated with the PBEsol functional compared with b) the experimental spectrum measured at ambient pressure, reproduced from Pereira et al. (2012) with permission from the American Physical Society.

The calculated Raman frequencies of senarmontite are compared with the experimental data from Pereira et al. (2012) at ambient pressure and temperature (Figure 3) and Mestl et al. (1994) (Table S3). As noticed in Pereira et al. (2012), the E vibration modes calculated were doubly degenerated while the F modes were triply degenerated. Despite some differences with the experimental data (average difference of peak frequency -7.9 % for PBEsol, Figure 6), the two spectra fit each other relatively well. The theoretical frequency at 305 cm^{-1} (E_g) calculated in this study had an almost null intensity and cannot be seen in the experimental spectrum presented by Pereira et al., (2012) nor in the theoretical spectrum, but is, however, present in the nine Raman frequencies that senarmontite has and is therefore reported in the theoretical study of Pereira et al., (2012) for the 335 cm^{-1} frequency (Table S3). Data from Pereira et al., (2012) were similar to the previous Raman frequencies found in the literature (Mestl et al., 1994).

3.2.4 Cervantite Raman frequencies

The calculated Raman frequencies of cervantite are compared to the experimental frequencies measured by Cody et al. (1979) for the validation of the model (Table S4). To attribute the theoretical frequencies to experimental ones, the average Ag – Bg (xyyx and xyzx polarisations, Figure 4) spectrum is modelled, as symmetries were not given in Cody et al., (1979) or in any other publication, and the most intense peaks were attributed to the most intense experimental peaks. These data being old and incomplete made the peak assignation less precise than for the other structures.

To quantify the errors between experimental and theoretical frequencies, the PBEsol model is chosen as a reference for the symmetries, as this model shows the best correspondence between the experimental and theoretical values for stibnite and valentinite. With the available data, the theoretical and experimental frequencies are showing good correspondence with each other (for PBEsol and PZ). The PBE pseudopotential calculations give a negative value (-8 cm^{-1}) as a Raman frequency indicating the inefficiency of PBE compared to PBEsol and PZ. The error between PBEsol and the experimental data is equal to -2.6 %. A particularity of cervantite frequencies compared to the other structures studied, is that IR shifts also have a Raman component.

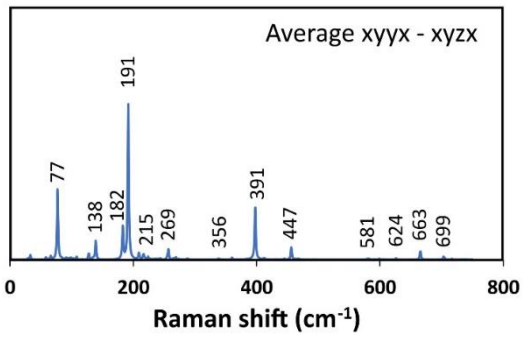

Figure 4: Average Raman spectrum of cervantite calculated with the PBEsol functional.

Experimental frequencies ranged from 43 to 858 cm^{-1}, with higher frequencies (> 713 cm^{-1}) having extremely low intensities (< 1 a. u..). The highest frequency for the theoretical spectrum is around 750 cm^{-1}, which is not in accordance with the experimental values reported by Cody et al. (1979). This may be attributed to the fact that measurements made by Cody et al. (1979) recorded some background noise in the high frequencies which were mistaken with peaks.

3.2.5 Sb_2O_5 Raman frequencies

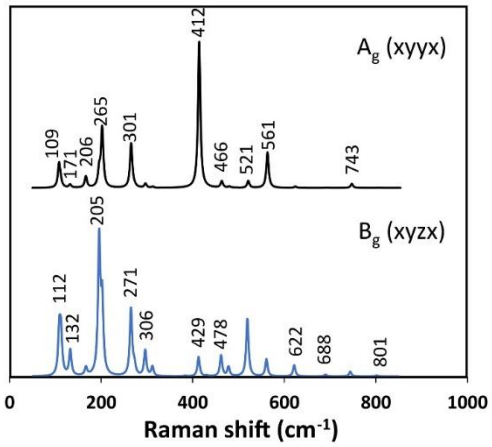

Figure 5: Raman spectrum of Sb_2O_5 calculated in this study with the PBEsol functional. The black line represents the A_g symmetry (xyyx) while the blue one represents the B_g symmetry (xyzx).

As PBEsol shows good agreements with experimental data for the previous modelled structures, it is decided to calculate Sb_2O_5 only with the PBEsol functionals (both us and nc pseudopotentials). No experimental data of the Raman spectrum of Sb_2O_5 was found in the literature for the validation of the model. The Raman frequencies of Sb_2O_5 with their intensities are reported in Table S5, as reference for future works implying monoclinic Sb_2O_5, as for its Raman spectrum given in Figure 5.

3.3. β-factors

Table 2: Recommended fits of the β-factors calculated for the PBEsol functional with us pseudopotentials and based on an equation of the type $ax^2 + bx^3$, with $x = 10^3/T$ (K).

Mineral	Temperature range (°C)	Fit parameters	
		a	b
Stibnite	0 - 1100	0.0635	-0.00056
Valentinite	0 - 1100	0.1561	-0.00397
Senarmontite	0 - 1100	0.1719	-0.00454
Cervantite	0 - 1100	0.2256	-0.00603
Sb_2O_5	0 - 1100	0.2960	-0.00964

The β-factors represent the equilibrium $^{123}Sb/^{121}Sb$ isotopic fractionation factor between the mineral and a hypothetical perfect gas with the natural average $^{123}Sb/^{121}Sb$ ratio (Méheut-Le Quéau, 2008). The differences between ln(β) values of the four studied Sb minerals provide an overview of the variability of Sb fractionation expected in nature (Equation 3). All β-factors are calculated with the PBEsol functional and the us Sb pseudopotential (Table S6) and the equations describing these fractionations as a function of temperature are listed in Table 2. The β-factors show significantly different values for the different phases (Figure 6). Stibnite β-factor (ln(β) = 0.71 ‰ at 22 °C) shows a low value compared to valentinite or senarmontite ($\Delta\ln(\beta)_{valentinite\text{-}stibnite/senarmontite\text{-}stibnite}$ = 0.93 and 1.09 ‰ at 22 °C, respectively), cervantite ($\Delta\ln(\beta)_{cervantite\text{-}stibnite}$ = 1.49 ‰ at 22 °C) and Sb_2O_5 ($\Delta\ln(\beta)_{Sb2O5\text{-}stibnite}$ = 2.32 ‰ at 22 °C, Figure 6 and Table S6). During the transformation process of these minerals, the different structures tend to present higher β-factors as they get oxidized ($\beta_{stibnite} < \beta_{valentinite/senarmontite} < \beta_{cervantite} < \beta_{Sb2O5}$). The site-by-site calculation for the trivalent and pentavalent Sb forms in cervantite shows that Sb(III) tends to be less enriched in the heavy isotope ^{123}Sb (ln(β) = 1.37 ‰ at 22 °C) than Sb(III) in senarmontite (ln(β) = 1.80 ‰ at 22 °C) or in valentinite (ln(β) = 1.64 ‰ at 22 °C). On

the contrary, the β-factor of Sb(V) in cervantite (ln(β) = 3.03 ‰ at 22 °C) is equal to the β-factor of Sb(V) in pure Sb_2O_5 (ln(β) = 3.03 ‰ at 22 °C). Site-by-site calculations for the two Sb sites in stibnite show very similar β-factor (ln(β) = 0.70 ‰ at 22 °C for the second site, and 0.72 ‰ for the 1st site, Table S7), despite a coordination number lower (3.0 vs 4.1) and shorter bond lengths (2.53 Å vs 2.70 Å) for the second site.

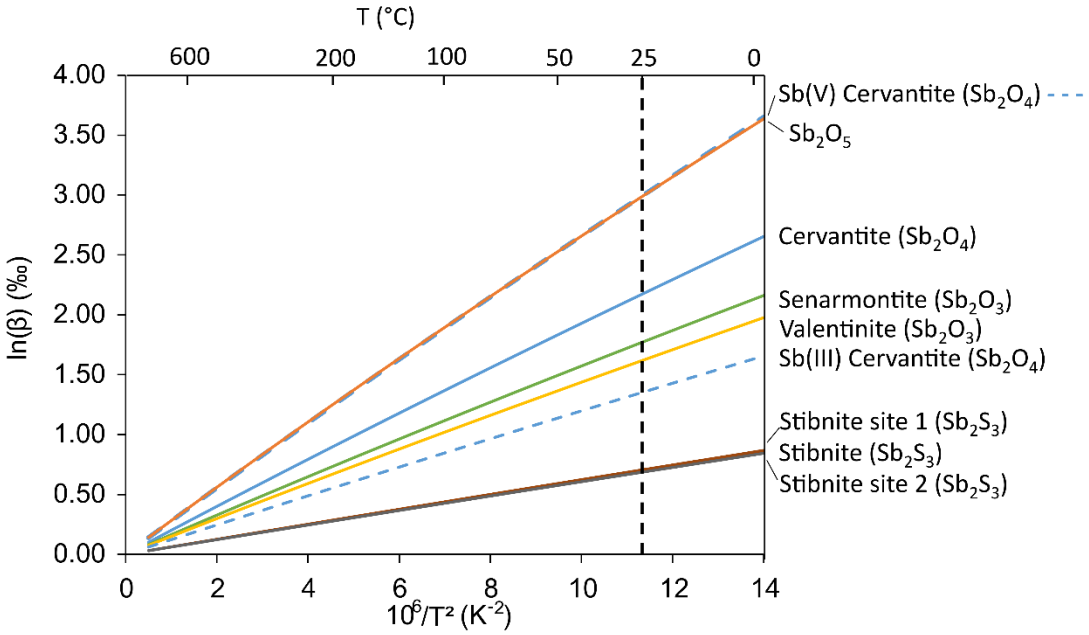

Figure 6: β-factors (in ‰) of the different mineral phases during the oxidation process of the stibnite (Sb_2S_3) to the synthetic fully oxidized mineral phase Sb_2O_5 as a function of temperature (T). The β-factors are calculated with the PBESOL functionals (us pseudopotentials). The Sb(III/V) cervantite (blue dashed lines) represents the β-factors of each individual Sb(III/V) site in cervantite.

3.4 Uncertainties of the β-factors

To evaluate the uncertainties associated with the β-factors, the calculations are made with LDA (PZ) and GGA (PBEsol and PBE) functionals. The β-factors calculated with the different functionals are represented in Figure 7 (us pseudopotentials). The variability between the three functionals is almost null for stibnite, with a difference of 0.02 ‰ between PZ and PBEsol. This difference between the functionals increases for valentinite, showing the highest difference of 0.09 ‰ between PBEsol and PZ. This difference is maximum for cervantite, with a 0.35 ‰ difference between PBE and PZ, while the difference is only 0.04 ‰ between PBEsol and PZ. These two pseudopotentials show the most similar atomic structure and vibrational properties (Table 1). The significant difference between PBE and the two other pseudopotentials could be explained by poorer reliability in the lattice reproduction and theoretical Raman frequencies for PBE and finally by a too high uncertainty. The errors on the Raman frequencies of the structures are evaluated through a linear regression between the theoretical and experimental frequencies. These regressions are reported in Figure 8. The errors are evaluated at 0.4 % for stibnite, 3.5 % for valentinite and cervantite and finally 6.5 % for senarmontite. As demonstrated in appendix B of Méheut et al. (2009), the error on the logarithmic β-factors given by the errors on the frequencies varies between n % (low temperature) and 2n % (high temperature). To have only one error per β-factors, the 2n % error will be used to estimate the errors of the structures. The error attributed to the β-factors are 0 % for stibnite, 7 % for valentinite and cervantite and 16 % for senarmontite (Table 3).

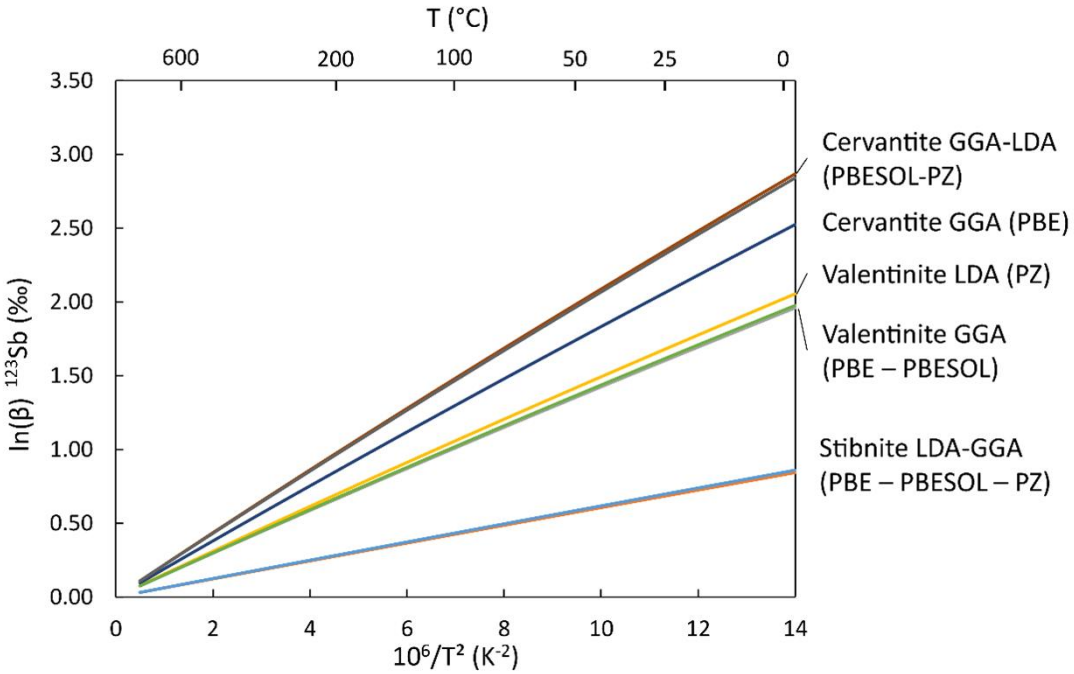

Figure 7: Comparison of the β-factors calculated using different functionals (GGA (PBE, PBEsol) and LDA (PZ)) for three different mineral phases (stibnite (Sb_2S_3), valentinite (Sb_2O_3) and cervantite (Sb_2O_4)).

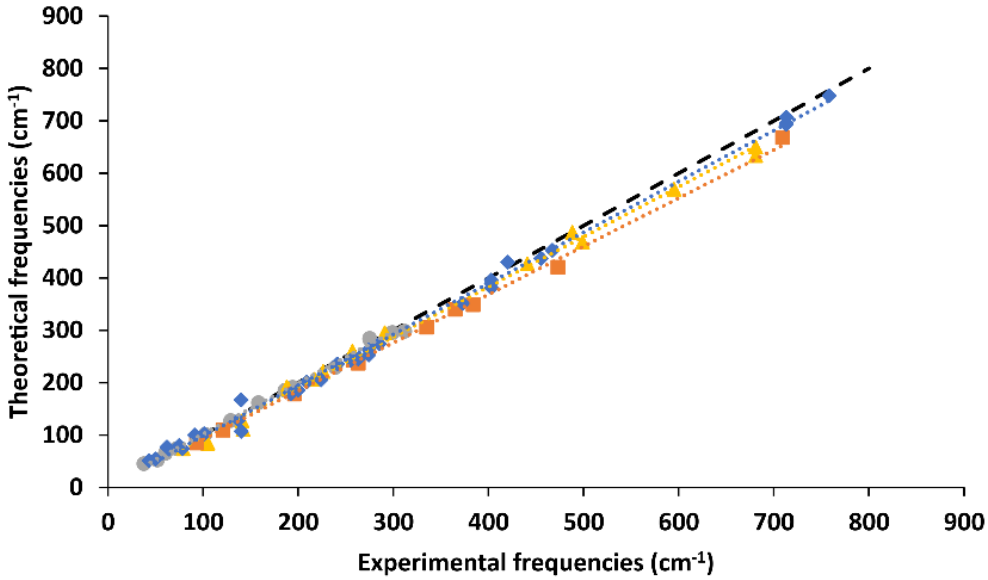

Figure 8: Theoretical Raman frequencies (PBEsol functional) as a function of the experimental Raman frequencies of the different studied minerals: stibnite (grey); valentinite (yellow), senarmontite (orange) and cervantite (blue). Linear regressions corresponding to each mineral are represented with dotted lines. The black dashed line represents the 1:1 relation.

Table 3: Raw and corrected β -factors for stibnite, valentinite, senarmontite and cervantite at 22 °C.

	Stibnite	Valentinite	Senarmontite	Cervantite
Error on Ln(β-factor) (%)	0	7	13	7
Ln(β-factor)	0.71	1.64	1.80	2.20
Corrected Ln(β-factor)	0.71	1.75	2.03	2.35

As the lattice parameters for stibnite are the least deformed compared with experimental measurements (except for axis c, composed with Van-Der-Waals bonds), it is consistent that stibnite has the smallest errors on the Raman frequencies and β-factors. Concerning senarmontite, an error of 13 % on the β-factor is estimated which translates into an error of 0.23 ‰ at 22°C for $\Delta^{123}Sb_{senarmontite-stibnite}$=1.5 ‰ and gives an estimate of the precision that can be expected using such approach.

Despite some differences between the various functionals (especially with PBE), all the models show a relatively good agreement with the experimental results. Only PBE does not show satisfying structural lattice reproduction for stibnite and valentinite with an important elongation of the a-axis, along with slightly less accurate Raman frequencies compared to the two other functionals. However, for stibnite, these structural and Raman differences do not have an impact on the final calculated β-factor. This is not the case for cervantite, where important β-factor differences are observed between PBE and the two other functionals (PZ and PBEsol).

Experimental and theoretical Raman spectrum show similar frequencies, but for cervantite, precise experimental data about the quality and symmetry of these frequencies are lacking. However, since the previous models (stibnite and valentinite) show a good correspondence with the data, it can be assumed that it is also the case for cervantite and Sb_2O_5, which does not have experimental data to support this theoretical work.

The first-principles calculations presented above quantify mass-dependent isotope fractionations originating from differences in the vibrational properties of the chemical bonds in Sb minerals. However, these calculations did not take into account the Nuclear Field Shield Effect (NFSE) for Sb nuclei, resulting from differences in volume and shapes of the atomic nuclei of the different isotopes (Schauble 2007, Fujii *et al.*, 2009). The number of protons is similar between isotopes of a single element, but their distribution in space within the nuclei can differ. This difference of size and shape can be represented as the mean-square charge radius $\langle r^2 \rangle$ (Fujii *et al.,* 2009). Usually, mass-dependent fractionation is predominant in isotopes of light elements, while NFSE becomes far more important than mass-dependent fractionation for the heavy elements (e.g. Hg, Tl, U, Yang and Liu, 2016). For Sn, an element close to Sb in terms of mass and volume, Schauble (2013) demonstrated a limited contribution of NFSE (around 5 % of the overall fractionation). More precisely, the fractionation coming from the NFSE can be written (Almoukhalalati et al., 2016, in atomic units):

$$ln\alpha_{NFSE} = \frac{\delta E_{FS}}{kT} = \frac{2\pi Z}{3} * \frac{1}{k * T} * (\bar{\rho}_e^A - \bar{\rho}_e^B) * \Delta\langle r^2_{123-121}\rangle \quad (7)$$

With $\bar{\rho}_e^A$ the effective electronic density in the nuclear volume for chemical species A (in a_0^{-3}), $\Delta\langle r^2_{123-121}\rangle$ is the change in mean-square charge radius between ^{123}Sb and ^{121}Sb, Z=51 is the number of protons of Sb, k (=3.16666 10^{-6} $Ha.K^{-1}$) is Boltzmann constant, T is the temperature in K.

The parameters controlling the NFSE are therefore the change in effective electronic density $\bar{\rho}_e$ between two species, and the change in mean-square charge radius $\langle r^2 \rangle$.

Equilibrium	Model	$\bar{\rho}_e^A - \bar{\rho}_e^B$ (a_0^3)	$ln\alpha_{NFSE}$ $^{123-121}$Sb at 22°C	$ln\alpha_{MD}$ $^{123-121}$Sb at 22°C (this work)
	CdO (monteponite)-αCd	-15.6		
Sb_2O_5-Sb_2O_3	**SnO_2(cassiterite) -SnO(romachite)**	**-26.2**	**-0.075±0.051‰**	1.23-1.38‰
	SnO(romachite)-αSn	6.2		
	HgO(montroydite)-αHg	-48.4		
	CdO (monteponite)-CdS (hawleyite)	-4.9		
Sb_2O_3-Sb_2S_3	**SnO(romachite) -SnS**	**-8.3**	**-0.024±0.016‰**	1.09-0.93‰
	HgO(montroydite)-HgS(cinnabar)	-18.9		

Table 4. Estimates (Schauble 2013) of changes in effective electron density at the nucleus for various equilibria similar to Sb_2O_5-Sb_2O_3 (oxygen reductions $M^{n+}O_{n/2}$ -$Mn^{(n-2)+}O_{(n-2)/2}$) or to Sb_2O_3-Sb_2S_3 (O-S exchanges). In bold are the most relevant estimate. $ln\alpha_{NFSE}{}^{123-121}Sb\ (22°C)$ is calculated from eq. 7 with $\Delta\langle r^2_{123-121}\rangle = 0.25\ \pm 0.17\ 10^{-10}\ a_0^2$ (Angeli and Marinova 2013). $ln\alpha_{MD}{}^{123-121}Sb$ is calculated from Table 2 (with Sb_2O_3 taken as valentinite for the first value and senarmontite for the second).

Regarding the change in effective electronic density, to our knowledge, there is no study in the literature estimating this quantity for Sb species. However, Schauble (2013) computed the NFSE effect for various species for Sn, Hg and Tl isotopes. The Sn system is particularly appealing, as it is just before Sb in the periodic table. As shown in Table 4, we suggest to model the change in effective density for the Sb_2O_5-Sb_2O_3 equilibrium with the SnO_2(cassiterite)-SnO(romachite) equilibrium, and for the Sb_2O_3-Sb_2S_3 equilibrium with the SnO(romachite) -SnS equilibrium. The NFSE estimated using these values and the change in nuclear radius $\Delta\langle r^2_{123-121}\rangle = 0.25\ \pm 0.17\ 10^{-10}\ a_0^2$ (Angeli and Marinova, 2013) is rather limited (below 5 %) with respect to the conventional mass-dependent fractionation. Note that the uncertainty on this effect is rather large due principally to large uncertainties on the estimate of $\Delta\langle r^2_{123-121}\rangle$ (Angeli et Marinova 2013). Other examples of changes in effective density are given in Table 4, for various other systems. This illustrates that for systems with similar Z, and for similar equilibria, the corresponding changes in effective densities remain in the same range as our estimate. As rough as our estimate may be, it is therefore unlikely that NFSE contributes significantly to the overall Sb fractionation.

4. Discussion

4.1. Parameters controlling the isotopic fractionation

The results allow to predict Sb isotope fractionation (direction and amplitude) between different secondary Sb mineral phases of the oxidation chain of stibnite and to identify the factors responsible for this fractionation. In order of importance of the magnitude of the induced fractionation, these factors are: the change of Sb oxidation state, the change of the first neighbour of Sb and the distortion of the atomic Sb - O polyhedron.

The change from Sb(III) oxidation state in Sb(III)-phases (valentinite and senarmontite) to mixed Sb(III)/Sb(V)-phase (cervantite) or Sb(V)-phases (Sb_2O_5) induced an increase of the β-factor. A number of theoretical studies have been carried out to quantify the equilibrium isotope fractionation between different oxidation states of metals (Cu, Fe, Mo, Cr, Se, Tl, …) (Asael et al., 2007; Polyakov and Mineev, 2000; Tossell, 2005). They predicted that oxidized species are preferentially enriched in heavy isotopes due to the difference in bond length and strength (Asael et al., 2007). Experimental studies showed the same trend. For Se, oxidative dissolution of selenide-bearing minerals ferroselite ($FeSe_2$) and berzelianite (Cu_2Se) produced an enrichment in the heavier isotopes in dissolved Se compared to the initial minerals, although factors other than redox changes could have been involved in fractionation (e.g. dissolution, adsorption…) Wasserman et al. (2021). Oxidative weathering of crustal Cr(III)-bearing minerals results in the release of ^{53}Cr-enriched mobile Cr(VI) to the solution (Gilleaudeau et al., 2016). Similar to chromium, redox transformations between Cu(I) and Cu(II) species are the main processes in natural systems resulting in Cu isotope fractionation (Little et al., 2017, 2014). For example, reduced and precipitated Cu(I) species are known to be lighter by 2 ‰ to 5 ‰ relative to dissolved Cu(II) species (Ryan et al., 2014). Among experimental studies dealing with metal(loid) isotope

fractionation related to redox changes, only two were dedicated to Sb. Antimony(V) reduction experiments were carried out by Rouxel et al. (2003) and showed that this process generated an isotopic fractionation between oxidized and reduced species $\Delta^{123}Sb_{Sb(V)-Sb(III)}$ of about 0.90 ‰. Mackinney (2016) also observed significant fractionation in the same direction, during the reduction of aqueous Sb(V) by sulphide to form solid $Sb(III)_2S_3$ resulting in a $\Delta^{123}Sb_{Sb(V)-Sb(III)2S3-}$ of 1.45‰. In this latter study, other factors contributing to Sb isotope fractionation are probably superimposed to the redox effect, such as the effect of the bounding environment (Sb-Cl bonds in $Sb(V)Cl_5$ and Sb-S bonds in Sb_2S_3) and phase change (liquid to solid).

The change in the first neighbour of Sb also showed a significant effect on Sb isotopes in the present study. Sb-O bonds tend to concentrate ^{123}Sb isotope compared to Sb-S bonds. Trivalent atomic Sb-O bonds in cervantite are on average shorter than trivalent Sb-S bonds in the stibnite (more than 0.6 Å difference, Table 1) and stibnite also has a higher coordination number for Sb(III) (Figure 1), which could also explain its lower retention of the heavy isotope (^{123}Sb) compared to Sb-O. The control on fractionation properties can also be explored based on vibrational analysis (Figure S1, see Méheut et al 2009 for details). The vibrational analysis expresses the contributions of each vibrational mode to the β-factor. Vibrational analyses for stibnite and valentinite are compared on Figure S1, showing that most of the Raman frequencies contribute to the β-factor. As a consequence, it is essentially shown that the higher valentinite β-factor is explained by its generally higher vibrational frequencies, therefore its generally stiffer bonds. Indeed, the heavy isotopes of an element tend to be concentrated in substances where that element forms the stiffest bonds (Schauble, 2004) and generally the lowest coordination number. Liu et al. (2021) in a first-principles study about Cu isotopes showed that similar changes from Cu – S to Cu – O structures favoured the heavy isotope by an increase of the β-factor around 1.2 to 1.8 ‰. Unfortunately, data in the literature are too scarce to compare the order of magnitude of the modelled Sb isotope fractionation with environmental Sb data.

However, there are some apparent discrepancies with respect to these general isotope fractionation rule of thumb. On average, cervantite has longer Sb – O bonds than valentinite but presents a significantly higher β-factor (> 0.5 ‰), which is clearly contradictory with those tendencies. The relation between the average atomic bond length and β-factor no longer holds when comparing atomic structures with different atomic bonds, oxidation level and coordination numbers. The β-factor calculated for trivalent antimony in cervantite on one hand and for pentavalent antimony in cervantite, on the other hand, showed that pentavalent Sb possesses a higher β-factor than trivalent Sb in this structure (Figure 6). Thus, the higher enrichment in heavy isotope in cervantite compared to valentinite is explained by the presence of Sb(V) which makes, on average, the cervantite enriched in the heavy isotope. The effect of the coexistence of different sites was also studied by Ducher et al. (2016) on the three different Zn sites in hydrozincite (1 tetra-coordinated and 2 hexa-coordinated sites). The two hexa-coordinated sites were consequently enriched in heavy isotopes compared with other hexa-coordinated sites of another mineral (smithsonite), between 0.50 to 0.65 ‰ while their Zn – O bond lengths were comparable. This difference was assumed to be caused by the difference in first-neighbours and the change of partial negative charge of the O atom in hydrozincite caused by the presence of a hydroxyl group instead of a single O atom.

The three trivalent Sb(III) – O phases (senarmontite, valentinite and Sb(III) in cervantite) exhibited slightly different (more than 0.14 Å) average Sb – O bond length. This difference could be explained by the inclusion of Sb(V) in cervantite besides Sb(III) or by the adaptation to the orthorhombic cell of the valentinite, which induces a distortion on the Sb – O polyhedral structure affecting atomic bond lengths, angles and volume, inducing a loss of symmetry and an increase of the disorder of the structure, as it was proposed for Ge (Pokrovsky et al., 2014). Nevertheless, these small Sb – O bond length differences affected only slightly the β-factor.

The Sb – S bond length and coordination number differences in stibnite between the two Sb sites also induce very small difference in the β-factor (0.02 ‰), which is much smaller than variations between the different atomic dispositions of the Sb_2O_3 minerals and sites.

4.2. Implications for environmental applications

Understanding the parameters controlling isotope fractionation that occurs during different geochemical processes is an important step for developing the applications of Sb isotopes to sources or processes tracking. This study provides information on the direction and amplitude of Sb isotope fractionation expected between solid phases that are important Sb-bearing minerals in the supergene environment. Theoretical Sb isotope fractionation spans over 2.3 ‰ at 22 °C which is similar to the range of isotopic composition observed in natural samples (Rouxel et al., 2003; Da Wang et al., 2021; Zhai et al., 2021). The studied minerals that compose the stibnite oxidation chain were chosen because of their ubiquity in the supergene zone, especially in Sb-sulphide mining areas. These minerals play an essential role in limiting Sb mobility in mining wastes and rivers impacted by mine drainage (Filella et al., 2009; Roper et al., 2012). All the studied secondary Sb minerals were found to be isotopically heavier than the initial stibnite. This suggests that the oxidative weathering of sulphide minerals in waste piles could significantly modify the Sb isotope ratio. This has a strong implication for the application of Sb isotopes as a tracer of contamination source; a range of Sb isotope signatures of about ~1 ‰ could be expected in a single mining district as a result of alteration processes. We showed that redox change from Sb(III) to Sb(V) was the transformation that most affected the Sb isotope composition, by up to 1.2 ‰ (Sb_2O_5 - senarmontite). This supports the idea that Sb isotopes could be a powerful tracer of redox and paleo-redox conditions. The calculated fractionation factor is close to the fractionation factor observed during experimental reduction of aqueous Sb(V) to Sb(III), which gave $\Delta^{123}Sb_{Sb(V)-Sb(III)}$ = 0.9 ‰ (Rouxel et al., 2003). Field observations showed the same trend; aqueous Sb(V) in the drainage water of an Sb mine showed a heavier isotope composition (+ 0.35 ‰) than Sb from the primary stibnite in the mine wastes (Tanimizu et al., 2011). However, a number of processes are superimposed to redox changes under environmental conditions, that can produce some differences in Sb isotope fractionation factors. Wang et al. (2021) showed that stibnite precipitation from hydrothermal systems was isotopically lighter than the ore-forming fluid with an $\alpha_{fluid-stibnite}$ between 0.9991 and 0.9994 ($\Delta^{123}Sb_{fluid-stibnite}$ between 0.6 to 0.9 ‰), which is similar to the values reported in the Table S6 ($\Delta^{123}Sb_{Sb2O5-stibnite}$ = 0.75 ‰ at 260 °C, which is within the temperature range of ore formation indicated in Wang et al. (2021)).
Furthermore, the β-factors determined in the present study are calculated with pure phases and perfect Sb – O structure, with a precise stoichiometric number of Sb sites, which is not the case for natural minerals. Impurities in the crystal could impact the β-factor by lowering it, through atomic structure distortions (and then Sb – O distances changes) or, valence modification (W. Wang et al. 2017; C. Gao et Liu 2021). Finally, it is noteworthy that when the studied transformations occur in the environment, kinetic fractionation processes could alter the isotopic signature of the mineral, especially during phase change (e.g. solid to liquid).
Nevertheless, this study provides trends for Sb isotope behaviour during oxidative dissolution of stibnite and subsequent precipitation of Sb(III) and Sb(V) oxides in sulphide mining environments (Filella et al., 2009; Resongles et al., 2013). Secondary minerals of stibnite, such as valentinite and cervantite are expected to have a higher $\delta^{123}Sb$ signature due to the nature of the atomic bonds (shorter and more energetic). These theoretical data will help in interpreting Sb isotope signatures along mine waste profiles or mine drainage. Moreover, the results give some clues for interpreting Sb isotope signature variations in other contaminated contexts such as the urban environment, where both Sb sulphides and Sb oxides have been evidenced in traffic-related dust (Varrica et al., 2013) and in natural system, including to better understand isotope variations during Sb ore formation.

5. Conclusion

Equilibrium Sb isotopes fractionation factors are calculated from first-principles in minerals involved in the oxidation process from stibnite to cervantite and a further oxidation step with Sb_2O_5. Good agreement is obtained between theoretical and experimental data, showing reliable calculated β-factors. Among the studied minerals, stibnite (Sb_2S_3) is found to have the lowest β-factor (ln(β) = 0.71 ‰ at 22°C) due to the weakest Sb – S bonds, then valentinite (ln(β) = 1.64 ‰ at 22°C), senarmontite (ln(β) = 1.80 ‰ at 22°c), cervantite (ln(β) = 2.20 ‰ at 22°C) and Sb_2O_5 (ln(β) = 3.03 ‰ at 22°C). Such a wide range of variation indicates that the isotopes of this element could be used as a geochemical tracer. The main factors controlling the isotopic fractionation are found to be, in order of importance, the oxidation

level (Sb(V) is isotopically heavier than Sb(III)), the nature of the atomic bond (Sb – S is isotopically lighter than Sb – O) and finally, the average bond length between Sb and its first neighbour and structural distortion of the atomic polyhedron (the most distorted the atomic structure is, the weakest are the atomic bonds). These calculations represent a first step to understand the geochemical cycle of Sb isotopes in the environment with the aim to use Sb isotopes for investigating the transformation processes and Sb sources. However, these β-factors should be considered cautiously in future environmental studies since equilibrium isotopic exchanges can be disturbed by kinetic fractionation. Nevertheless, these new theoretical data will be useful for future interpretation of Sb isotope signature in natural or impacted environments and to understand the origin of isotopic variations. To further improve the understanding of Sb isotopic system, future theoretical work should focus on estimating equilibrium mass-dependent isotope fractionation among aqueous Sb species and between aqueous and solid Sb species as well as quantifying precisely the mass-independent Sb isotope fractionation driven by the nuclear shield shift effect.

Conflicts of interest

There are no conflicts of interest to declare.

Acknowledgements

This work received financial support from the CNRS INSU EC2CO program (Project AntiBol). This work was granted access to the HPC resources of CALMIP supercomputing center under the allocation Grant P1037-2021.

References

Allen, J.P., Carey, J.J., Walsh, A., Scanlon, D.O., Watson, G.W., 2013. Electronic Structures of Antimony Oxides. J. Phys. Chem. C 117, 14759–14769. https://doi.org/10.1021/jp4026249

Almoukhalalati, A., Shee, A., Saue, T., 2016. Nuclear size effects in vibrational spectra. Physical Chemistry Chemical Physics 18, 15406–15417. 10.1039/C6CP01913G

Angeli, I. and Marinova, K.P. 2013. Table of experimental nuclear ground state charge radii: An update. Atomic Data and Nuclear Data Tables, 99(1), pp. 69–95. https://doi.org/10.1016/j.adt.2011.12.006.

Asael, D., Matthews, A., Bar-Matthews, M., Halicz, L., 2007. Copper isotope fractionation in sedimentary copper mineralization (Timna Valley, Israel). Chemical Geology 243, 238–254. https://doi.org/10.1016/j.chemgeo.2007.06.007

Ashley, P.M., Craw, D., Graham, B.P., Chappell, D.A., 2003. Environmental mobility of antimony around mesothermal stibnite deposits, New South Wales, Australia and southern New Zealand. Journal of Geochemical Exploration 77, 1–14. https://doi.org/10.1016/S0375-6742(02)00251-0

Aufmuth, P., Heilig, K. and Steudel, A. 1987. Changes in mean-square nuclear charge radii from optical isotope shifts. Atomic Data and Nuclear Data Tables, 37(3), pp. 455–490.: https://doi.org/10.1016/0092-640X(87)90028-3.

Baroni, S., de Gironcoli, S., Dal Corso, A., Giannozzi, P., 2001. Phonons and related crystal properties from density-functional perturbation theory. Rev. Mod. Phys. 73, 515–562. https://doi.org/10.1103/RevModPhys.73.515

Bigeleisen, J., Mayer, M.G., 1947. Calculation of Equilibrium Constants for Isotopic Exchange Reactions. J. Chem. Phys. 15, 261–267. https://doi.org/10.1063/1.1746492

Cai, Y., Yang, C., Xu, D., Gui, W., 2018. Quantitative analysis os stibnite content in a raw ore by Raman spectroscopy and chemometric tools. Journal of Raman spectroscopy 50, 454–464. https://doi.org/10.1002/jrs.5527

Chang, T.-L., Qian, Q.-Y., Zhao, M.-T., Wang, J., 1993. The isotopic abundance of antimony. International Journal of Mass Spectrometry and Ion Processes 123, 77–82. https://doi.org/10.1016/0168-1176(93)87056-X

Cheema, A.I., Liu, G., Yousaf, B., Abbas, Q., Zhou, H., 2020. A comprehensive review of biogeochemical distribution and fractionation of lead isotopes for source tracing in distinct interactive environmental compartments. Science of The Total Environment 719, 135658. https://doi.org/10.1016/j.scitotenv.2019.135658

Cody, C.A., Dicarlo, L., Darlington, R.K., 1979. Vibrational and Thermal Study of Antimony Oxides. Inorganic Chemistry 18, 1572–1576. https://doi.org/0020-1669/79/1318-1572$01.00/0

Dal Corso, A., 2014. Pseudopotentials periodic table : From H to Pu. Computational Materials Science 95, 337–350. http://dx.doi.org/10.1016/j.commatsci.2014.07.043

Degryse, P., Lobo, L., Shortland, A., Vanhaecke, F., Blomme, A., Painter, J., Gimeno, D., Eremin, K., Greene, J., Kirk, S., Walton, M., 2015. Isotopic investigation into the raw materials of Late Bronze Age glass making. Journal of Archaeological Science 62, 153–160. https://doi.org/10.1016/j.jas.2015.08.004

Degryse, P., Shortland, A.J., Dillis, S., van Ham-Meert, A., Vanhaecke, F., Leeming, P., 2020. Isotopic evidence for the use of Caucasian antimony in Late Bronze Age glass making. Journal of Archaeological Science 120, 105195. https://doi.org/10.1016/j.jas.2020.105195

Dillis, S., Ham-Meert, A.V., Leeming, P., Shortland, A., Gobejishvili, G., Abramishvili, M., Degryse, P., 2019. Antimony as a raw material in ancient metal and glass making: provenancing Georgian LBA metallic Sb by isotope analysis. STAR: Science & Technology of Archaeological Research 5, 1–15. https://doi.org/10.1080/20548923.2019.1681138

Ducher, M., Blanchard, M., Balan, E., 2016. Equilibrium zinc isotope fractionation in Zn-bearing minerals from first-principles calculations. Chemical Geology 443, 87–96. https://doi.org/10.1016/j.chemgeo.2016.09.016

Filella, M., Philippo, S., Belzile, N., Chen, Y., Quentel, F., 2009. Natural attenuation processes applying to antimony: A study in the abandoned antimony mine in Goesdorf, Luxembourg. Science of The Total Environment 407, 6205–6216. https://doi.org/10.1016/j.scitotenv.2009.08.027

Filip, M.R., Patrick, C.E., Giustino, F., 2013. GW quasiparticle band structures of stibnite, antimonselite, bismuthinite, and guanajuatite. Phys. Rev. B 87, 205125. https://doi.org/10.1103/PhysRevB.87.205125

Fujii, T., Moynier, F., Uehara, A., Abe, M., Yin, Q.-Z., Nagai, T., Yamana, H., 2009. Mass-Dependent and Mass-Independent Isotope Effects of Zinc in a Redox Reaction. J. Phys. Chem. A 113, 12225–12232. https://doi.org/10.1021/jp904882d

Fujii, T., Moynier, F., Blichert-Toft, J., Albarède, F., 2014. Density functional theory estimation of isotope fractionation of Fe, Ni, Cu, and Zn among species relevant to geochemical and biological environments. Geochimica et Cosmochimica Acta 140, 553–576. https://doi.org/10.1016/j.gca.2014.05.051

Gamrath, S., Palmeri, P., Quinet, P., Bouazza, S., Godefroid, M., 2018. MCDHF calculations of isotope shifts in neutral antimony. Journal of Quantitative Spectroscopy and Radiative Transfer 218, 38–45. https://doi.org/10.1016/j.jqsrt.2018.07.004

Gao, C., Liu, Y., 2021. First-principles calculations of equilibrium bromine isotope fractionations. Geochimica et Cosmochimica Acta 297, 65–81. https://doi.org/10.1016/j.gca.2021.01.010

Giannozzi, P., Andreussi, O., Brumme, T., Bunau, O., Nardelli, M.B., Calandra, M., Car, R., Cavazzoni, C., Ceresoli, D., Cococcioni, M., Colonna, N., Carnimeo, I., Corso, A.D., Gironcoli, S. de, Delugas, P., DiStasio, R.A., Ferretti, A., Floris, A., Fratesi, G., Fugallo, G., Gebauer, R., Gerstmann, U., Giustino, F., Gorni, T., Jia, J., Kawamura, M., Ko, H.-Y., Kokalj, A., Küçükbenli, E., Lazzeri, M., Marsili, M., Marzari, N., Mauri, F., Nguyen, N.L., Nguyen, H.-V., Otero-de-la-Roza, A., Paulatto, L., Poncé, S., Rocca, D., Sabatini, R., Santra, B., Schlipf, M., Seitsonen, A.P., Smogunov, A., Timrov, I., Thonhauser, T., Umari, P., Vast, N., Wu, X., Baroni, S., 2017. Advanced capabilities

for materials modelling with Quantum ESPRESSO. J. Phys.: Condens. Matter 29, 465901. https://doi.org/10.1088/1361-648X/aa8f79

Giannozzi, P., Baroni, S., Bonini, N., Calandra, M., Car, R., Cavazzoni, C., Ceresoli, D., Chiarotti, G.L., Cococcioni, M., Dabo, I., Corso, A.D., Gironcoli, S. de, Fabris, S., Fratesi, G., Gebauer, R., Gerstmann, U., Gougoussis, C., Kokalj, A., Lazzeri, M., Martin-Samos, L., Marzari, N., Mauri, F., Mazzarello, R., Paolini, S., Pasquarello, A., Paulatto, L., Sbraccia, C., Scandolo, S., Sclauzero, G., Seitsonen, A.P., Smogunov, A., Umari, P., Wentzcovitch, R.M., 2009. QUANTUM ESPRESSO: a modular and open-source software project for quantum simulations of materials. J. Phys.: Condens. Matter 21, 395502. https://doi.org/10.1088/0953-8984/21/39/395502

Gilleaudeau, G.J., Frei, R., Kaufman, A.J., Kah, L.C., Azmy, K., Bartley, J.K., Chernyavskiy, P., Knoll, A.H., 2016. Oxygenation of the mid-Proterozoic atmosphere: clues from chromium isotopes in carbonates. Geochemical Perspectives Letters 2, 178–187. https://doi.org/10.7185/geochemlet.1618

Gonçalves, R.A., Baldan, M.R., Chiquito, A.J., Berengue, O.M., 2018. Synthesis of orthorhombic Sb2O3 branched rods by a vapor–solid approach. Nano-Structures & Nano-Objects 16, 127–133. https://doi.org/10.1016/j.nanoso.2018.05.008

Gopalakrishnan, P., Manohar, H., 1975. Cervantite, Alpha -Sb2O4. Cryst. Struct. Communic.

He, M., Wang, N., Long, X., Zhang, C., Ma, C., Zhong, Q., Wang, A., Pervaiz, A., Shan, J., 2019. Antimony speciation in the environment: Recent advances in understanding the biogeochemical processes and ecological effects. Journal of Environmental Sciences 75, 14–39. https://doi.org/10.1016/j.jes.2018.05.023

Hiller, E., Lalinská, B., Chovan, M., Jurkovič, Ľ., Klimko, T., Jankulár, M., Hovorič, R., Šottník, P., Fľaková, R., Ženišová, Z., Ondrejková, I., 2012. Arsenic and antimony contamination of waters, stream sediments and soils in the vicinity of abandoned antimony mines in the Western Carpathians, Slovakia. Applied Geochemistry 27, 598–614. https://doi.org/10.1016/j.apgeochem.2011.12.005

Ibáñez, J., Sans, J.A., Popescu, C., López-Vidrier, J., Elvira-Betanzos, J.J., Cuenca-Gotor, V.P., Gomis, O., Manjón, F.J., Rodríguez-Hernández, P., Muñoz, A., 2016a. Structural, Vibrational, and Electronic Study of Sb2S3 at High Pressure. J. Phys. Chem. C 120, 10547–10558. https://doi.org/10.1021/acs.jpcc.6b01276

Jansen, M., 1979. Preparation and crystal structure of antimony oxyde hydrate (Sb2O5. 3/5H2O ; SB5O12 (OH).H20). Acta Crystallographica, Section B 35, 539–542.

Komárek, M., Ratié, G., Vaňková, Z., Šípková, A., Chrastný, V., 2021. Metal isotope complexation with environmentally relevant surfaces: Opening the isotope fractionation black box. Critical Reviews in Environmental Science and Technology 1–31. https://doi.org/10.1080/10643389.2021.1955601

Kyono, A., Kimata, M., 2004. Structural variations induced by difference of the inert pair effect in the stibnite-bismuthinite solid solution series (Sb,Bi)2S3. American Mineralogist 89, 932–940. https://doi.org/10.2138/am-2004-0702

Lazzeri, M., Mauri, F., 2003. First-Principles Calculation of Vibrational Raman Spectra in Large Systems: Signature of Small Rings in Crystalline SiO2. Phys. Rev. Lett. 90, 036401. https://doi.org/10.1103/PhysRevLett.90.036401

Little, S.H., Sherman, D.M., Vance, D., Hein, J.R., 2014. Molecular controls on Cu and Zn isotopic fractionation in Fe–Mn crusts. Earth and Planetary Science Letters 396, 213–222. https://doi.org/10.1016/j.epsl.2014.04.021

Little, S.H., Vance, D., McManus, J., Severmann, S., Lyons, T.W., 2017. Copper isotope signatures in modern marine sediments. Geochimica et Cosmochimica Acta 212, 253–273. https://doi.org/10.1016/j.gca.2017.06.019

Liu, F., Le, X.C., McKnight-Whitford, A., Xia, Y., Wu, F., Elswick, E., Johnson, C.C., Zhu, C., 2010. Antimony speciation and contamination of waters in the Xikuangshan antimony mining and smelting

area, China. Environ Geochem Health 32, 401–413. https://doi.org/10.1007/s10653-010-9284-z

Liu, S., Li, Y., Liu, Jie, Yang, Z., Liu, Jianming, Shi, Y., 2021. Equilibrium Cu isotope fractionation in copper minerals: a first-principles study. Chemical Geology 564, 120060. https://doi.org/10.1016/j.chemgeo.2021.120060

Lobo, L., Degryse, P., Shortland, A., Eremin, K., Vanhaecke, F., 2014. Copper and antimony isotopic analysis via multi-collector ICP-mass spectrometry for provenancing ancient glass. Journal of Analytical Atomic Spectrometry 29, 58–64. https://doi.org/10.1039/C3JA50303H

Lobo, L., Degryse, P., Shortland, A., Vanhaecke, F., 2013. Isotopic analysis of antimony using multi-collector ICP-mass spectrometry for provenance determination of Roman glass. Journal of Analytical Atomic Spectrometry 28, 1213–1219. https://doi.org/10.1039/c3ja50018g

Mackinney, J.S., 2016. Antimony isotopes as indicator of RedOx reactions in aqueous systems: fractionation during Sb(V) reduction by sulfide and isotope exchange kinetics between dissolved Sb(III) and Sb(V) (Thesis). University of Illinois at Urbana-Champaign.

Méheut, M., Lazzeri, M., Balan, E., Mauri, F., 2009. Structural control over equilibrium silicon and oxygen isotopic fractionation: A first-principles density-functional theory study. Chemical Geology, Applications of non-traditional stable isotopes in high-temperature geochemistry 258, 28–37. https://doi.org/10.1016/j.chemgeo.2008.06.051

Méheut, M., Lazzeri, M., Balan, E., Mauri, F., 2007a. Equilibrium isotopic fractionation in the kaolinite, quartz, water system: Prediction from first-principles density-functional theory. Geochimica et Cosmochimica Acta 71, 3170–3181. https://doi.org/10.1016/j.gca.2007.04.012

Méheut-Le Quéau, M., 2008. Calcul prédictif du facteur de partage isotopique entre minéraux dans le cadre de la théorie de la fonctionnelle de la densité (phdthesis). Université Pierre et Marie Curie - Paris VI.

Méheut, M., Ibañez-Mejia, M., Tissot, F.L.H., 2021. Drivers of zirconium isotope fractionation in Zr-bearing phases and melts: The roles of vibrational, nuclear field shift and diffusive effects. Geochimica et Cosmochimica Acta 292, 217–234. https://doi.org/10.1016/j.gca.2020.09.028

Mestl, G., Ruiz, P., Delmon, B., Knözinger, H., 1994. Sb_2O_3/Sb_2O_4 in Reducing/oxidizing Environments: An in Situ Raman Spectroscopy Study. Journal of Physical Chemistry 11276–11282. https://doi.org/0022-3654/94/2098-11276$04.50/0

Momma, K., Izumi, F., 2011. VESTA 3 for three-dimensional visualization of crystal, volumetric and morphology data. J Appl Cryst 44, 1272–1276. https://doi.org/10.1107/S0021889811038970

Monkhorst, H.J., Pack, J.D., 1976. Special points for Brillouin-zone integrations. Phys. Rev. B 13, 5188–5192. https://doi.org/10.1103/PhysRevB.13.5188

Moynier, F., Fujii, T., Telouk, P., 2009. Mass-independent isotopic fractionation of tin in chemical exchange reaction using a crown ether. Analytica Chimica Acta 632, 234–239. https://doi.org/10.1016/j.aca.2008.11.015

Moynier, F., Vance, D., Fujii, T., Savage, P., 2017. The Isotope Geochemistry of Zinc and Copper. Reviews in Mineralogy and Geochemistry 82, 543–600. https://doi.org/10.2138/rmg.2017.82.13

Perdew, J.P., Burke, K., Ernzerhof, M., 1996. Generalized Gradient Approximation Made Simple. Phys. Rev. Lett. 77, 3865–3868. https://doi.org/10.1103/PhysRevLett.77.3865

Perdew, J.P., Ruzsinszky, A., Csonka, G.I., Vydrov, O.A., Scuseria, G.E., Constantin, L.A., Zhou, X., Burke, K., 2008. Restoring the Density-Gradient Expansion for Exchange in Solids and Surfaces. Phys. Rev. Lett. 100, 136406. https://doi.org/10.1103/PhysRevLett.100.136406

Perdew, J.P., Zunger, A., 1981. Self-interaction correction to density-functional approximations for many-electron systems. Phys. Rev. B 23, 5048–5079. https://doi.org/10.1103/PhysRevB.23.5048

Pereira, A.L.J., Gracia, L., Santamaría-Pérez, D., Vilaplana, R., Manjón, F.J., Errandonea, D., Nalin, M., Beltrán, A., 2012. Structural and vibrational study of cubic Sb2O3 under high pressure. Phys. Rev. B 85, 174108. https://doi.org/10.1103/PhysRevB.85.174108

Pokrovsky, O.S., Galy, A., Schott, J., Pokrovski, G.S., Mantoura, S., 2014. Germanium isotope fractionation during Ge adsorption on goethite and its coprecipitation with Fe oxy(hydr)oxides. Geochimica et Cosmochimica Acta 131, 138–149. https://doi.org/10.1016/j.gca.2014.01.023

Polyakov, V.B., Mineev, S.D., 2000. The use of Mössbauer spectroscopy in stable isotope geochemistry. Geochimica et Cosmochimica Acta 64, 849–865. https://doi.org/10.1016/S0016-7037(99)00329-4

Resongles, E., Casiot, C., Elbaz-Poulichet, F., Freydier, R., Bruneel, O., Piot, C., Delpoux, S., Volant, A., Desoeuvre, A., 2013. Fate of Sb(V) and Sb(III) species along a gradient of pH and oxygen concentration in the Canoulès mine waters (Southern France). Environmental Science Processes and Impacts 15, 1536–1544. https://doi.org/10.1039/c3em00215b

Resongles, E., Freydier, R., Casiot, C., Viers, J., Chmeleff, J., Elbaz-Poulichet, F., 2015. Antimony isotopic composition in river waters affected by ancient mining activity. Talanta 144, 851–861. http://dx.doi.org/10.1016/j.talanta.2015.07.013

Roper, A.J., Willials, P.A., Montserrat, F., 2012a. Secondary antimony minerals: Phases that control the dispersion of antimony in the supergene zone. Chimie der Erde 72, 9–14.

Rouxel, O., Ludden, J., Fouquet, Y., 2003. Antimony isotope variations in natural systems and implications for their use as geochemical tracers. Chemical Geology 200, 25–40. https://doi.org/10.1016/S0009-2541(03)00121-9

Ryan, B.M., Kirby, J.K., Degryse, F., Scheiderich, K., McLaughlin, M.J., 2014. Copper Isotope Fractionation during Equilibration with Natural and Synthetic Ligands. Environ. Sci. Technol. 48, 8620–8626. https://doi.org/10.1021/es500764x

Schauble, E.A., 2004. Applying Stable Isotope Fractionation Theory to New Systems. Reviews in Mineralogy and Geochemistry 55, 65–111. https://doi.org/10.2138/gsrmg.55.1.65

Schauble, E.A., 2007. Role of nuclear volume in driving equilibrium stable isotope fractionation of mercury, thallium, and other very heavy elements. Geochimica et Cosmochimica Acta 71, 2170–2189. https://doi.org/10.1016/j.gca.2007.02.004

Schauble, E.A., Méheut, M., Hill, P.S., 2009. Combining Metal Stable Isotope Fractionation Theory with Experiments. Elements 5, 369–374. https://doi.org/10.2113/gselements.5.6.369

Schauble, E.A., 2013. Modeling nuclear volume isotope effects in crystals. Proceedings of the National Academy of Sciences 110, 17714–17719. https://doi.org/10.1073/pnas.1216216110

Scheurer, M., Schmutz, B., Happel, O., Brauch, H.-J., Wüsler, R., Storck, F.R., 2014. Transformation of the artificial sweetener acesulfame by UV light. Science of the Total Environment 425–432. http://dx.doi.org/10.1016/j.scitotenv.2014.02.047

Sereni, P., Musso, M., Knoll, P., Blaha, P., Schwarz, K., Schmidt, G., 2010. Polarization-Dependent Raman Characterization of Stibnite (Sb2S3).

Sherman, D.M., 2013. Equilibrium isotopic fractionation of copper during oxidation/reduction, aqueous complexation and ore-forming processes: Predictions from hybrid density functional theory. Geochimica et Cosmochimica Acta 118, 85–97. https://doi.org/10.1016/j.gca.2013.04.030

Sundar, S., Chakravarty, 2010. Antimony Toxicity. International Journal of Environmental Research and Public Health 7, 4267–4277. https://doi.org/10.3390/ijerph7124267

Svensson, C., 1975. Refinement of the crystal structure of cubic antimony trioxide, Sb2O3. Acta Cryst B 31, 2016–2018. https://doi.org/10.1107/S0567740875006759

Tanimizu, M., Araki, Y., Asaoka, S., Takahashi, Y., 2011. Determination of natural isotopic variation in antimony using inductively coupled plasma mass spectrometry for an uncertainty estimation of the standard atomic weight of antimony. Geochemical Journal 45, 27–32.

Tian, H., Zhou, J., Zhu, C., Zhao, D., Gao, J., Hao, J., He, M., Liu, K., Wang, K., Hua, S., 2014. A Comprehensive Global Inventory of Atmospheric Antimony Emissions from Anthropogenic Activities, 1995–2010. Environ. Sci. Technol. 48, 10235–10241. https://doi.org/10.1021/es405817u

Tossell, J.A., 2005. Calculating the partitioning of the isotopes of Mo between oxidic and sulfidic species in aqueous solution. Geochimica et Cosmochimica Acta 69, 2981–2993. https://doi.org/10.1016/j.gca.2005.01.016

Urey, H.C., 1947. The thermodynamic properties of isotopic substances. J. Chem. Soc. 562–581. https://doi.org/10.1039/JR9470000562

Varrica, D., Bardelli, F., Dongarrà, G., Tamburo, E., 2013. Speciation of Sb in airborne particulate matter, vehicle brake linings, and brake pad wear residues. Atmospheric Environment 64, 18–24. https://doi.org/10.1016/j.atmosenv.2012.08.067

Wang, D., Mathur, R., Zheng, Y., Qiu, K., Wu, H., 2021. Redox-controlled antimony isotope fractionation in the epithermal system: New insights from a multiple metal stable isotopic combination study of the Zhaxikang Sb–Pb–Zn–Ag deposit in Southern Tibet. Chemical Geology 584, 120541. https://doi.org/10.1016/j.chemgeo.2021.120541

Wang, D., Zheng, Y., Mathur, R., Ren, H., 2021. Sulfur isotopic characteristics of the Zhaxikang Sb–Pb–Zn–Ag deposit in southern Tibet. Australian Journal of Earth Sciences 68, 120–130. https://doi.org/10.1080/08120099.2020.1762738

Wang, W., Qin, T., Zhou, C., Huang, S., Wu, Z., Huang, F., 2017. Concentration effect on equilibrium fractionation of Mg-Ca isotopes in carbonate minerals: Insights from first-principles calculations. Geochimica et Cosmochimica Acta 208, 185–197. https://doi.org/10.1016/j.gca.2017.03.023

Wasserman, N.L., Schilling, K., Johnson, T.M., Pallud, C., 2021. Selenium Isotope Shifts during the Oxidation of Selenide-Bearing Minerals. ACS Earth Space Chem. 5, 1140–1149. https://doi.org/10.1021/acsearthspacechem.1c00036

Whitten, A.E., Dittrich, B., Spackman, M.A., Turner, P., Brown, T.C., 2004. Charge density analysis of two polymorphs of antimony(III) oxide. Dalton Trans. 23–29. https://doi.org/10.1039/B312550E

Wiederhold, J.G., 2015. Metal Stable Isotope Signatures as Tracers in Environmental Geochemistry. Environ. Sci. Technol. 49, 2606–2624. https://doi.org/10.1021/es504683e

Yang, S. and Liu, Y. 2016. Nuclear field shift effects on stable isotope fractionation: a review. Acta Geochimica, 35(3), pp. 227–239. https://doi.org/10.1007/s11631-016-0109-3.

Zhai, D., Mathur, R., Liu, S.-A., Liu, J., Godfrey, L., Wang, K., Xu, J., Vervoort, J., 2021. Antimony isotope fractionation in hydrothermal systems. Geochimica et Cosmochimica Acta. https://doi.org/10.1016/j.gca.2021.05.031

Zhou, J., Tian, H., Zhu, C., Hao, J., Gao, J., Wang, Y., Xue, Y., Hua, S., Wang, K., 2015. Future trends of global atmospheric antimony emissions from anthropogenic activities until 2050. Atmospheric Environment 120, 385–392. https://doi.org/10.1016/j.atmosenv.2015.09.018

Zhou, W., Zhou, A., Wen, B., Liu, P., Zhu, Z., Finfrock, Z., Zhou, J., 2022. Antimony isotope fractionation during adsorption on aluminum oxides. Journal of Hazardous Materials 429, 128317. https://doi.org/10.1016/j.jhazmat.2022.128317

Supplementary information to:

Equilibrium mass-dependent isotope fractionation of antimony between stibnite and Sb secondary minerals: a first-principles study

Colin Ferrari [*a], Merlin Méheut [b], Eléonore Resongles [a], Rémi Freydier [a] and Corinne Casiot[a]

[a]*HydroSciences Montpellier, Univ. Montpellier, CNRS, IRD, Montpellier, France*

[b] *Géosciences Environnement Toulouse, CNRS-UPS-OMP, 14 av. Edouard Belin, 31400 Toulouse, France*

*Corresponding author

Mailing address : Université de Montpellier – CC 57
163, rue Auguste Broussonnet,
34090 Montpellier, France
Email : colin.ferrari@umontpellier.fr

This PDF file includes: Tables S1 to S7 and Figure S1.

Additional tables:

Table S1: Calculated Raman frequencies (in cm^{-1}) of stibnite for different symmetries (this study: PBESOL, PBE and PZ) compared with theoretical and experimental frequencies from Ibáñez et al. (2016). Due to the high correlation between these frequencies, no Raman spectrum was calculated to assign these frequencies.

Calculated frequencies				Expce
This study				Ibáñez et al., 2016
PBEsol_us	PBE	PZ	PBEsol_nc	
A_g				
52	43	53	52	52
74	68	75	75	72
101	101	101	100	102
128	114	132	128	129
162	145	169	159	158
191	177	195	190	194
252	245	250	250	
266	273	262	261	
284	287	280	280	275
298	303	294	293	
B_{1g}				
45	42	45	44	
65	58	68	66	60
185	177	187	182	186
206	194	208	203	
229	218	232	225	239
B_{2g}				
47	45	48	46	
65	58	68	66	
194	180	198	191	
200	192	201	197	
231	219	233	227	
B_{3g}				
45	38	47	45	38
93	77	100	93	
113	108	114	112	
122	112	124	122	
162	142	168	159	
194	178	197	193	
254	247	253	251	
283	284	280	278	275
296	293	292	291	299
298	303	296	294	312

Table S2: Calculated Raman frequencies (in cm^{-1}) and intensities of the valentinite compared with experimental data from Gonçalves et al. (2018).

Calculated frequencies (this study)							Expce
		GGA			LDA		Gonçalves et al., 2018
PBESOL	PBE	PBESOL nc	Raman I	PZ	PZ nc	Raman I	
A_g							
74	71	74	13	78	79	13	79
110	123	134	377	129	137	413	142
188	174	191	66	195	200	117	190
206	195	210	781	219	223	899	217
295	305	295	1639	303	303	1421	291
487	472	493	1087	498	505	916	488
569	529	573	693	590	597	693	595
B_{1g}							
125	84	112	1	120	122		
136	137	138	112	139	141	93	
192	186	191	8	198	198	8	188
251	255	267	80	266	274	59	
427	495	432	231	437	444	185	441
514	421	521	5	529	538	0	
639	616	642	8	654	659	22	
B_{2g}							
84	75	44	0	91	54	1	105
103	99	103	4	115	107	4	
127	120	150	60	131	159	87	141
158	161	221	229	168	231	250	
260	261	278	6	258	285	1	257
474	461	475	118	483	484	123	
568	529	571	45	588	584	27	
650	665	637	317	665	652	391	681
B_{3g}							
44	24	85	6	53	92	4	
109	106	110	6	107	119	6	
150	160	132	0	158	137	0	
221	278	153	28	231	165	26	226
271	214	252	70	277	261	65	
468	458	480	10	475	489	8	499
564	556	572	6	576	594	3	
633	625	657	29	646	663	30	681

Table S3: Calculated Raman frequencies (cm^{-1}) and Raman intensities of the senarmontite (cm^{-1}) compared with experimental results from Mestl et al., (1994) and Peirera et al. (2012) and other theoretical Raman frequencies (from Peirera et al., 2012) calculated with the CRYSTAL09 program package.

	Calculated frequencies				Experimental frequencies	
	This study			Pereira *et al.* *(2012)*	Mestl *et al.* *(1994)*	Pereira *et al.* *(2012)*
	PBEsol_nc		PBEsol us			
	freq	Raman I	freq	freq	freq	freq
A_g						
	240	2702	237	263	254	255
	431	595	420	473	450	452
E_g						
	113	43	109	121	118	120
	305	0	306	335		
F_{2g}						
	89	22	85	93	82	85
	183	195	178	196	189	191
	347	29	340	365	355	358
	353	32	348	384	373	374
	672	103	668	709	712	715

Table S4: Calculated Raman frequencies (in cm^{-1}) and Raman intensities of the cervantite compared with previous literature data from Cody et al. (1979). Uncertainties on the assigned frequencies were noted as "?".

Calculated frequencies							Expce
GGA				LDA			Cody et al., 1979
PBESOL	PBE	PBESOL nc	Raman I	PZ	PZ nc	Raman I	
A_1							
63	0	59	3	60	64	4	50 ?
81	76	82	1	76	84	1	75 ?
119	84	116	14	116	127	10	140
176	170	176	1	159	180	1	(140) ?
187	179	191	1003	175	197	854	200
202	199	202	14	189	206	39	
246	219	245	3	223	254	2	241
256	236	252	16	232	259	20	255
267	261	269	4	256	276	3	
355	332	356	31	364	366	31	373
388	369	391	801	393	403	712	403
410	382	408	32	413	422	26	
445	425	447	297	443	459	280	455
555	521	558	1	541	580	4	
599	568	601	18	595	623	13	
658	622	663	278	629	686	225	?
696	667	699	79	690	720	51	713 ?
A_2							
56	42	54	1	55	59	1	43 ?
101	92	101	3	98	104	1	91 ?
106	98	104	3	103	109	3	101 ?
135	134	138	58	129	141	56	
208	198	208	27	180	214	25	
216	222	219	10	194	223	9	
251	248	251	91	236	255	84	263
262	255	269	31	255	275	28	
284	282	292	1	263	300	0	
331	330	327	0	298	336	0	
398	359	395	3	396	410	4	
407	375	415	1	414	431	0	
452	430	454	3	451	465	3	
478	449	478	0	479	493	0	
570	553	573	25	563	590	20	?
620	584	624	36	614	646	33	
698	671	702	44	677	725	39	713 ?
748	726	754	0	715	775	1	
B_1							
77	54	82	13	79	88	12	78 ?
132	92	105	0	96	112	0	
179	132	138	0	132	144	1	
201	159	174	1	169	180	1	
210	183	190	0	179	196	0	
229	187	210	2	200	220	3	
265	230	238	2	212	245	2	
279	240	263	5	239	272	4	274 ?
327	277	282	2	268	289	2	

390	315	340	13	352	350	15	
405	401	417	0	412	429	0	
456	410	440	31	441	452	23	420
483	473	501	1	484	516	4	
583	541	580	26	567	604	18	?
605	614	647	1	621	667	1	
693	643	677	5	657	700	4	
750	682	714	25	707	734	21	713 ?
B_2							
85	65	77	80	80	84	62	62 ?
111	125	132	8	127	136	8	137
135	180	182	55	172	186	39	192
174	199	206	3	184	210	3	209
188	212	215	46	195	219	39	224
209	219	222	2	197	228	2	
240	259	271	2	255	278	1	274 ?
265	279	287	4	263	294	5	285
278	322	322	28	293	330	20	
342	356	395	131	394	409	95	(403)
409	365	403	8	403	419	5	(403)
440	437	459	21	455	471	14	467
486	455	485	14	483	499	18	
575	558	581	44	573	600	37	?
639	571	612	13	606	633	11	
673	668	698	11	668	720	9	
709	727	756	114	719	778	79	758 ?

Table S5: Calculated Raman frequencies (in cm^{-1}) of Sb_2O_5. These frequencies were calculated with PBESOL-dn-rrkjus as this functional proved its accuracy on the previous models. No exploitable experimental data was found as comparison for the validation of this structure.

Calculated frequencies and Raman intensity

PBEsol_us	PBESOL_nc		PZ_nc	
freq	freq	Raman I	freq	Raman I
A_g				
108	109	47	113	32
168	171	16	177	12
201	206	293	209	195
262	265	322	274	315
294	301	51	309	25
412	412	1740	424	1407
462	466	131	477	128
514	521	198	534	130
555	561	652	583	441
736	743	109	766	71
B_g				
111	112	11	116	8
131	132	12	136	9
200	205	114	208	72
268	271	14	278	13
298	306	15	314	12
377	386	2	396	1
429	429	3	440	2
472	478	28	493	37
616	622	46	646	39
683	688	9	714	8
797	801	6	824	3

Table S6: Values of β-factors in function of the temperature (in K and °C) based on the PBEsol functional for the different studied structures.

				Cervantite site by site				
	Stibnite	Valentinite	Senarmontite	Sb(III)	Cervantite tot	Sb(V)	Sb_2O_5	
$10^6/T^2$ (K)	ln(β) (‰)	ln(β) (‰)	ln(β) (‰)	ln(β) (‰)	ln(β) (‰)	ln(β) (‰)	ln(β) (‰)	T (°C)
0.50	0.03	0.08	0.08	0.06	0.10	0.14	0.14	1141.05
1.00	0.06	0.15	0.16	0.12	0.20	0.28	0.28	726.85
1.50	0.09	0.22	0.25	0.18	0.30	0.42	0.42	543.35
2.00	0.13	0.30	0.33	0.25	0.40	0.56	0.56	434.05
2.50	0.16	0.37	0.41	0.31	0.50	0.69	0.70	359.35
3.00	0.19	0.45	0.49	0.37	0.60	0.83	0.83	304.25
3.50	0.22	0.52	0.57	0.43	0.70	0.96	0.97	261.35
4.00	0.25	0.59	0.65	0.49	0.79	1.10	1.10	226.85
4.50	0.28	0.66	0.73	0.55	0.89	1.23	1.23	198.25
5.00	0.31	0.74	0.81	0.61	0.99	1.36	1.37	174.05
5.50	0.34	0.81	0.88	0.67	1.08	1.50	1.50	153.25
6.00	0.37	0.88	0.96	0.73	1.18	1.63	1.63	135.05
6.50	0.40	0.95	1.04	0.79	1.27	1.76	1.76	119.05
7.00	0.43	1.02	1.12	0.85	1.37	1.89	1.89	104.85
7.50	0.47	1.09	1.19	0.91	1.46	2.02	2.02	91.95
8.00	0.50	1.16	1.27	0.96	1.56	2.15	2.15	80.45
8.50	0.53	1.23	1.35	1.02	1.65	2.28	2.27	69.85
9.00	0.56	1.30	1.42	1.08	1.74	2.41	2.40	60.15
9.50	0.59	1.37	1.50	1.14	1.84	2.53	2.53	51.25
10.00	0.62	1.44	1.57	1.20	1.93	2.66	2.66	43.05
10.50	0.65	1.51	1.65	1.26	2.02	2.78	2.78	35.45
11.00	0.68	1.57	1.72	1.31	2.11	2.91	2.91	28.35
11.50	0.71	1.64	1.80	1.37	2.20	3.03	3.03	21.75
12.00	0.74	1.71	1.87	1.43	2.29	3.16	3.15	15.55
12.50	0.77	1.78	1.94	1.49	2.39	3.28	3.27	9.65
13.00	0.80	1.84	2.02	1.54	2.47	3.40	3.39	4.25
13.50	0.83	1.91	2.09	1.60	2.56	3.53	3.52	-0.95
14.00	0.86	1.98	2.16	1.66	2.65	3.65	3.64	-5.85

Table S7: Values of β-factors in function of the temperature (in K and °C) based on the PBEsol functional for the two different Sb sites of the stibnite.

	Stibnite site by site			
	Site 1	Average	Site 2	
$10^6/T^2$ (K)	Ln(beta)	Ln(beta)	Ln(beta)	T (°C)
0.50	0.03	0.03	0.03	1141.05
1.00	0.06	0.06	0.06	726.85
1.50	0.09	0.09	0.09	543.35
2.00	0.13	0.12	0.12	434.05
2.50	0.16	0.16	0.15	359.35
3.00	0.19	0.19	0.18	304.25
3.50	0.22	0.22	0.21	261.35
4.00	0.25	0.25	0.25	226.85
4.50	0.28	0.28	0.28	198.25
5.00	0.31	0.31	0.31	174.05
5.50	0.35	0.34	0.34	153.25
6.00	0.38	0.37	0.37	135.05
6.50	0.41	0.40	0.40	119.05
7.00	0.44	0.43	0.43	104.85
7.50	0.47	0.46	0.46	91.95
8.00	0.50	0.49	0.49	80.45
8.50	0.53	0.52	0.52	69.85
9.00	0.56	0.55	0.55	60.15
9.50	0.59	0.59	0.58	51.25
10.00	0.62	0.62	0.61	43.05
10.50	0.65	0.65	0.64	35.45
11.00	0.69	0.68	0.67	28.35
11.50	0.72	0.71	0.70	21.75
12.00	0.75	0.74	0.73	15.55
12.50	0.78	0.77	0.76	9.65
13.00	0.81	0.80	0.78	4.25
13.50	0.84	0.83	0.81	-0.95
14.00	0.87	0.86	0.84	-5.85

Additional Figure:

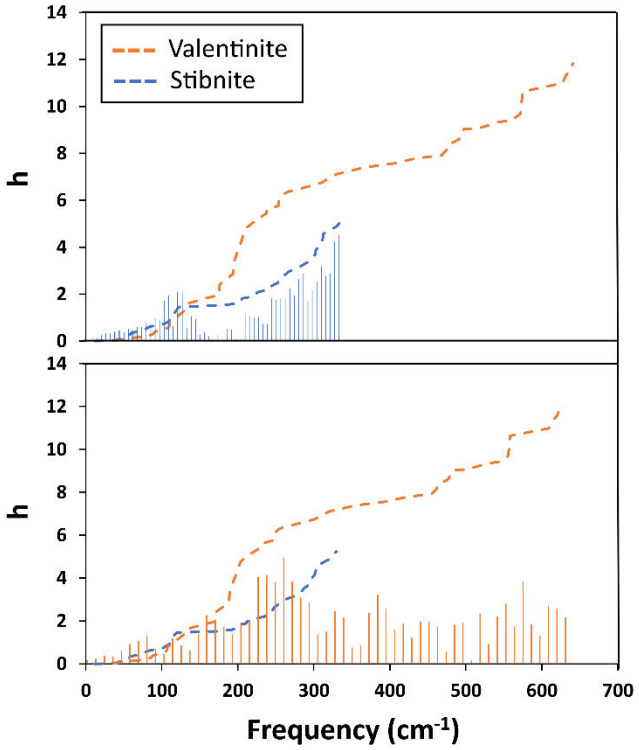

Figure S1: Contribution of the various frequencies to the β-factor (PBESOL_us calculation) of stibnite (blue) and valentinite (orange). The blue and orange bars represent the contribution of each individual frequency. The dashed blue and orange lines represent the cumulated β-factor (see Meheut et al 2009 for details).

References

Cody, C.A., Dicarlo, L., Darlington, R.K., 1979a. Vibrational and thermal study of antimony oxides. Inorganic Chemistry 18, 1572–1576. https://doi.org/0020-1669/79/1318-1572$01.00/0

Gonçalves, R.A., Baldan, M.R., Chiquito, A.J., Berengue, O.M., 2018a. Synthesis of orthorhombic Sb_2O_3 branched rods by a vapor–solid approach. Nano-Structures & Nano-Objects 16, 127–133. https://doi.org/10.1016/j.nanoso.2018.05.008

Mestl, G., Ruiz, P., Delmon, B., Knözinger, H., 1994. Sb_2O_3/Sb_2O_4 in reducing/oxidizing environments: an in situ raman spectroscopy study. Journal of Physical Chemistry 11276–11282. https://doi.org/0022-3654/94/2098-11276$04.50/0

Pereira, A.L.J., Gracia, L., Santamaría-Pérez, D., Vilaplana, R., Manjón, F.J., Errandonea, D., Nalin, M., Beltrán, A., 2012. Structural and vibrational study of cubic Sb_2O_3 under high pressure. Phys. Rev. B 85, 174108. https://doi.org/10.1103/PhysRevB.85.174108

PARTIE B : Fractionnement isotopique de l'antimoine lors de la sorption de Sb(V) et Sb(III) sur schwertmannite et ferrihydrite (article 3)

Colin Ferrari, Eléonore Resongles, Rémi Freydier, Corinne Casiot

Résumé en français

Les isotopes de l'antimoine ont suscité un intérêt ces dernières années, avec la perspective de les utiliser comme traceurs géochimiques. Cependant, peu d'études se sont concentrées sur les processus de fractionnement des isotopes de l'antimoine dans l'environnement, ce qui est essentiel pour développer les applications de ce nouvel outil géochimique.

Dans cette étude, le fractionnement isotopique à l'équilibre se produisant lors de la sorption de Sb(V) et Sb(III) sur deux phases minérales de fer typiques du drainage minier acide (DMA), la ferrihydrite et la schwertmannite, a été étudié dans des conditions contrôlées de pH et de rapport solide sur liquide. Le comportement de sorption et le fractionnement isotopique du Sb étaient similaires pour les différentes phases minérales et degrés d'oxydation du Sb, avec un $\Delta^{123}Sb_{solide\text{-}solution}$ de – 0,24 ± 0,06 ‰ pour le Sb(III) et de – 0,34 ± 0,08 ‰ pour le Sb(V) adsorbé sur la ferrihydrite et – 0,35 ± 0,07 ‰ pour Sb(III) et – 0,29 ± 0,02 ‰ pour Sb(V) adsorbé sur la schwertmannite. Le pH et le rapport Fe:Sb initial n'ont pas eu d'impact sur $\Delta^{123}Sb_{solide\text{-}solution}$, suite à un échange à l'équilibre en système fermé entre les espèces de Sb dissoutes et adsorbées.

Ce fractionnement pourrait être lié à l'apparition du fer comme deuxième plus proche voisin qui déforme le polyèdre atomique $Sb(OH)_3$ ou $Sb(OH)_6^-$. Cette étude révèle que le fractionnement isotopique à l'équilibre de Sb se produit lors de la sorption de Sb(III) et Sb(V) sur des minéraux de fer secondaires typiques des DMA, fournissant des données pour l'interprétation des signatures isotopiques de Sb dans les environnements miniers.

Antimony isotope fractionation during Sb(V) and Sb(III) sorption on schwertmannite and ferrihydrite

Colin Ferrari[*a], Eléonore Resongles [a], Rémi Freydier [a], and Corinne Casiot [a]

[a]HydroSciences Montpellier, Univ. Montpellier, CNRS, IRD, Montpellier, France

*Corresponding author:

Mailing address : Université Montpellier – HydroSciences CC57
Bâtiment HYDROPOLIS
15 avenue Charles Flahault
34090 Montpellier
Email : ferraricolin@gmail.com

Abstract

The application of antimony (Sb) isotopes as tracers for Sb environmental cycling is limited by a lack of knowledge of isotope fractionation factors associated with key (bio-)geochemical processes controlling its behaviour in surface environments. In this study, we investigated the equilibrium isotope fractionation generated by Sb(V) and Sb(III) sorption on two iron minerals typical of acid mine drainage (AMD), ferrihydrite and schwertmannite, under controlled conditions of pH and solid to liquid ratio. Sorption behaviour and Sb isotope fractionation were similar for the different mineral phases and Sb oxidation degrees, with fractionation factors $\Delta^{123}Sb_{solid\text{-}solution}$ of -0.24 ± 0.06 ‰ for Sb(III) and -0.34 ± 0.08 ‰ for Sb(V) sorbed on ferrihydrite and -0.35 ± 0.07 ‰ for Sb(III) and -0.29 ± 0.02 ‰ for Sb(V) sorbed on schwertmannite. The pH and initial Fe:Sb ratio did not have an impact on the $\Delta^{123}Sb_{solid\text{-}solution}$. The light ^{121}Sb isotope was preferentially sorbed on the mineral phases, following an equilibrium closed system between dissolved and adsorbed Sb species. This fractionation may be related to the apparition of iron as the second closest neighbour which distorts the $Sb(OH)_3$ or $Sb(OH)_6^-$ atomic polyhedron. This study reveals that Sb equilibrium isotope fractionation occurs during sorption of Sb(III) and Sb(V) onto secondary iron minerals, an important process which controls Sb mobility in AMD streams and provides data for interpreting Sb isotope signatures in the environment.

1. Introduction

Antimony (Sb) is a critical element for the modern industry, mainly for its application as a flame retardant in plastics and its use in lead alloys (European Commission, 2020; U.S. Geological Survey, 2022). As a consequence, Sb extraction has peaked over the last twenty years with an annual world production of 142 to 193 kT (2004-2018 data, U.S. Geological Survey, 2018) leading to a general increase of Sb levels in the environment (He *et al.*, 2019). In surface waters, the highest concentrations of this toxic element (up to ~29 $mg.L^{-1}$) are found in sulphide mining areas (Wang *et al.*, 2011; Guo *et al.*, 2018; Hao *et al.*, 2021) while Sb concentration in natural waters is usually low (< 1 $\mu g.L^{-1}$).

In mining Sb-rich environments, the alteration of sulphides produces acid leachates (acid mine drainage, AMD), that contain high concentrations of iron and sulphate. These constituents precipitate subsequently to iron oxidation and AMD neutralization by river water; they form secondary minerals, hydrous ferric oxides (HFO) and ferric hydroxysulphates (Bigham *et al.*, 1996). Due to their high specific surface area and positive surface charges, these minerals are good sorbents for antimony (Leuz *et al.,* 2006; Mitsunobu *et al.,* 2006; Mitsunobu *et al.*, 2010; Guo *et al.*, 2014; Qi and Pichler, 2016, 2017) and they control the transport of Sb in the water compartment downstream from mining sites (Filella, Williams and Belzile, 2009; Manaka *et al.*, 2007; Resongles *et al.*, 2013). The solid phases most commonly encountered in AMD streams and downstream rivers are schwertmannite ($Fe_8O_8(OH)_6SO_4$)) in the pH range 2.8-4.5 and ferrihydrite ($Fe_5HO_8,4H_2O$) at pH≥6.5 (Bigham et al., 1996).

Antimony isotope system (^{121}Sb and ^{123}Sb) is emerging due to its strong potential as a geochemical tracer (Teng *et al.,* 2017). Several studies were focused on sample preparation and optimization of Sb isotope ratio analysis by Multi Collector Inductively Coupled Plasma Mass Spectrometry (Asaoka *et al.*, 2011; Lobo *et al.*, 2012; Liu *et al.*, 2020; Kaufmann *et al.*, 2021; Ferrari *et al.*, 2021; Li *et al.*, 2021; Sun *et al.*, 2021). Others provided data on Sb isotope signatures in primary Sb minerals, manufactured materials and environmental samples (Rouxel *et al.*, 2003; Lobo *et al.*, 2013, 2014; Degryse *et al.*, 2015, 2020; Resongles *et al.*, 2015; Ferrari *et al.*, 2021). Only one experimental study (Zhou *et al.*, 2022) focused on Sb isotope fractionation during sorption, which is an important environmental process involved in Sb cycle; the authors found that although kinetic fractionation occurs at the early stage of the reaction, Sb adsorption on aluminium oxides does not produce significant equilibrium Sb isotope fractionation. Thus, the isotopic cycle of antimony and fractionation generated by processes in waters remain poorly known. In the perspective of using Sb isotopes to track pollution sources in watersheds impacted by sulphide ore mining, and/or to unravel the processes Sb undergoes in mine-impacted streams, it is essential to document Sb isotope fractionation during sorption on secondary iron minerals, in particular on schwertmannite and ferrihydrite, two minerals typical of AMD streams.

The objective of this study was to quantify the isotope fractionation factors at equilibrium between dissolved and sorbed Sb species (trivalent and pentavalent Sb) on two mineral phases widely distributed in sulphide mining environments, ferrihydrite and schwertmannite, and to make hypothesis regarding the possible origin of the observed fractionation.

2. Material & methods

2.1. Reagents and materials

Ultrapure water (Milli-Q®, resistivity > 18.2 MΩ.cm, Q-POP Element system, Millipore) was used for all experiments and reagent preparation. All consumables (e.g. sample bottles, tubes, SPE cartridge, pipette tips…) were soaked in 10 % w/w analytical grade HCl for 48 h and rinsed three times with ultrapure water before use. $Fe(NO_3)_3,9H_2O$ (Sigma-Aldrich®), $FeSO_4.7H_2O$ (Sigma-Aldrich®), 30 % w/w H_2O_2 (analytical grade, Fisher Scientific®), 1 mol.L^{-1} KOH (Merck®) were used for the synthesis of schwertmannite and 2-line ferrihydrite. $NaNO_3$ (Merck®) and NaOH (99.99% trace metal basis, Sigma-Aldrich®) were used for adsorption experiments. 30% w/w HCl (Suprapur, Merck®), 65–69% w/w HNO_3 (Analpure, Analityka®), ascorbic acid (analytical grade, Sigma-Aldrich®), KI (Suprapur, Merck®) and $NaBH_4$ (99.99% trace metal basis, Sigma-Aldrich®) were used for sample preparation for Sb concentration and isotope analyses. Ethylenediaminetetraacetic acid disodium salt (EDTA, analytical grade, J. T. Baker®) and potassium hydrogen-phthalate (KHP, SigmaUltra, 99.95%, Sigma-Aldrich) were used to prepare the eluent for Sb speciation analysis. Acetic acid (Suprapur, Merck®) and EDTA (analytical grade, J. T. Baker®) were used as additive for preserving Sb redox species in samples during Sb redox speciation analysis. Stock solutions of Sb(V) and Sb(III) at 1 g.L^{-1} were prepared separately by dissolving an appropriate amount of potassium hexahydroxoantimonate(V) ($KSb(OH)_6$, analytical grade, Merck®) and potassium antimony(III) oxide tartrate hemihydrates ($K(SbO)C_4H_4O_6.0.5H_2O$, Extrapure, Merck®) in ultrapure water. Antimony concentration in Sb(V) and Sb(III) stock solutions were checked by ICP-MS. These solutions were used for preparing calibration solutions for Sb speciation analysis and for adsorption experiments. A mono-elemental Sb standard solution (1000 µg mL^{-1} in 20 % w/w HCl, batch number 24-175SBX, SPEX CertiPrep) was used as Sb isotopic standard (Ferrari *et al.*, 2021).

All experiments were carried out in a lab with controlled temperature conditions (20 ± 1 °C). Sample dilutions for ICP-MS and HG-MC-ICP-MS analyses were carried out in class 10 000 cleanroom facility.

2.2. Ferrihydrite and schwertmannite synthesis and characterization

Two-line ferrihydrite was synthesized following the protocol of Schwertmann and Cornell (2000) and schwertmannite was synthesized following the protocol of Liu *et al.*, (2015) adapted from Regenspurg *et al.,* (2004). Details of the procedures are given in Supplementary Information.

The quality of the synthetized ferrihydrite and schwertmannite was checked using XRD (X-ray powder diffraction), BET (Brunauer-Emmett-Teller) and SEM (Scanning Electron Microscopy, schwertmannite only) analysis on the PAC and MEA platforms, Université de Montpellier. The methods and the results are briefly presented in Supplementary Information (Section S1, Figure S1 and S2).

2.3. Sorption experiments

Sorption experiments were conducted at different pH and initial Fe:Sb ratios. Every condition was made in duplicate or triplicate to check the reproducibility of the experiment. Intermediate suspensions of ferrihydrite or schwertmannite were prepared at 1 g.L^{-1} and agitated for 48 h before the experiment to ensure homogeneity. Then, suspensions (50 mL) containing 0.01 g.L^{-1} of ferrihydrite or schwertmannite in a 0.01 M $NaNO_3$ electrolyte were prepared in HDPE bottles and after a pH

adjustment step, the suspensions were doped with Sb(III) or Sb(V) to reach a final Sb concentration of 0.1, 0.5, 1 and 10 mg.L^{-1}. As a result, the initial Fe:Sb molar ratios were 144, 29, 14 and 1.4 for Sb(III) adsorption experiment on ferrihydrite and 126, 25, 13 and 1.3 for Sb(III) and Sb(V) adsorption experiments on schwertmannite and Sb(V) adsorption experiment on ferrihydrite. In addition, procedural blanks containing ferrihydrite or schwertmannite were prepared and treated as samples to ensure that no contamination occurred at any step of the experiment. Finally, bottles were wrapped in an aluminium sheet and agitated at 300 rpm on a stirring table for 48 h at 20 ± 1 °C.

The pH of the suspensions was adjusted to correspond to the stability domain of ferrihydrite and schwertmannite (Bigham *et al.*, 1996). The pH was thus fixed at 6, 7 and 7.5 for ferrihydrite and 2.5 and 4.5 for schwertmannite using 0.1 M NaOH and 0.1 M HCl, respectively. The pH was monitored twice a day and re-adjusted when needed.

Sacrifices of the suspensions were carried out after 48 h. This equilibrium time was defined based on preliminary kinetic monitoring for Sb(V) sorption on ferrihydrite and for Sb(III) and Sb(V) sorption on schwertmannite (Figure S3) and was consistent with the literature regarding Sb(III) sorption on ferrihydrite under conditions similar to the present study (initial Fe:Sb ratio = 100 , pH 7, in Qi and Pichler, (2016)). As concentration and isotopic equilibrium time may differ (Komárek *et al.*, 2021), it was also checked that isotopic equilibrium was reached after 48 h (Table S1). The results showed no significant difference in Sb isotope composition between 48 h and 96 h for all conditions (Table S1), which confirmed isotopic equilibrium achievement at 48 h.

Suspensions were filtered using Nalgene filtration unit and 0.22 µm pre-cleaned PVDF filters. The filters were dried in a vacuum desiccator. An aliquot (10 mL) of the filtrate was acidified at 1 ‰ HNO_3 for dissolved Sb and Fe concentration measurement by ICP-MS. Another aliquot was acidified at 1 % HCl for Sb isotope ratio analysis by HG-MC-ICP-MS. A third aliquot was either analysed the same day for redox Sb speciation or preserved in 20 mM EDTA and 87 mM acetic acid and stored at 4 °C until analysis (< 1 week), as recommended from our unpublished trials. The particulate phase collected on the filter was dissolved in 15 mL of 6 M HCl in a PTFE vial at 80 °C for 1 h for subsequent Sb isotope analysis.

2.4. Analytical methods

All analyses (ICP-MS, IC-ICP-MS, HG-MC-ICP-MS) were performed on the AETE-ISO platform (OSU OREME, Université de Montpellier) using routine protocols.

Antimony and iron concentrations in the dissolved (<0.22µm) and particulate (>0.22µm) fractions were measured by ICP-MS (Inductively Coupled Plasma Mass Spectrometry, iCAP TQ, ThermoScientific®) after an adequate dilution in 0.15 M HNO_3 (Ferrari *et al.*, 2021).

Antimony redox speciation analysis (Sb(V) and Sb(III) concentrations) was carried out by IC-ICP-MS (Ionic Chromatography coupled to ICP-MS, iCAP-Q, ThermoScientific®) using external Sb(III) and Sb(V) calibration. Chromatographic separation was performed using a Hamilton PRP-X100 column (15 cm x 4.6 mm i.d.) and precolumn (2 cm x 4.6 mm i.d.) with a Dionex ICS-5000 Ion Chromatography System (ThermoScientific®). A solution of 5 mmol.L^{-1} EDTA and 2 mmol.L^{-1} KHP (pH 4.5) was used as eluent with a flow rate of 1.5 mL.min^{-1}. A solution of indium at 1 µg.L^{-1} was continuously injected after the

chromatographic separation and used as internal standard to correct potential sensitivity drifts of ICP-MS (Resongles *et al.*, 2013).

Antimony isotope composition was determined by HG-MC-ICP-MS (Hydride Generation coupled with a Multi-Collector ICP-MS, Neptune Plus, ThermoScientific®) as described in Ferrari *et al.*, (2021). HG-MC-ICP-MS configuration and parameters have been adapted to improve signal stability and the new settings are reported in Table S2. Antimony isotope composition was measured using a sample-standard bracketing method and is reported in the δ^{123}Sb notation (Equation 1).

$$\delta^{123}Sb(‰) = \left(\frac{\left(\frac{^{123}Sb}{^{121}Sb}\right)_{sample} - \left(\frac{^{123}Sb}{^{121}Sb}\right)_{mean\ std}}{\left(\frac{^{123}Sb}{^{121}Sb}\right)_{mean\ std}}\right) \times 1000 \ (1)$$

δ^{123}Sb of the dissolved and particulate fractions were measured after diluting the samples to 2 µg.L^{-1} of Sb in a 3 M HCl with 0.5% w/v KI/ascorbic acid medium to ensure a full reduction of Sb(V) to Sb(III) as required for an optimal hydride generation (Ferrari *et al.*, 2021). The preliminary Sb purification step described in Ferrari et al. (2021) was not required in the present study due to the low Fe:Sb ratios (<150) and the absence of interfering elements (Se, As, Te, Sn,…) in the experimental samples (< detection limits). This was further confirmed by analysing the dissolved and particulate experimental blanks doped with 2 µg.L^{-1} of the in-house Sb isotopic standard. No shift of Sb isotope composition was observed compared to the pure Sb standard solution SPEX.

2.5. Sorption isotherms

Equation 2 was used to quantify the amount of the Sb sorbed onto ferrihydrite and schwertmannite (Q_t, in mg.g^{-1}) at equilibrium:

$$Q_t = \frac{C_{ads} * V}{m} \ (2)$$

with C_{ads} the concentration of Sb sorbed onto the mineral (mg.L^{-1}), V the volume of the solution (L), and m the mass of the mineral (g).

Non-linear Freundlich isotherm was used for modelling Sb(III) and Sb(V) sorption on ferrihydrite and schwertmannite, as it gave the best fit with experimental results (Equation 3):

$$Q_t = K_d C^{1/n} \ (3)$$

Where K_d is the distribution coefficient (L.g^{-1}), n is the correction factor, C the equilibrium Sb dissolved concentration (mg.L^{-1}) and Q_t the amount of equilibrium Sb adsorbed on ferrihydrite and schwertmannite (mg.g^{-1}) (Eq. 2). The linear form of Equation 3 was used for graphical representation (Equation 4):

$$\ln(Q_t) = \frac{1}{n}\ln(C) + \ln(K_d) \ (4)$$

3. Results

3.1 Antimony sorption behaviour

Adsorption isotherms of Sb(III) and Sb(V) on ferrihydrite and schwertmannite were best described by Freundlich isotherms, yielding $R^2 > 0.90$ (Figure 1 and Figure S4). Ferrihydrite and schwertmannite have similar adsorption reactivity towards Sb species. The adsorption isotherms and edges showed similar patterns for the two mineral phases and Sb species (Figures 1 and S4). Sb(III) sorption on schwertmannite increased at pH 4.5 compared to pH 2.5. Sb(V) sorption on ferrihydrite was higher at pH 6 than at pH 7 and 7.5. pH had little effect on the sorption of Sb(III) on ferrihydrite and Sb(V) on schwertmannite. The maximum Sb sorption densities obtained by the Freundlich isotherm fitting were 510 and 741 µg.m^{-2} for Sb(III) and Sb(V) on ferrihydrite, respectively; they were 3528 and 2660 µg.m^2 for Sb(III) and Sb(V) on schwertmannite, respectively.

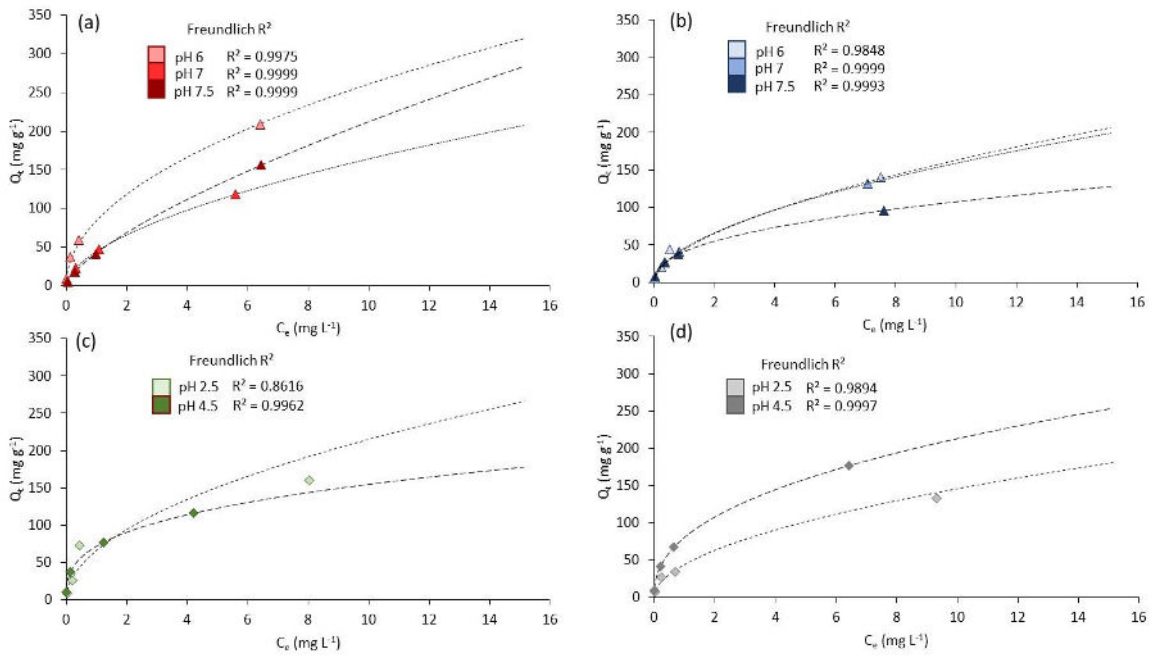

Figure 1: Freundlich sorption isotherms modelled for (a) Sb(V) and (b) Sb(III) on ferrihydrite at pH 6, 7 and 7.5 and for (c) Sb(V) and (d) Sb(III) on schwertmannite at pH 2.5 and 4.5. The dashed lines correspond to the Freundlich model calculated using Equation 2 and the symbols represent the experimental values.

In sorption experiments with Sb(III), some Sb(V) was detected in the dissolved phase at equilibrium. It represented 0.4 % to 10 % of total dissolved Sb at pH 6 (ferrihydrite), pH 7 (ferrihydrite), and pH 2.5 (schwertmannite), whatever the Fe:Sb ratio, and increased up to ~60 % at pH 7.5 and up to ~35 % at pH 4.5, at the highest Fe:Sb ratios (Figure S5). This suggests that partial oxidation of Sb(III) occurred during the experiments.

3.2. Antimony isotope fractionation

3.2.1 Isotope fractionation during Sb adsorption on ferrihydrite

There was a significant isotope fractionation of Sb between the dissolved and particulate phases. The isotope fractionation during adsorption of Sb(V) and Sb(III) on ferrihydrite followed a closed-system equilibrium fractionation model, with a parallel increase of the isotopic signature of the dissolved and particulate phases (Figure 2). The fractionation factor $\Delta^{123}Sb_{solid\text{-}solution}$ averaged -0.34 ± 0.08 ‰ for Sb(V) and - 0.24 ± 0.06 ‰ for Sb(III), with the dissolved phase preferentially enriched in the heavy isotope (^{123}Sb), for both Sb(III) and Sb(V) species. Under the experimental conditions, pH and Fe:Sb ratio did not influence the magnitude of $\Delta^{123}Sb_{solid\text{-}solution}$ fractionation factor. Only one data from Sb(III) sorption experiments deviated from the general trend for the dissolved phase in Figure 2b; it was the sample with 74 % adsorption at pH 7.5. which contained 37 % of Sb(V) (Figure S5) .

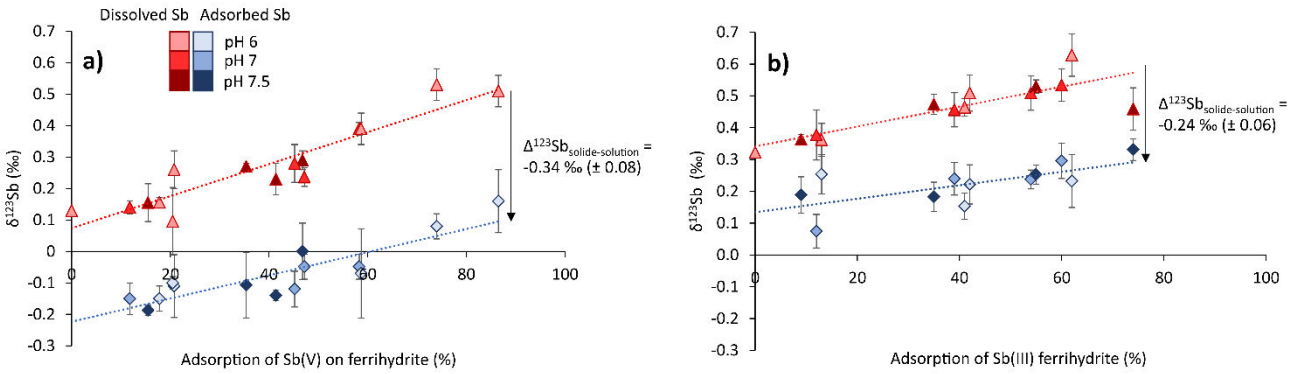

Figure 2: Antimony isotope composition ($\delta^{123}Sb$) of dissolved (red) and adsorbed (blue) phases during (a) Sb(V) and (b) Sb(III) adsorption on ferrihydrite.

3.2.2 Isotope fractionation during Sb adsorption on schwertmannite

The differentiation of $\delta^{123}Sb$ was also significant between the dissolved and particulate phases during Sb adsorption on schwertmannite. Similarly to the adsorption of Sb species on ferrihydrite, the adsorption of Sb(V) and Sb(III) on schwertmannite followed a closed system equilibrium fractionation model (Figure 3). The fractionation factor $\Delta^{123}Sb_{solid\text{-}solution}$ averaged -0.35 ± 0.07 ‰ for Sb(III) and -0.29 ± 0.02 ‰ for Sb(V), with the dissolved phase preferentially enriched in the heavy isotope (^{123}Sb).

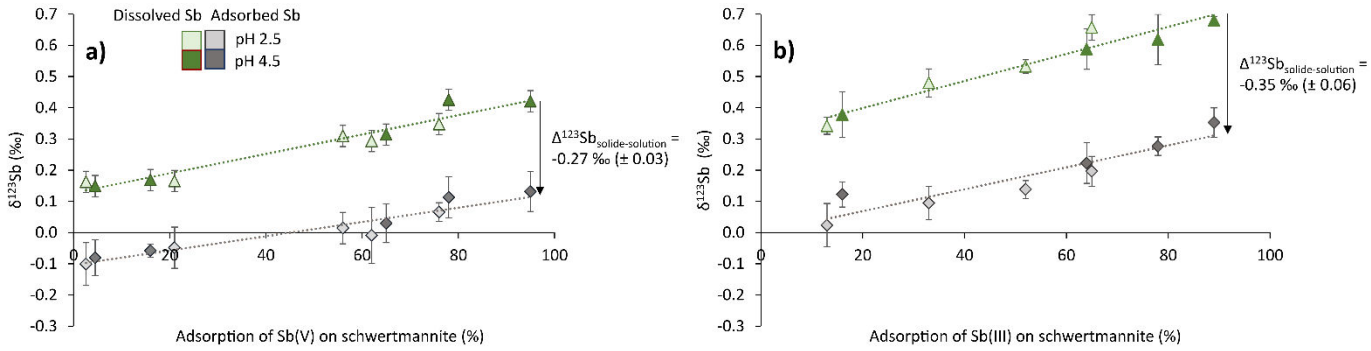

Figure 3: Antimony isotope composition ($\delta^{123}Sb$) of dissolved (green) and adsorbed (grey) phases during (a) Sb(V) and (b) Sb(III) adsorption on schwertmannite.

4. Discussion

This study showed a preferential adsorption of the light $^{121}Sb(III)$ and $^{121}Sb(V)$ isotopes onto ferrihydrite and schwertmannite, with a fractionation factor $\Delta^{123}Sb_{solid\text{-}solution}$ around -0.3 ‰. Only two other studies investigated the fractionation of antimony isotopes on iron- (Araki et al., 2009) or aluminium- (Zhou *et al.*, 2022) oxyhydroxides and these studies focused only on the sorption of Sb(V) species. Araki *et al.* (2009) found a "slight" enrichment in the heavy isotope in the aqueous phase compared to Sb(V) sorbed on ferrihydrite, similarly to the present study, but no fractionation factor value was published. Zhou *et al.* (2022) showed that no significant equilibrium isotope fractionation occurred during Sb(V) adsorption on γ-Al_2O_3 ($\Delta^{123}Sb_{aqueous\text{-}adsorbed}$ = ~ 0 ± 0.08 ‰) and attributed the lack of significant equilibrium isotope fractionation to the formation of an outer-sphere complex of Sb on γ-Al_2O_3, with similar bond length of Sb - O (~ 1.98 Å) and octahedral bond structure of $Sb(OH)_6^-$ in the aqueous and solid phases. This was the first study quantifying equilibrium Sb isotope fractionation caused by sorption on a metal oxyhydroxide.

There are general trends regarding fractionation of metal isotopes during sorption onto metal oxyhydroxides. Isotope fractionation during sorption is mostly controlled by differences in bonding environment (including the length and strength of bonds, coordination number) of the sorbed species compared to its aqueous counterpart or by differences in sorption behaviour of the different aqueous metal species that may coexist in solution (Wiederhold, 2015). The extent of isotope fractionation occurring during metal sorption remains usually limited (<1 ‰) (Wiederhold, 2015; Komárek *et al.*, 2021). Besides, a number of studies showed that the outer-sphere complexation generally generates lower fractionation ; indeed, the outer-sphere complexation is subject to weaker bonding than the inner-sphere complexation due to the control of complexing ligands by weak electrostatic forces on the surface and their participation in anion exchange (Essington and Stewart, 2018). The inner-sphere complexation is subject to stronger bonding (Essington and Stewart, 2018; Zhou *et al.*, 2022). Regarding fractionation direction, as a general rule for a number of geochemical processes, at isotopic equilibrium, heavier isotopes are generally enriched into stronger bonding environments (Wiederhold, 2015); however, both light and heavy isotope enrichments in the sorbed species have been observed in sorption studies on oxyhydroxides, depending on the bonding environment of sorbed and aqueous metal species (Balistrieri *et al.*, 2008; Komárek *et al.*, 2021). Therefore, the bonding environment of Sb in the solid and aqueous phases is of prime interest to interpret the observed Sb isotope fractionation factors.

4.1 Sorption of Sb(V) on ferrihydrite

For the sorption of Sb(V) on ferrihydrite, sorption mechanisms and local structures sorbed-Sb(V) can be obtained from previous sorption studies carried out in similar conditions. In the study of Araki *et al.* (2009) which evidenced slight enrichment in the heavy isotope in the aqueous phase compared to Sb(V) sorbed on ferrihydrite, Sb(V) was present as an inner-sphere complex of octahedral Sb species on the ferrihydrite surface (Mitsunobu *et al.,* 2006). Thus, the octahedral bond structure of $Sb(OH)_6^-$ was the same in the aqueous and solid phases, there was no change in the first coordination shell between aqueous and sorbed Sb(V). The sorption process involved the formation of Sb – O – Fe bonds with an edge-sharing and corner-sharing configurations (Scheinost *et al.*, 2006; McComb *et al.,* 2007,

Guo et al., 2014). This was confirmed by Mitsunobu *et al.* (2010) who also demonstrated the double corner-sharing complex character of the inner-sphere formation. One could have expected that this mode of complexation would generate no fractionation or slight enrichment in the heavy isotope in the sorbed Sb(V) species (stronger bonding due to inner-sphere complexation), while the reverse was observed in the present study. Nickel adsorption onto various Fe oxyhydroxides through inner-sphere complexes also showed lighter Ni isotope enrichment in the adsorbed fraction on ferrihydrite ($\Delta^{60/58}Ni_{solid\text{-}solution}$ value of -0.35 ± 0.10 ‰ for Ni on ferrihydrite, (Wasylenki *et al.*, 2015; Wang and Wasylenki, 2017; Gueguen *et al.*, 2018)). Considering that Ni - O bonds in the adsorbed complexes were not significantly longer and weaker (therefore, Ni bonding was not weaker) than in the predominant aqueous species, the authors ascribed this fractionation direction to distortions of bond angles and lengths occurring in the adsorbed complexes NiO_6 (Wasylenki *et al.*, 2015). More recently, Yan *et al.* (2021) observed the same effect for Cd; fractionation of Cd isotopes during sorption onto Fe oxyhydroxides and enrichment in the light isotopes in the solid were attributed to distortion of the CdO_6 complexes during adsorption (Yan *et al.*, 2021). For antimony, our theoretical calculations using the Density Functional Theory suggested that the appearance in the structure of a second neighbour other than the Sb species induced a slight distortion of the atomic polyhedron (both on Sb – O bond lengths and on the O – Sb – O angle) susceptible to cause isotopic fractionation of around 0.3 ‰ (Ferrari *et al.,* 2022). In the present study, the atomic distortion induced by iron as the second closest neighbour may be the cause of the slight enrichment in lighter Sb isotopes in the solid. Regarding the possible effect of surface coverage on the isotope fractionation during sorption (evidenced for example for Zn adsorption onto Mn oxyhydroxide, Bryan *et al.*, 2015), our data showed no influence, within a range of Fe:Sb molar ratios of 1.4 - 144 (Sb(III)) and 1.3 – 126 (Sb(V)). This was in agreement with the results of Mitsunobu *et al.* (2010) who showed that there was no change in the local structures of Sb species in Sb(V)-adsorbed ferrihydrite at various Fe:Sb ratios (20-1000).

4.2 Effect of pH on Sb sorption on ferrihydrite

pH has an important effect on the sorption of metals and metalloids onto Fe-oxyhydroxides because it influences both the surface charge of the solid (thus, the surface coverage) and the aqueous speciation of elements (thus the potential fractionation among the aqueous species and the possible different affinity of the different aqueous species for the solid). Therefore, pH changes may induce variations in metal isotope fractionation factors between sorbed and aqueous species (for example for Zn, see references in Komárek *et al.* (2021); for Mo (Goldberg *et al.,* 2009) ; or for Se (Xu *et al.*, 2020)). Here, we showed that Sb(V) sorption on ferrihydrite was higher at pH 6 than at pH 7 – 7.5. The point of zero charge (pzc) of synthetic Fe-oxides usually ranges between pH 7 and 9 (Parks, 1965; Schwertmann and Cornell, 2000), which suggests that the surface charge of ferrihydrite in the present sorption experiments could be slightly more positive at pH 6 than at pH 7 - 7.5. Regarding Sb speciation in solution, Sb(V) species belongs to the acid/base couple $Sb(OH)_5/Sb(OH)_6^-$, with a pKa value of 2.848 (25 °C) (Accornero *et al.,* 2008); thus, Sb(V) is in the form of anionic $Sb(OH)_6^-$ species in the whole pH range of sorption experiments on ferrihydrite (pH 6 – 7.5). Therefore, the higher Sb(V) sorption on ferrihydrite at pH 6 could be related to the slight change of ferrihydrite surface charge. However, this change did not significantly affect Sb isotope fractionation amplitude. A similar result was obtained for selenium; although pH influenced the amount of Se(IV) adsorbed on hematite, it did not significantly change Se isotopic fractionation (Xu *et al.*, 2020).

Regarding Sb(III), according to speciation calculations for tartrate complexes of antimony by Biver, (2021), it is in the form of uncharged $Sb(OH)_3$ species over the whole pH range of ferrihydrite sorption experiments (6.5 – 7.5). Thus, no organic ligand complexation (that could potentially fractionate Sb isotopes between different species in solution) was involved in the sorption process of Sb(III) on ferrihydrite in these experiments. This is consistent with the negligible effect of pH on sorption isotherms and Sb isotope fractionation between sorbed- and aqueous Sb observed in the present study.

4.3 Potential redox effect

Redox change is the factor which generally causes the most important metal isotope fractionation. Antimony is a redox sensitive element. In our sorption experiments with Sb(III), some Sb(V) (representing 0.4 % to 10 % of total dissolved Sb at pH 6 - 7 (ferrihydrite) and at pH 2.5 (schwertmannite) and up to ~60 % at pH 7.5 and up to ~35 % at pH 4.5, at the highest Fe:Sb ratios) was detected in the dissolved phase at equilibrium (after 48 h). This suggests that some Sb(III) was oxidized during the experiments. However, it was not possible to estimate the proportion of oxidized Sb due to simultaneous sorption. Previous studies showed that Sb(III) was oxidized to some extent during sorption on Fe-oxyhydroxides (Belzile et al., 2001; Leuz et al., 2006; Guo et al., 2014; Qi and Pichler, 2016; 2017). However, these studies were conducted in different experimental conditions and over different duration, thus it was not possible to get data allowing an accurate estimation of the Sb oxidation yield after 48 h, for comparison with the present experiments. For example, Guo *et al.* (2014), using XANES, indicated that the majority of Sb(III) adsorbed onto iron oxyhydroxides was oxidized into Sb(V) after six months of lab preservation of the freeze dehydrated 2-line ferrihydrite (HFO), probably due to the long duration of sample storage. Leuz *et al.* (2006) observed partial Sb(III) oxidation after seven days in sorption experiments with goethite. Belzile *et al.* (2001) showed that only 13 % of initial Sb(III) remained unoxidized after 48 h in sorption experiments with synthetic amorphous Fe oxyhydroxides; however, they used a high Fe:Sb molar ratio (4500) in their experiments, which probably increased Sb(III) oxidation rate, in agreement with the trend observed in our experiments (Figure S5). Two hypotheses were advanced for the Sb(III) oxidation process in previous sorption studies: (1) the ferrihydrite surface would act as a catalyser for Sb(III) oxidation by dissolved oxygen (Guo *et al.*, 2014; Qi and Pichler, 2016); (2) the oxidation of Sb(III) by O_2 and its complexation to the goethite surface would increase the electron density of the Sb atom, which enhances the oxidation process (Leuz *et al.* 2006) and (3) Sb(III) oxidation would proceed by an abiotic electron transfer from Sb(III) to Fe(III) (Belzile *et al.,* 2001; Qi and Pichler, 2016). In all these processes, Sb(III) oxidation would occur once Sb(III) was adsorbed on the surface. Qi and Pichler (2016) showed that Sb(V) may be released in solution after surface-catalysed oxidation due to competition with Sb(III) for sorption sites. This process may generate isotope fractionation between sorbed and aqueous Sb. The apparent fractionation factor for Sb(III) sorption on ferrihydrite obtained in the present study was not significantly different from that obtained for Sb(V), which suggests that Sb(III) oxidation did not significantly impact Sb isotope fractionation between dissolved and sorbed Sb. This may be explained either by the fact that i) Sb(III) oxidation does not significantly fractionate Sb isotopes, which is not concordant with the general rule, or ii) the proportion of Sb(III) oxidized is not sufficient to impact the global Sb isotope fractionation between aqueous and sorbed Sb.

4.4 Influence of the mineral nature

Isotope fractionation between the solid and dissolved phase may vary with mineralogy (Komárek *et al.*, 2021), for example in the case of the sorption of Mo on Fe-(oxyhydr)oxides, for which the fractionation increases in the order magnetite < ferrihydrite < goethite < hematite (Goldberg *et al.*, 2009) or in the case of Zn sorbed on ferrihydrite and goethite (Juillot *et al.*, 2008). This mineral effect could be related both to mineral surface speciation and solution chemistry (Goldberg *et al.*, 2009). Here, sorption experiments with schwertmannite were conducted at acid pH values (i.e. 2.5 – 4.5), corresponding to the stability domain of this mineral, which is different from that of ferrihydrite (i.e. 6 - 7.5); thus, the effects of mineral on Sb isotope fractionation during sorption cannot be distinguished from pH effect. We obtained similar sorption reactivity for schwertmannite at acid pH than for ferrihydrite at near-neutral pH and both Sb species were efficiently sorbed on this mineral. Sorption studies of antimony on schwertmannite are rare in the literature and there is no information on the bonding environment of sorbed-Sb(III) and -Sb(V) species. Nagano *et al.* (2011) showed that Sb oxyanions had a high affinity for natural schwertmannite found in AMD-impacted river and suggested the formation of inner-sphere complexes at the schwertmannite surface. Only one study, Li *et al.* (2016), investigated the sorption behaviour of Sb(III) and Sb(V) on schwertmannite separately, at different pH. Over the pH range 3.5 - 5.0, Sb(III) and Sb(V) are adsorbed efficiently and similarly (Li *et al.*, 2016). Our results corroborated these findings, with similar maximum Sb sorption densities obtained for Sb(III) (3528 µg.m², i.e. 176 $mg.g^{-1}$) and for Sb(V) (2660 µg.m², i.e. 133 $mg.g^{-1}$) in the studied pH range (2.5 – 4.5). pH had little effect on the sorption of Sb(V) on schwertmannite while Sb(III) sorption increased slightly at pH 4.5 compared to pH 2.5 (Figure 1). This behaviour is hard to explain since i) schwertmannite is protonated at pH 2.5-4.5 (the pH_{pzc} is 5.1 – 7.2, Li *et al.*, 2016), ii) aqueous speciation does not change for Sb(III) between pH 2.5 and pH 4.5 ; speciation calculations for tartrate complexes by Biver (2021) showed that Sb(III) is in the form of an anionic species $[Sb_2\{H\text{-}2Tar\}_2]^{2-}$ at acid pH, while it changes for Sb(V) at pH 4.5 (predominance of anionic $Sb(OH)_6^-$ species) compared to pH 2.5 (predominance of uncharged $Sb(OH)_5$ species). Therefore, the sorption behaviour and bonding environment of antimony species on schwertmannite requires further investigation. Nevertheless, the slight change of reactivity of Sb(III) with pH had no significant effect on Sb isotope fractionation between sorbed- and aqueous-Sb, and finally the amplitude and direction of Sb isotope fractionation factors with schwertmannite were similar to those obtained with ferrihydrite. In both cases, the isotope fractionation could arise from the distortion of the atomic polyhedron of Sb(III) and Sb(V) during sorption, as evidenced in several sorption studies for Ge (Pokrovsky *et al.*, 2014), Mo (Wasylenki *et al.*, 2011), Cd (Yan *et al.,* 2021) and Ni (Wasylenki *et al.*, 2015; Wang and Wasylenki, 2017; Gueguen *et al.*, 2018), and theoretical study for Sb (Ferrari *et al.*, 2022). Extended X-ray adsorption fine structure (EXAFS) measurements would be necessary to better characterise the local structure of Sb species in ferrihydrite and schwertmannite.

4.5 Environmental significance

Schwertmannite and ferrihydrite are typical Sb-bearing phases in rivers impacted by AMD and the main control of Sb mobility. The relatively uniform fractionation factor $\Delta^{123}Sb_{solid\text{-}solution}$ around -0.3 ‰ obtained between sorbed- and aqueous-Sb in the present study is of particular interest in the perspective of tracing sorption process in environmental studies. However, this value obtained in laboratory conditions with simple solution chemistry must be compared to apparent fractionation factors in real AMD streams worldwide. A few data are available from the literature; a slight heavy Sb isotopic enrichment was observed in a drainage water sample from the Ichinokawa mine in Japan

compared to the data from Sb minerals (Sb_2S_3) collected in the same area (Tanimizu *et al.*, 2011). The isotopic fractionation was ascribed to adsorption equilibrium with Fe hydroxides in the surrounding sediment. It was in line with the results of laboratory experiments of Sb(V) sorption on ferrihydrite which also indicated a slight enrichment of the heavier Sb isotope in the aqueous phase compared to adsorbed Sb (Araki *et al.,* 2009). In a recent study, Resongles *et al.* (2021) showed an apparent fractionation of -0.35‰ between river sediments and water in a stream impacted by AMD at the San José mine (Oruro, Bolivia), suggesting that adsorption may be an important process leading to an enrichment in heavy Sb isotope in AMD waters. These results tend to validate the fractionation factors obtained in the laboratory in the present study and show that Sb isotopes may be useful to investigate the mechanisms controlling Sb fate in mining-impacted rivers. Further research is necessary to document other processes, especially reduction and oxidation, that are likely to affect antimony in mine waters due to its sensitivity to redox changes and which are expected to fractionate Sb isotopes to a higher extent than sorption processes (Wiederhold, 2015).

5. Conclusion

This study showed that sorption on ferrihydrite and schwertmannite induced a slight enrichment in the light isotopes in sorbed Sb, with no significant effect of pH, Sb:Fe ratio, or redox Sb species under the study conditions. The $\Delta^{123}Sb_{solid\text{-}solution}$ values obtained for sorption on ferrihydrite were -0.24 ± 0.06 ‰ for Sb(III) and -0.34 ± 0.08 ‰ for Sb(V). For sorption on schwertmannite, the $\Delta^{123}Sb_{solid\text{-}solution}$ values obtained were -0.35 ± 0.07 ‰ for Sb(III) and -0.29 ± 0.02 ‰ for Sb(V). The observed isotopic fractionation followed a closed system equilibrium model and could result from the distortion of the atomic polyhedron formed by Sb(III) and Sb(V) due to the appearance of iron as second closest Sb neighbour during the Sb adsorption, thus decreasing the polyhedral symmetry. This study gives new interpretation tools for the understanding of the isotopic cycle of Sb in mining and natural environments.

6. Acknowledgements

This work received financial support from the CNRS INSU EC2CO program (Project AntiBol). We thank Sophie Delpoux and Léa Causse for the speciation and trace element analysis performed on the AETE-ISO platform, OSU OREME/Université de Montpellier and Laura Blanc, David Clousier and Léa Pradeilles for their help during the experiments. We would like to acknowledge Nicolas Donzel and Bernard Fraisse from the PAC platform and Frédéric Hernandez from the MEA platform, Université de Montpellier, for BET surface area measurement, DRX analysis and SEM images, respectively.

7. References

Accornero, M., Marini, L. and Lelli, M. (2008) 'The Dissociation Constant of Antimonic Acid at 10–40 °C', *Journal of Solution Chemistry*, 37(6), pp. 785–800. https://doi.org/10.1007/s10953-008-9280-4.

Araki, Y., Tanimizu, M. and Takahashi, Y. (2009) 'Antimony isotopic fractionation during adsorption on ferrihydrite', *Geochimica et Cosmochimica Acta Supplement*, 73, p. A49.

Asaoka, S. *et al.* (2011) 'Preconcentration Method of Antimony Using Modified Thiol Cotton Fiber for Isotopic Analyses of Antimony in Natural Samples', *Analytical Sciences*, 27, pp. 25–28.

Balistrieri, L.S. *et al.* (2008) 'Fractionation of Cu and Zn isotopes during adsorption onto amorphous Fe(III) oxyhydroxide: Experimental mixing of acid rock drainage and ambient river water',

Geochimica et Cosmochimica Acta, 72(2), pp. 311–328. https://doi.org/10.1016/j.gca.2007.11.013.

Belzile, N., Chen, Y.-W. and Wang, Z. (2001) 'Oxidation of antimony (III) by amorphous iron and manganese oxyhydroxides', *Chemical Geology*, 174(4), pp. 379–387. https://doi.org/10.1016/S0009-2541(00)00287-4.

Kaufmann, B. *et al.* (2021) 'In-situ determination of antimony isotope ratios in Sb minerals by femtosecond LA-MC-ICP-MS', *Journal of Analytical Atomic Spectrometry*, 36, pp. 1554-1567. https://doi.org/10.1039/D1JA00089F.

Bigham, J.M. *et al.* (1996) 'Schwertmannite and the chemical modeling of iron in acid sulfate waters', *Geochimica et Cosmochimica Acta*, 60(12), pp. 2111–2121. https://doi.org/10.1016/0016-7037(96)00091-9.

Biver, M. (2021) 'A Comprehensive Potentiometric Study of the Tartrate Complexes of Trivalent Arsenic, Antimony, and Bismuth in Aqueous Solution', *Inorganic Chemistry*, 60(23), pp. 18360–18369. https://doi.org/10.1021/acs.inorgchem.1c02962.

Bryan, A.L. *et al.* (2015) 'Zinc isotope fractionation during adsorption onto Mn oxyhydroxide at low and high ionic strength', *Geochimica et Cosmochimica Acta*, 157, pp. 182–197. https://doi.org/10.1016/j.gca.2015.01.026.

European Commission (2020) *'Communication From The Commission To The European Parliament, The Council, The European Economic And Social Committee And The Committee Of The Regions. Critical Raw Materials Resilience: Charting a Path towards greater Security and Sustainability*', Communication COM(2020)474.

Degryse, P. *et al.* (2015) 'Isotopic investigation into the raw materials of Late Bronze Age glass making', *Journal of Archaeological Science*, 62, pp. 153–160. https://doi.org/10.1016/j.jas.2015.08.004.

Degryse, P. *et al.* (2020) 'Isotopic evidence for the use of Caucasian antimony in Late Bronze Age glass making', *Journal of Archaeological Science*, 120, p. 105195. https://doi.org/10.1016/j.jas.2020.105195.

Essington, M.E. and Stewart, M.A. (2018) 'Adsorption of Antimonate, Sulfate, and Phosphate by Goethite: Reversibility and Competitive Effects', *Soil Science Society of America Journal*, 82(4), pp. 803–814. https://doi.org/10.2136/sssaj2018.01.0003.

Ferrari, C. *et al.* (2021) 'A single-step purification method for the precise determination of antimony isotopic composition of environmental, geological and biological samples by HG-MC-ICP-MS', *Journal of Analytical Atomic Spectrometry*, 36(4), pp. 776–785. https://doi.org/10.1039/D1JA90048J

Ferrari, C. *et al.* (2022) 'Equilibrium mass-dependent isotope fractionation of antimony between stibnite and Sb secondary minerals: A first-principles study', *Chemical Geology*, p. 121115. https://doi.org/10.1016/j.chemgeo.2022.121115.

Filella, M., Williams, P.A. and Belzile, N. (2009) 'Antimony in the environment : knows and unknowns', *Environmental Chemistry*, 6, pp. 95–105. https://doi.org/10.1071/EN09007.

Goldberg, T. *et al.* (2009) 'Mo isotope fractionation during adsorption to Fe (oxyhydr)oxydes', *Geochimica et Cosmochimica Acta*, 73, pp. 6502–6516. https://doi.org/10.1016/j.gca.2009.08.004.

Gueguen, B. *et al.* (2018) 'Variable Ni isotope fractionation between Fe-oxyhydroxides and implications for the use of Ni isotopes as geochemical tracers', *Chemical Geology*, 481, pp. 38–52. https://doi.org/10.1016/j.chemgeo.2018.01.023.

Guo, W. *et al.* (2018) 'Environmental geochemical and spatial/temporal behavior of total and speciation of antimony in typical contaminated aquatic environment from Xikuangshan, China', *Microchemical Journal*, 137, pp. 181–189. https://doi.org/10.1016/j.microc.2017.10.010.

Guo, X. *et al.* (2014) 'Adsorption of antimony onto iron oxyhydroxides: Adsorption behavior and surface structure', *Journal of Hazardous Materials*, 276, pp. 339–345. http://dx.doi.org/10.1016/j.jhazmat.2014.05.025.

Hao, C. *et al.* (2021) 'Contrasting water–rock interaction behaviors of antimony and arsenic in contaminated rivers around an antimony mine, Hunan Province, China', *Geochemistry*, 81(2), p. 125748. https://doi.org/10.1016/j.chemer.2021.125748.

He, M. *et al.* (2019) 'Antimony speciation in the environment: Recent advances in understanding the biogeochemical processes and ecological effects', *Journal of Environmental Sciences*, 75, pp. 14–39. https://doi.org/10.1016/j.jes.2018.05.023.

Juillot, F. *et al.* (2008) 'Zn isotopic fractionation caused by sorption on goethite and 2-Lines ferrihydrite', *Geochimica et Cosmochimica Acta*, 72(19), pp. 4886–4900. https://doi.org/10.1016/j.gca.2008.07.007.

Komárek, M. *et al.* (2021) 'Metal isotope complexation with environmentally relevant surfaces: Opening the isotope fractionation black box', *Critical Reviews in Environmental Science & Technology*, pp. 1–31. https://doi.org/10.1080/10643389.2021.1955601.

Leuz, A.-K., Mönch, H. and Johnson, A. (2006) 'Sorption of Sb(III) and Sb(V) to Goethite: Influence on Sb(III) Oxidation and Mobilization', *Environmental Science & Technology*, 40(23), pp. 7277–7282. https://doi.org/10.1021/es061284b.

Li, S. *et al.* (2021) 'A new purification method based on a thiol silica column for high precision antimony isotope measurements', *Journal of Analytical Atomic Spectrometry*, 36, pp. 157–164. https://doi.org/10.1039/D0JA00367K.

Li, Y. *et al.* (2016) 'Removal of antimonate and antimonite from water by schwertmannite granules', *Desalination and Water Treatment*, pp. 1–14. https://doi.org/10.1080/19443994.2016.1155176.

Liu, F. *et al.* (2015) 'Schwertmannite Synthesis through Ferrous Ion Chemical Oxidation under Different H2O2 Supply Rates and Its Removal Efficiency for Arsenic from Contaminated Groundwater', *PLOS ONE*, 10(9), p. e0138891. https://doi.org/10.1371/journal.pone.0138891.

Liu, J. *et al.* (2020) 'Chromatographic purification of antimony for accurate isotope analysis by MC-ICP-MS', *Journal of Analytical Atomic Spectrometry*, 35, pp. 1360–1367. https://doi.org/10.1039/D0JA00136H.

Lobo, L. *et al.* (2012) 'Investigation of natural isotopic variation of Sb in stibnite ores via multi-collector ICP-mass spectrometry - perspectives for Sb isotopic analysis of Roman glass', *Journal of Analytical Atomic Spectrometry*, 27, pp. 1304–1310. https://doi.org/10.1039/c2ja30062a.

Lobo, L. *et al.* (2013) 'Isotopic analysis of antimony using multi-collector ICP-mass spectrometry for provenance determination of Roman glass', *Journal of Analytical Atomic Spectrometry*, 28, pp. 1213–1219. https://doi.org/10.1039/c3ja50018g.

Lobo, L. *et al.* (2014) 'Copper and antimony isotopic analysis via multi-collector ICP-mass spectrometry for provenancing ancient glass', *Journal of Analytical Atomic Spectrometry*, 29(1), pp. 58–64. https://doi.org/10.1039/C3JA50303H.

Manaka, M. *et al.* (2007) 'Natural attenuation of antimony in mine drainage water', *Geochemical Journal*, 41(1), pp. 17–27. https://doi.org/10.2343/geochemj.41.17.

McComb, K.A., Craw, D. and McQuillan, A.J. (2007) 'ATR-IR Spectroscopic Study of Antimonate Adsorption to Iron Oxide', *Langmuir*, 23(24), pp. 12125–12130. https://doi.org/10.1021/la7012667.

Mitsunobu, S. *et al.* (2010) 'Antimony(V) Incorporation into Synthetic Ferrihydrite, Goethite, and Natural Iron Oxyhydroxides', *Environmental Science & Technology*, 44(10), pp. 3712–3718. https://doi.org/10.1021/es903901e.

Mitsunobu, S., Harada, T. and Takahashi, Y. (2006) 'Comparison of Antimony Behavior with that of Arsenic under Various Soil Redox Conditions', *Environmental Science & Technology*, 40(23), pp. 7270–7276. https://doi.org/10.1021/es060694x.

Nagano, T. *et al.* (2011) 'Evaluation of the Affinity of Some Toxic Elements to Schwertmannite in Natural Streams Contaminated with Acid Mine Drainage', *Water, Air, & Soil Pollution*, 216(1), pp. 153–166. https://doi.org/10.1007/s11270-010-0523-9.

Parks, G.A. (1965) 'The isoelectric points of solid oxides, solid hydroxides, and aqueous hydroxo complex systems.', *Chemical Reviews*, 65(2).

Pokrovsky, O.S. *et al.* (2014) 'Germanium isotope fractionation during Ge adsorption on goethite and its coprecipitation with Fe oxy(hydr)oxides', *Geochimica et Cosmochimica Acta*, 131, pp. 138–149. https://doi.org/10.1016/j.gca.2014.01.023.

Qi, P. and Pichler, T. (2016) 'Sequential and simultaneous adsorption of Sb(III) and Sb(V) on ferrihydrite: Implications for oxidation and competition', *Chemosphere*, 145, pp. 55–60. https://doi.org/10.1016/j.chemosphere.2015.11.057.

Qi, P. and Pichler, T. (2017) 'Competitive adsorption of As(III), As(V), Sb(III) and Sb(V) onto ferrihydrite in multi-component systems: Implications for mobility and distribution', *Journal of Hazardous Materials*, 330, pp. 142–148. https://doi.org/10.1016/j.jhazmat.2017.02.016.

Regenspurg, S., Brand, A. and Peiffer, S. (2004) 'Formation and stability of schwertmannite in acidic mining lakes', *Geochimica et Cosmochimica Acta*, 68(6), pp. 1185–1197. https://doi.org/10.1016/j.gca.2003.07.015.

Resongles, E. *et al.* (2013) 'Fate of Sb(V) and Sb(III) species along a gradient of pH and oxygen concentration in the Carnoulès mine waters (Southern France)', *Environmental Science Processes and Impacts*, 15, pp. 1536–1544. https://doi.org/10.1039/c3em00215b.

Resongles, E. *et al.* (2015) 'Antimony isotopic composition in river waters affected by ancient mining activity', *Talanta*, 144, pp. 851–861. http://dx.doi.org/10.1016/j.talanta.2015.07.013.

Resongles, E. *et al.* (2021) 'Antimony isotopic composition in stream waters impacted by acid mine drainage', Goldschmidt2021, Virtual, 4-9 July 2021.

Rouxel, O., Ludden, J. and Fouquet, Y. (2003) 'Antimony isotope variations in natural systems and implications for their use as geochemical tracers', *Chemical Geology*, 200, pp. 25–40. https://doi.org/10.1016/S0009-2541(03)00121-9.

Scheinost, A.C. *et al.* (2006) 'Quantitative antimony speciation in shooting-range soils by EXAFS spectroscopy', *Geochimica et Cosmochimica Acta*, 70(13), pp. 3299–3312. https://doi.org/10.1016/j.gca.2006.03.020.

Schwertmann, U. and Cornell, R.M. (2000) *Iron Oxides in the Laboratory - Preparation and characterization*. Second Edition. WILEY-VCH.

Sun, G. *et al.* (2021) 'Precise analysis of antimony isotopic composition in geochemical materials by MC-ICP-MS', *Chemical Geology*, p. 120459. https://doi.org/10.1016/j.chemgeo.2021.120459.

Tanimizu, M. *et al.* (2011) 'Determination of natural isotopic variation in antimony using inductively coupled plasma mass spectrometry for an uncertainty estimation of the standard atomic weight of antimony', *Geochemical Journal*, 45, pp. 27–32.

Teng, F.-Z., Dauphas, N. and Watkins, J.M. (2017) 'Non-Traditional Stable Isotopes: Retrospective and Prospective', *Reviews in Mineralogy and Geochemistry*, 82(1), pp. 1–26. https://doi.org/10.2138/rmg.2017.82.1.

U.S. Geological Survey (2018) 'Antimony - Historical Statistics (Data series 140 - 2018 update)'. Available at: https://www.usgs.gov/media/files/antimony-historical-statistics-data-series-140. Last access on 7/11/2022.

U.S. Geological Survey (2022) *2022 Final List of Critical Minerals*. Notices Federal Register / Vol. 87, No. 37.

Wang, S.-J. and Wasylenki, L.E. (2017) 'Experimental constraints on reconstruction of Archean seawater Ni isotopic composition from banded iron formations', *Geochimica et Cosmochimica Acta*, 206, pp. 137–150. https://doi.org/10.1016/j.gca.2017.02.023.

Wang, X. *et al.* (2011) 'Antimony distribution and mobility in rivers around the world's largest antimony mine of Xikuangshan, Hunan Province, China', *Microchemical Journal*, 97(1), pp. 4–11. https://doi.org/10.1016/j.microc.2010.05.011.

Wasylenki, L.E. *et al.* (2011) 'The molecular mechanism of Mo isotope fractionation during adsorption to birnessite', *Geochimica et Cosmochimica Acta*, 75(17), pp. 5019–5031. https://doi.org/10.1016/j.gca.2011.06.020.

Wasylenki, L.E. *et al.* (2015) 'Ni isotope fractionation during sorption to ferrihydrite: Implications for Ni in banded iron formations', *Chemical Geology*, 400, pp. 56–64. https://doi.org/10.1016/j.chemgeo.2015.02.007.

Wiederhold, J.G. (2015) 'Metal Stable Isotope Signatures as Tracers in Environmental Geochemistry', *Environmental Science & Technology*, 49(5), pp. 2606–2624. https://doi.org/10.1021/es504683e.

Xu, W. *et al.* (2020) 'Selenium isotope fractionation during adsorption by Fe, Mn and Al oxides', *Geochimica et Cosmochimica Acta*, 272, pp. 121–136. https://doi.org/10.1016/j.gca.2020.01.001.

Yan, X. *et al.* (2021) 'Cadmium Isotope Fractionation during Adsorption and Substitution with Iron (Oxyhydr)oxides', *Environmental Science & Technology*, 55(17), pp. 11601–11611. https://doi.org/10.1021/acs.est.0c06927.

Zhou, W. *et al.* (2022) 'Antimony isotope fractionation during adsorption on aluminum oxides', *Journal of Hazardous Materials*, 429, p. 128317. https://doi.org/10.1016/j.jhazmat.2022.128317.

Supplementary information to:

Antimony isotope fractionation during Sb(V) and Sb(III) adsorption on Fe secondary minerals (schwertmannite and ferrihydrite)

Colin Ferrari[*a], Eléonore Resongles[a], Rémi Freydier[a], and Corinne Casiot[a]

[a]*HydroSciences Montpellier, Univ. Montpellier, CNRS, IRD, Montpellier, France*

*Corresponding author:

Mailing address : Université de Montpellier – CC 57
163, rue Auguste Broussonnet,
34090 Montpellier, France
Email : colin.ferrari@umontpellier.fr

This PDF file includes:

Section S1: Synthesis and characterisation of ferrihydrite and schwertmannite

Section S2: Additional tables and figures (Table S1 to S2 and Figure S1 to S5).

Section S1: Synthesis and characterisation of ferrihydrite and schwertmannite

S1.1 Mineral synthesis protocols

The procedure for the synthesis of 2-line ferrihydrite was from Schwertmann and Cornell, (2000). First, 16 g of $Fe(NO_3)_3,9H_2O$ were dissolved in 200 mL of ultrapure water. Then, a 1 mol.L^{-1} KOH solution was added drop by drop until iron starts precipitating at pH 7.4-7.5. Next, the suspension was centrifuged at 4000 rpm for 3 minutes. The supernatant was removed, and the precipitate was rinsed three times with ultrapure water. Ferrihydrite was dried in a desiccator under vacuum for 4 to 5 days. Finally, the ferrihydrite was crushed in an agate mortar.

Schwertmannite was synthesized following the protocol of Liu *et al.*, (2015) adapted from the protocol of Regenspurg, Brand and Peiffer (2004). 18.3 g of $FeSO_4.7H_2O$ were dissolved in 1 L of ultrapure water and agitated. 1 mL of H_2O_2 was then added every 12 hours for 60 hours with pH monitoring. After 60 hours, the suspension was centrifugated, the supernatant was removed, and the red-orange precipitate was rinsed five times with ultrapure water before to be freeze-dried and crushed in an agate mortar.

S1.2 Mineral characterisation methods

The quality of the synthetized ferrihydrite and schwertmannite was checked using X-Ray powder Diffraction (XRD), Brunauer-Emmett-Teller (BET) method and Scanning Electron Microscopy (SEM, schwertmannite only) analyses. XRD analysis was carried out with a Bruker D8 Discover diffractometer using Cu–Kα1 radiation in step scan mode between 10° and 90° 2θ with a 0.020° 2θ step and a counting time of 10 s per step. The specific surface area was determined using the BET method by N_2 adsorption–desorption protocol (3Flex, Micromeritics) after degassing the sample at room temperature during 24 h (ferrihydrite) or at 50 °C during 24 h (schwertmannite). The structure of synthetized schwertmannite was observed using Scanning Electron Microscopy (SEM) images (FEI Quanta 200 FEG microscope) performed at the MEA platform, Université de Montpellier.

S1.3 Results

The BET surface area of the synthesized ferrihydrite was 282 $m^2.g^{-1}$, which is in accordance with the values of 200 – 300 $m^2.g^{-1}$ given by Schwertmann and Cornell (2000). The XRD diffractogram presented two peaks at 35 and 63° 2θ which is typical of 2-line ferrihydrite (Figure S1a). Schwertmannite specific surface area was 50 $m^2.g^{-1}$ which is in the same magnitude, yet slightly higher, than the specific surface area of schwertmannite synthesized using a similar protocol (4 to 16 $m^2.g^{-1}$) (Regenspurg, Brand and Peiffer, 2004; Paikaray, Göttlicher and Peiffer, 2011; Liu *et al.*, 2015). XRD diffractogram was characteristic of schwertmannite with six peaks at 18°, 26°, 35°, 47°, 55° and 61° 2θ (Figure S1b). The SEM image (Figure S2) showed that the surface of the synthetized schwertmannite p 144 resented needle-like structures forming the “hedge-hog” structure typical of natural schwertmannite (Liu *et al.*, 2015).

\

References

Liu, F. *et al.* (2015) 'Schwertmannite Synthesis through Ferrous Ion Chemical Oxidation under Different H_2O_2 Supply Rates and Its Removal Efficiency for Arsenic from Contaminated Groundwater', *PLOS ONE*, 10(9), p. e0138891. https://doi.org/10.1371/journal.pone.0138891.

Paikaray, S., Göttlicher, J. and Peiffer, S. (2011) 'Removal of As(III) from acidic waters using schwertmannite: Surface speciation and effect of synthesis pathway', *Chemical Geology*, 283(3), pp. 134–142. https://doi.org/10.1016/j.chemgeo.2010.08.011.

Regenspurg, S., Brand, A. and Peiffer, S. (2004) 'Formation and stability of schwertmannite in acidic mining lakes 11Associate editor: C. M. Eggleston', *Geochimica et Cosmochimica Acta*, 68(6), pp. 1185–1197. https://doi.org/10.1016/j.gca.2003.07.015.

Schwertmann, U. and Cornell, R.M. (2000) *Iron Oxides in the Laboratory - Preparation and characterization*. WILEY-VCH.

Section S2: Additional tables and figures (Table S1 to S2 and Figure S1 to S5).

Table S1: Antimony isotope composition of dissolved Sb(III) and Sb(V) after 48 h and 96 h in sorption experiments on schwertmannite for initial Sb concentrations of 0.1 mg.L^{-1} or 10 mg.L^{-1} showing that isotopic equilibrium was reached after 48 h.

Sb species	Initial dissolved Sb concentrations (mg.L^{-1})	Sorption experiment duration (h)	Sb adsorbed (%)	δ^{123}Sb (‰)	2 sd (‰)
Sb(III)	10	48	9.9%	0.36	0.05
		96	9.8%	0.39	0.07
	0.1	48	91.5%	0.80	0.03
		96	93.9%	0.78	0.07
Sb(V)	10	48	21.0%	0.14	0.05
		96	19.2%	0.14	0.04
	0.1	48	90.7%	0.43	0.10
		96	93.6%	0.47	0.03

Table S2: Hydride generation parameters used for Sb isotope ratio analysis by HG-MC-ICP-MS. These are optimized based on the ones indicated in Ferrari et al., (2021). The removal of the additional gas flow in the hydride generation system leaded to a better signal stability.

Hydride Generation Parameters	
System	HydrideICP - Elemental Scientific
Peristaltic Pump Speed	20 rpm
Reducing agent medium	$NaBH_4$ 1 % w/v in NaOH 0.05 % w/v
Acid medium	HCl 3 M
Waste tubing	Yellow/Blue - 1.52 mm ID / 1.28 $ml.min^{-1}$
Sample tubing	Black/Black - 0.76 mm ID / 0.48 $ml.min^{-1}$
$NaBH_4$ tubing	Orange/Yellow - 0.51 mm ID / 0.24 $ml.min^{-1}$
HCl tubing	Orange/Green - 0.38 mm ID / 0.12 $ml.min^{-1}$
Sample gas flow (Ar)	0.95 L min^{-1}
Instrument Settings	
Instrument	Neptune - Thermo Scientific
Forward power	1080 W
Skimmer Cone	X version
Sample Cone	Jet version
Measured isotopes	^{120}Sn, ^{121}Sb, ^{122}Sn, ^{123}Sb (^{123}Te), ^{126}Te
Cups	L1, C, H1, H2, H3
Sensitivity ^{121}Sb (V/ppb)	0.8
Acquisition Parameters	
Uptake time (s)	140
Number of blocks	1
Number of cycles per block	80
Integration Time (s)	4.194

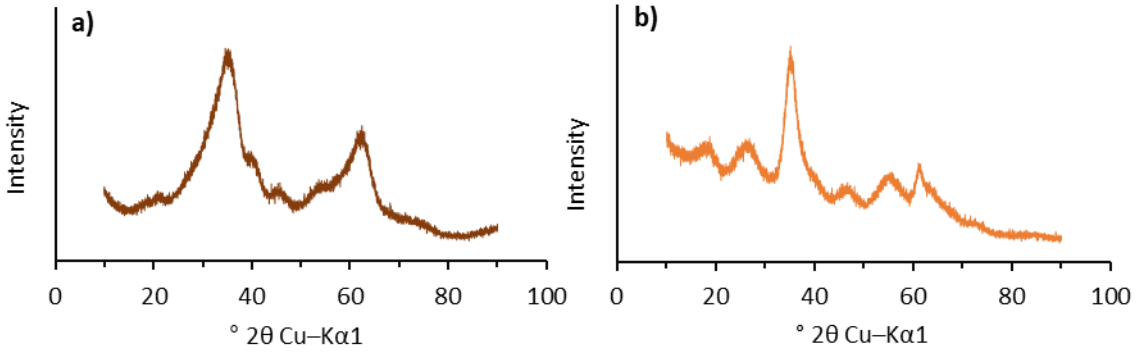

Figure S1: XRD diffractograms of a) synthetized ferrihydrite and b) schwertmannite.

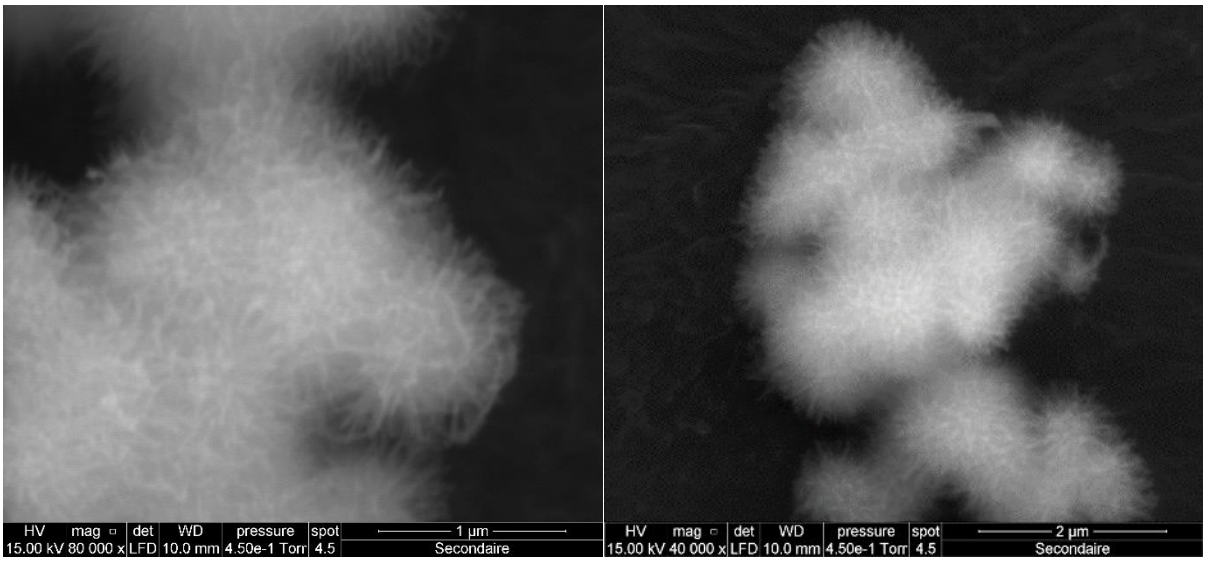

Figure S2: SEM images of the synthetized schwertmannite showing the "hedge-hog"-like structure characteristic of schwertmannite.

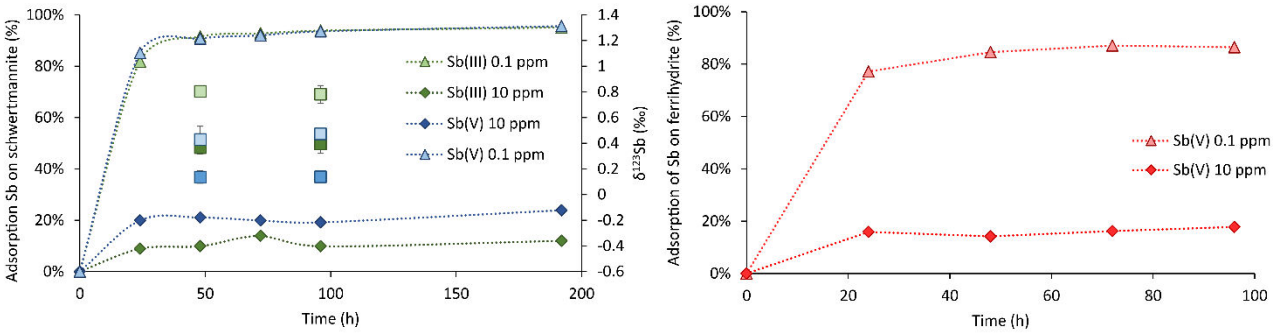

Figure S3: Kinetic monitoring of the sorption of Sb(III) and Sb(V) on schwertmannite at pH 4.5 (left) and of the sorption of Sb(V) on ferrihydrite at pH 6 (right), for two different Sb concentrations : 0.1 and 10 mg.L^{-1} (corresponding to two different initial Fe:Sb molar ratios : Fe:Sb =1.3 and 126). The isotopic equilibrium was reached within less than 48 hours in all conditions tested (squares points).

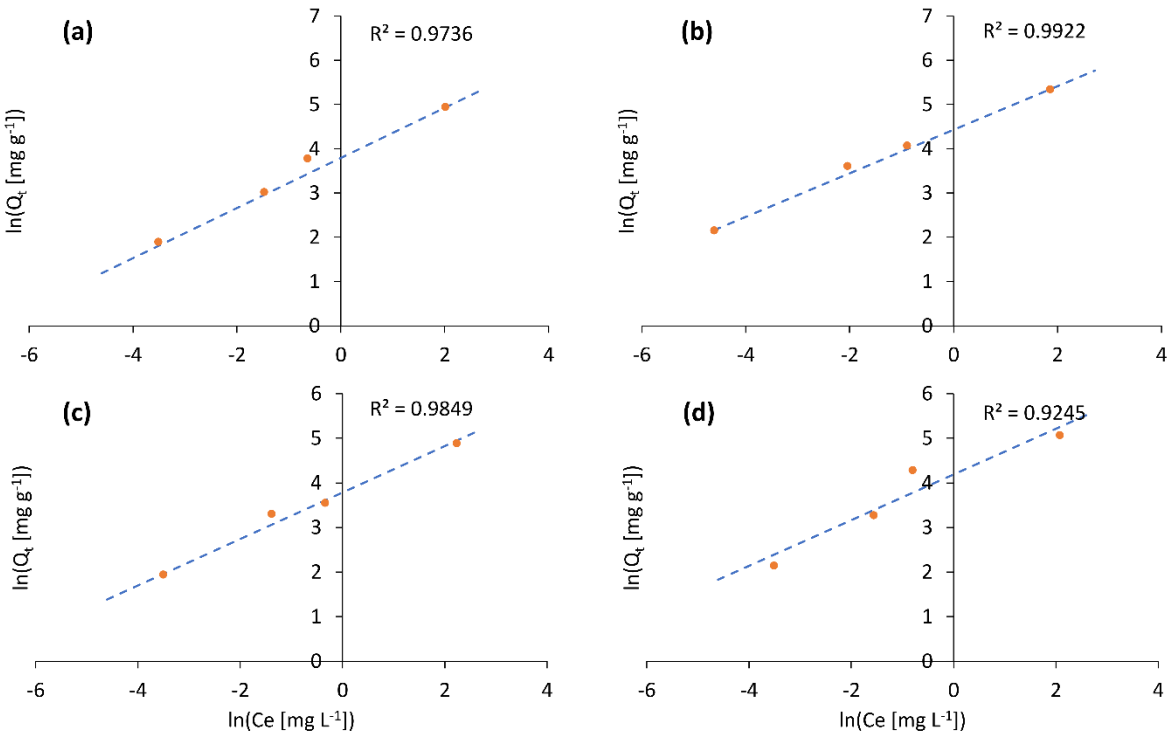

Figure S4: Linear Freundlich sorption isotherms of Sb(III) on (a) ferrihydrite and (c) schwertmannite, and Sb(V) on (b) ferrihydrite and (d) schwertmannite calculated with Equation 4.

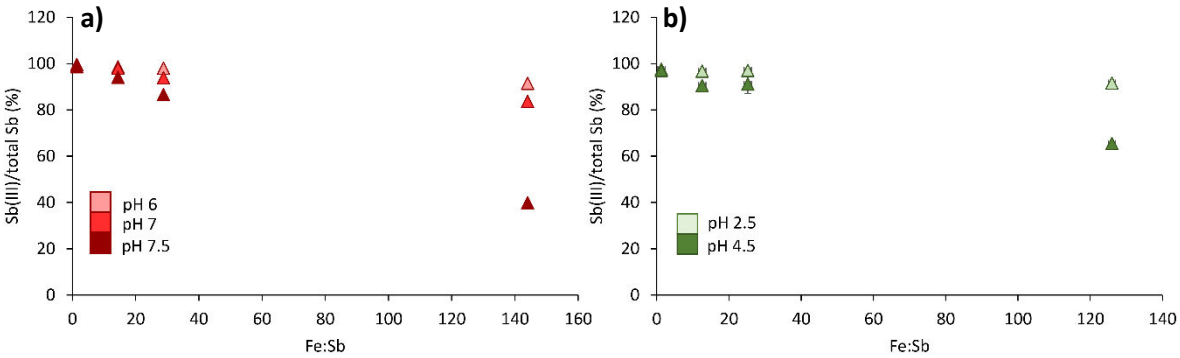

Figure S5: Variation of the proportion of Sb(II) in the dissolved phase at equilibrium (48 h) as a function of Fe:Sb molar ratio and pH in sorption experiments with ferrihydrite (a) and schwertmannite (b).

PARTIE C : Fractionnement isotopique de l'antimoine lors de l'oxydation de Sb(III) en Sb(V) : processus biotiques et abiotiques (article 4)

Ferrari Colin, Resongles Eléonore, Hery Marina, Désoeuvre Angélique, Freydier Rémi, Delpoux Sophie, Bruneel Odile, Casiot Corinne

Résumé en français

L'oxydation de l'antimonite (Sb(III)) en antimoniate (Sb(V)) joue un rôle important dans le contrôle de la mobilité du Sb dans les systèmes aquatiques. Le fractionnement des isotopes du Sb ($^{123}Sb/^{121}Sb$) lors de l'oxydation du Sb(III) a été étudié dans cet article. Nous avons analysé le rapport $^{123}Sb/^{121}Sb$ des espèces Sb(III) et Sb(V) dissoutes lors de l'oxydation biotique et abiotique de Sb(III) à pH 6 et 0,1 mM de Sb.

Une souche bactérienne porteuse du gène *AioA* du genre *Ensifer* isolée à partir de sédiments de rivière à haute teneur en Sb a été utilisée pour les expériences d'oxydation biotique. Lors de cette oxydation, le Sb(V) produit est enrichi en isotopes légers par rapport au Sb(III), avec un facteur de fractionnement $\Delta^{123}Sb_{Sb(III)-Sb(V)}$ de +0,20 ± 0,07 ‰. Ce $\Delta^{123}Sb$ est indépendant de la cinétique d'oxydation (dans la gamme 1,6 – 3,1 $\mu M.h^{-1}$). Au cours de l'oxydation abiotique avec H_2O_2 à pH 6, aucun fractionnement isotopique n'a été mis en évidence entre les espèces oxydée et réduite.

Ces résultats mettent en évidence l'influence de l'activité bactérienne sur la signature isotopique du Sb et suggèrent que les processus d'oxydation biotique et abiotique du Sb peuvent être différenciés à l'aide des isotopes du Sb. Cependant, l'absence de fractionnement au cours de l'oxydation abiotique reste inexpliquée et devrait être étudiée plus avant.

Antimony isotopic fractionation during Sb(III) oxidation to Sb(V): biotic and abiotic processes

Colin Ferrari[a*], Eléonore Resongles[a], Marina Héry[a], Angélique Désoeuvre[a], Rémi Freydier[a], Sophie Delpoux[a], Odile Bruneel[a], Corinne Casiot[a]

[a]*HydroSciences Montpellier, Univ. Montpellier, CNRS, IRD, Montpellier, France*

*Corresponding author

Mailing address : Université de Montpellier – CC 57
163, rue Auguste Broussonnet,
34090 Montpellier, France
Email : ferraricolin@gmail.com

Abstract

Oxidation of antimonite (Sb(III)) to antimonate (Sb(V)) plays an important role in the control of Sb mobility in aquatic systems. Fractionation of Sb isotopes ($^{123}Sb/^{121}Sb$) during Sb(III) oxidation has been investigated in the present study. We analysed $^{123}Sb/^{121}Sb$ ratio of dissolved Sb(III) and Sb(V) species during biotic and abiotic oxidation of Sb(III) at pH 6 and 0.1 mM Sb. Biotic experiments used a AioA gene carrier bacterial strain of the genus *Ensifer* isolated from high-Sb river sediments. During biotic oxidation, the Sb(V) produced was enriched in the light isotope compared to Sb(III), with a fractionation factor $\Delta^{123}Sb_{Sb(III)-Sb(V)}$ of +0.20 ± 0.07 ‰. This $\Delta^{123}Sb$ was independent of the oxidation kinetic (in the range 1.6 – 3.1 µM.h^{-1}). During abiotic oxidation with 60 mM H_2O_2 at pH 6, no isotopic fractionation was evidenced between the oxidized and the reduced species. These results highlight the influence of bacterial activity on Sb isotope signature and suggests that biotic and abiotic oxidation processes can be differentiated using Sb isotopes. However, the lack of fractionation during abiotic oxidation remains unclear and should be investigated further.

1. Introduction

Antimony is a contaminant of emerging concern. Accelerated anthropogenic contamination has been evidenced on a global scale (Krachler *et al.*, 2005; Hong *et al.*, 2012). At the Earth' surface, anthropogenic fluxes of Sb exceed natural fluxes with mining being the main factor of influence and moving around 155000 tons of Sb every year (Sen and Peucker-Ehrenbrink, 2012). Consequently, mining activity is a major source of Sb to the environment and Sb concentration in mining-impacted streams can reach extreme values of ~0.1 mM (Zhu *et al.*, 2009; Goix *et al.*, 2011). Dispersion of antimony downstream of mines is partly controlled by redox processes. Antimony is present mainly under the reduced form (trivalent form Sb(III)) in sulphide minerals (Vink, 1996), the most common being stibnite (Sb_2S_3). It is released into water upon sulphide mineral dissolution in the form of the uncharged Sb(III) hydroxide species ($Sb(OH)_3$) and tends generally to be easily oxidized into Sb(V) ($Sb(OH)_6^-$), even in relatively low Eh conditions (Filella *et al.,* 2001, 2002; Mitsunobu *et al.,* 2006). This oxidation process controls Sb mobility; indeed, Sb(III) is more efficiently retained onto suspended particulate matter and sediments than Sb(V) and can precipitate with iron and other various oxides and hydroxides at high Sb concentration (Roper *et al.,* 2012; Johnston *et al.*, 2020). Sb(V) can combine

with iron and oxygen to form tripuhyite, an efficient Sb sink in mine waters (Leverett *et al.*, 2012), but it is mobile in the absence of iron (Resongles *et al.*, 2013). The abiotic oxidation of Sb(III) by dissolved O_2 or H_2O_2 at environmentally relevant concentrations and acid or neutral pH is very slow (e.g., the half-life of Sb(III) with 10^{-6} M H_2O_2 at pH 7 is ~ 3.2 years, Quentel *et al.*, 2004; Leuz *et al.,* 2006; He *et al.*, 2019). Some bacteria living in Sb-rich soils, sediments or acid mine drainage can mediate this process (Li *et al.*, 2013, 2015, 2018; Nguyen and Lee, 2015; Terry *et al.*, 2015; Nguyen *et al.*, 2017; Laroche, 2019). Biotic Sb(III) oxidation by oxygen occurs as a detoxification or respiration (providing energy for growth) mechanism (Filella *et al.,* 2007; Lehr *et al.,* 2007; Li *et al.*, 2013, 2015; Wang *et al.*, 2015; He *et al.*, 2019). Several oxidation paths involving Aio, Ano or ArsV oxidase have been identified (Wang *et al.*, 2015, Li *et al.*, 2015; He *et al.*, 2018; Zhang *et al.*, 2021).

Change of redox state is generally a source of high isotopic fractionation for transition metals and metalloids (Criss, 1999; Schauble, 2004; Wiederhold, 2015). The effect of oxidation on the isotopic fractionation was experimentally studied for numerous metals and metalloids (Cr, Cu, Se, Te, Hg, Tl, U…), but no study was focused on Sb. Theoretical studies predicted equilibrium isotope fractionation between oxidation states of Cr, Cu, Zn, Se, Hg, Tl, and Sb with an enrichment of heavy isotopes in the oxidized species (Li and Liu, 2011; Ducher *et al.,* 2016; Liu *et al.*, 2021; Ferrari *et al.*, 2022). Field studies also evidenced significant isotope fractionation associated to the oxidation of metals. Copper minerals that have undergone numerous oxidation/reduction cycles show very large isotopic variations, in the order of about 20 ‰ (Maréchal *et al.,* 1999; Larson *et al.*, 2003; Mathur *et al.*, 2005, 2009, 2010; Asael *et al.*, 2007). Upon oxidative dissolution of Cr(III)-rich minerals to $Cr(VI)_{aq}$, Gilleaudeau *et al.* (2016) noted an enrichment of the aqueous phase in heavy isotopes by up to +1.77 ‰. This observation had also been made by Ellis *et al.* (2008) who quantified an isotopic fractionation of +1 ‰ upon oxidation of $Cr(III)_s$ to $Cr(VI)_{aq}$. This process did not follow a Rayleigh or kinetic fractionation but rather an equilibrium fractionation, also observed by Wang *et al.* (2010). Johnson (2004) showed that the reduction of Se(VI) into Se(IV) and Se(IV) into Se(0) is the main process fractionating selenium isotopes; fractionation ranged from -7 to -12 ‰ (-3 to -5 ‰ for the biotic reaction) for the reduction of Se(VI) to Se(IV) and from -6 to -12 ‰ (-6 to -9 ‰ for the biotic reaction) for the reduction of Se(IV) to Se(0). In contrast, the reduction of Se(0) to Se(-II) generated little or no apparent fractionation (Fry *et al.*, 1988; Johnson, 2004).

Biological processes can modify or even reverse the fractionation observed for abiotic redox changes, forming lighter oxidized phases. This is the case, for example, for copper, for which, upon oxidation of Cu sulphide in the presence of oxidizing bacteria, a fractionation factor $\Delta^{65}Cu_{ox\text{-}red}$ ranging from - 1‰ to -4.4 ‰ is observed, whereas for abiotic oxidation, a fractionation of +1 to +4 ‰ is demonstrated (Moynier *et al.*, 2017). This corroborates previous observations by Kimball *et al.* (2009), demonstrating that the bacterial activity of *Acidithiobacillus ferroxidans* oxidizing copper sulphide ($CuS + 2O_2 \rightarrow CuSO_4$, (Torma and Habashi, 1972)) favours light isotopes ($\Delta^{65}Cu_{ox\text{-}red}$ = -0.57 ± 0.14 ‰).

For antimony, few studies have investigated isotopic fractionation during redox changes. Rouxel *et al.* (2003) first showed that the reduction of $Sb(V)_{aq}$ into $Sb(III)_{aq}$ induced a preferential enrichment of the reduced phase with light isotopes of around -0.9 ‰. Tanimizu *et al.* (2011) showed that dissolved Sb(V) present in acid mine drainage (AMD) was around +0.35 ‰ heavier than the Sb present in the stibnite minerals contained in the mining wastes from which the AMD originated. However, it was not clear which of oxidation of Sb(III) into Sb(V), dissolution of stibnite or adsorption most contributed to

fractionation. Mackinney, (2016) also observed an important isotopic fractionation during the reduction of Sb(V) into Sb(III) and subsequent formation of $Sb(III)_2S_3$, with $\Delta^{123}Sb_{Sb(V)-Sb(III)}$ around +1.45 ‰; however, here again it was not clear which of precipitation or reduction most contributed to fractionation. No work studied the isotopic fractionation of antimony during the elementary oxidation of dissolved Sb(III) into Sb(V) in controlled laboratory experiments.

The goal of this work was to quantify the direction and the amplitude of Sb fractionation during biotic and abiotic oxidation of $Sb(III)_{aq}$ into $Sb(V)_{aq}$. The experimental conditions were chosen to represent a context of mining pollution, with high Sb concentration (0.1 mM), and a bacterial strain originating from a river sediment polluted by a stibnite mine. This represents a crucial step in the development of Sb isotopes as geochemical tracer in mining environments and in natural systems in general.

2. Material and methods

2.1 Reagents and materials

Sample preparation for ICP-MS, HG-ICP-MS and HG-MC-ICP-Ms was carried out in a class 10 000 cleanroom facility. Ultrapure water (Milli-Q®, resistivity > 18.2 MΩ cm, Q-POP Element system, Millipore) was used for all experiments and reagent preparation. All consumables destined to analysis and Sb isotope separation (e.g. sample bottles, tubes, SPE cartridge, pipette tips…) were soaked in 10% v/v analytical grade HCl or HNO_3 for 48 h and rinsed three times with ultrapure water before use. Suprapur® ≥ 3 % w/w HCl (Merck®), and Analpure 65–69 % w/w HNO_3 (Analityka®) were used for sample preparation and analysis. Other reagents and materials used in sample preparation for ICP-MS, HG-ICP-MS, HPLC-ICP-MS and HG-MC-ICP-MS analysis are presented in the following sections or described more in detail in Ferrari *et al.* (2021).

2.2 Oxidation experiments

2.2.1 Biotic experiments

For biotic oxidation experiments, a bacterial strain called “RDB” isolated from a river sediment draining an ancient Sb mine was used (Laroche, 2019). The ability of this strain to oxidize Sb(III) into Sb(V) had been shown previously (Laroche, 2019). This strain exhibits 98 % similarity with *Ensifer adhaerens* NLS4 isolated by Nguyen *et al.* (2017). It was shown to carry the *Aioa* gene responsible for resistance to Sb(III). RDB was cultivated in CAsO1 medium at pH 6, supplemented with Sb(III). The sterile CaSO1 medium was prepared as described in Battaglia-Brunet *et al.* (2002), except for some minor modifications: the final concentration of $(NH4)_2SO_4$ was 50 $mg.L^{-1}$ and that of the yeast extract was 0.4 $g.L^{-1}$. Sb(III) was added from a 0.1 M Sb(III) solution made with potassium antimony(III) oxide tartrate trihydrate (Extrapure, Merck®). The filtered Sb(III) solution was added to the cooled medium after autoclaving to a final concentration of 0.5 mM (for pre-cultures) or 0.1 mM (for kinetic experiments); the exact Sb(III) concentration in the cultures at t_0 was determined by HPLC-ICP-MS. Three kinetic experiments, called RDB0, RDB1-3 and RDB4 were conducted, including one (RDB1-3) in triplicate and with abiotic controls (Abio1-3 and Control-1-3) in parallel. For each experiment, the bacterial suspension used as inoculum was collected from a pre-culture in exponential growth phase centrifuged and resuspended in Sb(III)-free medium. Considering the fast kinetics (all Sb(III) oxidized within less than 80 h), and the complex logistics of sampling, separation and analysis, the inoculum

size and the starting time of experiments were adapted to obtain samples covering the complete range of percentage of oxidized Sb. Experiment RDB0 and experiments RDB1-3 and RDB4 were conducted with two different inoculum sizes. For experiments RDB1-3 and RDB4, after addition of the inoculum (1 mL), the initial optical density at 600 nm was about 0.022 ± 0.002. For experiment RDB0, the optic density after the inoculum was 0.032. This corresponded to initial bacterial cell concentration (estimated by Malassez counting chamber) of $6x10^5$ (RDB1-3), $1x10^6$ (RDB-4) and $1x10^7$ (RDB0) cells.mL^{-1}. The only difference between experiments RDB 1-3 and RDB 4 was the inoculation time. Experiment RDB 4 was inoculated half day after experiment RDB 1-3, in order to compensate for the lack of sampling during the night. This provided samples that covered the complete range of percentage of oxidized Sb. Two kinds of abiotic controls were made. Abio1-3 corresponded to the culture medium inoculated with autoclaved bacterial pellet; it was conducted in triplicate. Control1-3 corresponded to the culture medium without inoculum, in triplicate. All cultures (300 ml) were performed in acid-decontaminated, autoclaved Erlenmeyer flasks and protected with a cellulose cap. They were incubated at 28 °C with shaking at 100 rpm. Samples (1 mL) were collected at different times for DO (600 nm) measurement (Figure S1) and analysis of the speciation (Sb(III) and Sb(V) concentrations) and isotope ratio of Sb(III) and Sb(V). Samples were also taken occasionally (t=0, t=2.5, t=7.5, and t=48h) in RDB-1-3 experiment for bacterial cell counting using a Malassez counting chamber (Table S1).

2.2.2 Chemical oxidation

Abiotic and control experiments did not show significant Sb(III) oxidation by oxygen, as expected (Quentel *et al.*, 2004; Leuz and Johnson, 2005), therefore chemical oxidation was performed using hydrogen peroxide (Suprapur 30 % w/w H_2O_2, Merck®) as oxidant, at a concentration of 60 mM and pH 6, in accordance with previous studies (Quentel *et al.*, 2004; Leuz *et al.,* 2006). We took advantage of the selectivity of hydride generation toward the Sb(III) species to selectively measure the isotope ratio $^{123S}b/^{121}Sb$ of Sb(III) in these experiments. Indeed, our preliminary experiments showed that in a solution containing Sb(III) and Sb(V) at a concentration of 2 $\mu g.L^{-1}$ in 0.01 M $NaNO_3$, 100 % of Sb(III) was converted into volatile hydride, while a maximum of 10 % Sb(V) was converted. This result was consistent with previous studies (Xi *et al.*, 2015). Chemical oxidation experiment was conducted in duplicate. 20 ml of 0.15 M H_2O_2 solution were added to 30 ml of 0.13 mM Sb(III) in 0.01 M $NaNO_3$ solution at pH 6 (adjusted using a 0.1 M NaOH solution) to reach final concentrations of 0.1 mM Sb(III) and 60 mM H_2O_2. Vials were immediately agitated and maintained at constant temperature (21 °C), with no direct sunlight. An aliquot was collected every 26 min, immediately diluted in 3 M HCl to reach a 2 $\mu g.L^{-1}$ concentration of Sb(III), and analysed immediately by HG-MC-ICP-MS. This measurement provided Sb(III) isotopic composition, together with Sb(III) concentration, using semi-quantitative analysis, by comparison with the signal intensity of the in-house isotopic standard solution prepared at 2 $\mu g.L^{-1}$ of Sb (from the monoelemental solution Sb at 1000 µg mL^{-1} in 20 % w/w HCl, batch number 24-175SBX, SPEX CertiPrep). The solution drained from the gas-liquid separator (hydride-generation module) was sequentially collected for determination of the isotopic composition of Sb(V), after reduction into Sb(III) with 10 % w/v potassium iodide and ascorbic acid, as described before (Ferrari *et al.*, 2021).

2.3. Separation of Sb(III) and Sb(V) in biotic experiments

To analyse the isotope composition of Sb(III) and Sb(V) in the complex bacterial culture medium, physical separation of these two species is needed. For this, we selectively extracted Sb(III) on 0.2 g of thiol-functionalized mesoporous silica powder (hereafter referred to as TSP) at pH ~10, in 1 mL polypropylene SPE cartridges fitted with polyethylene frits (Supelco®). A modified elution protocol from Ferrari *et al.* (2021) was used (Table 1). Selective sorption conditions were based on sorption properties of Sb(III) and Sb(V) species on thiol-functionalized cotton fibers defined by Yu *et al.* (1983); Sb(V) is not sorbed at pH ≥ 5 while Sb(III) is fully sorbed in this pH range. Samples containing around 500 ng of antimony were passed through the TSP column after pH adjustment to ~10 (using a 5.7 mmol.L^{-1} NH_4OH solution, Suprapur, Merck®). The selectivity of the procedure has been tested with pure Sb(V) or Sb(III) solutions; the results can be seen in Table S2. The selective recovery yields for Sb(V) and Sb(III) in elution steps 3 and 7 of the elution schemes, respectively, were found between 92 and 104 %. In this modified protocol, the cleaning step 1 was carried out with ultrapure water rather than 6 M HCl to avoid Sb(V) reduction; a blank sample showed that despite this modification, the amount of Sb in elution step 7 was lower than 1 ng. Antimony concentration was determined in elution fractions 3+4 (corresponding to Sb(V)) and 7 (corresponding to Sb(III)) by HG-ICP-MS. This allowed to calculate to proportions of Sb(III) and Sb(V) in the samples. The value was compared with the result of HPLC-ICP-MS analysis. Differences of ~3.5 % on average, was obtained between HPLC measurements and physical separations of Sb(III) and Sb(V) (Table S3).

Table 3: Elution scheme for the separation of the Sb(III) and Sb(V) species using thiol-functionalized silica powder modified from Ferrari et al (2021) .

	Step	Volume (mL)	Eluent	Notes
1	Cleaning	10	Ultrapure water	
2	Conditioning	10	NH_4OH 5.7 mmol.L^{-1}	
3	Sample loading	10	NH_4OH 5.7 mmol.L^{-1}	Sb(V) collection (steps 3 and 4)
4	Rinse	5	NH_4OH 5.7 mmol.L^{-1}	
5	Washing	5	0.5 M HCl	
6	Washing	6	2.5 M HCl	
7	Sb(III) elution	6	6 M HCl	Sb(III) collection

2.4 Analytical methods

All the analyses (HPLC-ICP-MS, HG-ICP-MS, HG-MC-ICP-MS) were performed on the AETE-ISO platform (OSU OREME, Université de Montpellier).

HG-ICP-MS and HG-MC-ICP-MS measurement settings were taken from Ferrari *et al.* (2021), with slight modifications; for HG-MC-ICP-MS, short-term shifts in the Sb isotope ratio due to overpressure in the gas-liquid separator (Ferrari et al., 2021) were attenuated by suppressing additional gas for hydride generation. For better signal stability and reproducibility, the Sb concentration of the samples analysed was adjusted at 2 µg L^{-1} for all HG-MC-ICP-MS measurements. For the chemical oxidation experiments, the analysis time in HG-MC-ICP-MS was decreased in order to generate more measurement points during the oxidation kinetics, each measurement has been diminished from 80 cycles of 4.194 seconds (Ferrari *et al.*, 2021) to 40 cycles of 4.194 s (on samples and standards). Isotope

composition is expressed as δ^{123}Sb (Equation 1) and corresponds to the average value for three isotopic measurements if not specified otherwise.

$$\delta^{123}Sb(‰) = \left(\frac{\left(\frac{^{123}Sb}{^{121}Sb}\right)_{sample} - \left(\frac{^{123}Sb}{^{121}Sb}\right)_{mean\ std}}{\left(\frac{^{123}Sb}{^{121}Sb}\right)_{mean\ std}}\right) \times 1000 \text{ (Eq. 1)}$$

Where $\left(\frac{^{123}Sb}{^{121}Sb}\right)_{mean\ std}$ is the average of Sb isotope ratio of the in-house Sb isotope standard solution measured before and after the sample (Sb 1000 µg mL-1 in 20% w/w HCl, batch number 24-175SBX).

Monitoring of Sb(III) and Sb(V) concentrations in biotic experiments was carried out by High-Performance Liquid Chromatography coupled to ICP-MS (HPLC-ICP-MS) as described in Resongles *et al.* (2013).

3. Results

3.1 Biotic oxidation

3.1.1 Evolution of Sb(III) oxydation

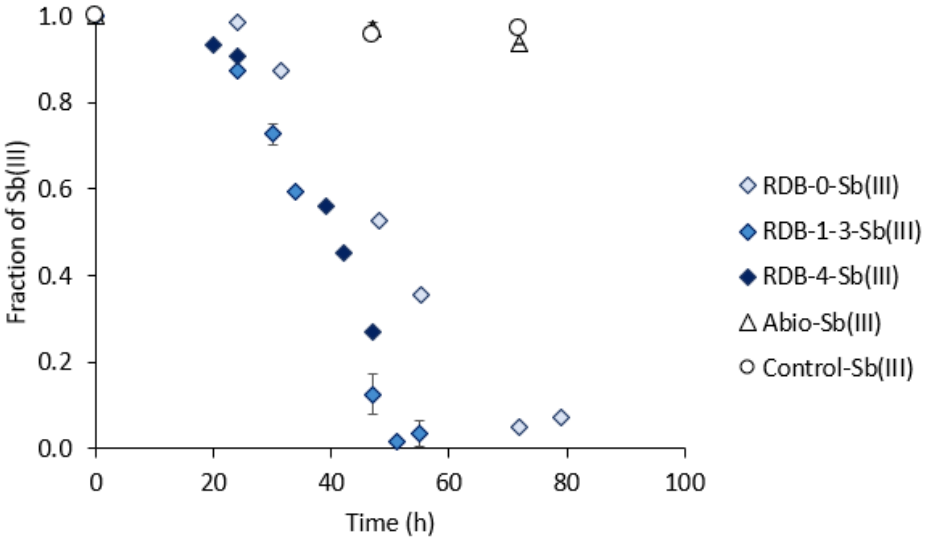

Figure 1: Evolution of the oxidation of Sb(III) in biotic experiments RDB0, RDB1-3 and RDB4. Diamonds represent the proportion of Sb(III). Triangles represent the abiotic experiment while circles are the control. Data for RDB1-3 and Abiotic experiments are represented by the mean values of the triplicates and associated standard error.

Oxidation of Sb(III) in the three experiments started after a lag period of about 20 h (Figure 1). It was decoupled from the exponential growth phase, which systematically occurred before 20 h, according to DO measurements and cell counting (Figure S1, Table S1). Sb(III) oxidation was completed within 51 h (in experiment RDB 1-3) to 70 h (in experiment RDB 0). The oxidation rate was slower for RDB0 than for RDB1-3 and RDB4, with respectively 50 % (RDB 0) and 84 ± 8 % (RDB 1-3 and RDB 4) of Sb(III) oxidized after 47 hours; the corresponding rate values were 1.6 and 3.1 ± 0.1 µM Sb.h^{-1}. The rate difference did not appear to be related to inoculum size or cell concentration during the stationary phase, the latter being approximately the same in all three experiments (Table S3, Figure S1). Control and Abiotic experiments did not show significant Sb(III) oxidation, with less than 8 % of Sb(III) oxidized

after 72 hours. This confirmed that Sb(III) oxidation was mediated by bacteria. It should be noted that the sum of dissolved Sb(III) and Sb(V) did not decrease during the experiments (data not shown), showing that no significant precipitation or sorption on bacterial cells occurred.

3.1.2 Isotopic composition of Sb(III) and Sb(V)

There is a significant fractionation of the δ^{123}Sb between Sb(III) and its biotic oxidation product. The oxidation of Sb(III) seems to follow a closed system equilibrium model but does not follow a Rayleigh fractionation and is more typical of an equilibrium pathway, with an almost parallel increase of the isotopic signature of Sb(III) and Sb(V) (Figure 2). The $\Delta^{123}Sb_{Sb(III)-Sb(V)}$ of the biotic oxidation of Sb(III) was measured at +0.20 ± 0.07 ‰ on average, with a preferential enrichment in light isotope for Sb(V). The same trend was observed for the three experiments; there is no significant influence of the oxidation kinetic on the fractionation factor $\Delta^{123}Sb_{Sb(III)-Sb(V)}$.

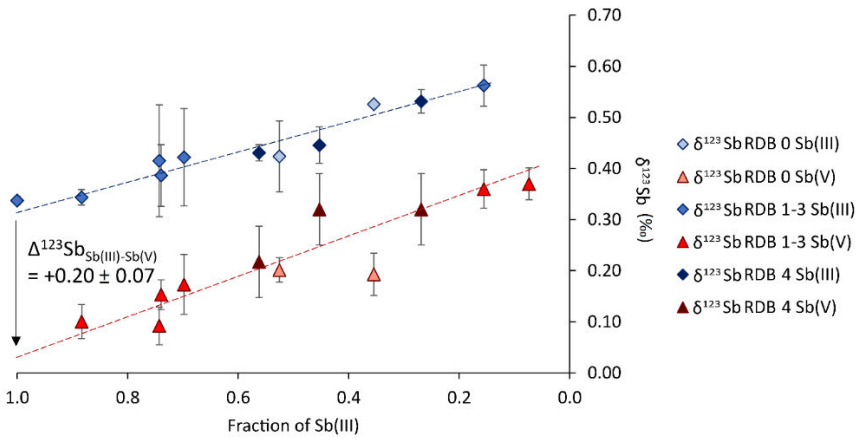

Figure 2: Isotopic composition (δ^{123}Sb) of Sb(III) and Sb(V) during biotic oxidation of Sb(III) by RDB at pH 6. Blue diamonds represent the signature of Sb(III) while red triangles represent the signature of Sb(V).

3.2 Chemical oxidation with H_2O_2

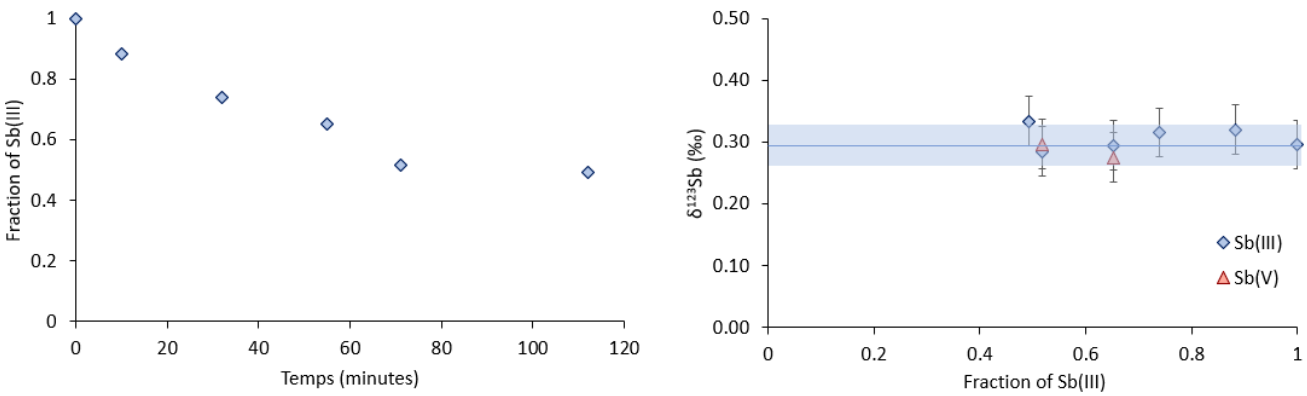

Figure 3: Abiotic oxidation kinetics of Sb(III) (left) and isotopic composition (δ^{123}Sb) of Sb(III) (blue) and Sb(V) (orange) during abiotic oxidation of 0.1 mM Sb(III) by 60 mM H_2O_2 at pH 6 (right). The blue line on the right represents the isotopic signature of the Sb(III) before the oxidation occurred (t= 0). Error bars correspond to the analytical uncertainty (± 0.04 ‰) determined in Ferrari et al. (2021).

Chemical Sb(III) oxidation with H_2O_2 reached 51 % after 112 minutes; it exhibited an average rate of 22.6 µM $Sb.h^{-1}$. The initial isotopic signature of Sb(III) ($\delta^{123}Sb$ = 0.30 ± 0.04 ‰) was identical to that measured in the biotic experiments à t_0 ($\delta^{123}Sb$ = 0.30 ± 0.04 ‰), despite the use of a different separation procedure. The experiment did not show significant fractionation during the oxidation reaction progress between remaining Sb(III) ($\delta^{123}Sb$ = 0.33 ± 0.04 ‰) and produced Sb(V) ($\delta^{123}Sb$ = 0.29 ± 0.02 ‰) (Figure 3).

4. Discussion

4.1 Fractionation related to biotic versus abiotic Sb(III) oxidation

It is commonly observed for metals that redox processes generate significant isotope fractionation and the oxidized species are generally enriched with the heavier isotopes compared to the reduced species (Wiederhold, 2015). Conversely, organisms tend to incorporate and use lighter isotopes of metals (Zhu *et al.*, 2002). In the case of biological oxidation, this process can result in an oxidized phase isotopically lighter than the source, as reported for copper between $Cu(II)_{aq}$ and Cu(I) in minerals (Moynier *et al.*, 2017). Fractionation factors $\Delta^{65}Cu_{ox\text{-}red}$ for biotic Cu(I) oxidation have been reported between -0.5 and -4.4 ‰ (Moynier *et al.*, 2017). Mathur *et al.* (2005) found fractionation direction differences between abiotic and biotic oxidation for the copper isotopes; for abiotic oxidation, they found enrichment in ^{65}Cu in the oxidized species $Cu(II)_{aq}$ with a fractionation factor $\Delta^{65}Cu_{dissolved\text{-}mineral}$ between +1.3 and +2.6 ‰ depending of the starting mineral (chalcopyrite and chalcocite respectively). For the biotic oxidation, no significant fractionation was measured between the oxidized and the starting material phase. This lack of fractionation has been attributed to the presence of a heavy isotope sink within the bacteria cells. Finally, this corroborates the observations of Kimball *et al.* (2009) who demonstrated that the bacterial activity of *Acidithiobacillus ferroxidans* favours light isotopes in $Cu(II)_{aq}$ ($\Delta^{65}Cu_{ox\text{-}red}$ = -0.57 ± 0.14 ‰) during copper (I) sulphide oxidation.

In the present study, the amplitude of Sb isotope fractionation during biotic oxidation ($\Delta^{123}Sb_{Sb(III)\text{-}Sb(V)}$ = +0.20 ± 0.07 ‰) was smaller than for copper. However, with actual separation and analytical protocols (Ferrari *et al.*, 2021), this fractionation factor is wide enough to be evidenced in experimental or field samples.

Despite the different kinetics between experiments RDB0 and experiments RDB 1-3 and RDB 4, no significant fractionation factor difference $\Delta^{123}Sb_{Sb(III)\text{-}Sb(V)}$ was observed (Figure 2). This suggests that the isotopic fractionation does not depend on the kinetic of Sb(III) oxidation in the conditions (high oxidation rates, high Sb(III) concentration) of this study. However, as is commonly the case for this kind of process (Mathur *et al.*, 2005; Wiederhold, 2015), it was not possible to describe this isotopic fractionation by a Rayleigh model. This has been already observed in the case of the Cr(III) oxidation to Cr(VI) (Ellis *et al.*, 2008), for which it was suggested that Cr(III) oxidation implies multiple steps and does not involve purely kinetic oxidation, but that equilibrium and kinetic isotope effect compete during the reaction (Ellis *et al.*, 2008; Wang et al., 2010). Therefore, considering the nearly parallel evolution of $\delta^{123}Sb$ in the reactant and products as a function of the fraction of Sb(III) oxidized in the present study and the relatively small fractionation amplitude, the biotic Sb(III) oxidation doesn't seem to be unilateral, it seems to involve isotopic exchanges between Sb(III) and Sb(V) species.

Studies about antimony fractionation during changes in redox conditions tend to show that the oxidized phase is preferentially enriched in heavy isotopes, as was noticed by Rouxel *et al.* (2003) reporting a shift of $\Delta^{123}Sb_{Sb(III)-Sb(V)}$ around -0.9 ‰ during Sb(V) abiotic reduction. Thermodynamic calculations on Sb isotope fractionation have shown the same trend (Ferrari *et al.*, 2022), the oxidized phase was predicted to be preferentially enriched in the heavy isotope, with a fractionation factor $\Delta^{123}Sb_{Sb(V)-Sb(III)}$ of about +1.2 ‰ between senarmontite ($Sb(III)_2O_3$) and $Sb(V)_2O_5$. It was then expected a clear differentiation between Sb(III) and Sb(V) during the abiotic oxidation as is the case for most of the transition metals (Schauble, 2004). Due to the experimental protocol, the oxidation could not be monitored until its completion (only ~50% of Sb(III) was oxidized at the end of the experiment, after 112 minutes). However, at these percentages, both equilibrium or Rayleigh fractionations should have been visible, mainly on the signature of the newly formed Sb(V).

It is noteworthy that the absence of fractionation evidenced during chemical oxidation in the present study was independent of the experimental protocol; indeed, similar results were obtained in a preliminary chemical oxidation experiment with a concentration of 60 mM of H_2O_2 at pH 9 in which a physical separation of Sb(III) and Sb(V) with TSP was done prior to Sb isotope measurement (Table S4). The rate of oxidation may influence isotope fractionation; for selenium, Wasserman *et al.* (2021) noted a clear differentiation between $\delta^{82/76}Se$ values depending on the initial concentration of H_2O_2, a significantly lower $\delta^{82/76}Se$ value of the oxidation product was obtained for the highest H_2O_2 concentration, which could be explained by the higher oxidation kinetic. In the present study, the lack of fractionation during chemical oxidation might be related to the high reaction rate (22.6 µM $Sb.h^{-1}$). However, this hypothesis was not consistent with previous results from Rouxel *et al.* (2003) who obtained significant fractionation of Sb isotopes during an experiment in which all Sb(V) was reduced into Sb(III) within ~15 min, thus at a high reduction kinetics.

4.2 Environmental implications

Our observations have implications for the interpretation of antimony isotope ratios in sulphide mining environments, for which the Sb concentrations used in this study are relevant. The fractionation produced during biological oxidation is opposite in direction to that produced by sorption of Sb(III) and Sb(V) onto iron minerals (Ferrari et al., in prep.), which is another major process involved in Sb transport in mine waters. Thus, Sb isotope signatures could allow to trace these different processes. However, the fractionation factors measured were relatively small, which may limit the possibility to highlight significant variations of Sb isotope signature in real environmental conditions. Furthermore, the fractionation factors obtained in laboratory conditions with a pure bacterial strain must be confronted to the apparent fractionation factors in real natural environments where a whole bacterial community is likely to interact with Sb. The Sb isotope fractionation may vary according to the bacterial strain, in relation with different metabolic pathway, as seen for selenium reduction (Schilling et al., 2020). Therefore, the present results have to be considered as a first step toward a better comprehension of Sb isotope data during redox processes in mine waters.

Concerning abiotic oxidation, this is a common process occurring in mine drainage, where important oxidants are iron and manganese (oxyhydr)oxides (Belzile *et al.,* 2001). The role of these phases in Sb(III) oxidation, besides their effect on both Sb(III) and Sb(V) retention by sorption (Guo *et al.*, 2018; Resongles *et al.*, 2013) will probably make them important factors for the control of Sb isotope signature in mine waters.

5. Conclusion

In this study, isotopic fractionation generated by biotic and abiotic $Sb(III)_{aq}$ oxidation into $Sb(V)_{aq}$ was investigated for the first time. Biotic oxidation with a pure bacterial strain of the genus *Ensifer* was found to favour the light isotopes of antimony in the oxidized phase, with a $\Delta^{123}Sb_{Sb(III)-Sb(V)}$ of +0.20 ± 0.07 ‰. This isotopic fractionation did not follow a Rayleigh fractionation model and was more typical of an equilibrium fractionation. This could reveal the occurrence of different steps in the oxidation of Sb(III) to Sb(V) via biotic processes, and a competition between the equilibrium and kinetic fractionation. It was found that the fractionation amplitude $\Delta^{123}Sb_{Sb(III)-Sb(V)}$ did not vary with the reaction kinetic. The fractionation factor measured for biological Sb(III) oxidation was found smaller than the ones determined for other elements such as copper, but precise determination of $\delta^{123}Sb(III)$ and $\delta^{123}Sb(V)$ is possible with actual HG-MC-ICP-MS protocols. No isotopic fractionation was evidenced for the chemical oxidation with H_2O_2 in our experimental conditions. The reasons remain unclear, and investigations should be pursued further.

6. Acknowledgements

This work received financial support from the CNRS INSU EC2CO program (Project AntiBol). We thank Léa Causse for trace element analysis performed on the AETE-ISO platform, OSU OREME/Université de Montpellier and David Clousier and Naoual Azhir el Yousfi for their help during the experiments.

Bibliography:

Asael, D. *et al.* (2007) 'Copper isotope fractionation in sedimentary copper mineralization (Timna Valley, Israel)', *Chemical Geology*, 243(3), pp. 238–254. https://doi.org/10.1016/j.chemgeo.2007.06.007.

Battaglia-Brunet, F. *et al.* (2002) 'An arsenic(III)-oxidizing bacterial population: selection, characterization, and performance in reactors', *Journal of Applied Microbiology*, 93(4), pp. 656–667. https://doi.org/10.1046/j.1365-2672.2002.01726.x.

Belzile, N., Chen, Y.-W. and Wang, Z. (2001) 'Oxidation of antimony (III) by amorphous iron and manganese oxyhydroxides', *Chemical Geology*, 174(4), pp. 379–387. https://doi.org/10.1016/S0009-2541(00)00287-4.

Criss, R.E. (1999) *Principles of Stable Isotope Distribution*. Oxford University Press, USA.

Ducher, M., Blanchard, M. and Balan, E. (2016) 'Equilibrium zinc isotope fractionation in Zn-bearing minerals from first-principles calculations', *Chemical Geology*, 443, pp. 87–96. https://doi.org/10.1016/j.chemgeo.2016.09.016.

Ellis, A. *et al.* (2008) 'Environmental Cycling of Cr Using Stable Isotopes: Kinetic and Equilibrium Effects', 2008, pp. H53F-08.

Ferrari, C. *et al.* (2021) 'A single-step purification method for the precise determination of antimony isotopic composition of environmental, geological and biological samples by HG-MC-ICP-MS', *Journal of Analytical Atomic Spectrometry*, 36(Issue 4), pp. 776–785. https://doi.org/10.1039/D0JA00452A.

Ferrari, C. *et al.* (2022) 'Equilibrium mass-dependent isotope fractionation of antimony between stibnite and Sb secondary minerals: A first-principles study', *Chemical Geology*, p. 121115. https://doi.org/10.1016/j.chemgeo.2022.121115.

Filella, M., Belzile, N. and Chen, Y.-W. (2001) 'Antimony in the environment: a review focused on natural waters. I. Occurence', *Earth-Sciences Reviews*, 57, pp. 125–176.

Filella, M., Belzile, N. and Chen, Y.-W. (2002) 'Antimony in the environment: a review focused on natural waters. II. Relevant solution chemistry', *Earth-Sciences Reviews*, 59, pp. 265–285.

Filella, M., Belzile, N. and Lett, M.-C. (2007) 'Antimony in the environment: a review focused on natural waters. III. Microbial relevant interactions', *Earth Sciences Reviews*, 80, pp. 195–217. https://doi.org/10.1016/j.earscirev.2006.09.003.

Fry, B. *et al.* (1988) 'Sulfur isotope effects associated with oxidation of sulfide by O2 in aqueous solution', *Chemical Geology: Isotope Geoscience section*, 73(3), pp. 205–210. https://doi.org/10.1016/0168-9622(88)90001-2.

Gilleaudeau, G.J. *et al.* (2016) 'Oxygenation of the mid-Proterozoic atmosphere: clues from chromium isotopes in carbonates', *Geochemical Perspectives Letters*, 2(2), pp. 178–187. https://doi.org/10.7185/geochemlet.1618.

Goix, S. *et al.* (2011) 'Influence of source distribution and geochemical composition of aerosols on children exposure in the large polymetallic mining region of the Bolivian Altiplano', *Science of The Total Environment*, 412–413, pp. 170–184. https://doi.org/10.1016/j.scitotenv.2011.09.065.

Guo, W. *et al.* (2018) 'Environmental geochemical and spatial/temporal behavior of total and speciation of antimony in typical contaminated aquatic environment from Xikuangshan, China', *Microchemical Journal*, 137, pp. 181–189. https://doi.org/10.1016/j.microc.2017.10.010.

He, M. *et al.* (2019) 'Antimony speciation in the environment: Recent advances in understanding the biogeochemical processes and ecological effects', *Journal of Environmental Sciences*, 75, pp. 14–39. https://doi.org/10.1016/j.jes.2018.05.023.

Hong, S. *et al.* (2012) 'Evidence of Global-Scale As, Mo, Sb, and Tl Atmospheric Pollution in the Antarctic Snow', *Environmental Science & Technology*, 46(21), pp. 11550–11557. https://doi.org/10.1021/es303086c.

Johnson, T.M. (2004) 'A review of mass-dependent fractionation of selenium isotopes and implications for other heavy stable isotopes', *Chemical Geology*, 204(3), pp. 201–214. https://doi.org/10.1016/j.chemgeo.2003.11.015.

Johnston, S.G. *et al.* (2020) 'Antimony and arsenic speciation, redox-cycling and contrasting mobility in a mining-impacted river system', *Science of The Total Environment*, 710, p. 136354. https://doi.org/10.1016/j.scitotenv.2019.136354.

Kimball, B.E. *et al.* (2009) 'Copper isotope fractionation in acid mine drainage', *Geochimica et Cosmochimica Acta*, 73(5), pp. 1247–1263. https://doi.org/10.1016/j.gca.2008.11.035.

Krachler, M. *et al.* (2005) 'Increasing atmospheric antimony contamination in the northern hemisphere: snow and ice evidence from Devon Island, Arctic Canada', *Journal of Environmental Monitoring*, 7(12), pp. 1169–1176. https://doi.org/10.1039/B509373B.

Laroche, E. (2019) *Acteurs et mécanismes des bio-transformations de l'arsenic, de l'antimoine et du thallium pour la mise en place d'éco-technologies appliquées à la gestion d'anciens sites miniers*. Université de Montpellier.

Larson, P.B. *et al.* (2003) 'Copper isotope ratios in magmatic and hydrothermal ore-forming environments', *Chemical Geology*, 201(3), pp. 337–350. https://doi.org/10.1016/j.chemgeo.2003.08.006.

Lehr, C.R., Kashyap, D.R. and McDermott, T.R. (2007) 'New Insights into Microbial Oxidation of Antimony and Arsenic', *Applied and Environmental Microbiology*, 73(7), pp. 2386–2389. https://doi.org/10.1128/AEM.02789-06.

Leuz, A.-K. and Johnson, C.A. (2005) 'Oxidation of Sb(III) to Sb(V) by O2 and H2O2 in aqueous solutions', *Geochimica et Cosmochimica Acta*, 69(5), pp. 1165–1172. https://doi.org/10.1016/j.gca.2004.08.019.

Leuz, A.-K., Mönch, H. and Johnson, A. (2006) 'Sorption of Sb(III) and Sb(V) to Goethite: Influence on Sb(III) Oxidation and Mobilization', *Environement Sciences and Technologies*, 40(23), pp. 7277–7282. https://doi.org/10.1021/es061284b.

Leverett, P. *et al.* (2012) 'Tripuhyite and schafarzikite: two of the ultimate sinks for antimony in the natural environment', *Mineralogical Magazine*, 76(4), pp. 891–902. https://doi.org/10.1180/minmag.2012.076.4.06.

Li, J. *et al.* (2013) 'Phylogenetic and genome analyses of antimony-oxidizing bacteria isolated from antimony mined soil', *International Biodeterioration & Biodegradation*, 76, pp. 76–80. https://doi.org/10.1016/j.ibiod.2012.06.009.

Li, J. *et al.* (2015) 'Proteomics and Genetics for Identification of a Bacterial Antimonite Oxidase in Agrobacterium tumefaciens', *Environmental Science & Technology*, 49(10), pp. 5980–5989. https://doi.org/10.1021/es506318b.

Li, J. *et al.* (2018) 'Novel Hyper Antimony-Oxidizing Bacteria Isolated from Contaminated Mine Soils in China', *Geomicrobiology Journal*, 35(8), pp. 713–720. https://doi.org/10.1080/01490451.2018.1454556.

Li, X. and Liu, Y. (2011) 'Equilibrium Se isotope fractionation parameters: A first-principles study', *Earth and Planetary Science Letters*, 304(1), pp. 113–120. https://doi.org/10.1016/j.epsl.2011.01.022.

Liu, S. *et al.* (2021) 'Equilibrium Cu isotope fractionation in copper minerals: a first-principles study', *Chemical Geology*, 564, p. 120060. https://doi.org/10.1016/j.chemgeo.2021.120060.

Mackinney, J.S. (2016) *Antimony isotopes as indicator of RedOx reactions in aqueous systems: fractionation during Sb(V) reduction by sulfide and isotope exchange kinetics between dissolved Sb(III) and Sb(V)*. Thesis. University of Illinois at Urbana-Champaign. https://www.ideals.illinois.edu/bitstream/handle/2142/90949/MACKINNEY-THESIS-2016.pdf?sequence=1&isAllowed=y.

Maréchal, C.N., Télouk, P. and Albarède, F. (1999) 'Precise analysis of copper and zinc isotopic compositions by plasma-source mass spectrometry', *Chemical Geology*, 156(1), pp. 251–273. https://doi.org/10.1016/S0009-2541(98)00191-0.

Mathur, R. *et al.* (2005) 'Cu isotopic fractionation in the supergene environment with and without bacteria', *Geochimica et Cosmochimica Acta*, 69(22), pp. 5233–5246. https://doi.org/10.1016/j.gca.2005.06.022.

Mathur, R. *et al.* (2009) 'Exploration potential of Cu isotope fractionation in porphyry copper deposits', *Journal of Geochemical Exploration*, 102(1), pp. 1–6. https://doi.org/10.1016/j.gexplo.2008.09.004.

Mathur, R. *et al.* (2010) 'Patterns in the Copper Isotope Composition of Minerals in Porphyry Copper Deposits in Southwestern United States', *Economic Geology*, 105(8), pp. 1457–1467. https://doi.org/10.2113/econgeo.105.8.1457.

Mitsunobu, S., Harada, T. and Takahashi, Y. (2006) 'Comparison of Antimony Behavior with that of Arsenic under Various Soil Redox Conditions', *Environmental Science & Technology*, 40(23), pp. 7270–7276. https://doi.org/10.1021/es060694x.

Moynier, F. *et al.* (2017) 'The Isotope Geochemistry of Zinc and Copper', *Reviews in Mineralogy and Geochemistry*, 82(1), pp. 543–600. https://doi.org/10.2138/rmg.2017.82.13.

Nguyen, V.K. *et al.* (2017) 'Microbial oxidation of antimonite and arsenite by bacteria isolated from antimony-contaminated soils', *International Journal of Hydrogen Energy*, 42(45), pp. 27832–27842. https://doi.org/10.1016/j.ijhydene.2017.08.056.

Nguyen, V.K. and Lee, J.-U. (2015) 'Antimony-Oxidizing Bacteria Isolated from Antimony-Contaminated Sediment – A Phylogenetic Study', *Geomicrobiology Journal*, 32(1), pp. 50–58. https://doi.org/10.1080/01490451.2014.925009.

Quentel, F. *et al.* (2004) 'Kinetic Studies on Sb(III) Oxidation by hydrogen Peroxide in Aqueous Solution', *Environement Science and Technology*, 38(10), pp. 2843–2848. https://doi.org/10.1021/es035019r.

Resongles, E. *et al.* (2013) 'Fate of Sb(V) and Sb(III) species along a gradient of pH and oxygen concentration in the Canoulès mine waters (Southern France)', *Environmental Science Processes and Impacts*, 15, pp. 1536–1544. https://doi.org/10.1039/c3em00215b.

Roper, A.J., Williams, P.A. and Filella, M. (2012) 'Secondary antimony minerals: Phases that control the dispersion of antimony in the supergene zone', *Geochemistry*, 72, pp. 9–14. https://doi.org/10.1016/j.chemer.2012.01.005.

Rouxel, O., Ludden, J. and Fouquet, Y. (2003) 'Antimony isotope variations in natural systems and implications for their use as geochemical tracers', *Chemical Geology*, 200, pp. 25–40. https://doi.org/10.1016/S0009-2541(03)00121-9.

Santini, J.M. *et al.* (2002) 'Characteristics of newly discovered arsenite-oxydizing bacteria', *Environmental chemistry of arsenic*, pp. 329–342.

Schauble, E.A. (2004) 'Applying Stable Isotope Fractionation Theory to New Systems', *Reviews in Mineralogy and Geochemistry*, 55(1), pp. 65–111. https://doi.org/10.2138/gsrmg.55.1.65.

Sen, I.S. and Peucker-Ehrenbrink, B. (2012) 'Anthropogenic Disturbance of Element Cycles at the Earth's Surface', *Environmental Science & Technology*, 46(16), pp. 8601–8609. https://doi.org/10.1021/es301261x.

Tanimizu, M. *et al.* (2011) 'Determination of natural isotopic variation in antimony using inductively coupled plasma mass spectrometry for an uncertainty estimation of the standard atomic weight of antimony', *Geochemical Journal*, 45, pp. 27–32.

Terry, L.R. *et al.* (2015) 'Microbial Oxidation of Antimony(III) with Oxygen or Nitrate by Bacteria Isolated from Contaminated Mine Sediments', *Applied and Environmental Microbiology*, 81(24), pp. 8478–8488. https://doi.org/10.1128/AEM.01970-15.

Torma, A.E. and Habashi, F. (1972) 'Oxidation of copper (II) selenide by Thiobacillus ferrooxidans', *Canadian Journal of Microbiology* [Preprint]. https://doi.org/10.1139/m72-278.

Vink, B.W. (1996) 'Stability relations of antimony and arsenic compounds in the light of revised and extended Eh-pH diagrams', *Chemical Geology*, 130(1), pp. 21–30. https://doi.org/10.1016/0009-2541(95)00183-2.

Wang, D.T. *et al.* (2010) 'Stable Isotope Fractionation during Chromium(III) Oxidation by δ-MnO2', 2010, pp. H53F-1109.

Wang, Q. *et al.* (2015) 'Arsenite Oxidase Alsop Functions as an Antimonite Oxidase', *Applied and Environmental Microbiology*, 81(6). https://doi.org/10.1128/AEM.02981-14.

Wasserman, N.L. *et al.* (2021) 'Selenium Isotope Shifts during the Oxidation of Selenide-Bearing Minerals', *ACS Earth and Space Chemistry*, 5(5), pp. 1140–1149. https://doi.org/10.1021/acsearthspacechem.1c00036.

Wiederhold, J.G. (2015) 'Metal Stable Isotope Signatures as Tracers in Environmental Geochemistry', *Environmental Science & Technology*, 49(5), pp. 2606–2624. https://doi.org/10.1021/es504683e.

Xi, J. *et al.* (2015) 'Comparison of masking agents for antimony speciation analysis using hydride generation atomic fluorescence spectrometry', *Frontiers of Environmental Science & Engineering*, 9(6), pp. 970–978. https://doi.org/10.1007/s11783-014-0716-3.

Yu, M.-Q., Liu, G.-Q. and Jin, Q. (1983) 'Determination of trace arsenic, antimony, selenium and tellurium in various oxidation states in water by hydride generation and atomic-absorption spectrophotometry after enrichment and separation with thiol cotton', *Talanta*, 30(4), pp. 265–270. https://doi.org/10.1016/0039-9140(83)80060-5.

Zhang, J. *et al.* (2022) 'Oxidation of organoarsenicals and antimonite by a novel flavin monooxygenase widely present in soil bacteria', *Environmental Microbiology*, 24(2), pp. 752–761. https://doi.org/10.1111/1462-2920.15488.

Zhu, J. *et al.* (2009) 'Environmental characteristics of water near the Xikuangshan antimony mine.', *Acta Scientiae Circumstantiae*, 29.

Zhu, X.K. *et al.* (2002) 'Mass fractionation processes of transition metal isotopes', *Earth and Planetary Science Letters*, 200(1), pp. 47–62. https://doi.org/10.1016/S0012-821X(02)00615-5.

Antimony isotopic fractionation during Sb(III) to Sb(V) oxidation: biotic and abiotic perspectives

Supplementary Information

Colin Ferrari[a], Eléonore Resongles[a], Marina Héry[a], Angélique Désoeuvre[a], Rémi Freydier[a], Sophie Delpoux[a], Odile Bruneel[a], Corinne Casiot[a]

[a]*HydroSciences Montpellier, Univ. Montpellier, CNRS, IRD, Montpellier, France*

*Corresponding author

Mailing address : Université de Montpellier – CC 57
163, rue Auguste Broussonnet,
34090 Montpellier, France
Email : colin.ferrari@umontpellier.fr

This PDF file includes: Tables S1 to S4 and Figure S1.

Additional tables:

Table S1: Evolution of the optical density and the bacterial cell concentration in biotic (RDB0, RDB1-3 and RDB4) and abiotic (Abio1-3 and Control1-3) experiments over time. The optical density in Abio 1-3 increased after day 42 due to a bacterial contamination during the samplings, however, this did not affect the Sb(III) oxidation.

	RDB 0		**RDB 1-3**		**RDB 4**		**Abio 1-3**		**Control 1-3**	
Time (hours)	Count (cells.mL^{-1})	DO	Count (cells.mL^{-1})	DO	Count (cells.mL^{-1})	DO	Count (cells.mL^{-1})	DO	Count (cells.mL^{-1})	DO
0	1.10E+07	0.032	6.15E+05	0.023	1.10E+06	0.020	1.62E+06	0.089		0.017
3		0.022		0.025						
7	8.75E+06	0.062	9.37E+05	0.072			1.28E+06	0.088		0.019
16					1.80E+07	0.492				
20					1.28E+07	0.462				
24		0.449	2.04E+07	0.461	1.83E+07	0.445		0.095		0.018
30		0.450	1.37E+07	0.426			1.67E+06	0.075		0.005
31.5		0.453								
34				0.438						
39						0.415				
42						0.414		0.223		0.002
47	1.74E+08	0.452		0.417		0.430		0.258		0.003
51				0.420				0.291		0.006
55		0.455		0.425						
58				0.430						
63					1.77E+07	0.419				
68						0.414		0.370		0.014
72		0.452	1.63E+07	0.422		0.406		0.366		0.008
79		0.454	1.65E+07	0.410				0.354		0.017

Table S2: Recovery rate of pure Sb(III) and pure Sb(V) solutions on TSP.

Solution	Step	[Sb] loaded/eluted (ng)	Yield (%)	Total Sb recovered (%)
Pure Sb(V) solution	Initial loaded Sb(V) solution	448.4	91.1	92.7
	Sb(V) collection	408		
	Sb(III) collection	7.6		
Pure Sb(III) solution	Initial loaded Sb(III) solution =	488		
	Sb(V) collection	< QL		
	Sb(III) collection	507	103.8	103.8

Table S3: Comparison between the percentage of oxidation calculated through HPLC and recovered through the physical separation of Sb(III) and Sb(V) on TSP.

		HPLC measurement	TSP separation	
Ech	**Sb(III)/Sb(V)**	**[Sb] (%)**	**[Sb] (%)**	**Difference (%)**
RDB 1 t=0	Sb(III)	98.3	98.1	0.3
	Sb(V)	1.7	1.9	
RDB-1 t = 24	Sb(III)	86.6	88.6	-2.0
	Sb(V)	13.4	11.4	
RDB 1 t=30h	Sb(III)	72.3	67.3	5.0
	Sb(V)	27.7	32.7	
RDB 2 t=30h	Sb(III)	72.6	69.4	3.2
	Sb(V)	27.4	30.6	
RDB 3 t=30h	Sb(III)	68.1	69.7	-1.6
	Sb(V)	31.9	30.3	
RDB 4 t=39h	Sb(III)	54.5	57.2	-2.7
	Sb(V)	45.5	42.8	
RDB 4 t=42h	Sb(III)	43.6	47.6	-4.0
	Sb(V)	56.4	52.4	
RDB 4 t=47h	Sb(III)	25.2	33.7	-8.5
	Sb(V)	74.8	66.3	
RDB 1 t=47h	Sb(III)	13.9	24.9	-11.1
	Sb(V)	86.1	75.1	
RDB 3 t=47h	Sb(III)	5.7	19.1	-13.5
	Sb(V)	94.3	80.9	

Table S4: δ^{123}Sb of the Sb(III) and Sb(V) species physically separated on TSP in the same H_2O_2, Sb and $NaNO_3$ concentrations than the online experiment described in 2.2.2 Chemical oxidation, but at pH 9.

	Time (min)	Oxidation (%)	δ^{123}Sb (‰)	2 sd (‰)
Sb(III)	25	10	0.34	0.01
	70	18	0.33	0.01
	140	19	0.33	0.04
Sb(V)	25	10	0.35	0.05
	70	18	0.34	0.06
	140	19	0.31	0.06

Additional figure:

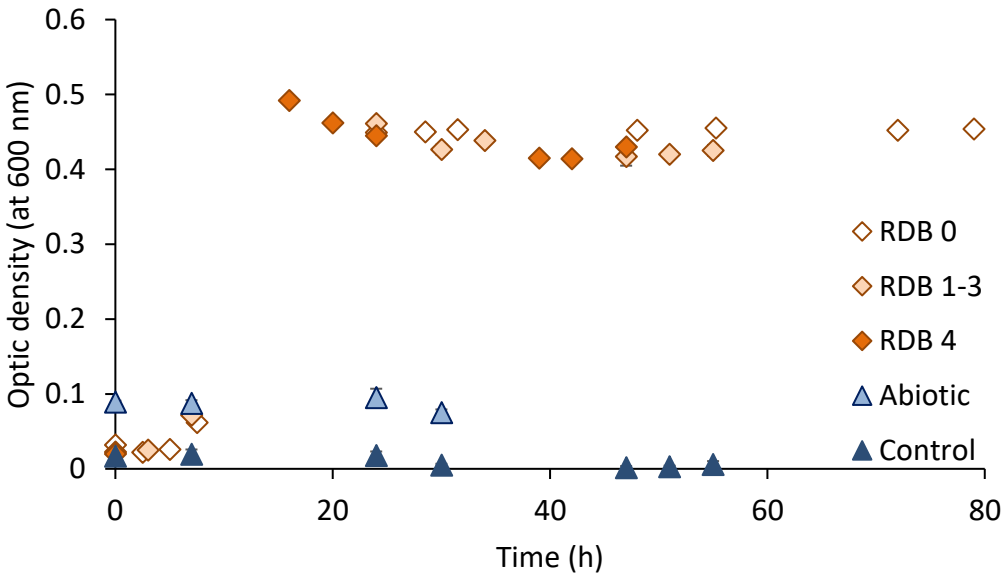

Figure S1: Optic Density measured at 600 nm for biotic (green diamonds), abiotic (light blue triangles), and control (dark blue diamonds) batch.

Chapitre 4 :
Utilisation des isotopes de l'antimoine en contexte minier

Introduction

Ce chapitre s'intéresse principalement à l'isotopie de l'antimoine dans l'environnement de la ville minière de Oruro (Bolivie), en particulier dans les eaux de surface impactées par le drainage minier acide de la mine de San José. De nombreux processus contrôlent le devenir des métaux et des métalloïdes en aval des mines (précipitation, adsorption, oxydation, mélanges…) dont la plupart sont susceptibles de fractionner les isotopes de l'antimoine, la mesure des isotopes de Sb pourrait donc donner des informations quant au devenir de l'antimoine au sein de ces cours d'eau. Cette dernière partie vise à confronter les résultats théoriques et expérimentaux avec les observations de terrain, ce qui permettra de valider l'utilisation des isotopes de Sb comme traceurs dans le contexte minier.

Le choix de la ville d'Oruro comme site d'étude a découlé de plusieurs critères. Tout d'abord, il s'agit d'un site minier et industriel au sein d'une zone urbaine de presque 300 000 habitants, et dont le drainage minier acide (Canal Rosso) traverse la ville et collecte également les eaux usées urbaines non traitées. Les concentrations en antimoine rencontrées dans le drainage minier acide à l'exhaure de la mine San José sont de l'ordre de 8 $mg.L^{-1}$. A l'est de la ville, (Vinto) se trouve un complexe métallurgique avec plusieurs fonderies qui traitent principalement des minerais d'étain mais aussi d'antimoine. Ce complexe est une source de contamination à la fois pour l'atmosphère et aussi pour le cours d'eau qui coule à proximité. Enfin, le trafic routier y est dense et remet beaucoup de poussières en suspension. Les concentrations en antimoine y sont élevées, et les sources multiples, ce qui en fait un site d'étude modèle pour le développement de l'utilisation de l'isotopie de l'antimoine pour le traçage géochimique.

Les paramètres physico-chimiques, les concentrations en carbone organique dissous, en éléments majeurs et traces ainsi que la spéciation de l'antimoine ont été mesurés afin de caractériser la physico-chimie des cours d'eau et de compléter les analyses isotopiques. Cette étude sur le drainage minier acide et sur la rivière impactée par les fonderies a été complétée par des mesures isotopiques de l'antimoine sur des points non impactés par les activités anthropiques (« fond géochimique et isotopique ») ainsi que par des analyses d'eaux de boisson en plusieurs points de la ville de Vinto. Cette étude s'étend sur deux campagnes de prélèvement différentes, à la fin de la saison des pluies (Mars 2019) et à la fin de la saison sèche (Octobre 2021).

Sb isotopes in surface waters of the mining and smelting city of Oruro, Bolivia

Colin Ferrari *[a], Eléonore Resongles [a], Rémi Freydier [a], Marisol Flores[b], Mauricio Ormachea[b], Gerardo Zamora[c] and Corinne Casiot [a]

Résumé en français

Nous avons étudié la composition isotopique de l'antimoine (Sb) le long de deux rivières, l'une impactée par l'activité minière et l'autre par des fonderies, pendant les deux saisons de l'altiplano (saisons sèche et saison humide). L'antimoine a été mesuré dans l'eau, les sédiments et les particules en suspension à cinq stations selon un gradient de pH (de 1.6 à 6.5) et de concentration de Sb (de 8057 à 7 µg.L^{-1}). La gamme de variation isotopique totale de cette étude est de 1 ‰ (-0.09 ≤ δ^{123}Sb ≤ +0.93 ‰), en prenant en compte tous les échantillons. Le cours d'eau principal impacté par le drainage minier acide a montré une augmentation progressive du δ^{123}Sb en phase dissoute le long de son écoulement, de +0.42 à +0.70 ‰, concomitante aux précipitations de Fe et à la diminution de la concentration de Sb ; ceci suggère que l'atténuation naturelle du Sb par sorption sur des (oxy)hydrosulfates de Fe néoformés favorise les isotopes légers dans le solide. Le facteur de fractionnement apparent entre l'eau et les sédiments $\Delta^{123}Sb_{eau\text{-}sédiments}$ était en moyenne de +0.3 ‰. L'affluent impacté par l'activité de fonderie présentait du Sb dissous plus léger, avec un δ^{123}Sb variant de +0.29 à +0.36 ‰. Le lac Uru-Uru qui reçoit les deux rivières a présenté une valeur intermédiaire de δ^{123}Sb de +0.28 ‰ en saison des pluies et de +0.55 ‰ en saison sèche, au cours de laquelle seule la rivière impactée par l'exploitation minière coule. Cette étude confirme le potentiel des isotopes de Sb pour le traçage des sources et des processus dans les systèmes aquatiques impactés par l'activité minière et métallurgique.

Sb isotopes in surface waters of the mining and smelting city of Oruro, Bolivia

Colin Ferrari *[a], Eléonore Resongles [a], Rémi Freydier [a], Marisol Flores[b], Mauricio Ormachea[b], Gerardo Zamora[c] and Corinne Casiot [a]

Abstract

In this study, we investigated the isotopic composition of antimony (Sb) along two rivers, one impacted by mining activity and the other by smelting activities during the wet and dry seasons. Antimony was measured in water, sediments, and suspended particulate matter at five stations along a gradient of pH (from 1.6 to 6.5) and Sb concentration (from 8057 to 7 µg.L^{-1}). Antimony isotopic composition varied over a range of about 1 ‰ considering all sample types (-0.09 ≤ δ^{123}Sb ≤ +0.93 ‰). The main stream impacted by acid mine drainage showed a progressive increase of δ^{123}Sb in the dissolved phase along its flow, from +0.42 to +0.70 ‰, concomitant to Fe precipitation and Sb concentration decrease; this suggested that natural Sb attenuation by sorption onto neoformed Fe (oxy)hydrosulphates favours light isotopes in the solid. The apparent fractionation factor between water and sediment $\Delta^{123}Sb_{water\text{-}sediments}$ averaged +0.3 ‰. The tributary impacted by smelting activity exhibited lighter dissolved Sb, with δ^{123}Sb, ranging from +0.29 to +0.36 ‰. Lake Uru-Uru which receives both rivers exhibited an intermediate δ^{123}Sb value of +0.28 ‰ in the wet season, and +0.55 ‰ in the dry season, during which only the mining-impacted river flows. This study confirms the potential of Sb isotopes for both processes and source tracking in aquatic systems impacted by mining and metallurgic activities.

1. Introduction

Antimony is one of the most mined metalloids in the world and its presence is ubiquitous in our daily life, in plastics as flame retardant or catalyst for PET, in batteries or lead alloys as a hardener, in brake linings as lubricants, in glass as a decolouring agent and in semiconductors for more flexible devices… (Biefeld, 2002; Von Uexküll *et al.*, 2005; Dupont *et al.*, 2016). The environments most affected by antimony contamination are found in areas impacted by sulphide mining (He *et al.*, 2012). In this respect, the Xikuangshan antimony mining and smelting area in China showed important contamination of surface water and groundwater with Sb (Tang and Liu, 2009; Liu *et al.*, 2010; Guo *et al.*, 2018; Liang *et al.*, 2018; Long *et al.*, 2022). The main route of transfer of antimony from sulphide mining sites to the aquatic compartment is through the generation of acid mine drainage (AMD) originating from the oxidation of sulphide minerals in contact with water and oxygen; these acid leachates can contain several milligrams per litre of antimony (Filella *et al.*, 2009; Filella *et al.*, 2009; Ritchie *et al.*, 2013). The fate of Sb in AMD and downstream hydrosystem involves complex biogeochemical processes including redox changes (from Sb(+III) to Sb(+V)), sorption of neoformed Fe-hydroxysulphates or precipitation of secondary Sb minerals (Filella *et al.*, 2009; Resongles *et al.*, 2013). Smelters or other metallurgical industries are also possible sources of Sb; this element is enriched in

atmospheric dust, soils and streams around smelters (Wilson *et al.*, 2004; Wang *et al.*, 2011; Goix *et al.*, 2013).

Bolivia is the fifth Sb producer after China, Russia, Tajikistan, and Turkey, with a production of 3100 tons of Sb per year (Brown *et al.*, 2019). The exploitation of stibnite and other metal sulphides in the mining city of Oruro in the Bolivian Altiplano induced Sb enrichment in water, soil, and atmospheric particles (Goix, 2012), together with human blood impregnation (Barbieri *et al.*, 2016). Several studies have focused on Oruro for its metal contamination in the aerosols and their impact on the health of the population (Barbieri *et al.*, 2011, 2014, 2016; Goix *et al.*, 2011, 2013; Goix, 2012; Ruiz-Castell *et al.*, 2012; Quaghebeur *et al.*, 2019), but only a few have been focused on water contamination in the AMD system and none of them applied Sb isotopes to investigate its environmental cycling within this complex site. The use of Sb isotopes in this environment impacted by multiple sources of contamination could contribute to identifying the sources and processes affecting Sb.

Antimony has two stable isotopes, ^{121}Sb and ^{123}Sb, with average abundances of 57.213 % and 42.787 % (Chang *et al.*, 1993). The main Sb ore, stibnite (Sb_2S_3), exhibits a significant range of Sb isotopic composition (δ^{123}Sb) around 1 ‰ (Lobo *et al.*, 2012) which enabled the use of Sb isotope signature for provenance determination of Roman glass. A few studies have investigated Sb isotope signatures in the environment; a significant range of variation of δ^{123}Sb (~1 ‰) was reported in rocks, sediments, soils, and river waters (Rouxel et al 2003; Resongles et al. 2015), showing the potential of Sb isotopes as tracers of Sb sources and/or biogeochemical processes in the environment (Rouxel *et al.*, 2003; Tanimizu *et al.*, 2011; Resongles *et al.*, 2015; Li *et al.*, 2021). In river systems impacted by historic metal and Sb mines, Resongles *et al.*, (2015) used the δ^{123}Sb signature to determine the contribution of two sub-watersheds to the total dissolved Sb load. A few studies investigated fractionation of Sb isotopes by geochemical processes; sorption of Sb on Al-oxides or Fe-oxyhydroxides induced no or slight isotope fractionation (Araki *et al.*, 2009; Ferrari *et al.*, 2021b; Zhou *et al.*, 2022). The reduction of Sb(V) into Sb(III) produced enrichment in the lighter isotope of about 0.9 ‰ in the reduced species (Rouxel *et al.*, 2003).

The behaviour of Sb isotopes has never been studied in hydrosystems impacted by AMD while several metal isotope systems have been successfully applied to investigate metal fate in these contexts. Yang *et al.*, (2019) studied the cadmium isotopic composition within the AMD of the Dabao mountain (China). They showed that the $\delta^{114/110}$Cd varied from 0.21 to 1.03 ‰, with a $\Delta^{114/110}Cd_{water-sediment}$ measured up to 1.61 ‰ close to the source. Variations of Cd isotopic composition was associated with different processes (adsorption, complexation, coprecipitation with hydroxides). Copper showed relatively high isotopic variations (δ^{65}Cu) within mining-impacted streams (Balistrieri *et al.*, 2008; Kimball *et al.*, 2009; Masbou *et al.*, 2020) with isotopic variations generally below 0.5 ‰ within the stream. These isotopic variations were also explained by several processes: oxidative dissolution (enrichment in heavy isotopes), weathering contributions (enrichment in light isotopes), adsorption on iron secondary phases (enrichment of the dissolved phase in light isotopes), or biotic precipitation.

In the present study, the fate of Sb isotopes was studied along two river systems impacted by acid mine drainage and smelter effluents in the mining city of Oruro (Bolivia). Together with Sb concentrations and dissolved redox speciation, Sb isotope ratios were determined in the dissolved phase, suspended particulate matter, and sediment, during two contrasted hydrological periods. The

objective was to document the range of Sb isotope signatures in such systems and investigate their possible use as source or process tracers.

2. Materials & methods

2.1. Site description

Oruro is one of the largest mining cities in the Bolivian Altiplano, located in the Cordillera Oriental, 230 km southeast of La Paz, at an altitude of 3700-4200 m asl. Bolivia is currently the 5th world producer of Sb, with more than 3100 tons produced in 2014 (Brown *et al.*, 2019). Antimony deposits containing up to 10 to 20 % of Sb are present in Mesozoic and Tertiary intrusions in the Middle Ordovician and Early Silurian sedimentary rocks (Arce-Burgoa and Goldfarb, 2009). The climate is characterised by two seasons, the dry season, from May to October, and the wet season, from November to April, with a precipitation average of 375 mm annually. Oruro is known for its polymetallic ore deposits (As, Au, Cu, Pb, Sb, Sn, and Zn) (Goix *et al.*, 2011), with Sb occurring under the form of sulphides including stibnite (orthorhombic Sb_2S_3), metastibnite (amorph Sb_2S_3), tetrahedrite ($(Cu,Fe)_{12}Sb_4S_{13}$), pyrargyrite (Ag_3SbS_3) or boulangerite ($Pb_5Sb_4S_{11}$) (Keutsch and Brodtkorb, 2008). Several mines are exploited in Oruro such as the San José mine, with numerous mine galleries on the Western part of the city (Figure 1). AMD flows outside from the San José mine gallery and joins the Rio Tagarete forming the Canal Rosso which crosses the city, collecting as well untreated urban waste waters. The Canal Rosso joins the Uru-Uru Lake in the south, for a total distance of around 16 km. Antimony concentration in this AMD was previously measured at 8080 ± 701 µg.L^{-1} at the exit of the mine gallery, with a decrease down to 19 ± 7 µg.L^{-1} at 10 km downstream (Goix, 2012). In the East part of Oruro, in the city of Vinto, the largest Sn smelter of the country is responsible of a severe metal(loid) contamination of airborne particles (Goix *et al.*, 2016). Antimony concentrations in surface waters draining the smelter complex were not determined previously but drinking water in the Vinto area showed high Sb levels, up to 49 µg.L^{-1}, whose origin remains to clarify (Goix, 2012).

2.2. Sampling

Two sampling campaigns have been conducted, the first one at the end of the wet season, in March 2019, and the second one at the end of the dry season, in October 2021. Water, suspended particulate matter (sampling in 2021 only), and sediments were collected (Figure 1): 1) at five stations along the river continuum from the San Jose mine gallery exit to the Uru-Uru Lake (station SJ1, CR1, CR2, CR3 and LUU), 2) at two stations along the river draining the Vinto smelter area (stations V1 and V2), and 3) at two natural reference sites not impacted by AMD or urban and smelting activities (stations CC and PAR, sampled in 2021 only). One reference site was located along the Cala-Cala River (station CC), upstream from the confluence with the river draining the Vinto smelter area; this site had been identified by Tapia *et al.*, (2012) to be representative of the geochemical background. The second reference site was located on the Paria river (station PAR) in the Paria village, around 10 km NNE of the city of Oruro; this river joins the Canal Rosso about 20 km downstream (between stations CR2 and CR3). Between 2019 and 2021, the canal between SJ1 and CR1 stations was fully covered with concrete and water sampling at the station CR1 was only possible using a bucket through a manhole cover. In 2021, stations V1 and V2 were not collected due to river drying at these sites at the end of the dry

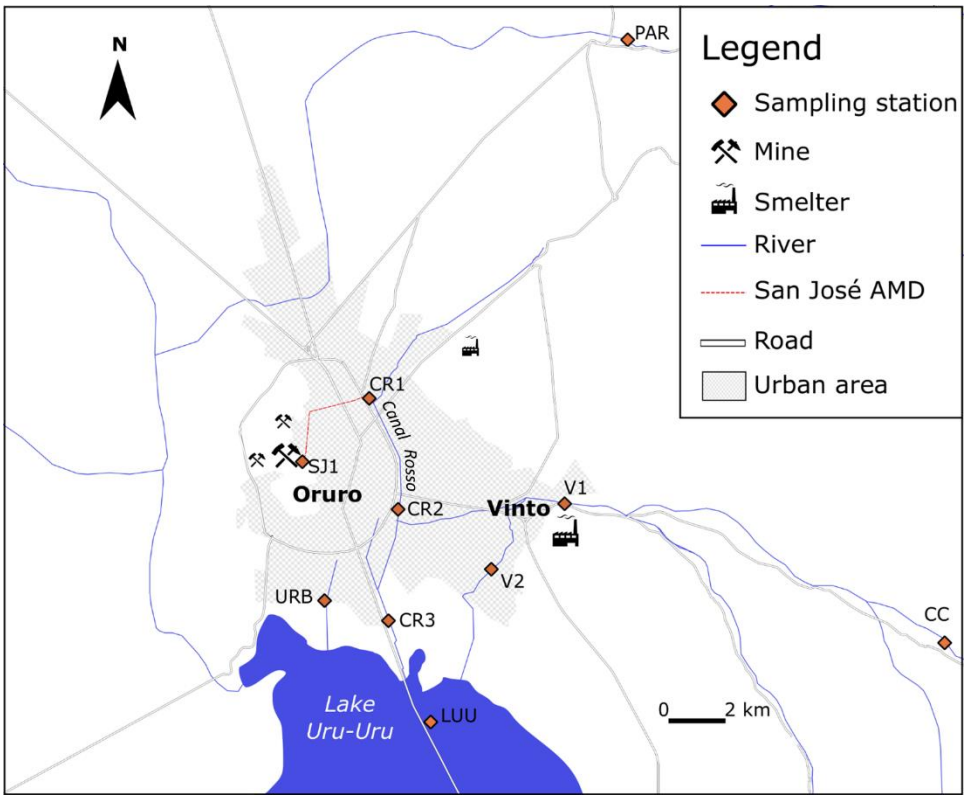

Figure 1: Location of the sampling stations and of the main mining and industrial activities in the city of Oruro (Bolivia).

season. A fourth sample set consisted of three drinking waters samples collected in different parts (East, Centre, and South-West) of the urban/smelting area of Vinto.

a. Sample collection and field measurements

The pH, conductivity, redox potential and dissolved oxygen concentration (DO) were measured in the field using an HQ40D portable multi-meter (Hach®) during the 2021 campaign. Measured redox potential was corrected to give redox potentials relative to a Normal Hydrogen Electrode (NHE).

Water samples were collected in acid-cleaned 2 L HDPE bottles and filtered the same day upon return to the laboratory through acid-cleaned, pre-weighed 0.22 µm PVDF filters (Millipore®) fitted on polycarbonate filter holders (Sartorius®). A subsample (20 ml) of the filtrate was centrifuged the same day in an ultrafiltration unit (< 10 kDa, Vivaspin®, Sartorius®) to obtain the "truly dissolved" phase. The 0.22 µm PVDF filter with suspended particulate matter was preserved in a filter box before processing in the laboratory. Filtered samples (< 0.22 µm and < 10 kDa) were stored in acid-cleaned HDPE bottles acidified with 0.1 % of HNO_3 (Suprapur, Merck®) for analysis of Sb concentration and Sb isotope ratio. Samples for redox Sb speciation analysis (Sb(+III) and Sb(+V)) were filtrated in the field using a disposable syringe and a 0.22 µm cellulose acetate filter; they were collected in polypropylene tubes and stabilised with 20 mM EDTA (J. T. Baker) and 87 mM acetic acid (Suprapur, Merck®), with a dilution by 10 (CR2, CR3, LUU) or 100 (SJ1, CR1) with ultrapure water to lower iron concentration as recommended from our unpublished trials. Water samples for dissolved organic carbon analysis were filtrated in the field using a glass syringe and a disposable 0.22 µm PVDF filter, the filtrated was

collected in a decontaminated glass bottle and stabilised in 0.1 % H_3PO_4 (Suprapur, Merck®). All water samples were kept at 4 °C until analysis.

Surface sediments were collected with a stainless-steel spatula in a plastic box and homogenised before being put in a 30 mL PE vial and kept in a cool box at 4°C until return to the laboratory.

2.3. Materials and reagents

Sample preparation for concentration and isotope analyses was carried out in a class 10 000 cleanroom facility. Ultrapure water (Milli-Q®, resistivity > 18.2 MΩ cm, Q-POP Element system, Millipore) was used for all experiments and reagent preparation. All consumables used for Sb analysis and Sb chemical separation (e.g., sample bottles, tubes, SPE cartridge, pipette tips…) were soaked in 10% v/v analytical grade HNO_3 or HCl, respectively, for 48 h and rinsed three times with ultrapure water before use. 30% w/w HCl (Suprapur, Merck®), 65–69% w/w HNO_3 (Analpure, Analityka®) and 40% w/w HF (Suprapur, Merck®) were used for sample preparation and analysis. Sodium borohydride (1 % w/v), ascorbic acid (analytical grade, Sigma-Aldrich®) and potassium iodine (KI, Suprapur, Merck®) were used for hydride generation. Ethylenediaminetetraacetic acid disodium salt (EDTA) (J. T. Baker) and potassium hydrogen-phthalate (SigmaUltra, 99.95%, Sigma-Aldrich) were used for the mobile phase in High-Performance Liquid Chromatography. A pure Sb standard solution SPEX (Sb 1000 µg mL^{-1} in 20 % w/w HCl, batch number 24-175SBX) was used as an in-house isotopic standard (Ferrari *et al.*, 2021a).

Solutions of Sb(III) and Sb(V) were prepared by dissolving 0.2742 g of potassium antimony(III) oxide tartrate trihydrate (Merck®) and 0.2158 g of potassium hexahydroxoantimonate (Merck®), respectively, in 100 mL of ultrapure water, to obtain a Sb concentration of ~1000 mg L^{-1}. The exact Sb concentrations of these solutions were then determined by Inductively Coupled Plasma Mass Spectrometry (ICP-MS).

a. Sample preparation

Sediments and filters with suspended particulate matter (SPM) were air-dried at 50 °C for 24 hours. Sediments were sieved at 2 mm before being powdered in an agate mortar. A subsample (50 mg) was digested using microwave-assisted acid digestion (UltraWAVE, Milestone®) following the protocol detailed for sediments in Ferrari *et al.* (2021a). Suspended particulate matters on filters were dissolved in 60 mL PTFE vials on a hot plate at 100 °C for 24 h with 4 mL of concentrated HNO_3, and 3 mL of concentrated HF. The solution was evaporated to dryness and the residue was re-dissolved in 30 mL of 10 % v/v HNO_3. For each set of samples, a certified reference material (GSD 3 and PACS 3) and a procedural blank were included.

Antimony separation from water (<0.22 µm) and digested sediments and SPM before Sb isotope ratio measurement was carried out according to the procedure presented in Ferrari *et al.* (2021a). This procedure is adapted to a wide range of Sb concentrations and sample matrices including mine water and sediments. Briefly, 100 ng of Sb in a 0.5 M HCl matrix with 10 % w/v KI and ascorbic acid were passed through a Thiol-functionalised silica powder cartridge to adsorb Sb. Other metals and trace elements were eluded with the injection of 5 mL of 0.5 M HCl and 6 mL of 2.5 M HCl. Finally, Sb was recovered with the elution of 6 mL of 6 M HCl. Purification blanks showed that no contamination occurred during the procedure (Sb in blank < 1 ng). Antimony recovery during the purification step was

checked on some sediment samples (PAR, URB, V1, and V2) with different matrices and Sb concentrations and was found to be equal at 99 ± 1% (n=4).

b. Analytical methods

All the ICP-MS analyses were performed on the AETE-ISO platform (OSU OREME, Université de Montpellier) and the the other chemical analysis were performed on the ABIHS platform (HSM).

Concentration of Dissolved Organic Carbon (DOC) was determined using a TOC-VCSH Shimadzu carbon analyser. Total Sb, Fe and S concentration in waters (<10 kDa and < 0.22 µm), sediments, and SPM was determined by Inductively Coupled Plasma Mass Spectrometry (ICP-MS) after an adequate dilution in 1 % v/v HNO_3, according to the procedure described in Ferrari *et al.* (2021a). The quality of the ICP-MS analysis was checked using certified reference materials for total Sb, Fe and S concentrations in water (SLRS-6 or NIST 1643e) and sediments (PACS-2) and concentrations were within 5 – 10 % of the certified values. Antimony, Fe, S in digestion blanks were negligible (<1 % of the concentrations in samples). A contamination with 1.7 $\mu g.L^{-1}$ of Sb occurred during the ultrafiltration step but it represented less than 10 % of Sb concentration measured in the <10 kDa fraction of water samples except for the reference station PAR (29 % of Sb < 10 kDa) and the lake station LUU (25 % of Sb < 10 kDa). The blank contribution to Sb concentration in the < 10 kDa fraction was deduced for all samples.

Determination of Sb(III) and Sb(V) concentrations in the dissolved phase (< 0.22 µm) was carried out by High-Performance Liquid Chromatography coupled to ICP-MS (HPLC-ICP-MS) as described in Resongles *et al.* (2013). The mobile phase consisted of 5 $mmol.L^{-1}$ EDTA and 2 $mmol.L^{-1}$ potassium hydrogen-phthalate, with a pH around 4.5. Samples were diluted in a 20 mM EDTA and 17 mM acetic acid matrix.

Antimony isotope ratio was measured in water (<0.22 µm), SPM and sediments by Hydride Generation Multi-Collector Inductively Coupled Plasma Mass Spectrometry (HG-MC-ICP-MS). Details of the sample conditioning and analytical settings are presented in Ferrari *et al.*, (2021a). Briefly, samples were diluted to 2 $\mu g.L^{-1}$ of Sb in 3 M HCl with 0.5 % w/v of KI-ascorbic acid, at least 3 hours before the analysis. Slight changes have been made in the present study to improve signal stability; the suppression of the additional gas in the entrance of the HG module, the increase of Sb concentration when possible (from 1 to 2 $\mu g.L^{-1}$), and the adjustment of the Ar gas flow to avoid short- and long- term pressure instabilities (parameters summarized in Table S1). Every sample was analysed 3-times using the sample-standard bracketing method. Antimony isotope composition is expressed as $\delta^{123}Sb$ notation (Equation 1), and is the average value for the three isotopic measurements if not specified otherwise.

$$\delta^{123}Sb(‰) = \left(\frac{\left(\frac{^{123}Sb}{^{121}Sb}\right)_{sample} - \left(\frac{^{123}Sb}{^{121}Sb}\right)_{mean\ std}}{\left(\frac{^{123}Sb}{^{121}Sb}\right)_{mean\ std}}\right) \times 1000 \text{ (Eq. 1)}$$

where $\left(\frac{^{123}Sb}{^{121}Sb}\right)_{mean\ std}$ is the average of Sb isotope ratio of the in-house Sb isotope standard solution measured before and after the sample.

The quality of Sb isotope measurement was checked by measuring the Sb isotope composition of certified reference material published in Ferrari et al. (2021a). CRM of sediments PACS-3 and GSD-3 were measured at 0.14 ± 0.06 ‰ and 0.15 ± 0.04 ‰, respectively, matching the published values.

3. Results

3.1. Main physico-chemical parameters, Sb concentrations, and speciation

The river continuum from the San Jose mine AMD discharge to the entrance of the lake Uru-Uru exhibited an acid pH. It increased continuously between upstream to downstream stations, from 1.56 at the gallery exit (SJ1) to 5.23 at the last station in the Canal Rosso (CR3) and finally 6.51 in lake Uru-Uru (LUU) during the dry season in 2021 with no significant variation compared to the end of the rainy season in 2019 (Table 1). This pH gradient was typical of those observed in rivers downstream AMD input (Nordstrom, 2000; Nordstrom *et al.*, 2015). The conductivity measured during the dry season decreased from 93.3 $mS.cm^{-1}$ at the gallery exit (SJ1) to 13.5 $mS.cm^{-1}$ in the intermediate station in Canal Rosso (CR2) and then increased to 18.3 $mS.cm^{-1}$ in lake Uru-Uru (LUU). Redox potential and oxygen concentrations reflected oxidizing conditions at the gallery exit and in the Canal Rosso. DOC increased from 12 $mg.L^{-1}$ at the gallery exit up to 66 $mg.L^{-1}$ at station CR2 in Canal Rosso, suggesting an input of wastewater effluents in the canal.

The urban canal (URB) exhibited neutral pH. The negative Eh value and low oxygen concentration (0.14 $mg.L^{-1}$) reflected reducing conditions. Conductivity (5 $mS.cm^{-1}$) and DOC (22 $mg.L^{-1}$) were relatively high, although both were lower than in Canal Rosso.

Reference samples from Paria (PAR) and Cala-Cala (CC) rivers (two sites considered as representative of the natural geochemical background) exhibited neutral pH. Conductivity was relatively high in Paria River (1.1 $mS.cm^{-1}$), although lower than at contaminated sites. Redox potential revealed oxidizing conditions, although a low DO value was measured (1.7 $mg.L^{-1}$) in Cala-Cala River, which could be attributed to the fact that this stream is intermittent at the end of the dry season and only supplied by groundwaters. DOC concentrations were in the order of magnitude of those measured in the Canal Rosso receiving urban effluents.

Dissolved Sb concentrations (< 0.22 µm) were extremely high at the exit of the mine gallery (SJ1), with similar values during the dry season (8057 µg $Sb.L^{-1}$) and wet season (7824 $\mu g.L^{-1}$) (Table 1). Sb concentration decreased drastically along the Canal Rosso and lake Uru-Uru. Sb concentrations in the Canal Rosso were 2 to 4 times higher during the dry season than during the wet season (4070 vs 2242 $\mu g.L^{-1}$ at CR1, 97 vs 25 $\mu g.L^{-1}$ at CR2 and 20 vs 10 $\mu g.L^{-1}$ at CR3) while in the lake Uru-Uru they were 3 times lower during the dry season (7.2 vs 22 $\mu g.L^{-1}$ at LUU). These concentration variations were consistent with the previous measurements made by Goix (2012). In the urban canal (URB), Sb concentration was lower (18.5 $\mu g.L^{-1}$) than in Canal Rosso but the high Fe and S concentrations (4469 and 251342 $mg.L^{-1}$, respectively) suggested AMD inflow. In the upstream reference samples from rivers Paria and Cala-Cala, Sb concentrations (2-4 $\mu g.L^{-1}$) were drastically lower than in Canal Rosso but higher than the worldwide river averages of 0.07 $\mu g.L^{-1}$ (Gaillardet *et al.,* 2003), which reflected the high geochemical background in the area. In the river draining the Vinto smelter area (V1 and V2 stations), Sb concentrations (31 to 33 $\mu g.L^{-1}$) were higher than at the reference station CC located upstream, reflecting enrichment from the Vinto smelter. In drinking water samples from the Vinto smelters' area,

Sb concentrations varied between 7 and 8.3 µg.L^{-1} (Table 2), thus slightly above the European and American drinking water standards (5 and 6 µg.L^{-1} respectively), but below the Bolivian standards (15 µg.L^{-1}). These values were higher than in the surface water reference samples, which could denote either natural groundwater enrichment with Sb or contamination from the smelting activities.

SPM concentration was higher in lake Uru-Uru (SPM = 7 g.L^{-1}) than in Canal Rosso (SPM averaged 46 ± 7 mg.L^{-1} at SJ1, CR2, CR3) but the Fe content was similar in LUU and SJ1, CR1, CR2 stations (5.1 – 8.8 % Fe) . Station CR3 showed higher Fe enrichment (21.7%) while the urban canal showed a lower Fe content (1.4 %), in relation with a different composition of SPM from urban effluents. Antimony concentration increased in SPM between the mine gallery exit (2614 mg.kg^{-1} at SJ1) and the Canal Rosso (3837 mg.kg^{-1} at CR1). Then it decreased by a factor of ten in the Canal Rosso downstream from the confluence with the Rio Tagarete (262 mg.kg^{-1} at CR2 and 94 mg.kg^{-1} at CR 3), and further decreased four-fold in lake Uru-Uru. Sediments contained highly variable Sb concentrations depending on the station and the season. Concentrations in Canal Rosso were higher during the dry season while the reverse was observed in the river draining the Vinto smelter (V1 and V2 stations) and in lake Uru-Uru. At the two reference stations on rivers Paria and Cala-Cala, Sb concentrations in SPM and sediments were lower than at other locations (16-21 mg.kg^{-1}), although one order of magnitude higher than the world river average for SPM (2.19 ± 2.41 µg.g^{-1}, (Viers *et al.*, 2009)), which reflected the high natural geochemical background in the area.

The distribution of Sb between the "truly dissolved" (< 10 kDa) fraction (Sb(III) and Sb(V) species), the colloidal fraction (between 10 kDa and 0.22 µm), and the SPM fraction (> 0.22 µm) along the AMD-impacted river continuum until lake Uru-Uru and in the urban canal is presented in Figure 2. Antimony was predominantly in the "truly dissolved fraction" at all stations except in lake Uru-Uru and the oxidised Sb(V) species represented more than 80.6 % of total dissolved Sb (< 0.22 µm). The colloidal fraction was negligible (≤ 1 % of total Sb) except at the stations LUU and URB (~10 % of total Sb). The particulate fraction (> 0.22 µm) represented 1.2 % of total Sb at the exit of the mine gallery (SJ1), then increased to 11-19 % in the Canal Rosso (CR2, CR3) and urban canal (9 %), and up to 72 % in lake Uru-Uru. Considering the concomitant decrease of dissolved Sb concentration, this reflected Sb sorption or coprecipitation onto particulate matter. Redox speciation in the dissolved fraction changed, with a decrease of the proportion of Sb(III) from 19.4 % at the mine gallery exit (SJ1) to 3.7 % at the first station (CR1) in Canal Rosso, and finally 0 % in downstream stations CR2, CR3 and lake Uru-Uru (LUU). In the urban canal, Sb(III) represented 16 % of total dissolved Sb.

Finally, the mining wastes and smelting slags had drastically different compositions; mining wastes were composed of 11% Fe, 11% S and a high Sb content of 2604 mg.kg^{-1}. Smelting slags were essentially composed of Fe (21 %) and had a low Sb content of 41.7 mg.kg^{-1}.

Table 1: Main physico-chemical parameters and concentrations of Sb, Fe, S, and DOC in water (< 0.22 µm), SPM, and sediments from the rivers at the end of the wet (March 2019) and dry (October 2021) seasons. Antimony isotopic composition (δ^{123}Sb ±- 2σ) are also reported.

	Station	**San José Mine**	**Canal Rosso**			**Uru-Uru Lake**	**Vinto River**		**Urban Canal**	**Paria River**	**Cala-Cala River**
		SJ1	**CR1**	**CR2**	**CR3**	**LUU**	**V1**	**V2**	**URB**	**PAR**	**CC**
Dry season (October 2021)	Temperature (°C)	22.8	15.3	11.8	9.4	25.5	-	-	14.5	11.5	15.2
	pH	1.56	1.85	4.48	5.23	6.51	-	-	7.90	8.30	7.29
	Eh (mV)	616.8	602.5	412.5	350.4	175.5	-	-	2.3	336.7	336.3
	Conductivity (µS.cm^{-1})	93300	65700	13450	14710	18300	-	-	5410	1125	422
	DO (mg.L^{-1})	4.54	5.21	4.64	2.46	2.75	-	-	0.14	7.07	1.71
	River water (< 0.22 µm)										
	DOC (mg.L^{-1})	12.0	44.5	65.9	55.2	45.2	-	-	21.9	6.6	3.5
	Fe (mg L^{-1})	3716	2930	249	233	122	-	-	4.47	0.50	0.005
	S (mg L^{-1})	4258	3965	499	549	679	-	-	251	48.1	34.1
	Sb (µg L^{-1})	8057	4070	97.4	19.9	7.2	-	-	18.5	4.12	2.01
	Sb(III) (%)	19.0	4.0	0.0[a]	0.0[a]	0.0[a]	-	-	15.8	0.0[a]	11.3
	δ^{123}Sb (‰)	0.42 ± 0.02	0.43 ± 0.01	0.54 ± 0.02	0.70 ± 0.03	0.55 ± 0.01	-	-	0.61 ± 0.06	0.36 ± 0.04	0.33 ± 0.02
	Suspended particulate matter (> 0.22 µm)										
	SPM concentration (mg.L^{-1})	38.4	*(369)*[c]	47.3	51.9	7061	-	-	63.9	14.6	-
	Fe (mg.kg^{-1})	51139	74432	60562	217148	88149	-	-	14458	39524	-
	S (mg.kg^{-1})	<270000[b]	<72000[b]	<34400[b]	<19700[b]	<11200[b]	-	-	75080	<14000[b]	-
	Sb (mg.kg^{-1})	2614	3837	262	94.3	24.1	-	-	28.6	20.9	-
	δ^{123}Sb (‰)	0.26 ± 0.02	0.32 ± 0.02	0.31 ± 0.01	0.49 ± 0.05	0.31 ± 0.04	-	-	-	-	-
	Sediments (< 2 mm)										
	Fe (mg.kg^{-1})	14083	80463	38535	94766	82061	28140	36032	52446	24567	25394
	S (mg.kg^{-1})	<550000[b]	<96000[b]	<12000[b]	25314	<6100[b]	<2500[b]	<21000[b]	17412	<1100[b]	<1100[b]
	Sb (mg.kg^{-1})	715	1431	273	259	47.3	34.9	78.2	54.7	20.4	16.3

	δ^{123}Sb (‰)	0.22 ± 0.02	0.36 ± 0.02	0.23 ± 0.03	0.25 ± 0.02	0.20 ± 0.04	0.18 ± 0.05	0.13 ± 0.06	0.11 ± 0.04	0.13 ± 0.05	0.24 ± 0.07
Wet season (March 2019)		**San José Mine**	**Canal Rosso**			**Uru-Uru Lake**	**Vinto River**		**Mining waste**	**Smelting slag**	
	Station	**SJ1**	**CR1**	**CR2**	**CR3**	**LUU**	**V1**	**V2**	**-**	**-**	
	pH	1-2	2	4-5	5	7	6-7	7	-	-	
	River water (< 0.22 µm)										
	Fe (mg L^{-1})	3114	1768	291	164	0.18	0.03	0.06	-	-	
	S (mg L^{-1})	3651	2673	962	691	522	35.0	40.8	-	-	
	Sb (µg L^{-1})	7824	2242	24.8	10.2	21.9	31.4	33.3	-	-	
	δ^{123}Sb (‰)	0.46 ± 0.02	0.42 ± 0.07	0.55 ± 0.04	0.60 ± 0.02	0.28 ± 0.02	0.29 ± 0.02	0.36 ± 0.03	-	-	
	Sediments (< 2 mm)										
	Fe (mg.kg^{-1})	166029	44242	64852	45924	71221	36993	31923	113421	208599	
	S (mg.kg^{-1})	201750	51601	10547	35418	13317	<686[b]	<626[b]	108514	<6189[b]	
	Sb (mg.kg^{-1})	14528	211	203	57.2	82.1	154	418	2604	41.7	
	δ^{123}Sb (‰)	-0.09 ± 0.02	0.08	0.23 ± 0.05	0.23 ± 0.04	0.22 ± 0.05	0.03 ± 0.08	0.23 ± 0.03	0.14 ± 0.07	0.29 ± 0.04	

[a]Sb(III) was below detection limit (0.01 µg.L^{-1})
[b]Sulphur concentration < detection limit (150 µg.L^{-1}) x dilution factor ICP-MS analysis.
[c]SPM concentration is overestimated due to resuspension of sediments during the sampling (low water column).

Table 2: Drinking water in the city of Vinto.

Sample name	**DW1**	**DW2**	**DW3**
Fe (mg L^{-1})	0.49	0.64	0.50
S (mg L^{-1})	103	113	127
Sb (µg L^{-1})	7.99	8.35	7.04
δ^{123}Sb (‰)	0.64 ± 0.03	0.67 ± 0.02	0.93 ± 0.01

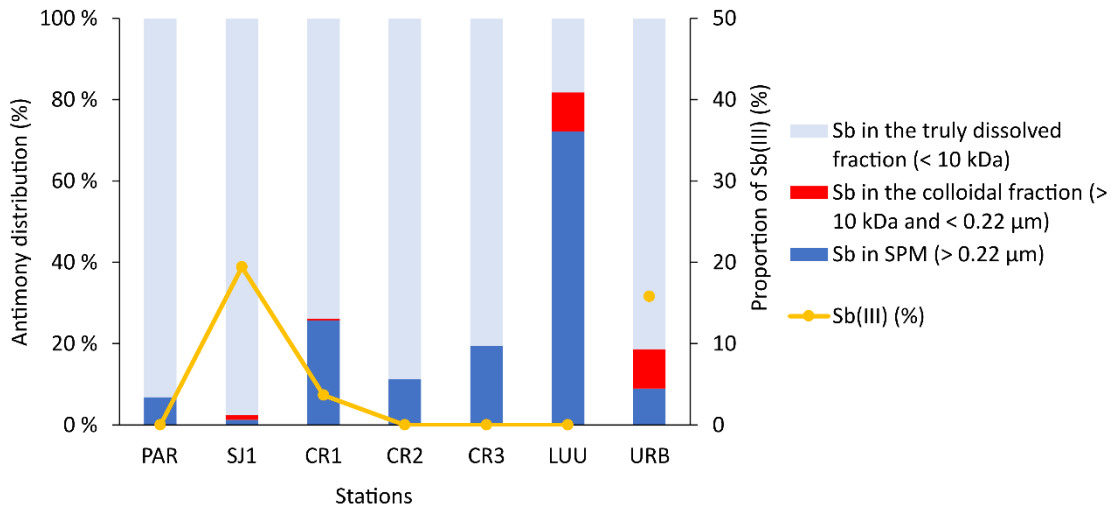

Figure 2: Distribution (in %) of Sb in the water column among the truly dissolved (<10 kDa), colloidal (> 10 kDa and < 0.22 µm) and particulate (> 0.22 µm) fractions. The colloidal fraction was calculated by the difference between Sb concentrations in the dissolved fraction filtrated at 0.22 µm and ultrafiltrated at 10 kDa. The yellow line represents the proportion of Sb(III) compared to total Sb (Sb(III) + Sb(V)) in the fraction < 0.22 µm. The proportion of Sb associated with the particulate fraction at the CR1 station represents an overestimate because bottom sediments were resuspended during the sampling due to the low water column and the inaccessibility of the site (covered canal accessible only through a manhole cover).

3.2. Antimony isotopic composition

Antimony isotope composition in the various samples (tailings, water, SPM, and sediments) collected in the study area ranged from -0.09 to +0.93 ‰. The mine tailing sample exhibited an Sb isotopic composition (δ^{123}Sb) of 0.14 ± 0.07 ‰, while the Vinto smelting slag was slightly isotopically higher, with an isotopic signature of 0.29 ± 0.04 ‰.

The surface waters along the river continuum between the mine gallery exit, the Canal Rosso, and the lake Uru-Uru were preferentially enriched in heavier Sb isotope compared to SPM or sediments. On average, the apparent fractionation factor between sediment or SPM and dissolved Sb (< 0.22 µm) was $\Delta^{123}Sb_{water\text{-}sediment}$ = 0.28 ± 0.15 ‰ and $\Delta^{123}Sb_{water\text{-}SPM}$ = 0.21 ± 0.04 ‰, respectively (excluding CR1 for the SPM due to sediment resuspension during sampling). The Sb isotope composition of SPM was close to that of sediments; the apparent fractionation factor $\Delta^{123}Sb_{SPM\text{-}sediment}$ was on average 0.04 ± 0.06 ‰, excluding station CR3 where $\Delta^{123}Sb_{SPM\text{-}sediment}$ = 0.24 ‰ (Figure 3).

Antimony isotope composition in water (< 0.22 µm) increased from the San José mine (δ^{123}Sb = 0.4 to 0.5 ‰ at SJ1) to downstream stations (δ^{123}Sb = 0.6 to 0.7 ‰ at CR3) along the river continuum and then decreased (δ^{123}Sb = 0.3 to 0.5 ‰) in lake Uru-Uru (Figure 3). The same spatial trend was observed during the wet and dry seasons, although the decrease in lake Uru-Uru was more significant in the wet season (0.28 ‰) than in the dry season (0.55 ‰). Water in the urban canal exhibited δ^{123}Sb values of 0.61 ± 0.06 ‰, close to the Canal Rosso signature. Water in the Vinto River upstream and downstream from the Vinto smelter exhibited an Sb isotope composition around 0.3 ‰, thus significantly different from the Canal Rosso signature. Water sampled at the reference sites Cala-Cala and Paria, representative of the geochemical background, exhibited similar isotopic composition (δ^{123}Sb = 0.33 ± 0.02 ‰ and 0.36 ± 0.04, respectively), significantly different from the Canal Rosso signature (δ^{123}Sb =

0.6 – 0.7 ‰), but similar to the Vinto River signature (δ^{123}Sb ≈ 0.3 ‰). Drinking water samples exhibited Sb isotopic composition between 0.64 and 0.93 ‰, thus significantly higher than the natural geochemical background (δ^{123}Sb ≈ 0.35 ‰); two samples had a signature close to Canal Rosso (δ^{123}Sb = 0.64 ± 0.03 ‰ for DW1 and 0.67 ± 0.02 ‰ for DW2), while the third one had the highest value of all the data set (δ^{123}Sb = 0.93 ± 0.01 ‰ for DW3).

Sediments at the mine gallery exit (SJ1) and at the CR1 station exhibited a different Sb isotope signature (Δ^{123}Sb ≈ 0.3 ‰) in the wet and dry seasons, with a lowest value in the wet season (δ^{123}Sb = -0.09 ‰ at SJ1 and 0.08 ‰ at CR1) compared to the dry season (δ^{123}Sb = 0.22 ‰ at SJ1 and 0.36 ‰ at CR1). At downstream stations along Canal Rosso and lake Uru-Uru (CR2, CR3, LUU), Sb isotope composition in sediments and SPM remained relatively stable at 0.2 - 0.3 ‰, both in the wet and dry seasons.

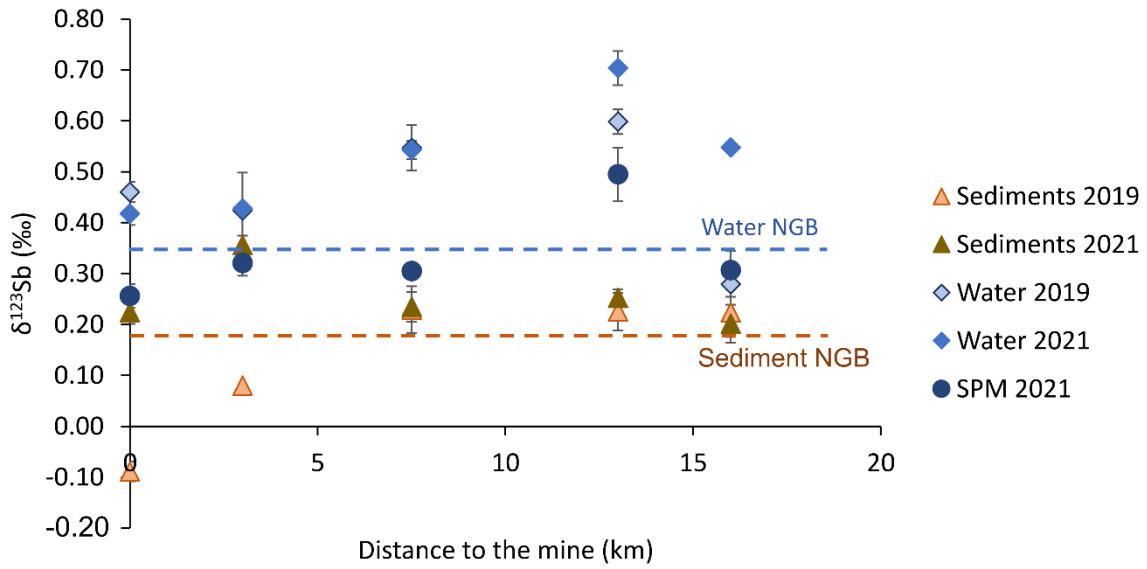

Figure 3: Variability of the Sb isotopic composition during the wet season (2019) and the dry season (2021) as a function of the distance to the San José mine gallery exit. Diamonds represent δ^{123}Sb in the dissolved fraction, circles represent δ^{123}Sb in the SPM and triangles represent δ^{123}Sb in the sediments.

4. Discussion

4.1. Antimony contamination in surface waters of the mine and the smelter areas

The geochemical background (both water and SPM) determined in the rivers Paria and Cala-Cala were higher than world river averages for SPM and sediments (Filella *et al.*, 2001; Viers *et al.*, 2009). This confirmed high Sb levels originating from the sulphide mineralisation in the area (Goix, 2012; Calas *et al.*, 2015). Antimony concentrations at the exit of the San José mine gallery and in Canal Rosso were among the highest measured in AMD environments worldwide (Filella *et al.*, 2001; Tang and Liu, 2009; Li *et al.*, 2020; Long *et al.*, 2022). The values were roughly the same between the dry and wet seasons and similar to those measured in 2011 by Goix (2012), showing persistent AMD contamination. The decrease of dissolved Sb concentration and concomitant increase of particulate and sedimentary Sb along Canal Rosso reflected natural attenuation of the dissolved Sb contamination. This process involves Sb sorption or coprecipitation with Fe upon pH neutralisation, it was described in other high-Sb AMD (Manaka *et al.*, 2007; Filella *et al.*, 2009; Resongles *et al.*, 2013). Redox speciation showed that

the decrease of dissolved Sb concentration in the AMD was accompanied by a decrease in the percentage of dissolved Sb(III), which reflected Sb(III) oxidation or preferential sorption/precipitation of Sb(III) upon Sb(V). Greater retention of Sb(III) during AMD neutralisation was observed in other AMD (Resongles *et al.*, 2013). The natural attenuation process, besides dilution, resulted in relatively low Sb concentration values in both dissolved and particulate/sedimentary phases in lake Uru-Uru, only twice (for dissolved phase and sediment) those measured at the reference sites representative of the natural geochemical background. The urban canal (URB) showed lower Sb concentrations in water, SPM and sediments than the Canal Rosso that directly received AMD from the San José mine gallery; however, they were significantly higher than the natural geochemical background; furthermore, the high Fe concentration in water, SPM and sediment were characteristic of AMD chemistry, which confirmed AMD input. The Vinto River downstream of the Vinto smelter showed Sb concentrations (dissolved phase and sediment) above the natural geochemical background, which reflected input from the Vinto smelter; however, direct input of liquid effluent was not observed, and leaching of slags and soils contaminated by atmospheric fallout could be involved instead. Drinking water in the Vinto smelting area also exhibited Sb concentrations higher than the geochemical background values, which could denote groundwater contamination by anthropogenic activities.

4.2. Antimony isotope ratios and contamination sources

The natural geochemical background in the area exhibited a δ^{123}Sb signature of about 0.3 ‰ in water and ~0.1-0.2 ‰ in sediments. Indeed, the two references areas (CC and PAR stations) had similar δ^{123}Sb in water (0.33 ± 0.02 ‰ and 0.36 ± 0.04 ‰, respectively) and very close signatures in sediment (0.24 ± 0.07 ‰ and 0.13 ± 0.05 ‰, respectively). It is noteworthy that the different redox Sb speciation in Cala-Cala River water (Sb(III)) represented 11.3 % of total dissolved Sb) and in Paria River water (Sb(III)) represented 0 % of total dissolved Sb) did not affect Sb isotope composition.

The Vinto River samples (2019 sampling survey for water and sediments, and 2021 for sediments only) exhibited similar Sb isotope values (0.3-0.4 ‰ in water, 0.1-0.2 ‰ in sediments) than the natural signature, although Sb concentrations were significantly higher than the natural geochemical background. During the wet season, the sediment sampled upstream the Vinto smelter (V1) showed relatively low δ^{123}Sb (0.03 ± 0.08 ‰) before increasing to 0.23 ± 0.03 ‰ in V2. The δ^{123}Sb signature of dissolved Sb also slightly increased between V1 and V2 ($\Delta^{123}Sb_{V2-V1}$ = 0.07 ‰). These changes in the isotopic composition could be explained by the contribution of Sb contamination from the large-scale smelting slag storage area in the vicinity of the river, the slags exhibiting a relatively higher δ^{123}Sb signature (0.29 ± 0.04 ‰). High-temperature processes usually fractionate metal isotopes, with enrichment in the light isotopes in the atmospheric dust and enrichment in the heavy isotopes in slags (Sonke *et al.*, 2008; Wiederhold, 2015). This was consistent with an increase of the isotopic composition of the smelting slag compared to the mining residue ($\Delta^{123}Sb_{slag-tailing}$ = +0.15 ‰), however a better characterisation of the processed ore and fume dust would be required to fully validate this hypothesis.

Surface waters impacted by the AMD in Canal Rosso had a δ^{123}Sb signature higher than 0.4 ‰, while the natural geochemical background value was lower than 0.4 ‰ suggesting that it is possible to pinpoint AMD influence in waters using the Sb isotope signature. In this respect, the signature of the water in the urban canal was higher than 0.4 ‰, which confirms that AMD input contributes to Sb enrichment in this canal as well. However, the Sb isotope composition of sediments from the urban

canal (0.11 ± 0.04 ‰) was lower than the composition of sediments from the Canal Rosso (0.23 - 0.36 ‰); it was closer to the composition of sediments from the natural geochemical background, which suggests that geochemical processes modify the original Sb isotope signature in sediments. Indeed, the $\Delta^{123}Sb_{water\text{-}sediment}$ for the urban canal is 0.50 ‰, with Fe and S concentrations respectively 3 and 1 orders of magnitude lower than in the AMD, respectively, and presenting a neutral pH (7.9). This indicates that most probably the main process occurring in this canal differs from that occurring in the Canal Rosso and may be related to the adsorption of Sb on other phases than iron oxyhydroxides phases and is more probably related to organic matter.

Water from the lake Uru-Uru exhibited a significant change in Sb isotope composition between the wet and dry periods. During the dry period (2021), the signature (0.55 ± 0.01 ‰) was close to that of the AMD (> 0.4 ‰). During the wet period (2019), the signature (0.28 ± 0.02 ‰) was close to that of the Vinto River water (0.29-0.36 ‰). Thus, the contribution of at least two different sources (the AMD-impacted stream and the smelting-impacted stream) is evidenced in the Uru-Uru Lake water. The Sb isotope composition of sediments did not vary with the season, with $\delta^{123}Sb$ around 0.2 ‰, close to Canal Rosso sediments and the natural geochemical background.

The Sb isotope composition of the drinking water samples (DW1 = 0.64 ± 0.03 ‰, DW2 = 0.67 ± 0.02 ‰; DW3 = 0.93 ± 0.01) was higher than that of the natural geochemical background (~0.3 ‰). According to the local people, the drinking water in Vinto is from groundwater pumped in Cala Cala and Sepulturas (close to the smelter) localities. The contrasted isotope signature observed in these drinking waters may arise from an anthropogenic contamination due to leaching of smelter residues or from fractionation compared to surface water geochemical background related to natural processes occurring within the aquifer (redox change, adsorption). Thus, more research is needed to better understand the origin of such an Sb isotope shift.

4.3. Antimony isotope ratios and geochemical processes in AMD

The isotopic composition of antimony in AMD at the gallery exit was heavier than that of the Sb-rich mine tailing, suggesting that the oxidative dissolution of sulphide minerals preferentially releases the Sb heavy isotope in water. Tanimizu *et al.*, (2011) measured an apparent fractionation factor between water and stibnite $\Delta^{123}Sb_{aqueous\text{-}mineral}$ of +0.35 ‰. On average, the $\Delta^{123}Sb_{aqueous\text{-}mineral}$ from the dry and wet seasons was measured at 0.30 ‰, which is consistent with the previous observation of Tanimizu *et al.*, (2011). Important differences in the isotopic composition of the sediments in SJ1 were noted between the dry and the wet season $\Delta^{123}Sb_{dry\text{-}wet}$ = +0.42 ‰. This important difference is associated with higher Sb concentrations during the wet season (14528 $mg.kg^{-1}$) than during the dry season (715 $mg.kg^{-1}$). This difference may be explained by a difference in the nature of the sampled sediments. Indeed, based on visual observations, sediments sampled in the AMD stream at the exit of the San José mine in the wet season likely consisted of primary minerals (sulphides) exploited in the mine while sediments sampled in the dry seasons were made of secondary neoformed minerals.

The apparent fractionation factor between water and sediment in Canal Rosso $\Delta^{123}Sb_{water\text{-}sediments}$ was 0.28 ± 0.19 ‰ in the dry season and 0.34 ± 0.03 ‰ in the wet season, considering the three stations (CR1, CR2, CR3). In acid mine drainage, one of the most important factors controlling the mobility of Sb is its sorption onto Fe-, Al-, or Mn- oxyhydroxides due to the important specific surface area of these phases (Fukushi *et al.*, 2003; Manaka *et al.*, 2007). These processes are playing an

important role in the immobilisation of Sb in the sediments (Hiller *et al.*, 2012). A few studies investigated the behaviour of Sb isotopes during sorption. Recently, Zhou *et al.*, (2022) have experimentally studied isotopic fractionation occurring during Sb adsorption on aluminium oxides (ϒ-Al_2O_3) and despite the absence of isotopic fractionation at the equilibrium ($\Delta^{123}Sb_{water\text{-}adsorbed\ phase}$ = 0 ± 0.08 ‰), there was an appearing kinetic fractionation of about $\Delta^{123}Sb_{water\text{-}solid}$ = +0.25 ‰. Ferrari et al. (in prep) studied the isotopic fractionation of Sb on ferrihydrite and schwertmannite, two iron oxyhydroxide and hydrosulphate commonly found in sulphide mining environments (Bigham *et al.*, 1996); they have found an equilibrium Sb isotope fractionation between dissolved and sorbed Sb $\Delta^{123}Sb_{water\text{-}solid}$ ranging from +0.24 to +0.34 ‰, with an equilibrium reached in less than 48 hours. The apparent fractionation factors determined between the dissolved and particulate antimony in the AMD in the present study match the equilibrium isotopic fractionation during Sb adsorption on secondary iron minerals (ferrihydrite and schwertmannite). The progressive increase of $\delta^{123}Sb$ in water and SPM along the AMD stream (stations SJ1 to CR3) could thus be related to the adsorption of Sb on (oxy)hydroxides resulting in the progressive depletion of light isotopes in the dissolved phase, accompanied with a progressive increase of $\delta^{123}Sb$ of newly sorbed Sb in SPM. The isotopic composition of the sediments did not evolve in the same extent as for water and SPM along the river continuum. The similarity in isotope composition observed between SPM and sediments (except at CR3) is likely due sedimentation of the particles on the top of the bottom sediment, ending up with a similar isotopic signature (same processes of adsorption). However, in this open system, the absence of important changes in the isotopic fractionation in sediments and SPM while the $\delta^{123}Sb$ of dissolved water progressively increases could be explained by i) the transportation/sedimentation of SPM and remobilisation of sediments along the river continuum, leading to a homogenisation of the signature of the sediments or ii) to a pool size effect.

In the urban canal (URB), the apparent fractionation factor between dissolved and sorbed Sb $\Delta^{123}Sb_{dissolved\text{-}sediments}$ of +0.50 ‰ was higher than in Canal Rosso. The mixing of AMD with wastewater effluent in the urban canal may involve complex (bio-)geochemical processes, besides sorption on Fe secondary minerals, that would deserve further research.

Conclusion

In this study, Sb composition was measured in the AMD of the San José mine, crossing the city of Oruro and in the smelting-impacted stream of Vinto, in the Bolivian Altiplano. Antimony in the AMD was mainly transported under the dissolved oxidized form, with a signature ranging from 0.42 to 0.70 ‰. Various processes could be associated with the different $\delta^{123}Sb$ observed in this system. The significant variation of $\delta^{123}Sb$ along the river continuum impacted by acid mine drainage could result from the progressive adsorption of Sb onto secondary ferrous (oxy)hydroxides, favoring the light Sb isotope, with an isotopic fractionation factor $\Delta^{123}Sb_{water\text{-}sediment}$ of 0.27 ± 0.16 ‰ and 0.33 ± 0.18 ‰ for the dry and wet season respectively. Indeed, this apparent fractionation factor matches the direction and magnitude of isotope fractionation observed during laboratory experiments of Sb adsorption on Fe secondary mineral (Ferrari et al. in prep).

During the wet season, the smelting-impacted river in Vinto had an isotopic composition lighter than the AMD-impacted stream of Oruro and its contribution to Sb contamination in the lake Uru-Uru could explain the intermediate $\delta^{123}Sb$ signature observed at the entrance of the Uru-Uru Lake as a result of the mixing of the two contaminated streams. During the dry season, the smelting-impacted

river did not flow and the isotopic composition of the Uru-Uru Lake was closer to that of the AMD-impacted stream likely reflecting its dominant contribution to Sb contamination at this station in the lake.

This field study is the first to document Sb isotope variability in a mining and industrial context confirming their promising potential as environmental tracers. However, more experimental studies are required to characterise Sb isotope fractionation associated to various geochemical processes and further identify the processes occurring in this complex and multi-source environment.

5. References

Araki, Y., Tanimizu, M. and Takahashi, Y. (2009) 'Antimony isotopic fractionation during adsorption on ferrihydrite', *Geochimica et Cosmochimica Acta Supplement*, 73, p. A49.

Arce-Burgoa, O.R. and Goldfarb, R.J. (2009) 'Metallogeny of Bolivia', *SEG Discovery*, (79), pp. 1–60. https://doi.org/10.5382/SEGnews.2009-79.

Balistrieri, L.S. *et al.* (2008) 'Fractionation of Cu and Zn isotopes during adsorption onto amorphous Fe(III) oxyhydroxide: Experimental mixing of acid rock drainage and ambient river water', *Geochimica et Cosmochimica Acta*, 72(2), pp. 311–328. https://doi.org/10.1016/j.gca.2007.11.013.

Barbieri, E. *et al.* (2014) 'Indoor metallic pollution and children exposure in a mining city', *Science of The Total Environment*, 487, pp. 13–19. https://doi.org/10.1016/j.scitotenv.2014.03.136.

Barbieri, F.L. *et al.* (2011) 'Hair Trace Elements Concentration to Describe Polymetallic Mining Waste Exposure in Bolivian Altiplano', *Biological Trace Element Research*, 139(1), pp. 10–23. https://doi.org/10.1007/s12011-010-8641-1.

Barbieri, F.L. *et al.* (2016) 'Toxic trace elements in maternal and cord blood and social determinants in a Bolivian mining city', *International Journal of Environmental Health Research*, 26(2), pp. 158–174. https://doi.org/10.1080/09603123.2015.1061114.

Biefeld, R.M. (2002) 'The metal-organic chemical vapor deposition and properties of III–V antimony-based semiconductor materials', *Materials Science and Engineering: R: Reports*, 36(4), pp. 105–142. https://doi.org/10.1016/S0927-796X(02)00002-5.

Bigham, J.M. *et al.* (1996) 'Schwertmannite and the chemical modeling of iron in acid sulfate waters', *Geochimica et Cosmochimica Acta*, 60(12), pp. 2111–2121. https://doi.org/10.1016/0016-7037(96)00091-9.

Brown, T.J. *et al.* (2019) *World Mineral Production, 2014-18*. British Geological Survey.

Calas, A. *et al.* (2015) 'The use of biomonitor *Tillandsia capillaris* to characterize the extent of atmospheric contamination by metals in the mining city of Oruro (Bolivia)', *Pollution Atmosphérique : climat, santé, société*, 226, pp. 1–9.

Chang, T.-L. *et al.* (1993) 'The isotopic abundance of antimony', *International Journal of Mass Spectrometry and Ion Processes*, 123(1), pp. 77–82. https://doi.org/10.1016/0168-1176(93)87056-X.

Dupont, D. *et al.* (2016) 'Antimony Recovery from End-of-life Products and Industrial Process Residues: A critical Review', *J. Sustain. Metall.*, 2, pp. 79–103. https://doi.org/10.1007/s40831-016-0043-y.

Ferrari, C., Resongles, E., Freydier, Remi, *et al.* (2021) 'A single-step purification method for the precise determination of antimony isotopic composition of environmental, geological and biological samples by HG-MC-ICP-MS', *Journal of Analytical Atomic Spectrometry*, 36(Issue 4), pp. 776–785. https://doi.org/10.1039/D0JA00452A.

Ferrari, C., Resongles, E., Freydier, Rémi, *et al.* (2021) 'Antimony isotopic fractionation in the environment: first insights from theorical and experimental investigations', in. *Goldschmidt*.

Filella, M. *et al.* (2009) 'Natural attenuation processes applying to antimony: A study in the abandoned antimony mine in Goesdorf, Luxembourg', *Science of The Total Environment*, 407(24), pp. 6205–6216. https://doi.org/10.1016/j.scitotenv.2009.08.027.

Filella, M., Belzile, N. and Chen, Y.-W. (2001) 'Antimony in the environment: a review focused on natural waters. I. Occurence', *Earth-Sciences Reviews*, 57, pp. 125–176.

Filella, M., Williams, P.A. and Belzile, N. (2009) 'Antimony in the environment: knows and unknowns', *Environmental Chemistry*, 6, pp. 95–105. https://doi.org/10.1071/EN09007.

Fukushi, K. *et al.* (2003) 'A natural attenuation of arsenic in drainage from an abandoned arsenic mine dump', *Applied Geochemistry*, 18(8), pp. 1267–1278. https://doi.org/10.1016/S0883-2927(03)00011-8.

Gaillardet, J., Viers, J. and Dupré, B. (2003) 'Trace Elements in River Waters', *Treatise on Geochemistry*, 5, p. 605. https://doi.org/10.1016/B0-08-043751-6/05165-3.

Goix, S. *et al.* (2011) 'Influence of source distribution and geochemical composition of aerosols on children exposure in the large polymetallic mining region of the Bolivian Altiplano', *Science of The Total Environment*, 412–413, pp. 170–184. https://doi.org/10.1016/j.scitotenv.2011.09.065.

Goix, S. (2012) *Origine et impact des pollutions liées aux activités minières sur l'environnement et la santé, cas de Oruro (Bolivie)*. Université de Toulouse. https://tel.archives-ouvertes.fr/tel-00781152/file/Goix_these.pdf.

Goix, S. *et al.* (2013) 'Transplantation of epiphytic bioaccumulators (Tillandsia capillaris) for high spatial resolution biomonitoring of trace elements and point sources deconvolution in a complex mining/smelting urban context', *Atmospheric Environment*, 80, pp. 330–341. https://doi.org/10.1016/j.atmosenv.2013.08.011.

Goix, S. *et al.* (2016) 'Metal concentration and bioaccessibility in different particle sizes of dust and aerosols to refine metal exposure assessment', *Journal of Hazardous Materials*, 317, pp. 552–562. https://doi.org/10.1016/j.jhazmat.2016.05.083.

Guo, W. *et al.* (2018) 'Environmental geochemical and spatial/temporal behavior of total and speciation of antimony in typical contaminated aquatic environment from Xikuangshan, China', *Microchemical Journal*, 137, pp. 181–189. https://doi.org/10.1016/j.microc.2017.10.010.

He, M. *et al.* (2012) 'Antimony pollution in China', *Science of The Total Environment*, 421–422, pp. 41–50. https://doi.org/10.1016/j.scitotenv.2011.06.009.

Hiller, E. *et al.* (2012) 'Arsenic and antimony contamination of waters, stream sediments and soils in the vicinity of abandoned antimony mines in the Western Carpathians, Slovakia', *Applied Geochemistry*, 27(3), pp. 598–614. https://doi.org/10.1016/j.apgeochem.2011.12.005.

Keutsch, F. and Brodtkorb, M.K. de (2008) 'Metalliferous paragenesis of the San José mine, Oruro, Bolivia', *Journal of South American Earth Sciences*, 25(4), pp. 485–491. https://doi.org/10.1016/j.jsames.2007.12.003.

Kimball, B.E. *et al.* (2009) 'Copper isotope fractionation in acid mine drainage', *Geochimica et Cosmochimica Acta*, 73(5), pp. 1247–1263. https://doi.org/10.1016/j.gca.2008.11.035.

Li, C. *et al.* (2020) 'High Antimony Source and Geochemical Behaviors in Mine Drainage Water in China's Largest Antimony Mine', *Polish Journal of Environmental Studies*, 29(5), pp. 3663–3673. https://doi.org/10.15244/pjoes/114970.

Li, S. *et al.* (2021) 'A new purification method based on a thiol silica column for high precision antimony isotope measurements', *Journal of Analytical Atomic Spectrometry*, 36, pp. 157–164. https://doi.org/10.1039/D0JA00367K.

Liang, Z. *et al.* (2018) 'Strong Associations Between Biogeochemical Factors and Sb Species in Sediments of the World's Largest Sb Mine (Xikuangshan) in China', *Journal of Geophysical Research: Biogeosciences*, 123(5), pp. 1548–1556. https://doi.org/10.1029/2018JG004481.

Liu, F. *et al.* (2010) 'Antimony speciation and contamination of waters in the Xikuangshan antimony mining and smelting area, China', *Environmental Geochemistry and Health*, 32(5), pp. 401–413. https://doi.org/10.1007/s10653-010-9284-z.

Lobo, L. *et al.* (2012) 'Investigation of natural isotopic variation of Sb in stibnite ores via multi-collector ICP-mass spectrometry - perspectives for Sb isotopic analysis of Roman glass', *Journal of Analytical Atomic Spectrometry*, 27, pp. 1304–1310. https://doi.org/10.1039/c2ja30062a.

Long, Z.-Y. *et al.* (2022) 'Fingerprinting the metal source and cycling of the world's largest antimony deposit in Xikuangshan, China', *GSA Bulletin* [Preprint]. https://doi.org/10.1130/B36377.1.

Manaka, M. *et al.* (2007) 'Natural attenuation of antimony in mine drainage water', *Geochemical Journal*, 41(1), pp. 17–27. https://doi.org/10.2343/geochemj.41.17.

Masbou, J. *et al.* (2020) 'Strong temporal and spatial variation of dissolved Cu isotope composition in acid mine drainage under contrasted hydrological conditions', *Environmental Pollution*, 266, p. 115104. https://doi.org/10.1016/j.envpol.2020.115104.

Nordstrom, D.K. (2000) 'Advances in the Hydrogeochemistry and Microbiology of Acid Mine Waters', *International Geology Review*, 42(6), pp. 499–515. https://doi.org/10.1080/00206810009465095.

Nordstrom, D.K., Blowes, D.W. and Ptacek, C.J. (2015) 'Hydrogeochemistry and microbiology of mine drainage: An update', *Applied Geochemistry*, 57, pp. 3–16. https://doi.org/10.1016/j.apgeochem.2015.02.008.

Quaghebeur, W. *et al.* (2019) 'Arsenic contamination in rainwater harvesting tanks around Lake Poopó in Oruro, Bolivia: An unrecognized health risk', *Science of The Total Environment*, 688, pp. 224–230. https://doi.org/10.1016/j.scitotenv.2019.06.126.

Resongles, E. *et al.* (2013) 'Fate of Sb(V) and Sb(III) species along a gradient of pH and oxygen concentration in the Canoulès mine waters (Southern France)', *Environmental Science Processes and Impacts*, 15, pp. 1536–1544. https://doi.org/10.1039/c3em00215b.

Resongles, E. *et al.* (2015) 'Antimony isotopic composition in river waters affected by ancient mining activity', *Talanta*, 144, pp. 851–861. http://dx.doi.org/10.1016/j.talanta.2015.07.013.

Ritchie, V.J. *et al.* (2013) 'Mobility and chemical fate of antimony and arsenic in historic mining environments of the Kantishna Hills district, Denali National Park and Preserve, Alaska', *Chemical Geology*, 335, pp. 172–188. https://doi.org/10.1016/j.chemgeo.2012.10.016.

Rouxel, O., Ludden, J. and Fouquet, Y. (2003) 'Antimony isotope variations in natural systems and implications for their use as geochemical tracers', *Chemical Geology*, 200, pp. 25–40. https://doi.org/10.1016/S0009-2541(03)00121-9.

Ruiz-Castell, M. *et al.* (2012) 'Child neurodevelopment in a Bolivian mining city', *Environmental Research*, 112, pp. 147–154. https://doi.org/10.1016/j.envres.2011.12.001.

Sonke, J.E. *et al.* (2008) 'Historical variations in the isotopic composition of atmospheric zinc deposition from a zinc smelter', *Chemical Geology*, 252(3), pp. 145–157. https://doi.org/10.1016/j.chemgeo.2008.02.006.

Tang, B. and Liu, S. (2009) 'Severe pollution of Xikuangshan antimony mine constitutes great environmental risk to local inhabitants', *Chinese environment* [Preprint].

Tanimizu, M. *et al.* (2011) 'Determination of natural isotopic variation in antimony using inductively coupled plasma mass spectrometry for an uncertainty estimation of the standard atomic weight of antimony', *Geochemical Journal*, 45, pp. 27–32.

Tapia, J. *et al.* (2012) 'Geochemical background, baseline and origin of contaminants from sediments in the mining-impacted Altiplano and Eastern Cordillera of Oruro, Bolivia', *Geochemistry: Exploration, Environment, Analysis*, 12(1), pp. 3–20. https://doi.org/10.1144/1467-7873/10-RA-049.

von Uexküll, O. *et al.* (2005) 'Antimony in brake pads-a carcinogenic component?', *Journal of Cleaner Production*, 13(1), pp. 19–31. https://doi.org/10.1016/j.jclepro.2003.10.008.

Viers, J., Dupré, B. and Gaillardet, J. (2009) 'Chemical composition of suspended sediments in World Rivers: New insights from a new database', *Science of The Total Environment*, 407(2), pp. 853–868. https://doi.org/10.1016/j.scitotenv.2008.09.053.

Wang, X. *et al.* (2011) 'Antimony distribution and mobility in rivers around the world's largest antimony mine of Xikuangshan, Hunan Province, China', *Microchemical Journal*, 97(1), pp. 4–11. https://doi.org/10.1016/j.microc.2010.05.011.

Wiederhold, J.G. (2015) 'Metal Stable Isotope Signatures as Tracers in Environmental Geochemistry', *Environmental Science & Technology*, 49(5), pp. 2606–2624. https://doi.org/10.1021/es504683e.

Wilson, N.J., Craw, D. and Hunter, K. (2004) 'Antimony distribution and environmental mobility at an historic antimony smelter site, New Zealand', *Environmental Pollution*, 129(2), pp. 257–266. https://doi.org/10.1016/j.envpol.2003.10.014.

Yang, W.-J. *et al.* (2019) 'Cadmium stable isotope variation in a mountain area impacted by acid mine drainage', *Science of The Total Environment*, 646, pp. 696–703. https://doi.org/10.1016/j.scitotenv.2018.07.210.

Zhou, W. *et al.* (2022) 'Antimony isotope fractionation during adsorption on aluminum oxides', *Journal of Hazardous Materials*, 429, p. 128317. https://doi.org/10.1016/j.jhazmat.2022.128317.

Supplementary information to:

Sb isotopes in surface waters of the mining and smelting city of Oruro, Bolivia

Colin Ferrari *[a], Eléonore Resongles [a], Rémi Freydier [a], Marisol Flores[b], Mauricio Ormachea[b], Gerardo Zamora[c] and Corinne Casiot [a]

[a]*HydroSciences Montpellier, Univ. Montpellier, CNRS, IRD, Montpellier, France*

*Corresponding author:

Mailing address : Université de Montpellier – CC 57
163, rue Auguste Broussonnet,
34090 Montpellier, France
Email : colin.ferrari@umontpellier.fr

This PDF file includes:

Additional table (Table S1).

Table S1: Hydride generation parameters used for Sb isotope ratio analysis by HG-MC-ICP-MS. These are optimized based on the ones indicated in Ferrari et al., (2021). The removal of the additional gas flow in the hydride generation system leaded to a better signal stability.

Hydride Generation Parameters	
System	HydrideICP - Elemental Scientific
Peristaltic Pump Speed	20 rpm
Reducing agent medium	$NaBH_4$ 1 % w/v in NaOH 0.05 % w/v
Acid medium	HCl 3 M
Waste tubing	Yellow/Blue - 1.52 mm ID / 1.28 $ml.min^{-1}$
Sample tubing	Black/Black - 0.76 mm ID / 0.48 $ml.min^{-1}$
$NaBH_4$ tubing	Orange/Yellow - 0.51 mm ID / 0.24 $ml.min^{-1}$
HCl tubing	Orange/Green - 0.38 mm ID / 0.12 $ml.min^{-1}$
Sample gas flow (Ar)	0.95 L min^{-1}
Instrument Settings	
Instrument	Neptune - Thermo Scientific
Forward power	1080 W
Skimmer Cone	X version
Sample Cone	Jet version
Measured isotopes	^{120}Sn, ^{121}Sb, ^{122}Sn, ^{123}Sb (^{123}Te), ^{126}Te
Cups	L1, C, H1, H2, H3
Sensitivity ^{121}Sb (V/ppb)	0.8
Acquisition Parameters	
Uptake time (s)	140
Number of blocks	1
Number of cycles per block	80
Integration Time (s)	4.194

Conclusion générale

L'objectif général de cette thèse est de contribuer à explorer le potentiel des isotopes de l'antimoine comme traceur de source et de processus biogéochimiques dans les milieux aquatiques, et plus particulièrement ceux pollués par l'activité minière, où les concentrations les plus élevées en antimoine sont mesurées. Le travail s'est organisé en différentes étapes complémentaires : une première étape de développement analytique visant à améliorer le traitement de l'échantillon préalable à l'analyse du rapport isotopique $^{123}Sb/^{121}Sb$, puis une seconde étape au cours de laquelle différentes approches (théorique, expérimentale, de terrain) ont été utilisées pour documenter les fractionnements isotopiques associés à des processus importants contrôlant le devenir de Sb dans les environnements miniers.

Le protocole de séparation de l'antimoine développé, utilisant de la poudre de silice mésoporeuse fonctionnalisée avec des groupements fonctionnels thiols, a montré une excellente efficacité pour isoler l'antimoine présent à basse concentration dans des matrices complexes, permettant ainsi l'analyse du rapport isotopique $^{123}Sb/^{121}Sb$ par ICP-MS-MC. Ce protocole ne nécessite pas d'étape préalable d'élimination des cations divalents, contrairement aux protocoles précédemment établis, ce qui le rend plus simple à mettre en œuvre et limite la perte d'antimoine. Il a été validé pour différentes matrices (roches, sédiments, plantes, sols, poussières, plastiques, sang et urine humaines) et pour de très faibles concentrations en antimoine (un minimum de 40 ng de Sb est requis pour les analyses). Cette méthode élimine la plupart des éléments susceptibles d'interférer au cours de l'analyse par HG-MC-ICP-MS (As, Cd, Co, Cr, Cu, Fe, Ni, Pb, Se, Sn). Les vastes possibilités d'exploitation de cette méthode de séparation constituent une avancée notable pour le développement des recherches sur l'isotopie de Sb dans l'environnement. Par ailleurs, le réglage des paramètres instrumentaux du couplage HG-MC-ICP-MS ont fait l'objet de plusieurs modifications au cours de la thèse, depuis les réglages initiaux utilisés au cours de la première année de ces travaux, et mentionnés dans le chapitre 2 et l'article Ferrari et al. (2021), jusqu'aux réglages actuels qui ont permis d'atteindre une stabilité et une précision optimales. Ces réglages optimaux sont synthétisés dans le chapitre 3, tableau S2.

L'étude des fractionnements isotopiques associés à différents processus biogéochimiques élémentaires a fourni les premières valeurs pour l'antimoine. Si l'étude théorique a montré un fractionnement important, de l'ordre de 0.9 ‰, lors de la chaine d'oxydation de la stibnite vers la cervantite, les études expérimentales et de terrain ont révélé des fractionnements isotopiques moindres (de l'ordre de 0.2-0.3 ‰) lors de l'oxydation biologique de l'espèce dissoute Sb(III) en Sb(V) ou lors de la sorption de ces espèces sur des minéraux de fer. L'étude théorique a permis d'identifier les principaux facteurs qui fractionnent le plus les isotopes de l'antimoine : le changement de degré d'oxydation de l'antimoine (les minéraux contenant Sb(V) sont plus lourds isotopiquement que ceux contenant du Sb(III)), le changement du plus proche voisin de l'antimoine (les liaisons Sb – O sont plus fortes que les liaisons Sb – S), et enfin, la distorsion du polyèdre atomique Sb – O et Sb – S (par exemple lors du changement du second voisin le plus proche (Sb(III) par Sb(V) notamment). Ces résultats ont permis d'interpréter en partie les résultats des études expérimentales : le fractionnement $\Delta^{123}Sb_{solide-solution}$ de -0.24 ± 0.06 ‰ et -0.35 ± 0.06 ‰ associé à l'adsorption de Sb(III) et Sb(V) sur des oxyhydroxydes de fer (ferrihydrite et schwertmannite) pourrait ainsi être expliqué par la distorsion du polyèdre atomique lors de l'ajout du fer comme second voisin le plus proche, ce qui, à l'instar des structures modélisées, provoque un enrichissement préférentiel en isotopes légers de la phase déformée, d'environ 0.3 ‰. En ce qui concerne le processus d'oxydation de Sb(III) en Sb(V) en solution, les résultats expérimentaux, en cours d'interprétation, se sont révélés distincts des prévisions

théoriques et des observations relatives à d'autres couples rédox, tant pour l'oxydation chimique que pour l'oxydation microbiologique. En effet, l'oxydation chimique par H_2O_2 n'a pas montré de fractionnement isotopique significatif entre les phases oxydée et réduite. L'oxydation biologique a engendré un fractionnement $\Delta^{123}Sb_{Sb(V)-Sb(III)}$ de faible amplitude, de -0.20 ± 0.07 ‰, avec un enrichissement en isotopes légers dans la phase oxydée. Si ce résultat reste cohérent avec le prélèvement préférentiel des isotopes légers par les processus biologiques, la compréhension de l'origine de ce fractionnement de faible amplitude mérite des recherches plus approfondies.

Les résultats de l'étude de terrain se sont révélés cohérents avec les résultats issus des expérimentations de laboratoire. En effet, compte-tenu de l'atténuation naturelle de Sb observée le long du drainage minier acide de San José jusqu'au lac Uru-Uru à Oruro (Bolivie), l'augmentation progressive de la composition isotopique de Sb dissous le long de ce continuum a pu être attribuée à l'adsorption de Sb sur des oxyhydroxydes de fer néoformés, avec un fractionnement isotopique entre l'eau et le sédiment $\Delta^{123}Sb_{eau\text{-}sédiments}$ de l'ordre de 0,3 ‰, similaire à celui mesuré lors des expérimentations. Bien que certains processus doivent encore être étudiés individuellement en laboratoire afin d'être identifiés sur le terrain, cette étude a montré que l'isotopie de l'antimoine pouvait, en complément de traceurs géochimiques traditionnels, fournir des informations sur l'occurrence d'un processus ou la mobilisation d'une source particulière, même dans des environnements complexes comme les environnements miniers.

L'ensemble des processus étudiés et les fractionnements associés sont schématisés et résumés sur la Figure 36.

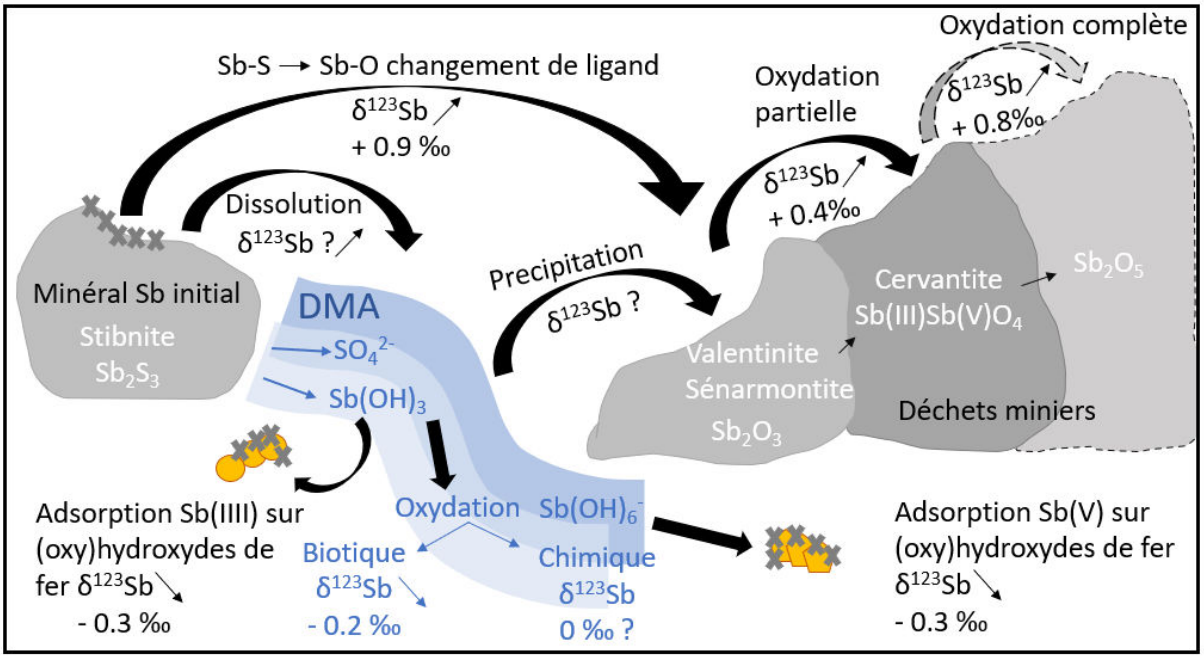

Figure 36: Schéma récapitulatif des processus étudiés et leur impact sur le fractionnement isotopique de l'antimoine. Les points d'interrogation représentent des processus qui n'ont pas été étudiés dans le cadre de cette thèse et qui ne sont pas actuellement quantifiés ou pour lesquels une incertitude sur la valeur subsiste.

Perspectives :

Ce travail souligne l'importance d'étudier, par des approches expérimentales ou théoriques, les processus environnementaux susceptibles d'induire un fractionnement isotopique de l'antimoine afin d'interpréter les signatures dans l'environnement et éventuellement de pouvoir utiliser les isotopes de Sb comme traceurs de sources et de processus dans des environnements complexes. Il est important de poursuivre la caractérisation de certains autres processus clés associés aux environnements miniers (dissolution de minéraux sulfurés, précipitation de minéraux secondaires) et de mieux comprendre les fractionnements associés au processus d'oxydation biotique et abiotique en solution. Des études théoriques concernant le fractionnement entre différentes espèces en solution, en particulier entre des espèces libres et complexées (avec le chlorure, la matière organique, etc…) ou entre les espèces sorbées sur différents types de surfaces (phases minérales naturelles, matière organique) et les espèces dissoutes seraient nécessaires pour la compréhension des causes des fractionnements isotopiques observés dans la nature. L'exploration des isotopes de l'antimoine dans d'autres environnements, en particulier l'environnement urbain, dans lequel cet élément est enrichi, pourrait contribuer à mieux caractériser les sources de ce polluant émergent et les processus qu'il subit au cours de son cycle biogéochimique.

Résumé

L'antimoine (Sb) est un polluant d'intérêt prioritaire émergent dans l'environnement et potentiellement cancérigène. L'objectif général de cette thèse est de contribuer à explorer les potentialités des isotopes stables de l'antimoine ($^{121}Sb/^{123}Sb$) pour tracer les sources et les processus dans les milieux aquatiques et principalement en aval de sites miniers. Après avoir dans un premier temps développé et validé une nouvelle méthode de séparation et d'analyse des isotopes de l'antimoine, les fractionnements isotopiques associés à différents processus biogéochimiques ont été étudiés par une approche théorique, une approche expérimentale, ainsi qu'une étude de terrain, sur l'hydrosystème en aval du drainage minier acide de San José à Oruro (Bolivie). Le sens et l'amplitude de ces fractionnements ont été caractérisés afin de pouvoir interpréter les signatures $\delta^{123}Sb$ dans l'environnement. Les études théoriques ont mis en évidence les principaux processus fractionnant les isotopes de l'antimoine : l'oxydation partielle ou totale de Sb(III) dans les minéraux ($\Delta^{123}Sb_{V\text{-}III}$ de +0.4 à +1.2 ‰), le changement du plus proche voisin de l'antimoine ($\Delta^{123}Sb_{Sb\text{-}O\,-\,Sb\text{-}S} \approx +0.9$ ‰), et enfin, la distorsion du polyèdre atomique Sb – O et Sb – S ($\Delta^{123}Sb_{distordu\text{-}symmétrique} \approx -0.3$ ‰). Les études expérimentales ont montré une adsorption préférentielle des isotopes légers sur les oxyhydroxydes de fer ($\Delta^{123}Sb_{adsorbé\text{-}dissous} \approx -0.3$ ‰), un enrichissement en isotopes légers de $Sb(V)_{aq}$ ($\Delta^{123}Sb_{Sb(V)\text{-}Sb(III)} \approx -0.2$ ‰) lors de l'oxydation microbiologique de $Sb(III)_{aq}$, et une absence de fractionnement lors d'une oxydation chimique avec H_2O_2. L'étude de terrain a montré une augmentation de $\delta^{123}Sb$ de +0.42 à +0.70 ‰ dans l'eau en aval du DMA de San José, en lien avec l'atténuation naturelle de l'antimoine par sorption sur les minéraux de fer, et a mis en évidence des variations saisonnières de $\delta^{123}Sb$ des eaux du lac Uru-Uru, de +0.28 ‰ à +0.55 ‰, attribuées à une contribution variable du DMA et de la rivière drainant la fonderie de Vinto. Dans leur ensemble, les résultats confirment le potentiel qu'ont les isotopes de l'antimoine comme traceurs de sources et de processus dans les milieux aquatiques, en particulier dans les environnements miniers et industriels, et suggèrent la nécessité de poursuivre les recherches visant à caractériser d'autres processus importants et à mieux comprendre l'origine des fractionnements observés.

Abstract

Antimony (Sb) is an emerging priority pollutant in the environment and a potentially carcinogenic element. The general objective of this thesis is to contribute to exploring the potential of stable isotopes of antimony ($^{121}Sb/^{123}Sb$) to trace sources and processes in aquatic environments and especially downstream from mining sites. After development and validation of a new method for the separation and analysis of antimony isotopes, the isotopic fractionations associated to different biogeochemical processes were studied by a theoretical approach, an experimental approach, as well as a field study conducted on the hydrosystems downstream from the acid mine drainage of the San José mine in Oruro (Bolivia). The direction and amplitude of these fractionations have been characterized in order to interpret the $\delta^{123}Sb$ signatures in the environment. Theoretical studies have highlighted the main processes fractionating antimony isotopes: the partial or total oxidation of Sb(III) in minerals ($\Delta^{123}Sb_{V\text{-}III}$ from +0.4 to +1.2 ‰), the change of the nearest neighbor of antimony ($\Delta^{123}Sb_{Sb\text{-}}$

$_{O-Sb-S}$ ≈ +0.9 ‰), and finally, the distortion of the atomic polyhedron Sb – O and Sb – S ($\Delta^{123}Sb_{distordu-symmetrical}$ ≈ -0.3 ‰). Experimental studies have shown a preferential adsorption of light isotopes on iron oxyhydroxides ($\Delta^{123}Sb_{adsorbed-dissolved}$ ≈ -0.3 ‰), an enrichment in light isotopes in $Sb(V)_{aq}$ ($\Delta^{123}Sb_{Sb(V)-Sb(III)}$ ≈ -0.2 ‰) during the microbiological oxidation of $Sb(III)_{aq}$, and a lack of fractionation during chemical oxidation with H_2O_2. The field study showed a decrease in $\delta^{123}Sb$ from +0.42 to +0.70 ‰ downstream from the AMD of San José, in relation with the natural attenuation of antimony by sorption on iron minerals, and highlighted seasonal variations of $\delta^{123}Sb$ in the waters of Lake Uru-Uru, from +0.28‰ to +0.55‰, attributed to a variable contribution of the AMD and the river draining the Vinto smelter. Taken together, the results support the potential of antimony isotopes as tracers of sources and processes in aquatic environments, particularly in mining and industrial areas, and suggest the need for further research in order to characterize other important processes and to better understand the origin of the observed fractionations.